The implementation of alkali-activated concrete in jointless ground floors

Maarten E. Meek

Master Thesis

2019

TU Delft

abt

The implementation of alkali-activated concrete in jointless ground floors

by

Maarten Eelke Meek

In partial fulfilment of the requirements for the degree of

Master of Science
in Civil Engineering

at the Delft University of Technology,
to be defended publicly on the 27th of May, 2019 at 15:30 PM.

Thesis committee:

Dr. ir. drs. C.R. Braam (chair)	TU Delft
Dr. ir. M.A.N. Hendriks	TU Delft
Ing. T. van Wolfswinkel	ABT
Ir. J.N. Houben (coordinator)	TU Delft

An electronic version of this thesis is available at http://repository.tudelft.nl/.

Acknowledgements

Summary

The concrete industry is facing significant environmental challenges, since sustainable development is currently an important issue and the production of concrete provides a considerable contribution to earth's global warming. This is mainly accountable to cement, one of the main components of concrete, of which Ordinary Portland cement (OPC) is the world's most used cement type. To produce cement clinkers, high-temperature decomposition of limestone is required. This process is energy-intensive and responsible for 5-8% of the global carbon dioxide (CO_2) emissions. The Netherlands has the ambition to reduce the CO_2-emission of its concrete sector by a minimum of 35% by the year 2030 relative to the emission of the year 2010, and the goal to reach a 95% CO_2 reduction in the year 2050 relative to the year 1990.

Alkali-activated concrete (AAC), also known as geopolymer concrete, is realised without cement and is therefore an interesting candidate to reach the set CO_2 objectives of The Netherlands. Alkali-activated material (AAM) is the binder in AAC and is realised with pozzolanic materials, called the precursors, in combination with an alkaline activator, hence the name. Common precursors are fly ash and blast furnace slag, while typical alkaline activators are sodium-hydroxide and sodium silicate. The pozzolanic materials react in the alkaline environment created by the activator, resulting in a hardened binding material. This AAM acts similar to cement paste, such that, in addition with aggregates, a concrete without cement can be realised. The CO_2 equivalent emissions of AAM can have an 80% or greater reduction compared to traditional Portland cement. Compared to the more common applied blast furnace cement CEM III/B a reduced CO_2 footprint between 25–65% is achievable with AAM, the reduction mainly depends on the type and concentration of the alkali-activator used. This reduced CO_2 footprint for AAM and a display of excellent strength and chemical resistance properties show the potential AAC has.

Alkali-activated concrete shows promising behaviour for structural concrete applications. However, since it is relatively new, it has not been established worldwide. There are currently no regulations for the structural application of AAC, and it is therefore hardly implemented in a structural manner. However, the mechanical properties of AAC make it interesting to be used in certain structural applications, e.g. the concrete ground floor industry.

This thesis is about the implementation of AAC in jointless elastically supported ground floors. Nowadays, these floors are realised with a hybrid reinforcement. Hybrid meaning that, in addition to traditional reinforcement meshes, also steel fibres are added to the concrete mixture. Besides the promising sustainable aspects, AAC also tends to show promising mechanical properties for industrial concrete ground floors. In this thesis, AAC is assessed for the use in jointless elastically supported ground floors to find out whether a more sustainable jointless ground floor is achievable with AAC. The main research question of this thesis is therefore:

"To what extent can elastically supported jointless concrete ground floors be constructed in a more efficient way when realised in alkali-activated concrete compared to traditional concrete?"

The research question is divided into several sub-questions to approach an answer for the main research question properly. Initially, the structural design principles of the jointless floor are researched, for which design guides are followed and design calculations are performed to find the governing design aspect and the most relevant concrete properties. The control of cracking follows to be this governing design aspect, where crack formation occurs from the restrainment of the shrinkage. Then, the material AAC is introduced and from a literature study a link is made for the relevant concrete material properties between AAC and OPC concrete of similar strength class. As the shrinkage of the concrete is the governing imposed load for the jointless ground

floor, the influence of the total shrinkage value and the floor thicknesses is dealt with. From which it follows that a reduction in shrinkage is essential for a jointless floor to be realised in a thinner cross-section. A parametric study is performed on the relevant concrete properties, the reinforcement and the steel fibre residual flexural strength, to find their influence on the crack-widths and on the floor's ability to carry the external loads. Based on this study, an optimal cross-section for a jointless AAC ground floor is considered. Finally, in the last chapter, more accurate crack-width calculations are performed by studying the non-linear behaviour of the material with theoretical models and with finite element analysis (FEA). The FEA is performed with the software program DIANA, a commonly used tool suitable for the analysis of non-linear behaviour for structural elements. There is some doubt around DIANA's accuracy for crack-widths computations, which is studied in this final chapter as well. Following this summary a diagram is presented visualising this process of the thesis.

The concrete industrial jointless ground floors are concrete floors with large areas without dilatation joints. In practice, dilatations are unable to fully prevent crack formation and are accompanied by discomfort for passing reach trucks. The dilatation free floors, i.e. the jointless floors, are on the contrary durable and user friendly. Performed calculations, that are in line with design guides for elastically supported ground floors, show that the ultimate limit state (ULS) unity checks are met rather easily for an elastically supported concrete floor. When loaded by back-to-back racking's, resulting in heavy point loads, or by bulk loads, resulting in heavy uniformly distributed loads, the relatively thin floor is sufficiently able to carry the loads to the subsoil. The control of cracking in the serviceability limit state (SLS) is therefore, in most cases, governing for jointless concrete ground floors. The crack-widths must be controlled to ensure the functionality and durability of the concrete floor. A maximum crack-width of 0.3 mm is set for indoor environments. To ensure the control of cracking, the preferable design of a jointless concrete floor has a minimum thickness of 160 mm, with a minimum top reinforcement mesh with a bar diameter of 7 mm and a centre-to-centre distance of 100 mm (ϕ7-100 mm) combined with a minimum steel fibre content of 30 kg/m^3.

Crack formation occurs from an imposed, restrained deformation that results in imposed loads that cause tensile stresses, reaching the concrete tensile strength. The governing imposed deformation is the drying shrinkage. The evaporation of water within the concrete occurs through the top surface of the floor only, if the concrete floor is realised on a suitable subsoil. Since the top part of the floor shrinks more than the bottom part, a shrinkage gradient develops over the height of the floor's cross-section. This causes a warping effect and by reaching the bending cracking moment of the cross-section, crack formation occurs at the top surface. The shrinkage essentially defines the slenderness of the floor and thus the minimum thickness. The minimum thickness is to ensure that crack formation only occurs from bending and prevents that the warping effect lifts the floor from the ground. When the floor is not thick enough, the uniform shrinkage over the height develops too rapid, making the floor crack from pure tension. The latter must be prevented since this results in uncontrollable crack-widths with the applied minimum reinforcement.

Through examination of the crack-width calculations, its results for different values and the effect of the drying shrinkage, as explained above, the most important concrete properties are defined. For a jointless concrete floor these are (i) the shrinkage size, (ii) the tensile strength, (iii) the modulus of elasticity and (iv) the bond strength. The typical AAC values for these material properties are derived from literature and a link is made between AAC and OPC concrete. It follows that, for AAC, a reduced shrinkage size is possible, but also an increased shrinkage size. The shrinkage size is influenced by the type and concentration of the precursor and activator and whether proper curing is applied. A reduced shrinkage size is associated with a slower drying shrinkage development rate, allowing for the jointless floor to be realised in thinner cross-sections. AAC tends to show higher tensile strengths and lower moduli of elasticity compared to

OPC concrete of similar strength grades. The former is disadvantageous since it will increase the tensile stresses that have to be taken over by the reinforcement, resulting in larger crack-widths; the latter is beneficial since internal or external loads will cause lower stresses. The possible reduced thickness outweighs the increased tensile strength since the bending cracking moment of the cross-section is reduced. The bond strength of AAC is better and results in shorter anchorage lengths and smaller crack-widths, a proposed relation for the improved bond strength of AAC is introduced.

A reduced final shrinkage of 0.3‰ is considered, a realisable value with AAC. It follows that a reduced floor thickness of 130 mm is possible, being the first step to a more utilised jointless floor. Further optimisation of the AAC floor is done through a parametric study. To find suitable AAC floor cross-sections of reduced thickness that require less steel, either by applying a finer reinforcement mesh or by lowering the necessary steel fibre content. For this a multitude of variants is computed by performing the crack-width and ULS unity checks calculations for varying concrete and reinforcement properties. Analysis of the results finds that, due to the reduced bending cracking moment of the cross-section, one can reduce the minimum bar diameter applied for the top reinforcement mesh without increasing the steel fibre content above normal values. A floor constructed in AAC with a reduced shrinkage size can be realised with a thickness of 130 mm, a top reinforcement mesh of ϕ6-100 mm with a steel fibre content of 35 kg/m³ and fulfil the SLS and ULS unity checks.

In the parametric study the crack-widths are computed by the so called direct method, which assumes linearization of the stresses within the discontinuity area. To compute crack-widths of increased accuracy, the non-linear material behaviour within the discontinuity area around cracks is examined, and bond-slip crack-width calculations are performed. This is done for a reinforced concrete tensile member. With different bond stress-slip relations, the stresses and slip values are computed in an analytical manner and with FEA in DIANA. For the FEA a 2D-model of the reinforced tensile member is made. This is done with a bond-slip reinforcement interface and discrete cracking interfaces to simulate the opening of the concrete crack. The crack-widths computed with the direct method, the analytical method and the FEA method are compared.

The results show that the direct method underestimates the crack-widths. The underestimation of the crack-widths increases for higher concrete tensile strengths, due to an overestimation of the bond stress. Additionally, the results show that, in comparison to the analytical method, DIANA computes the steel and concrete stresses accurately. However, significant differences are found for the bond stress development, resulting in the underestimation of the crack-widths. The analytical approach follows the theory in a more direct fashion and is used to study the improved bond strength of AAC with the fib Model Code 2010 bond-slip relation and the proposed improved bond-slip relation for AAC. With the improved bond-slip relation for AAC 26% smaller crack-widths are found compared to the bond-slip relation for traditional concrete, which is beneficial considering the governing design aspect for the jointless floor being the control of cracking.

To conclude, it is possible to realise an industrial jointless floor in alkali-activated concrete that per square meter floor can save in materials around 20% concrete and 30% steel, in reinforcement and fibres, compared to the standard industrial jointless floor realised in traditional concrete. From a sustainable point of view the jointless floor realised in alkali-activated concrete is more efficient in two aspects. First, due to the improved material properties the just named reduction of materials is possible. And second, the floor is realised in a concrete that has a lower CO_2 footprint since the production of its materials are more sustainable.
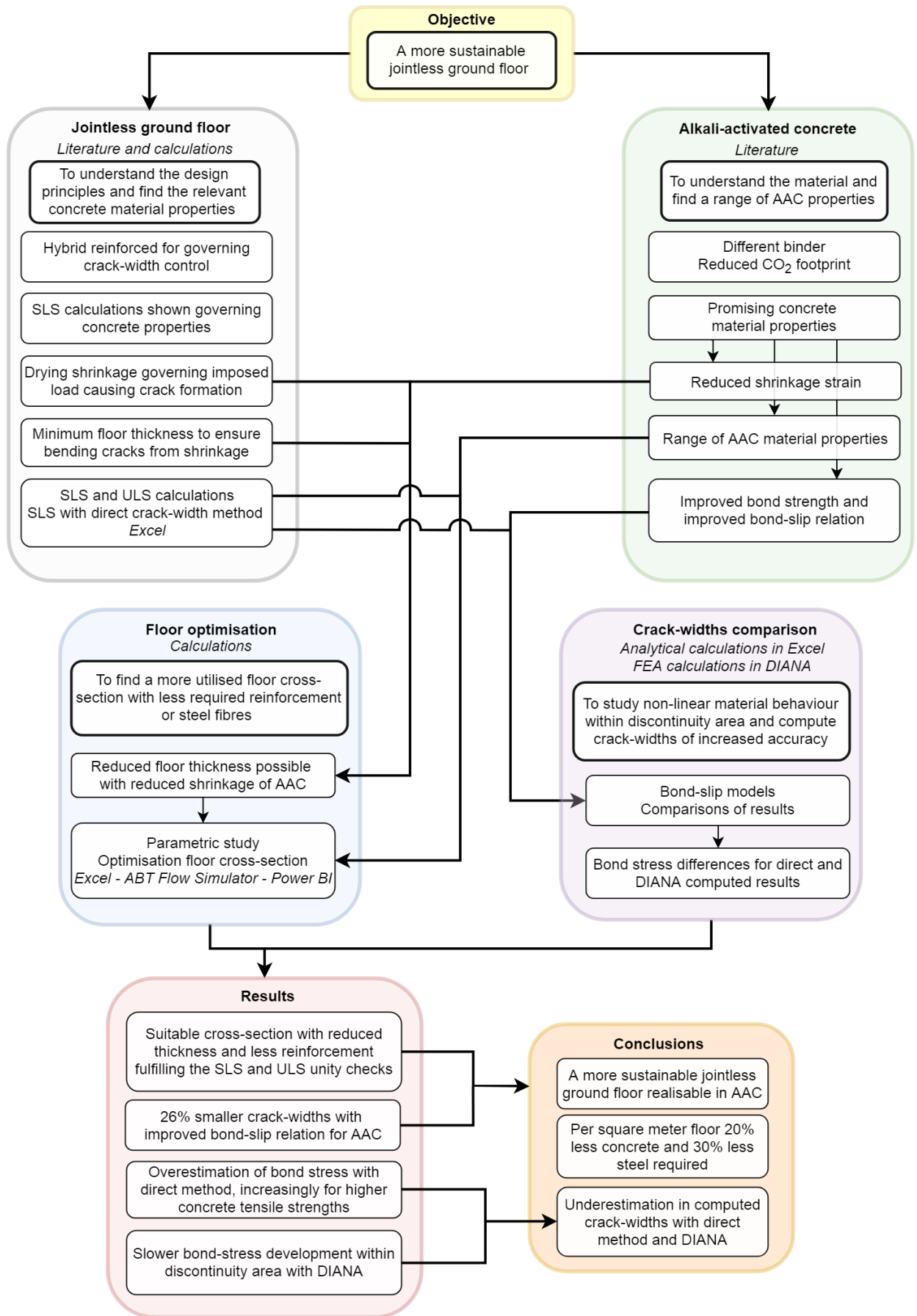
Thesis process diagram

Objective

A more sustainable jointless ground floor

Jointless ground floor
Literature and calculations

To understand the design principles and find the relevant concrete material properties

Hybrid reinforced for governing crack-width control

SLS calculations shown governing concrete properties

Drying shrinkage governing imposed load causing crack formation

Minimum floor thickness to ensure bending cracks from shrinkage

SLS and ULS calculations
SLS with direct crack-width method
Excel

Alkali-activated concrete
Literature

To understand the material and find a range of AAC properties

Different binder
Reduced CO_2 footprint

Promising concrete material properties

Reduced shrinkage strain

Range of AAC material properties

Improved bond strength and improved bond-slip relation

Floor optimisation
Calculations

To find a more utilised floor cross-section with less required reinforcement or steel fibres

Reduced floor thickness possible with reduced shrinkage of AAC

Parametric study
Optimisation floor cross-section
Excel - ABT Flow Simulator - Power BI

Crack-widths comparison
Analytical calculations in Excel
FEA calculations in DIANA

To study non-linear material behaviour within discontinuity area and compute crack-widths of increased accuracy

Bond-slip models
Comparisons of results

Bond stress differences for direct and DIANA computed results

Results

Suitable cross-section with reduced thickness and less reinforcement fulfilling the SLS and ULS unity checks

26% smaller crack-widths with improved bond-slip relation for AAC

Overestimation of bond stress with direct method, increasingly for higher concrete tensile strengths

Slower bond-stress development within discontinuity area with DIANA

Conclusions

A more sustainable jointless ground floor realisable in AAC

Per square meter floor 20% less concrete and 30% less steel required

Underestimation in computed crack-widths with direct method and DIANA

| Chapter 1 | Chapter 2 & 3 | Chapter 4 | Chapter 5 | Chapter 6 | Chapter 5 & 6 | Chapter 8 |

TABLE OF CONTENTS

List of abbreviations

AAC	Alkali-activated concrete
AAM	Alkali-activated material
BFS	Blast furnace slag
C-(A)-S-H	Calcium-(Alumino)-Silicate-Hydrate
CO_2	Carbon dioxide
EFC	Earth Friendly Concrete
FA	Fly ash
FEA	Finite element analysis
GPC	Geopolymer concrete
N-A-S-H	Sodium-Alumino-Silicate-Hydrate
OPC	Ordinary Portland cement
RCA	Recycled Concrete Aggregate
RH	Relative humidity
SLS	Serviceability limit state
UC	Unity check
UDL	Uniformly distributed load
ULS	Ultimate limit state

1 INTRODUCTION

1.1 Background

The concrete industry is facing challenges as sustainable development is an important environmental issue at the present time. The production of concrete is a contributor to the global warming of the planet. One of the main components for concrete is cement, Ordinary Portland cement (OPC) is the world's most used cement type. This is due to the fact that OPC can be produced from limestone, a natural resource that is available almost everywhere. Combined with the relatively low costs and the very well-known good performing properties OPC offers to concrete.

Nowadays about 10 billion m^3 of concrete is produced each year, this means a little more than 1 m^3 of concrete per person per year. This makes concrete the second-most used commodity in the world, only behind water being the most used commodity, meaning enormous volumes of production for cement are needed (Aïtcin, 2000). To produce Portland cement clinkers from limestone high-temperature decomposition of limestone is required. This process is very energy-intensive and responsible for 5-8% of the global carbon dioxide (CO_2) emissions (Provis & Van Deventer, 2014). As the demand for cement is growing rapidly worldwide, the last 20 years the cement consumption saw an almost exponential growth. It is estimated that by the year 2020 the demand of OPC will reach 4.3 billion tonnes, which was 3.2 billion tonnes in 2010 and half of that in 2000. This will result in unsustainable CO_2 emissions but also in the over-exploitation of the natural resources, particularly the limestone quarries (Garcia-Lodeiro, Palomo, & Fernández-Jiménez, 2015a).

On the 10th of July 2018 the "Betonakkoord", the 'Concrete Agreement', was signed in The Netherlands by several ministries and companies. With this agreement it has been stated that by 2030 the CO_2 emission must be reduced by minimally 35% in the concrete sector, preferably 49%, relative to the emissions of the year 2010. In the year 2050 this should be reduced to 95%, relative to the CO_2 emissions of 1990. This also shows a need for an increase of the demand for 'green concrete'. Circularity is also an important aspect of the "Betonakkoord", by 2030 the concrete in The Netherlands should be fully recyclable.

An interesting candidate to reach the set CO_2 objectives of The Netherlands can be alkali-activated concrete (AAC). AAC is a concrete that is realised without using cement. The binding material for AAC is not realised with water plus cement like traditional concrete but through a different chemical process and with different materials. The alkali-activated material (AAM) is the binder in an AAC and is realised with pozzolanic materials in combination with an alkali activator, hence the name. The pozzolanic materials react in the alkaline environment created by the activator resulting in a hardened binding materials which exists out of alkali-activated aluminosilicates. This AAM acts similar like cement paste, such that in addition with aggregates a concrete without cement can be realised. Figure 1.1 shows the difference and similarity between

regular concrete and AAC. Alkali-activated concrete is more well known by the popularly name of geopolymer concrete, however the term alkali-activated concrete is the general correct term for the concrete described here and therefore used throughout this thesis report.
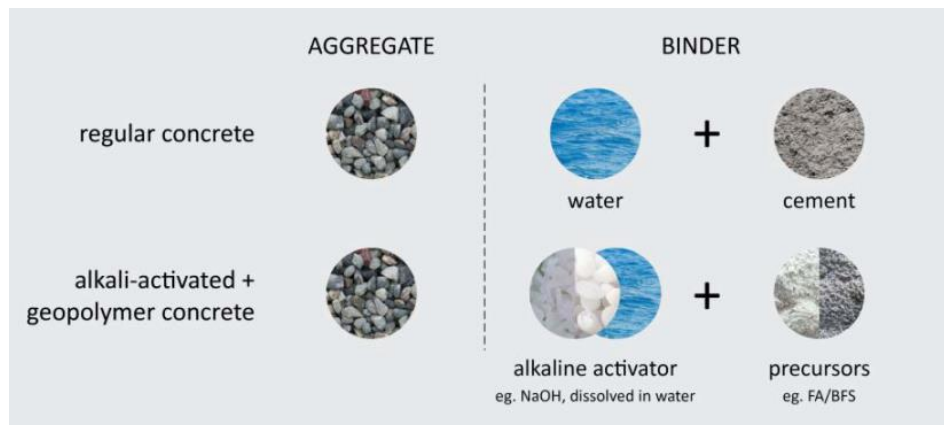
Figure 1.1 Composition of regular concrete and alkali-activated concrete (Prinsse, 2017).

One of the primary advantages of alkali-activated materials compared to traditional cement from an environmental perspective is the lower CO_2 emission rate from production. In geopolymer synthesis from ashes and/or slags a high temperature calcination step is absent. The calcination of cement clinkers does not only require a lot of fossil fuel-derived energy, it also releases CO_2 as a reaction product. Approximately 0.815 tonnes of CO_2 is released per tonne of binder from the cement clinker production. In comparison, the CO_2 emission of alkali-activated materials are considered to be lower. The CO_2 equivalent emissions of AAM, from the production of the dissolved solids sodium and silica which are the principal emitting components, can in general deliver an 80% or greater reduction compared to traditional Portland cement (Duxson, Provis, Lukey, & van Deventer, 2007). This much smaller CO_2 footprint for AAM and a display of very good strength and chemical resistance properties show the potential AAC has.

Even though the knowledge of alkali-activated materials has been around for more than 70 years, only in the last decades has it received a lot of attention due to the rising environmental issues in the world. Alkali-activated concrete shows promising behaviour for structural concrete applications, however due to its relatively new being worldwide use has not been established yet. The last years an increase of research is seen around alkali-activated materials, but there is still not enough knowledge about the performance of this cement free binding material, that more research is required. As for now, there are no regulations and codes yet to apply alkali-activated concrete structurally, which is one of the reasons more research is required to see the implementation of alkali-activated concrete within concrete structures.

The appraised promising performance of alkali-activated concrete and its reduced CO_2 footprint compared to traditional concrete has given rise to its introduction and first non-structural implementations within The Netherlands. Certain mechanical concrete properties of alkali-activated concrete make the material interesting to implement it in certain structural applications. The concrete ground floor industry is one of these applications and is the structural application that is considered for the implementation of alkali-activated concrete within this thesis.

1.2 Scope

In The Netherlands new warehouses and big industrial halls are being build yearly. The proportion of modern distribution centres has increased considerably in the recent years. This is

partly down to the burgeoning online shopping market and the scarcity of immediately available modern logistics real estate. Only in the first six months of 2017 around 363,000 m² of logistics real estate has been realised (Bertens & Geijtenbeek, 2017). The strong increase is partly due to the rise of mega-halls; distribution - and storage centres with an area of 40,000 m² or more. The demand in square meters for storage, transhipment and groupage over the years is shown in Figure 1.2. In 2017 the entire demand for logistics real estate was 2,376,000 square meters of which around 1.5 million square meters was demand for new build (Bak, 2018).
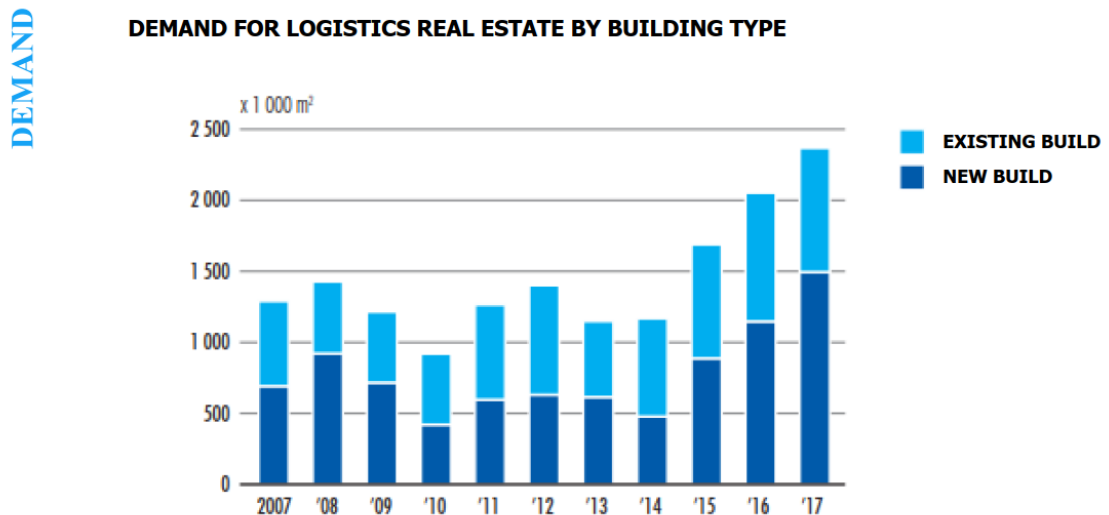
Figure 1.2 Demand in square meters for logistics real estate by building type throughout the years. Picture edited from Bak (2018).

The one thing that most of these warehouses and industrial facilities have in common is the ground floor, which is realised in concrete. The total supply for logistics real estate met its demand area wise of 2017, for which at least 500,000 square meters was new build (Bak, 2018). So in 2017 an area of roughly 100 football fields of new industrial concrete ground floors was made.

A lot of CO_2-emissions could be saved here if these huge areas of newly made concrete floors could be realised with a concrete that is more environment friendly. In this thesis alkali-activated concrete is studied to see the possibility whether alkali-activated concrete could be this new material for the industrial ground floors. Such industrial concrete ground floors, like in Figure 1.3, are floors that can be realised in two different systems. Either directly on the subgrade such that the floor is elastically supported by the soil or so that the floor is supported by foundation piles.

Figure 1.3 A jointless concrete ground floor (ABT, 2015c).

In The Netherlands a lot of the industrial ground floors are made without piles, so the floor is elastically supported by the ground, i.e. a floor on grade. With proper soil conditions a difference in settlements between a floor on grade and a floor on piles isn't necessarily present. A floor on grade carries the load directly to the subsoil and the floor can therefore be realised thinner and with less reinforcement. Because there is no pile foundation required to be build, a concrete floor on grade can be constructed faster and cheaper (Loonen N. , 2018).

Since the 1990's such industrial ground floors are being realised in the jointless floor manner, a floor made without dilatation joints. This originated from the damage expertise as damages were often seen at the position of dilatation joints. Concrete floors realised in a jointless manner allow an industrial floor to be constructed, durable and user friendly, that can satisfy all the demands of the user. A jointless concrete ground floor of high quality and proper durability can be realised with areas larger than 10.000 m² (ABT, 2015c). In typical storage warehouses racking's will be placed on the concrete floor which can accommodate for high point loads and in the case of bulk storage for high uniformly distributed loads. Figure 1.4 shows two examples for the use of such a concrete ground floor.

Figure 1.4 Typical floor loadings. Left: a racking warehouse. Right: bulk storage. Figures adapted from (Loonen N. , 2018).

Concrete floors elastically supported by the ground and realised without dilatation joints, i.e. a jointless floor, are the considered floor type for this study. In modern structural concrete ground floors, the jointless floor designs made at ABT are made with the addition of steel fibres to the concrete mixture. Steel fibres with end anchorages are used as these offer the most effectiveness (ABT, 2015b). The concrete floors are reinforced with traditional reinforcing steel bars and with steel fibres, this combination is called hybrid reinforced concrete.

In the principle of jointless floor design, limiting the concrete shrinkage is one of the most important aspects (ABT, 2015a). As a concrete floor that undergoes less shrinkage can be realised with a thinner cross-section, a lot of concrete materials can be saved when talking about the huge quantities of square meters realised each year. This is where the implementation of alkali-activated concrete becomes interesting. Besides the promising sustainable benefits alkali-activated concrete can show less shrinkage compared to traditional OPC based concrete (DELTA Concrete Consult, 2018). The performance of alkali-activated concrete, considering the structural properties like the compressive strength, tensile strength and modulus of elasticity, are similar to traditional concrete.

The compressive strength of concrete is mostly dependent of the aggregates, because the aggregates aren't different between alkali-activated concrete and traditional concrete the compressive strength is comparable between the two. Whereas the tensile strength is more defined by the binding material, which is completely the case for shrinkage, differences can be found for these concrete material properties.

In order to see whether alkali-activated concrete can be used as a construction material in industrial jointless concrete floors it is important to investigate all the relevant aspects of such a structure. Throughout this thesis information is provided to answer certain questions like: *What are the most important structural aspects of an elastically supported industrial concrete ground floor? What is the effect of shrinkage on the behaviour of a jointless concrete floor? What is alkali-activated concrete and how do its mechanical properties develop over time? What kind of benefits can alkali-activated concrete offer in comparison to Ordinary Portland cement concrete?*

One of the effects the shrinkage will have on the floor is that it causes cracks to arise at the top surface of the concrete floor, which have to be controlled. It will follow that the control of cracking is one of the essential aspects towards the design of a jointless concrete ground floor. With a good insight into the structure, strength and stiffness properties of the used material linear and non-linear material behaviour can be studied. Initially, with linear material behaviour and calculations, the global structure will studied. Afterwards, the cracking behaviour will be computed with a more realistic interaction between the concrete and reinforcement, by studying the non-linear material behaviour around cracks. With design models and the finite element analysis (FEA) software DIANA, these non-linear calculations will be computed. In combination with the answers to the sub-questions and with the (non)-linear analysis of the concrete structure an answer will be formed for the main research question of this thesis:

 "To what extent can elastically supported jointless concrete ground floors be constructed in a more efficient way when realised in alkali-activated concrete compared to traditional concrete?"

This thesis is about the implementation of AAC in jointless elastically supported ground floors. Thus, AAC is assessed for the use in jointless elastically supported ground floors to find out whether a more sustainable jointless ground floor is achievable with AAC. This assessment is done by dividing the research question into several sub-questions to approach an answer for the main research question properly.

1.3 Outline

Initially, the structural design principles of the jointless floor are researched, for which design guides are followed and design calculations are performed to find the governing design aspect and the most relevant concrete properties. The control of cracking follows to be this governing design aspect, where crack formation occurs from the restrainment of the shrinkage. Then, the material AAC is introduced and from a literature study a link is made for the relevant concrete material properties between AAC and OPC concrete of similar strength class. As the shrinkage of the concrete is the governing imposed load for the jointless ground floor, the influence of the total shrinkage value and the floor thicknesses is dealt with. From which it follows that a reduction in shrinkage is essential for a jointless floor to be realised in a thinner cross-section.

A parametric study is performed on the relevant concrete properties, the reinforcement and the steel fibre residual flexural strength, to find their influence on the crack-widths and on the floor's ability to carry the external loads. Based on this study, an optimal cross-section for a jointless AAC ground floor is considered. Finally, more accurate crack-width calculations are performed by studying the non-linear behaviour of the material with theoretical models and with FEA. The FEA is performed with the software program DIANA, a commonly used tool suitable for the analysis of non-linear behaviour for structural elements. There is some doubt around DIANA's accuracy for crack-widths computations, which is studied in this final chapter as well. On the next page, the outline of this thesis and the chapters follows.

This first chapter introduces the research topic, the implementation of alkali-activated concrete in jointless ground floors. In chapter 2 the introduction to the constructive aspects of industrial concrete ground floors is made. In chapter 3 the imposed loads are introduced and their influence on the behaviour of a concrete floor is addressed. These first chapters address the design manner for the governing design aspect of the jointless floor. Chapter 4 provides the introduction to alkali-activated concrete. The way it is realised, how it is been used throughout time and what its material properties are, is discussed here. In chapter 5 the parametric study is done for a jointless concrete floor, to see the influence of certain parameters concerning the crack-widths and ultimate limit state unity checks. The optimised jointless ground floor realised with typical alkali-activated concrete material properties is considered here. The crack-width calculations are further examined in chapter 6, with the usage of bond-slip models and by comparing theory to finite element analysis. An improved bond-slip relation for alkali-activated concrete is examined here as well. The design method and process is discussed in chapter 7 and in chapter 8 the answer to the research question follows with the conclusions drawn from this thesis.
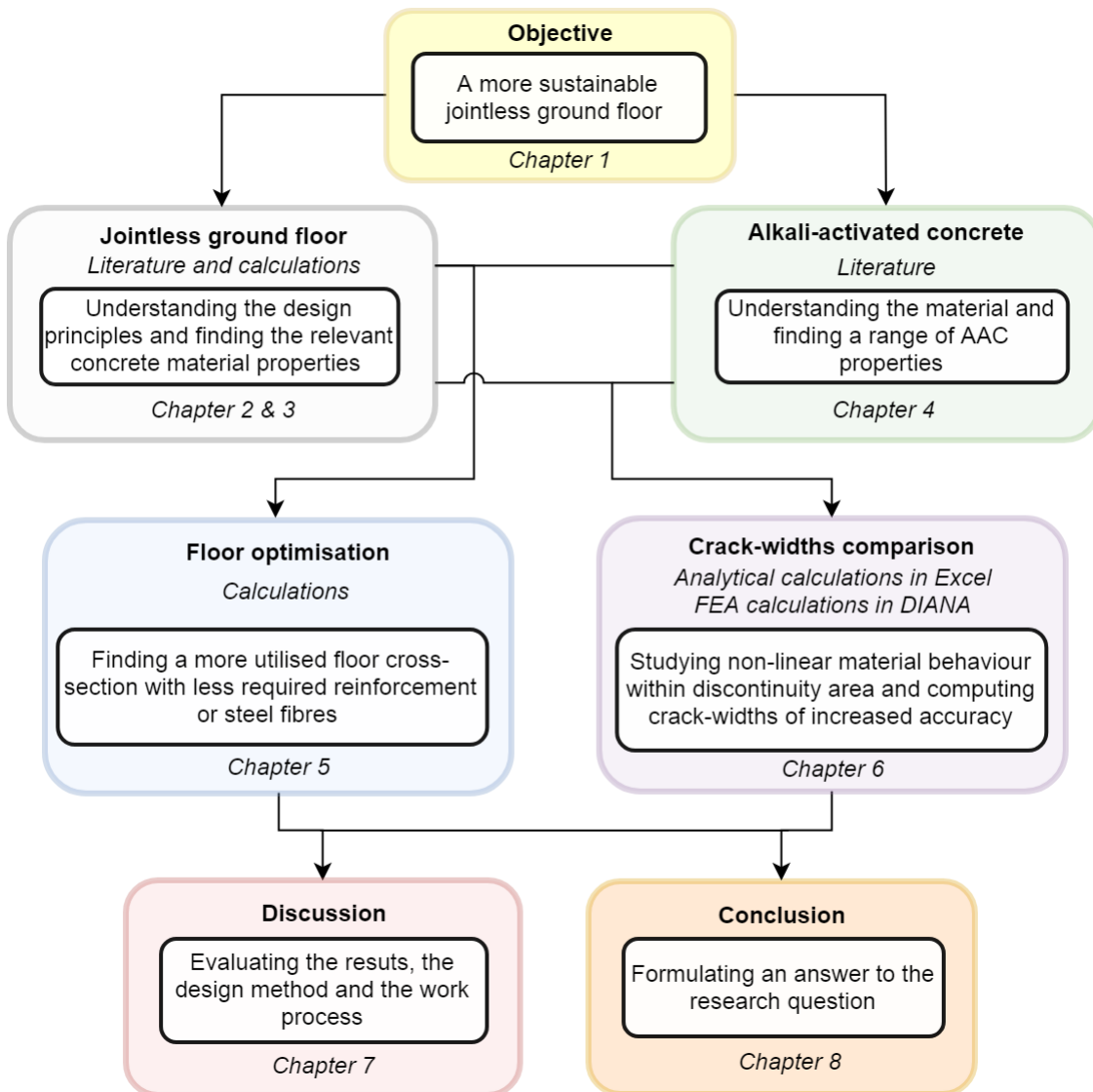
2 Concrete industrial ground-supported floors

This chapter will focus on the design of concrete industrial floors on grade, or in other words a concrete floor that is elastically supported by the ground. The design of a concrete floor will be defined by the constructive – and user aspects. The constructive aspects are defined by the applied loads and the integration of the concrete floor with the sub-ground and its load-bearing capacity. In the design of an industrial floor, two types of loads can be distinguished, namely loads relating to transport- and storage loads and imposed deformations as a result of shrinkage, temperature changes and settlement differences. User aspects like flatness, levelness and slip resistance are not in the scope of this thesis and will therefore receive only little attention in this report.

The industrial concrete floors can be supported in two ways, either by piles or directly supported by the ground. In case that the sub-ground is made of well compacted sand the latter is the optimal solution. The differences in settlement for a similar floor on piles will be minimal (Loonen N. , 2018). The concrete industrial floor on grade is a commonly applied floor type in The Netherlands and the considered floor type of this thesis .

There are different ways to execute concrete floors on grade, i.e. in plain concrete, with reinforcement, with steel fibres in the concrete or a mixture of the last two. The floor can be jointed or jointless. Jointed floors will have a lesser risk of cracking but are associated with joint maintenance and repair costs. With jointless floors the size of the bays are larger and as the distance between stress relief joints is bigger the risk of cracking increases, the control of cracking must be taken into account in the design.

Figure 2.1 Warehouse with back-to-back racking's on a concrete floor (The Concrete Society, 2016).

The performance of the floor depends on the design, the specification of the floor and the techniques that are used in its construction. As stated before a floor can be constructed in several ways, whether a floor will be constructed with joints or without joints is an important aspect to be considered in the design of a floor. A jointless floor will have a very different reinforcement lay-out than a jointed floor, whereas a jointed floor requires less reinforcement, it does require more regularly inspections and maintenance. All these aspects will define the performance of an industrial concrete floor.

Looking at the constructive aspects the most important requirements for a concrete industrial floor are the following:

- The floor must be able to carry the required static point loads, dynamic loads, uniformly distributed loads and imposed loads without unacceptable cracking, deflections or damage to joints.
- Joints and reinforcement should be detailed to minimise the risk of cracking.

Other requirements, as examples, that should also be considered are more related to the user aspects:

- The floor should remain serviceable and maintained properly.
- The floor surface should have the required finishing and suitable surface regularity.
- The floor surface should have suitable abrasion, chemical and slip resistance.

The next part will go a bit further into detail about these user aspects and the different floor types. The constructive aspects shown above are of more importance for this report and will receive more attention.

Figure 2.2 Industrial jointless concrete floor of the BIC Eindhoven hall being cast (left) and after hardening (right).

2.1 Jointed or jointless concrete floors

Joints are an important feature for a concrete floor. As concrete shrinks it will undergo deformations that can be partly restrained by the subground, such restrained deformations will result in stresses that can reach the tensile strength of concrete and cracking will occur. A way to prevent this is by applying joints within the floor, joints allow the floor to move horizontally such that the floor will be less restrained and the risk of cracking is reduced.

However joints can be a source of problems as the edges of a concrete floor slab are vulnerable to damage, which can be caused by the passing of forklift trucks. So the downside of joints are

accommodated with unwanted cracks that can occur due to the dynamic loads. Besides the possibility that cracking can occur, the gaps of the joints will result in discomfort, for the driver or so that the cargo that is being transported could fall of. Therefore, joints are in general associated with discomfort, a lot of maintenance and repair costs.

In The Netherlands a lot of concrete floors with industrial purposes, that are being executed directly on the subgrade, are executed in a jointless manner. In such cases the concrete floor is only able to freely move near its free edges. The majority of the floor bay is restrained and the shrinkage of the concrete will result in cracks. The control of cracking becomes one of the main design aspects of the concrete floor. In the design this must be taken into account through the concrete exposure class that defines the allowable crack width. In order to satisfy the crack width criteria a proper concrete and reinforcement design is asked. In chapter 3 the imposed loads that a jointless concrete floor will undergo will be given more attention.

2.1.1 Types of joints

Though joints aren't part of the scope of this thesis some examples of joints are provided that can be applied in a jointed concrete floor. Joints are provided to relieve the tensile stresses induced by drying shrinkage or temperature changes and to cater breaks in the construction process.

A commonly applied joint is the sawn restrained-movement joint shown in Figure 2.3. These joints are made by making sawn cuts at predefined locations in the concrete floor, they allow limited movement to relieve the shrinkage-induced stresses. Typically these joints are applied every 6 meters, for narrow joint openings the joint is relatively damage resistant but intensive traffic like pallet trucks can damage the joints. The crack aggregate interlocking allows for load transfer across the joint.

Figure 2.3 A sawn restrained-movement joint with a crack below the cut (BetonLexicon, 2018).

In the case that the induced deformations may not impose stresses that will reach the tensile strength and impose cracks, expansion joints can be applied. Such free-movement joints allow a floor to move horizontally. A good suitable example of an expansion joint is the Cosinus Slide joint, shown in Figure 2.4. This expansion joint allows load transfer through the floor itself, where this is normally done through dowels in typical expansion joints. The double sinus corrugation of the joint is arranged in such a way that small concrete vertical consoles are shaped. The shape of the joint allows for continuous support where it also minimises discomfort (Hengelhoef Concrete Joints, 2018).
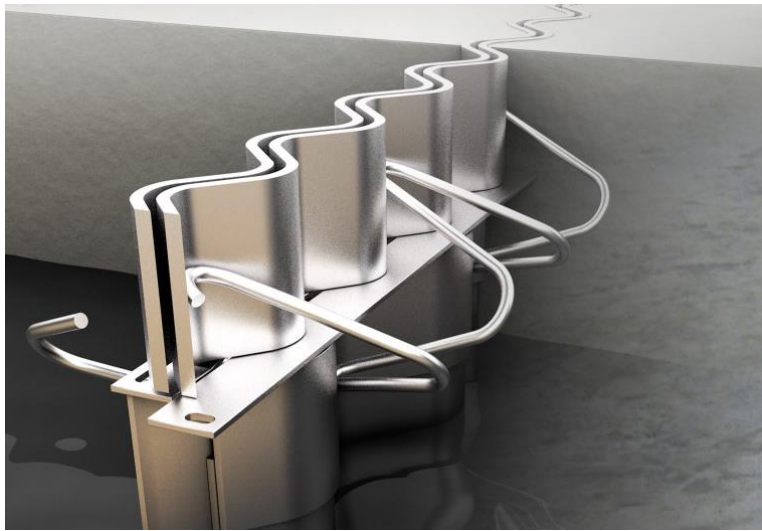
Figure 2.4 Cosinus Slide Joint (Hengelhoef Concrete Joints, 2018).

The type of joint that will be present in jointless floors are the formed joints, as there is an upper limit to the amount of concrete that can be poured in one go. To achieve the jointless floor principal for large bays, the reinforcement of the floor will be continuous in the formed joints. Usually a small corner profile is applied on the top reinforcement and below the reinforcement, herringbone steel is placed. The corner profile is needed for floors where dynamic loads are present, to prevent the surface from crumbling at the joint. In the case of a steel fibre reinforced concrete floor extra coupling reinforcement will be added in the formed joint as the steel fibres aren't continuous at the joint. Figure 2.5 shows an example of such a hybrid reinforced joint before and after the daily production of the concrete pour.
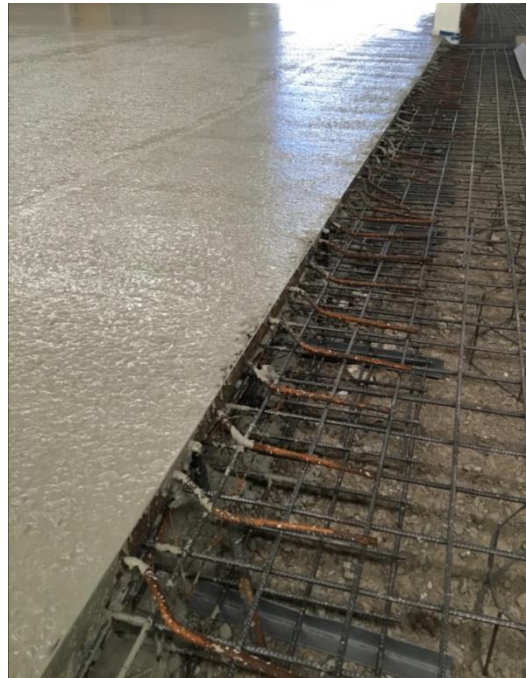
Figure 2.5 Formed joint for a hybrid reinforced concrete floor.

2.2 Floor surfaces

Each concrete floor will have its own floor characteristics and specific criteria considering the surface. Aspects like the abrasion-, chemical-, slip resistance and surface regularity are certainly

important to be considered to meet the client's requirements. The execution of the floor must be done properly to achieve a suitable surface. The floor must have appropriate flatness and levelness to ensure that an industrial hall can function satisfactorily, considering that high racking's and high-lift equipment can be present in an industrial hall.

In general the concrete floors in industrial halls will not have a screed or finishing layer on the top surface. Such floors require monolithic finishing, which consists of sanding and plastering the concrete surface several hours after pouring and compacting. This method of monolithic finishing allows for a dense and durable smooth surface to be obtained. Timing on this is critical, starting the monolithic finishing process to soon and the equipment will sink in the concrete. If the process is started to late the concrete will have stiffened to much that the finishing can't be done properly. The time when the mechanical finishing can start has to be decided by the concrete finisher as the time where the concrete floor has stiffened sufficiently differs per concrete mixture (VOBN, 2003).

Figure 2.6 Equipment used for the monolithic finishing of the concrete surface.

For floors with large bays, e.g. a jointless floor, cracking of the surface becomes the main criteria. With an increase of the distance between the stress relief joints the shrinkage induced stresses will reach stresses that the concrete cracks. Fine cracks generally will have no structural significance, fine cracks are actually always bound to occur in concrete structures. It is nearly impossible to design a concrete structure that won't crack.

The control of cracking is the main aspect that has to be considered for jointless concrete floors that are supported elastically by the subground. In general the crack width may not exceed a width of 0.4 mm for an indoor concrete floor according to the norm. Depending on the durability class this maximum allowable crack width could be less. If the cracks exceed the allowable crack width the durability of the structure will be affected. It can result in corrosion of the steel reinforcement, weakening and diminishing the lifespan of the structure. For indoor floors this durability aspect is of less importance, but the same crack width criteria holds as the floor otherwise risks the loss of its functionality. In warehouse halls a wide crack in the wrong location, for example below the leg of a high scaffold, could result in the tipping over of the scaffolding which could be very dangerous.

Cracks in a jointless floor will be present due to the restraint of the shrinkage, another phenomena that a concrete surface undergoes due to shrinkage is curling. Differential shrinkage over the height of the floor causes the floor to curl upwards, because the top surface is exposed the surface dries and shrinks more than the bottom of the floor. This curling can occur at the edges of the slabs and may result in cracking. The self-weight counters the curling partly, the floor curls upwards such that the floor could be lifted from the ground. Where eventually due to the self-weight or a dynamic load, if this edge is also a joint, a crack will occur. In the middle of the bay of a jointless floor where the floor will be fully restrained the difference in shrinkage will result in a strain gradient over the height, resulting in bending moments. In these cross-sections the cracking moment will be reached, that at the outer fibres, the top surface, the tensile strength is reached and cracks will arise.

The cracking and curling of a jointless concrete floor, due to shrinkage, are two topics of this thesis that will receive further attention in chapter 3.

2.3 Floor loads

In the beginning of this chapter the constructive requirement was stated which implied that the floor must be able to withstand the static point loads, dynamic loads, uniformly distributed loads and imposed loads without unacceptable deflections, cracking or damage to the joints. So besides the own weight of the floor there can be external and imposed loads. The external variable loads that are common for industrial halls will receive some attention in this part, the imposed loads are treated in chapter 3. The variable loads for building constructions in The Netherlands are defined according to the NEN-EN 1991-1-1, the table below shows the minimum variable loads according to this code.

Table 2-1 Variable load values on floors for storage and industrial use.

Category of loaded areas	q_k [kN/m^2]	F_k [kN]
E1- stores	≥ 5	≥ 7
E1- libraries	≥ 2.5	≥ 3
E1- other	≥ 5	≥ 10
E1- industrial use	≥ 3	≥ 7

The values from Table 2-1 show the minimum loads, for each specific project these values should be determined as they can be a lot higher than these minimum values. The variable floor load can range from 5 kN/m^2 for office spaces up to 75 kN/m^2 for very high-rise warehouses (Loonen N. , 2002). Warehouse floors are often designed on an uniformly distributed load q_k, this can be the case for bulk- or pallet loads. Table 2-2 shows values for the variable loads that are more representative for typical warehouses.

Table 2-2 Representative variable loads for warehouses. Data from VOBN (2003).

Category warehouse	q_k [kN/m²]	F_k [kN]	Indication user-load
Lightly loaded	15	20	Racks up to 5 meter high
Medium loaded	15 - 50	20 - 100	Racks from 5 to 10 meter high
Heavy loaded	50	100	Racks higher than 10 meter

Generally warehouse floors are designed on the basis of a uniformly distributed load, which is suitable for bulk- and pallets loads. However, in the case of high racking's the point loads should not be underestimated. A typical layout for a warehouse is such that in between two aisles, two racking's are placed back-to-back. This means that close to each other, two relatively high point loads can act on the concrete floor, where a typical value for one point load can be 95 kN (Punt & Meer, 2017).

For dynamic loads the normative load must be determined on the basis of the heaviest possible vehicle that can use the industrial floor (Bouquet & Frénay, 1998). For forklift trucks the load specifications are also defined in the Eurocode NEN-EN 1991-1-1. The dynamic effect should be taken into account for transport vehicles like forklift trucks, by multiplying the static load with a dynamic magnification factor. This dynamic effect for mobile loads should be applied in cases where an abrupt height difference in the floor may be present, for example at thresholds and plate edges. For a properly build jointless concrete floor such abrupt height differences will just be present in the case of thresholds, which is not a common thing in warehouses with heavy movement equipment.

The Eurocode 2 defines six different classes FL 1-6 which are depending on their net weight, dimensions and the lifting load. Table 2-3 shows these classes with the corresponding axle load, which is the static load that should be considered when the dynamic effect has to be taken into account.

Table 2-3 Loads of the forklift trucks according to the FL-classes.

Class forklift truck	Net weight [kN]	Lifting load [kN]	Axle load [kN]
FL 1	21	10	26
FL 2	31	15	40
FL 3	44	25	63
FL 4	60	40	90
FL 5	90	60	140
FL 6	110	80	170

The heaviest class FL 6 is applicable for forklift trucks at container storages of multiple layers where the axle loads can reach 200 kN, such axle loads can also be expected on concrete floors in

airplane hangars. Whereas for warehouses with high racking's a common lifting capacity for reach trucks, a type of forklift truck used in warehouses that can reach certain heights to stack pallets, is around 50 kN (VOBN, 2003). These kind of reach trucks are class FL 4 or even class FL 5, meaning axle loads up to 140 kN could be reached.
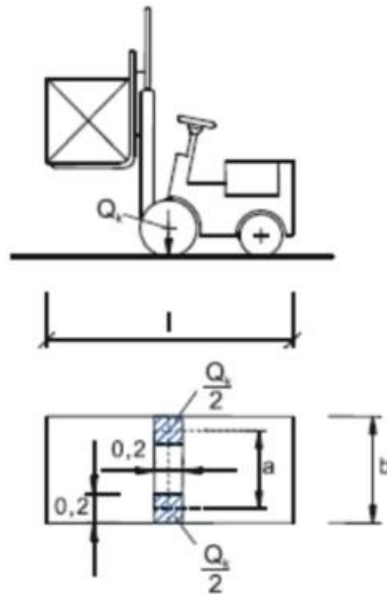
Figure 2.7 Dimensions of forklifts (NEN, 2011).

The above figure shows how the vertical axle loads of a forklift truck can be schematised. The dimensions shown depend on the FL-class, where the axle width *a* ranges from 0.85 meter to 1.80 meter for class FL 1 to class FL 6, respectively (NEN, 2011).

Considering a heavy kind of forklift truck for a warehouse of class FL 5 with an assumed axle width of 1.50 meter. The axle load Q_k of 140 kN has to be divided into two static point loads of 70 kN that are acting on the concrete floor 1.50 meter apart from each other. Looking back at the static point loads that can be present from the back-to-back racking's, two static point loads of 95 kN act on the concrete floor. The back-to-back racking uprights are typically 0.25 to 0.35 meter apart (The Concrete Society, 2016). This shows that the static point loads from racking's are governing for the industrial warehouse concrete floors considered, as the point loads of racking's can be higher and closer located next to each other.

In section 2.5 the theories for the structural design for ground-supported floors are presented. Like the method of Westergaard to find the stresses from concentrated point loads and the yield line theory with Meyerhof's formulas. For the concentrated point loads, the governing back-to-back scenario is considered from now on.

2.4 Soils and ground-support

In The Netherlands the soil conditions are in a lot of areas such that the foundation for floors on grade are suitable. However for a foundation on grade it is for most cases not possible to apply the floor directly on the present soil. In general a part of the topsoil layer is removed and at the location replenished with sand. In most cases though a foundation layer is best suitable or even necessary, where the main reason to apply a foundation layer is to improve the load-bearing capacity of the floor.

The load-bearing capacity of the subsoil is important to keep the structure robust and stable. Sand is a load-bearing layer because sand is slightly compressible, this soil characteristic has been termed by Westergaard as the modulus of subgrade reaction k. It is defined by the force that, distributed over unit area, will give a unit deflection with the units N/mm²/mm or N/mm³. The table below show some representable values for different soil type for this unit k. Where peat has a very low value that it can be defined as a very compressible soil, the opposite of gravel shows a soil type that is hard to compress.

Table 2-4 Recommended values for the modulus of subgrade reaction for different soil types.

Soil Type	Modulus of subgrade reaction k [N/mm³]
Peat	0.01 - 0.02
Clay	0.02 – 0.04
Loam	0.03 – 0.06
Sand	0.04 – 0.10
Gravel/sand	0.08 – 0.13

As a good foundation layer and work floor for a jointless industrial floor a well compacted coarse-grained Recycled Concrete Aggregate (RCA) layer is often applied. Membranes can be applied to reduce the friction between the concrete slab and the sub-base. Without a membrane and the use of RCA a high horizontal shear resistance is achieved between the two. This allows the shrinkage size of the floor to be reduced significantly, enabling the floor to be executed jointless. This does, however, mean that the shrinkage of the concrete will be restrained which will result in stresses. These stresses are part of the imposed loads that act on the concrete floor discussed in chapter 3.

A minimum RCA-layer of 200 mm with a modulus of subgrade reaction of 0.06 N/mm³ can be suitable for a floor on grade. Such a foundation layer is also suitable to allow lifting equipment on the sub-base, making it ideal as a working floor. Another benefit is that with the right humidity during the pouring of the concrete floor, some water is extracted from the young concrete floor. Later this water is slowly absorbed back in to the concrete which reduces the shrinkage speed of the concrete floor. The proper humidity of the RCA-layer is important, if it's too low the concrete will dry out much faster where cracks can occur with unacceptable crack widths at the bottom. If the humidity is too high the young wet concrete might mix with the sub-base reducing the concrete quality (ABT, 2015d).

Soil investigation must be done to examine the ground conditions at the building site. This should be done by a geotechnical engineer who can interpret the results and decide whether the sub-soil is suitable as an elastic support system and what adjustments should done considering the long-term settlements.

2.5 Structural design

The primary design objectives for a concrete industrial floor that is elastically supported are to carry the intended loads and to control the cracking. This part will consider the structural design of the floor and its ability to carry the intended loads. For the normative point loads there are two

ultimate strength modes of failure, namely flexure and punching. Uniformly distributed loads are considered as well. The introduction to steel-fibre reinforced and hybrid (steel-fibres with traditional reinforcement) reinforced concrete is made as hybrid reinforced concrete floors are nowadays a common practice for the construction of jointless concrete floors in The Netherlands.

2.5.1 Ultimate limit state

The strength requirements can be considered through several methods. For the point loads the methods of Meyerhof and Westergaard are applicable, whereas for the uniformly distributed loads Hetényi's method is adopted. Requirements related to strength are considered in the ultimate limit sate (ULS). The Concrete Society (2016) recommends a minimum design thickness of 150 mm for ground supported slabs. Conclusions here are made considering this minimum thickness of the floor, for a concrete hybrid reinforced floor, on which the normative back-to-back racking point loads act. The assumption is made that the back-to-back racking base plates are 300 mm apart, which means that the dual point loads can be considered to act jointly as a single load. More information can be found in Appendix A, which also shows the formulas and the calculations that are made to come to the conclusions made in this chapter.

2.5.1.1 Flexure

Slab design in the ULS for flexure under point loads is based on the yield line theory. Adequate ductility and rotation capacity is required to allow for the redistribution of bending moments, which allows for the yield lines and the sagging and hogging moment capacities to be fully mobilised. Meyerhof's design formulas for internal, edge and corner loads can be used for this (Meyerhof, 1962). Through the theory of Meyerhof it can be found that the ultimate load design for internal loads is the highest. It is approximately 2 and 4 times higher than the load capacity of the edge and corner loads, respectively.

With proper ductility and the redistribution of bending moments a relatively thin concrete floor, with a below average reinforcement net and steel fibre dosage, will be able to carry the intended and governing back-to-back double point load.

The flexural tensile stresses in a concrete slab due to a point load can be calculated with the formulas of Westergaard. These are based on an infinite long thin plate founded on a Winkler-foundation (Westergaard, 1926). Over the years the theory and formulas of Westergaard have been reviewed, therefore there are different notations to be found for the calculations of the stresses. Similar results with Meyerhof's theory can be found, that is that the tensile stresses at internal locations will be lower than the tensile stresses found at the free edges and corners of the floors. This shows another benefit to the jointless floor principle, where the amount of free edges and corners are at a minimum.

The flexural tensile stresses computed through Westergaard's formulas might show stresses that exceed the tensile strength of the concrete. This means that cracking will occur, however for the ultimate load capacity to be reached according to Meyerhof's yield line theory cracking must occur for the yield line patterns to be achieved.

2.5.1.2 Punching shear

The second ultimate strength mode of failure from point loads is punching. The punching shear capacity is determined by checking the shear capacity at the critical perimeter. The Eurocode 2 provides the design methods for the shear stress of the concrete and the length of the critical parameter. RILEM guidance suggest that steel fibres in addition to traditional reinforcement will increase the shear capacity of concrete (RILEM, 2003). For higher steel fibre contents than usually

applied in the industrial concrete floors this increase of shear capacity can also be found in steel fibre only floors.

As the concrete floor is in direct contact with the subgrade a proportion of the load within the punching shear parameter can be considered to be applied directly to the subgrade. The bearing pressure in the subgrade is assumed to increase linearly from zero at some distance from the point load to a peak bearing pressure under the load. The volume of the bearing pressure that is contained by the critical perimeter is the proportion of the punching shear that can be deduced from the imposed shear load.

Calculations show that the punching shear criteria will be met when the same thin concrete floor and points loads that are representable for high racking's are considered. The ultimate strength failure mode of punching shear will not occur.

2.5.1.3 Uniformly distributed loads

Whereas point loads are the governing type of external loads for industrial concrete ground floors, block or pallet stacking are very common applications in warehouses. These are common examples of uniformly distributed loads. Floors that will be loaded by uniformly distributed loads can be calculated based on the theory for beams on elastic foundation by Hetényi (Hetényi, 1971). Two general cases are considered of the situations that Hetényi designed, where the maximum sagging and hogging bending moments will occur. These are defined by the breadth of the load or the spacing in between the aisles, which have the same width which is commonly known as the critical aisle width. The analysis is based on elastic distribution of the bending moments so the cracking moment should be considered and not the residual moment if Hetényi's work is adopted.

The same conclusions are drawn from the calculations made in Appendix A, which is that the ultimate limit state strength criteria will be met. Where the same floor properties have been assumed with a uniformly distributed load that is at the upper limit seen in industrial warehouses.

2.5.2 Serviceability limit state

In the previous part it was stated that the ultimate limit state criteria could be met rather easily for an elastically supported concrete floor. The unity checks were all satisfied where the minimum recommended thickness of 150 mm is considered with reinforcement ratio's and steel fibre contents that are below the average that is seen within The Netherlands. Considering only the ULS criteria it could be said that the jointless floors could be realised with thinner sections and with less steel. However most of the floors applied in The Netherlands have a preferable thickness, a steel fibre content and a reinforcement net that is higher than the example values taken in Appendix A.

This is because the serviceability limit state (SLS) is governing between the SLS and ULS. As stated before the control of cracking is important and can be considered to be the main criterion for the design of a jointless concrete floor on grade.

At ABT, a company where a number of jointless concrete floors in The Netherlands have been designed, the preferable design of a jointless concrete floor nowadays has a minimum thickness of 160 mm, a top reinforcement mesh of ϕ7-100 mm in combination with a steel fibre content of minimally 30 kg/m^3. According to senior advisor N. Loonen at ABT, these minimum values are all based on the idea to control the crack-widths and keep the crack-widths within acceptable limits (personal communication, December 2018).

The same ULS calculations are remade with these preferred properties in Appendix A. All ULS checks are fulfilled where the considered loads are of the highest kind seen in The Netherlands. This confirms that the SLS can be seen as governing. The two main aspects in SLS are the control of cracking and the limitation of deflections. The latter is not really applicable with floors that are realised directly on the subgrade. The limitation of settlements and settlement differences are important though, these are however mainly depending on the composition of the subsoil and can't simply be calculated through the modulus of subgrade reaction k.

Looking just at the jointless concrete floor, so not at the subsoil composition, the main criteria that remains is the aforementioned control of cracking. In a jointless floor cracks will arise and it is important that the crack widths remain within certain limits. According to the Eurocode 2 crack widths should be limited so it does not impair the functionality or durability. For indoor warehouses the durability of the top surface of the concrete floor can be considered to be no issue as there won't be any hazards present indoors. For outside concrete floors like loading docks this will be an issue as road salts can be present which can impair the reinforcement and therefore the durability of the floor.

The requirements around the crack widths have become stricter over the years. Around the year 2000 the maximum crack width for industrial floors was around w_{max} = 0.5 mm, which has been reduced to around w_{max} = 0.3 mm in 2018. Nowadays owners of warehouses often prefer crack widths that don't exceed 0.2 mm, which might become the new standard in the coming years. The reduction of the maximum allowable crack width can be accommodated to the heavier usage of the floor. The equipment that is used to transport commodities, like forklift trucks, have seen an increase of the axle loads and therefore went from using rubber tyres to more stiff tyres. Polyurethane tyres are commonly seen nowadays and are able to withstand such loads. When such a forklift truck with a heavy axle load and stiff tyres passes a concrete crack that is too wide it could further damage the floor, this will in the end result in a floor that loses its functionality. Therefore crack widths are limited for indoor floors as well, where durability aspects don't really play a role but because it will secure the functionality of the floor.

The reasons why a jointless concrete floor will crack and in what way these cracks can be controlled will be addressed further in chapter 3.

2.5.2.1 Crack width requirements

The low tensile strength of concrete, which is about ten times lower compared to its compressive strength, provides the principal idea of designing for (hybrid) reinforced concrete to make the concrete resist the compressive forces and the reinforcing steel (and fibres) the tensile forces. That controlled cracks occur in a (hybrid) reinforced concrete structure under service load are therefore not a reason for worrying but a proof for the correctness of the design.

To ensure that the durability and aesthetics of a concrete structure are not endangered, requirements on the allowable crack width are made. These requirements depend on the exposure class and the kind of reinforcing that is applied, which could be prestressing steel as well. From the Eurocode 2 EN 1992-1-1 table 7.1N the following requirements are given.

Table 2-5 Recommended values of w_{max} [mm] (NEN-EN 1992-1-1 table 7.1N, 2011)

Exposure Class	Reinforced members and prestressed members with unbonded tendons	Prestressed members with bonded tendons
	Quasi-permanent load combination	Frequent load combination
X0, XC1	0,4[1]	0,2
XC2, XC3, XC4		0,2[2]
XD1, XD2, XS1, XS2, XS3	0,3	Decompression
Note 1: For X0, XC1 exposure classes, crack width has no influence on durability and this limit is set to guarantee acceptable appearance. In the absence of appearance conditions this limit may be relaxed.		
Note 2: For these exposure classes, in addition, decompression should be checked under the quasi-permanent combination of loads.		

The Dutch National Annex to the EN 1992-1-1 prescribes other crack width limits and load combinations. These crack width limits relevant to concrete industrial floors are shown in the following table.

Table 2-6 Recommended crack width limits w_{max} according to the Dutch National Annex to EN 1992-1-1.

Exposure class	Reinforcing steel and/or not bonded prestressing steel
	Frequent load combination
X0, XC1	$w_{max} \leq 0.4$ mm
XC2, XC3, XC4	$w_{max} \leq 0.3$ mm
XD1, XD2, XD3, XS1, XS2, XS3	$w_{max} \leq 0.2$ mm

If the applied concrete cover on the reinforcement is larger than the nominal concrete cover a factor k_x may be applied to the crack width limit. The Dutch National Annex gives the following equation for this factor:

$$k_x = \frac{c_{applied}}{c_{nom}} \leq 2.0 \tag{2.1}$$

The nominal concrete cover c_{nom} follows from durability requirements and is defined as a minimum cover c_{min} plus an allowance in design for deviation Δc_{dev}:

$$c_{nom} = c_{min} + \Delta c_{dev} \tag{2.2}$$

The minimal concrete cover is provided to achieve a safe transmission of bond forces, to protect the steel against corrosion and to ensure an adequate fire resistance. There are some requirement to c_{min} to satisfy the bond and environmental conditions where the latter one is in general the normative. The minimum cover values for reinforcement taking account of the exposure class and the structural classes is given by $c_{min,dur}$ in table 4.4N from EN 1992-1-1.

Table 2-7 Values of minimum cover, $c_{min,dur}$, requirements with regard to durability for reinforcement steel (NEN-EN 1992-1-1 table 4.4 N, 2011).

Environmental Requirement for $c_{min,dur}$ (mm)							
Structural Class	**Exposure Class according to Table 4.1**						
	X0	XC1	XC2 / XC3	XC4	XD1 / XS1	XD2 / XS2	XD3 / XS3
S1	10	10	10	15	20	25	30
S2	10	10	15	20	25	30	35
S3	10	10	20	25	30	35	40
S4	10	15	25	30	35	40	45
S5	15	20	30	35	40	45	50
S6	20	25	35	40	45	50	55

Industrial concrete ground floors are usually not higher of a structural class than class S2, where with an indoor environment the exposure class XC1 can be considered to which the minimum cover of c_{min} = 10 mm follows. The principles for outside industrial floors concerning the exposure classes will be stricter, where exposure classes XC4, XD3 or XF2 are seen. The relation between the exposure classes to the environmental conditions is given in table 4.1 from the Eurocode EN 1992-1-1.

In the Dutch National Annex to EN 1992-1-1 an addition to the minimal cover shall be made in the design to allow for the deviation. The recommended value for Δc_{dev} is 10 mm. This adds up to a nominal concrete cover, following Eq. (2.1), to c_{nom} = 20 mm. Looking at the same assumed dimensions used for the floor design in Appendix A, the applied concrete cover is $c_{applied}$ = 30 mm for the top reinforcement mesh of the floor. Considering an indoor floor with exposure class XC1 the applied concrete cover $c_{applied}$ = 30 mm is higher than the nominal concrete cover c_{nom} = 20 mm such that the allowable crack width w_{max} = 0.4 mm, from Table 2-6, may theoretically be multiplied by the factor that becomes k_x = 1.5, following Eq. (2.2). This results in a theoretical allowable crack width of w_{max} = 0.4 · 1.5 = 0.6 mm. However, practically and through requirements from the owners of the warehouses the maximum allowable crack widths can be set lower, as stated before, down to w_{max} = 0.3 mm or even 0.2 mm to ensure the functionality of the floor.

2.5.3 Steel fibre reinforced concrete

As mentioned in the previous section the requirements for the maximum crack widths became stricter throughout the years. The control of cracking is traditionally done with reinforcement, so this meant that to fulfil these stricter requirements the amount of steel needed in the concrete floors increased. Eventually the reinforcement meshes reached dimensions where the prices became rather high, this asked for a new approach and the introduction to hybrid reinforced concrete floors was made. In addition to the traditional reinforcement, steel fibres would be added to the mixture. Steel fibres with end anchorages, a diameter of d = 1 mm and a length l = 40 mm or longer with high tensile strengths up to 1,500 MPa are used in the concrete ground floor industry.

Concrete is known to have little tensile strength in comparison to its compressive strength. When the tensile strength is reached and the concrete cracks, the residual tensile strength of concrete is pretty much non-existing it is negligible. The addition of steel fibres in concrete will provide a residual tensile strength capacity after a crack is appeared. This means that, unlike with plain concrete, tensile stresses still can be transferred through the crack due to the fibres. Steel fibres can bridge a small crack and the special shape at its ends provides anchorage within the concrete providing the residual tensile strength at the crack, Figure 2.8 shows a visualisation. When concrete is reinforced with traditional steel bars in the combination with steel fibres this is addressed as hybrid reinforced concrete in this report.

The reason hybrid reinforced concrete was introduced in to the industrial floor business was to reduce the size of the reinforcement meshes. According to ABT and Bekaert, a steel fibre supplier, the implementation of steel fibres in combination with a traditional top reinforcement mesh provides the best relation between the amount of steel to durability for an industrial floor.

Figure 2.8 Steel fibres in a concrete mixture bridging a crack (Bekaert, 2013).

Considering that the durability and life expectancy of an industrial concrete floor are dependent on the widths of the cracks that will appear, it is important the crack widths remain within acceptable limits. When a crack appears in traditional reinforced concrete the crack width depends on the tensile stress that has to be taken over by the reinforcement, the higher this steel stress is, the larger the crack will be. That is where the steel fibres are beneficial, as a part of the tensile stress will be taken over by the steel fibres bridging the crack, thus reducing the steel stress in the reinforcement bars. The lower tensile stresses in the steel reinforcement bars will result in less big crack widths.

Besides being optimal for the control of cracking, steel fibres will also increase the loading capacity of the concrete floor, improve fatigue resistance and increase the impact resistance (Bekaert, 2013). The increase of loading capacity can be contributed to the fact that the residual tensile strength is present and the bending moment capacity of a concrete section is increased with the addition of steel fibres. The parameters, f_{Rj}, that represent the residual flexural tensile strengths are evaluated from the F-CMOD relationship, Figure 2.9 shows an example of such a curve. This figure also shows the residual tensile capacity of plain concrete, the grey area, which is negligible in comparison to the area below the black line that represents fibre reinforced concrete.
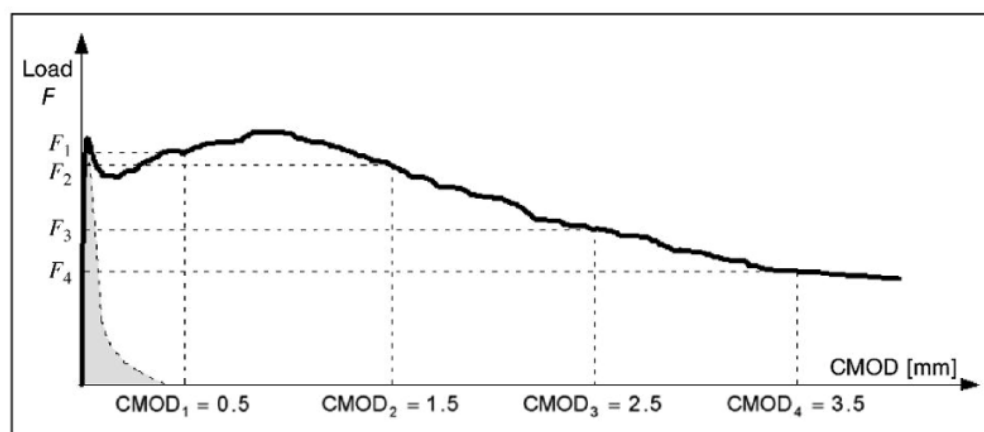
Figure 2.9 Typical load F-CMOD curve for plain concrete (greyed part) and fibre reinforced concrete (Fédération Internationale du Béton, 2013).

The increase in the ultimate bending moment capacity of a hybrid reinforced concrete floor can be seen when the stress and strain blocks are visualised, which is done in Figure 2.10. The left diagram in this figure shows the stress block where the residual flexural strength is visible, in terms of σ_{r1} and σ_{r4}, in the bottom section that is under tension.
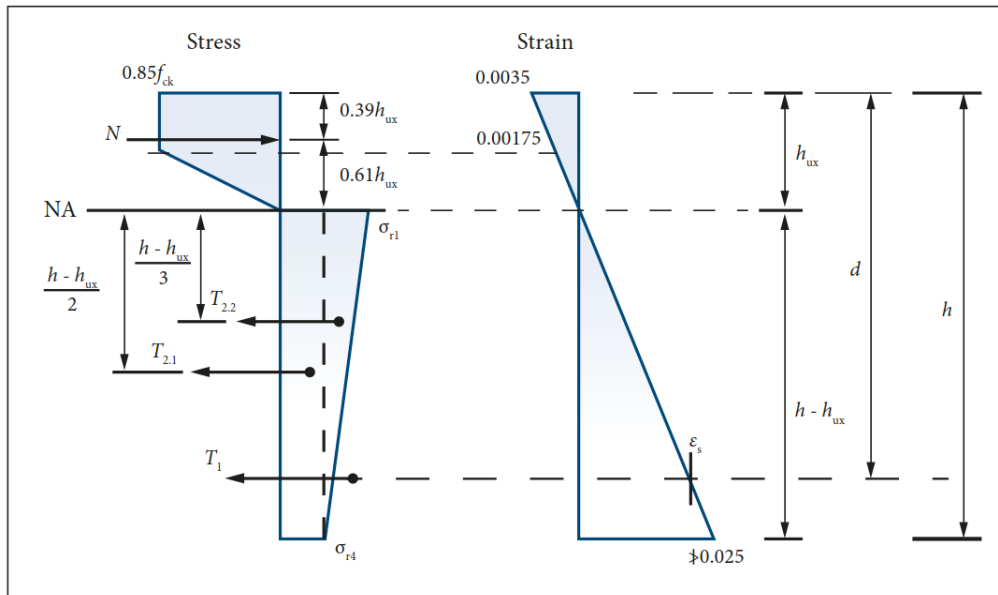
Figure 2.10 Stress and strain diagram in ULS for a hybrid reinforced concrete (The Concrete Society, 2016).

For plain concrete the tensile stress in the tensile section is always considered to be zero and the only tensile forces in such a stress-strain block will be at the location of the reinforcement bars, which is this case is noted as T_1. The addition of steel fibres provide the tensile stress areas which contribute the two tensile forces $T_{2,1}$ and $T_{2,2}$ shown in Figure 2.10. These additional tensile forces provide the increase of the bending moment capacity of such a cross-section. In Appendix A the formulas are shown which have been used to calculate the forces shown in Figure 2.10 and the bending moment capacity of the hybrid reinforced concrete floor section.

A stress and strain diagram like in Figure 2.10 for steel fibre reinforced concrete in SLS and the influence of the steel fibres for the crack-width calculations is introduced in section 3.4.

3 IMPOSED LOADS ON INDUSTRIAL CONCRETE FLOORS

In concrete structures cracking is a common phenomenon. Control of cracking is an important aspect for concrete structures. By controlling the cracking of concrete the objective is either to limit the crack width or to prevent cracking, the latter can be very expensive or actually impossible for most typical concrete structures. Requirements concerning durability, tightness, appearance and comfort are generally the main criteria to control the cracking of concrete.

For concrete structures there are different reasons for cracking to occur. A bad production can cause cracks within hours after casting. Thermal cracking caused by heating can occur, but also afterwards during the cooling process of concrete. Cracks can arise due to external loads, this is by now a well-known issue designers can deal with. Another important reason for cracking are the imposed deformations introduced in the form of shrinkage and temperature changes that are restrained, which provide restraint stresses. For concrete floors that are elastically supported shrinkage is important concerning the crack-widths.

Shrinkage is one of the imposed deformations that will occur in an industrial concrete floor. For the jointless floor these restrained deformations result in imposed loads. This chapter introduces the imposed loads seen within the jointless industrial concrete floors that are elastically supported by the subsoil. The result of the imposed loads, which occurs mainly due to drying shrinkage, the phenomenon warping or curling, is described and what is done to control the corresponding crack formation the concrete floor will see.

3.1 Imposed deformations

Imposed deformations are generally the result of temperature changes, shrinkage of concrete and the settlement of the subsoil. The first two will result in volume changes of the concrete where the latter one may deform the shape of the structure. Volume changes occurring due to the imposed deformations are not necessarily a problem, however when speaking of "restrained deformations" they are certainly a thing to consider. When a structure is free to move the volume of a concrete structure can freely swell or shrink, but if this volume change is restrained they will result in stresses. The restrained deformation of a structural element that would occur can be seen as an imposed and restrained strain that acts on the concrete structure. Simply following Hooke's law $\sigma = E \cdot \varepsilon$ such a restrained deformation will result in a stress.

The type and degree of the imposed deformation, the amount of restrainment and time-depending factors all influence the extent of which the imposed deformations are translated in to imposed loads. So the full response of a concrete structure depends on several things of which a few are listed below.

The imposed deformations will be the result of the volume changes of the concrete structure. The most common imposed deformations a concrete structure undergoes are the result of the following aspects:

- Shrinkage
  - Autogenous shrinkage
  - Drying shrinkage
- Temperature changes
  - Cooling down of the concrete hydration heat
  - Heating and cooling from external sources
- Settlement of the subsoil

The imposed deformations result in imposed internal loads when the imposed deformations are restrained. Several examples of structures with concrete restrainment are:

- An industrial floor on grade or on piles
- A concrete wall casted on an older concrete floor
- Round walls of reservoir silo's

The restrained imposed deformations will result in either compressive or tensile stresses in the concrete. The magnitude of these stresses are dependant of the following:

- The magnitude and the time of the occurring imposed deformation
- The modulus of elasticity of the concrete
- Relaxation of the stresses
- The amount of restrainment

An industrial jointless floor constructed on a foundation layer with a high horizontal friction between the foundation layer and the concrete floor certainly applies for a restraining concrete structure. The imposed deformation that has the most influence on a jointless concrete floor is shrinkage, which in the horizontal direction will be restrained due to the horizontal friction when a RCA-layer is applied as stated in 2.4. The different types of shrinkage and the response of the concrete floor are discussed in section 3.2.

3.1.1 Temperature changes

Concrete swells and shrinks just like any material when the temperature of the concrete is heated up or cooled down. Temperature changes can be caused by the development of hydration heat in hardening concrete, climate influences, industrial processes like heat or cold cargo storage and calamities like fires.

For jointless concrete floors the heating up of concrete due to the development of the hydration heat isn't really an issue as the concrete is still hardening and the imposed deformations are not restrained. Once hardened the concrete will cool down and the corresponding shrinkage will be restrained. When the swelling of the concrete is restrained it will result in compressive stresses, where the restrained shrinking, i.e. cooling down, results in tensile stresses. The compressive stresses can be taken up by the concrete itself, where this is not the case for the tensile stresses.

With mass concrete structures the temperature can rise significantly. Underground water-retaining floors, which are very thick compared to industrial concrete ground floors, can see an increase of temperature of 30 ⁰C, depending on the cement type. The floor will cool down to the original temperature if the surrounding climate is still the same (Riemens, 2016). Such floors can be about four times as thick as an industrial jointless concrete floor, the way thinner jointless

floors won't see such an temperature rise from the hydration process. The increase of temperature will be the highest in the middle of the floor. Due to the relatively thin concrete floor the heat will be conducted into the subsoil at the bottom which has a constant temperature and at the top the temperature increase is minimal as the heat radiates outwards.

External sources like the surrounding climate can also induce thermal loads on a concrete floor. This is mostly seen with outdoor floors and with cooling- and freezing storages. Indoor industrial concrete floors don't really see temperature changes as the external climates, the subsoil and the indoor climate, have temperatures that are almost constant. When the top surface does see an increase from e.g. solar radiation of the sun, the concrete floor will have a positive temperature gradient and cause the floor to curl downwards. This phenomenon of curling, i.e. warping, is discussed in section 3.3. A temperature gradient won't have to be taken into account when the temperature difference between the subsoil and the indoor environment is less than 10 ⁰C (CURNET, 2011).

As a thin concrete indoor floor is considered for this thesis the temperature rise from the hydration heat is considered to be negligible, which is especially the case when considering alkali-activated concrete that in general shows a lower development of heat in the hardening phase. A temperature rise at the top surface is possible for a concrete floor which would cause downwards curling, however due to drying shrinkage the upwards curling will be higher. Therefore, as the heating effect of the sun is excluded, the curling of the indoor concrete floors will always be upwards (Alhasani & Zaraei, 1996).

3.1.2 Settlements of the ground

When a floor on grade is built on a soil that is sensitive to subsidence like clay or peat, settlement differences will occur. If the concrete floor settles evenly the floor won't curl and no negative consequences will be seen. When the soil is made of well compacted sand, floors on grade will be the best suitable option as the settlement compared to that of a floor on piles isn't higher (Loonen N. , 2018). A floor on grade is directly supported on the ground so a pile foundation won't be realised, this makes a floor on grade a faster and cheaper system to build. In addition to that less concrete and reinforcement steel is required for a floor on grade compared to a floor on piles which makes it so that floors on grade are also preferable in situations where the subsoil isn't made out of compacted sand. So settlement differences have to be taken into account.

Proper soil investigation is required to be able to calculate the settlements of a floor, it can't simply be calculated with the modulus of subgrade reaction k. Inhomogeneity in the soil needs to be apprehended beforehand, as an inhomogeneity in the soil or differences in the loads can cause settlement differences. Settlement differences can make the functional use of a floor impossible, due to crack formation or tilted warehouse racking's. Such differences can be contributed to the user aspects flatness and levelness, which are important especially for warehouses with very high racking's. With regard to super-flat floors, there is often the misunderstandings that sagging is out of the question. The experience shows, however, that sagging occurs very evenly, such that the resulting height difference does not lead to discomfort. It are particularly the short distance inconsistencies of flatness which appear during the production of the floor that lead to discomfort (ABT, 2015c).

According to the CUR-Recommendation 36 the settlements of the subsoil have to be accounted as imposed deformations and in the case of settlement differences as permanent loads. Due to the curvature within the floor bending moments will occur (CURNET, 2011). The bending moment as a consequence of settlement differences can be calculated with the following formula:

$$M = K \cdot (EI) \tag{3.1}$$

Where the curvature K depends on the maximum settlement and the length over which the settlement takes place.

The stiffness of thick floors will be higher than that of a thin floor and this can be adverse to the bearing capacity. This is because with unreinforced or steel fibre reinforced floors the stiffness reduction may not be accounted for, due to limited post-cracking strength. So these floor types will, as a consequence of settlement differences, fail about two to three times faster, which is expressed in excessive crack-widths.

As stated before the thermal loads seen with industrial floors will be overruled by the drying shrinkage and as the settlement differences are highly dependent of the geotechnical composition of the subsoil. The focus of the imposed loads seen with industrial jointless concrete floors, considering the concrete structural part, is towards the shrinkage. Specifically the drying shrinkage, which in addition to the different types of shrinkage is handled in the next section.

3.2 Shrinkage

Shrinkage deformation is caused by the change of the moisture content of the concrete, just like any imposed deformation shrinkage will cause stresses when the deformation is restrained. The following distinction is made between the following types of shrinkage:

- Plastic shrinkage
- Chemical shrinkage
- Autogenous shrinkage
- Drying shrinkage

The plastic, chemical and autogenous shrinkage are relevant in the hardening stage of shrinkage. In terms of imposed deformations, the first two types could be negligible if the floor is constructed properly. Autogenous – and drying shrinkage will provide deformations that are considerable for industrial concrete floors which are elastically supported.

Plastic shrinkage occurs when no proper preventive measures are applied after casting the concrete floor. Due to gravitational forces the heavier parts in the wet concrete tend to move downwards and the water moves upwards towards the surface. A thin water layer can be seen on top of the concrete surface, which in case of a high evaporation rate will disappear completely and plastic shrinkage is likely to occur. Preventive measures are necessary and are standard protocol for concrete industrial floors, examples are to keep the concrete surface wet, cover the surface with a plastic or foil layer or by applying a curing compound. Plastic cracking is simply avoided through this.

Chemical shrinkage is the result of the hydration product having a smaller volume than the reacting products, which for traditional concrete are water and cement. This differs with alkali-activated concrete, which in chapter 4 receives attention concerning the chemistry and their potential for concrete floors. Chemical shrinkage will manifest itself mainly as capillary pores within the reaction product, i.e. the binding material, and hardly as an deformational change of a

concrete element. It is therefore negligible as on the macro-level no stresses will be generated (Breugel, Braam, Van der Veen, & Walraven, 2016).

3.2.1 Autogenous shrinkage

With ordinary concrete the available water in the fresh mixture will gradually be consumed during the progress of the hydration process. The water within the internal pores is being consumed and this causes the concrete to internally dry out resulting in a volume reduction, i.e. autogenous shrinkage. Autogenous shrinkage will more or less happen evenly throughout the concrete, which is not the case with drying shrinkage for concrete floors that are elastically supported. The autogenous shrinkage will therefore result in an imposed deformation that is uniform throughout the concrete section. As the horizontal direction of a jointless floor is restrained the autogenous shrinkage will act as an imposed load which is uniform over the height of the concrete floor.

Autogenous shrinkage depends on the chemistry during the hardening of the concrete and the amount of water that is in the concrete mixture. Traditional concrete shows higher amounts of autogenous shrinkage with lower water-cement ratio's. With alkali-activated concrete the chemistry is different as there will be no cement present, instead of the water-cement ratio the term water-binder ratio is used. Where the binder is made up of the precursors and activators used within the mixture, see chapter 4 for further details. Most studies show that alkali-activated concrete shows higher amounts of autogenous shrinkage compared to ordinary Portland cement concrete.

The Eurocode NEN-EN 1992-1-1 section 3.1.4 provides formula's to calculate the autogenous and drying shrinkage of concrete sections in terms of strain. The Eurocode 2 applies for traditional concrete and is not applicable for AAC. Figure 3.1 shows an example of the average calculated autogenous, drying and combined total shrinkage for a concrete section of a typical indoor jointless floor. The graph shows the average shrinkage strain curves calculated according the Eurocode 2 for a concrete floor with a thickness of 160 mm, concrete class of C30/37. The concrete surface can only dry out through the top surface, which means that the fictional thickness of the floor is twice the height, the fictional height is used to calculate the shrinkage strains.
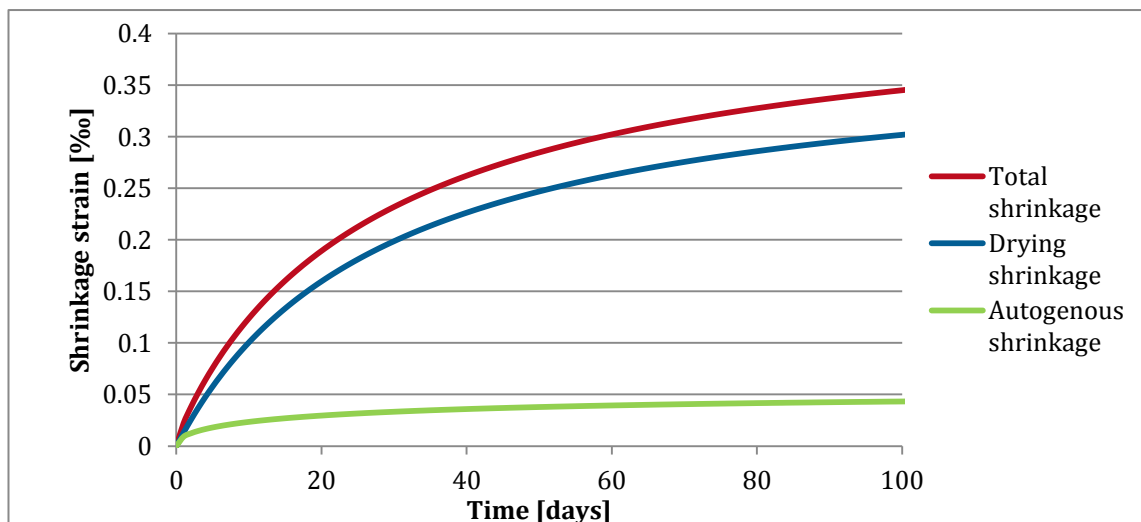

Figure 3.1 Average shrinkage of a concrete floor of 160 mm thick in terms of strain over time.

The graph shows that the autogenous shrinkage strain remains constant after a certain time has passed and that it is only a fraction of the total shrinkage that will occur. The shrinkage strains are the imposed deformations and depending on the modulus of elasticity and restrainment to be

considered as the imposed loads inducing stresses in the concrete. The same principles occur with AAC, considering the autogenous – and drying shrinkage, so the above may provide an example estimation about the proportions, not the actual values, between the two types of shrinkage for an AAC jointless floor. The actual proportions and values have to be found through testing.

3.2.2 Drying shrinkage

The loss of moisture from the concrete to the environment is called drying shrinkage. The rate at which water is discharged depends on the relative humidity (RH), the free surfaces and the permeability of the concrete. Of which the latter in a way depends on the amount of water used in the concrete mix.

For concrete industrial floors supported on the ground, the drying shrinkage will be mainly through the upper surface. The possible higher moisture content of the sublayer results in the reduced shrinkage at the bottom of the slab. Shrinkage between the top and bottom surfaces can differ meaning the thickness is of importance for the total shrinkage behaviour.

The surrounding climate is another important aspect considering shrinkage. The geographic location and whether the structure is indoors or outdoors defines the relative humidity of the surrounding climate for the structure. For example, in the winter the RH is lower indoors, which will result in faster shrinkage for indoor structures. For indoor industrial warehouses a good estimation for the RH is 50%, which means the drying shrinkage will occur in a quicker way compared to an outdoor environment with a higher relative humidity.

The mix of the concrete is also a factor that affects shrinkage, the water-cement ratio value for normal concrete is a very important factor. For ordinary concrete the type of cement and amount influences the shrinkage. For alkali-activated concrete the concrete mix is also important considering shrinkage. Literature shows a lot of different results for all kind of mixtures used, instead of cement the type of precursor and alkaline solutions are points of interest.

The drying shrinkage is considered to be the most important factor that has to be considered when designing the jointless concrete floor. This is the case because the drying shrinkage in the early age will only occur at the top surface. With a proper foundation layer there will be no loss of moisture through the bottom surface to the subsoil, at a later stage the bottom part of the floor will see drying shrinkage but this loss of moisture still occurs through the upper surface. Figure 3.2 shows this phenomenon where the development of shrinkage strain over time is visualised.
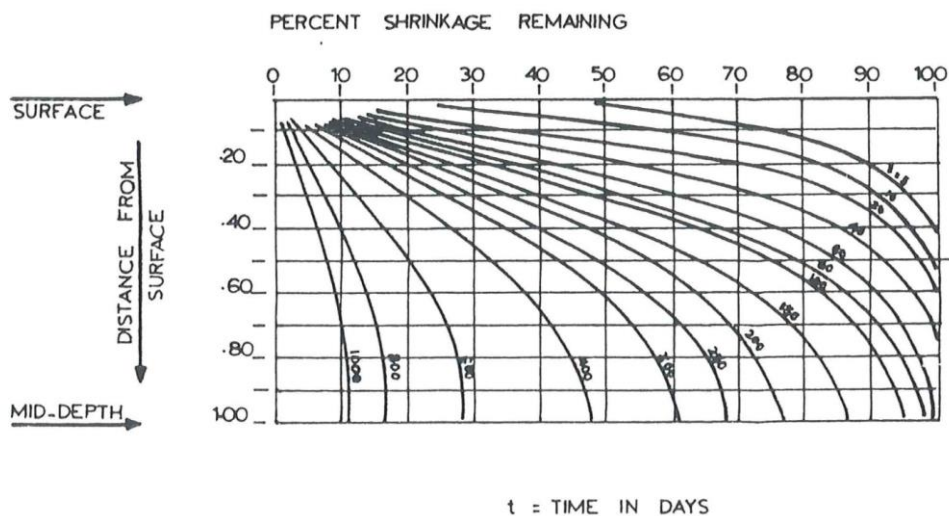

Figure 3.2 Development of shrinkage strain across the depth of a concrete member. The member is reinforced, of 150 mm thickness, and only allowed to dry through the top. Mid-depth represents the bottom surface of the floor (Abdul-Wahab & Jaffer, 1983).

After the ending of the curing period water starts to evaporate at the top surface and a shrinkage strain develops. This particular example in the figure shows the first sign of the development of a shrinkage strain at the bottom of the floor only after approximately 90 days. So after the curing period water starts to evaporate from the top part of the floor creating a moisture gradient between the top and bottom surfaces. The moisture gradient translates to a differential drying shrinkage across the depth of the floor and that causes a strain gradient. Even after a longer period the bottom part of the floor won't see a fully developed drying shrinkage strain.

As explained above the concrete floor will see a shrinkage gradient. As a result tensile stresses will develop at the top surface of the floor because the concrete can't freely shrink due to the underlying layers restraining the concrete of shortening. The result of this is that the free ends of the floor will be lifted and the so-called warping of the floor occurs.

3.3 Warping of slabs

Warping or curling of concrete slabs on grade, i.e. a concrete floor elastically supported, is caused by differential changes in moisture content and temperature. The changes cause different imposed length changes across the depth forcing the slab to curl up or down.

For indoor industrial floors upward curling is generally the occurring deformation. Upward curling is caused by a negative gradient, which is created when the temperature or the moisture content is lower at the top surface of the slab. Slabs on grade generally have a lower moisture content at the top surface because the top dries much faster than the bottom as stated in section 3.2.2. Typically indoor industrial floors are sealed from the outside environment, excluding the heating effect of the sun. Therefore the shrinkage gradient becomes the governing source of warping and with its negative gradient the slab wants to warp upwards as shown in Figure 3.3 (b).

(a)   (b)

Figure 3.3 (a) Downward warping of a slab and (b) upward warping (Alhasani & Zaraei, 1996).

It should be noted that for industrial floors the top surface is in general warmer than at the bottom, causing some warping in the opposite direction. However this amount of downwards warping is much less than the upward warping caused from the shrinkage gradient that the direction of warping remains upwards as shown in the right part of Figure 3.3 (Abdul-Wahab & Jaffer, 1983)

When the imposed deformations are restrained they result in stresses. Shrinkage strains develop tensile stresses and often lead to cracking. Floor slabs are restrained by the lower part of the slab that shrinks less than the top part and the lower part is restrained by the friction between the subgrade and the slab. With jointless concrete floors only the free edges have the possibility to curl up a bit, as is illustrated in Figure 3.4. The self-weight of the concrete floor will counter this.

Figure 3.4 A shrinkage gradient in a jointless floor causing the free ends to curl upwards which will be restrained due to the self-weight.

The warping of the concrete floor will be restrained, either by the self-weight or by the floor itself as it is restrained at the bottom. The imposed deformation of warping is therefore restrained and shall result in warping stresses, which in the earlier age of the floor will give tensile stresses. These tensile stresses will reach the tensile strength of the concrete with a jointless floor. For floors with a smaller distance between the joints, the first crack will appear in the middle of the floor where the tensile stresses will be the highest.

In the Dutch CUR-Recommendation 36 for the design of elastically supported concrete floors and pavements it is stated that a shrinkage gradient has to be accounted over the height of the slab. This gradient is 0.3 times the final shrinkage value ε_{cs}. Translating this gradient for a fully restrained floor into a K-value and calculate the occurring bending moment with Eq. (3.1) the bending moment found will be significantly higher than the cracking moment. Building a jointless concrete floor that will not crack at all is not possible, therefore it is important to control the crack-widths such that the floor won't lose its functionality.

3.4 Control of cracking

With a jointless concrete floor the distances between the free edges are quite big, in theory they can be infinite long, which means that some distance from the free edges the concrete floor will be fully restrained in the horizontal direction. At the edges the floor wants to curl upwards due to the imposed deformation caused by the differential drying shrinkage, the self-weight would prevent this and a crack could occur near the free edge as well. The restrained shortening of the top surface away from the free edges will result in tensile stresses which will reach the tensile strength of the concrete. In a jointless concrete floor cracks can be guaranteed to occur at the top surface due to the drying shrinkage. To control these cracks is considered to be the main criteria when designing the jointless elastically supported concrete floor.

In The Netherlands the concrete floors for a lot of the bigger industrial warehouses are being built without joints. As stated before, at ABT these floor designs see the following minimum dimensions and steel amounts that are preferably applied, all considered to control the crack-width:

- Thickness floor h = 160 mm
- Top reinforcement mesh of ϕ7-100 mm
- With a steel fibre dosage of 30 kg/m^3

The thickness or height of the floor is important to ensure that the appearing cracks will occur due to bending and not from pure tension. The concrete floor thickness is to ensure that the drying shrinkage at the top is faster than at the bottom of the floor slab and that as such the shrinkage gradient is to be considered. The shrinkage gradient ensures the bending moment which provides tensile warping stresses at the top surface of the concrete floor. When considering flexure in a concrete section it is allowed to calculate with the "fictional" flexural tensile strength $f_{ctm,fl}$ of concrete which is higher than the actual tensile strength f_{ctm}.

In the case of a thinner floor section there is the possibility that the bottom section of the floor undergoes drying shrinkage at the same time as the top section of the floor. This means that the shrinkage strain will more or less be uniform over the height of the floor and that instead of flexure, pure tension will be the imposed load in the concrete floor. In that case the concrete cracks that will occur will be wider and possibly throughout the entire concrete section, which is not wished for. Therefore, this minimum floor thickness is applied to ensure that significant uniaxial tension is prevented.

With a proper height for a jointless concrete floor the occurring cracks from the drying shrinkage will initially only be at the top surface of the floor. To control these crack-widths the top reinforcement net is applied, also called the 'shrinkage reinforcement'. Theoretically a finer reinforcement mesh where the centre-to-centre distance between the reinforcement bars is less would reduce the crack-widths. However for construction and practical purposes the centre-to-centre distance is not less than 100 mm, as this is still a suitable distance for construction workers to put their hands between the steel bars and be able to lift the reinforcement meshes. The other solution is to increase the diameter of the reinforcement bars, in section 2.5.2 it is stated the criteria around the maximum allowable crack-widths became stricter and stricter in the previous years and because of that the increase of the diameter of the reinforcement bars was actually the solution.

Eventually to fulfil the SLS requirements concerning the maximum allowable crack-widths the jointless floor industry reached basic top reinforcement nets of ϕ10-100 mm. As this came with a too big increase in price the introduction to hybrid reinforced concrete floors was made. This meant that steel fibres were added to the concrete mixture. Nowadays this is done with typically an average dosage of 35 kg/m³. The steel fibres provide a residual tensile strength reducing the force that has to be reintroduced by bond to the steel reinforcement bars, thus reducing the crack-width.

The *fib*-model code 2010 section 7.7.4.2 provides the following expression to calculate the design crack-width at the level of the reinforcement:

$$w_d = \frac{1}{2}\frac{\phi_s}{\rho_{s,eff}}\frac{(f_{ctm} - f_{Ftsm})}{\tau_{bm}}\frac{1}{E_s}(\sigma_s - \beta\sigma_{sr} + \eta_r\varepsilon_{sh}E_s) \tag{3.2}$$

Here the term *(f$_{ctm}$ – f$_{Ftsm}$)* shows the action of the fibres, the term *f$_{Ftsm}$* is a value for the residual tensile strength of fibre reinforced concrete. The effect of fibres also has to be taken into account in the terms σ_s and σ_{sr} which account for the steel stress in a crack and the maximum steel stress in the crack formation stage, respectively (Fédération Internationale du Béton, 2013). The result is a design crack width w_d that will be less as a virtue of the action of the steel fibres.

Looking at the bottom surface of the floor and considering the durability aspects related to the crack-widths, these are less of a problem. As there are no reinforcement bars present in the bottom part of the concrete floor, the size of the crack-widths here are not governing considering the corrosion of the reinforcement. As the distance from cracks at the bottom to the top reinforcement mesh is big enough corrosion won't occur the and the corrosion of steel fibres is negligible. The lack of dynamic loads at the bottom adds up to this that the control of the crack-width at the top surface is more important and governing compared to the bottom surface.

3.4.1 Concrete material properties and cracking minimisation

The design aspects mentioned above about the thickness, reinforcement and steel fibres are all to minimise the crack-width. To reduce the width of the cracks in a concrete floor, the concrete properties itself are of importance as well. With a proper concrete mixture some structural properties of the concrete can be directed in a way that the occurring tensile stresses from the imposed loads can be minimised.

With concrete floors the following concrete properties are of most importance when considering the minimisation of the tensile stresses or crack-widths:

- The tensile strength f_{ctm} or flexural tensile strength $f_{ctm,fl}$
- The modulus of elasticity E_{cm}
- The shrinkage size ε_{sh}
- The bond strength τ_{bm}

The tensile strength of the concrete determines when the concrete is going to crack. Concrete industrial ground floors are in general made with a relatively low concrete class around C30/37. The lower concrete class is preferred because of the accommodating lower tensile strength. With a traditional reinforced concrete floor the crack-width depends on the steel stress in the reinforcement. When the concrete cracks the tensile stresses in the concrete have to be taken over by the steel reinforcement, so if the tensile strength is less the resulting stresses within the steel will be less as well, resulting in a less wide crack.

The stresses within the concrete are directly related to its modulus of elasticity. Just like with the preferable lower tensile strength a concrete with a lower modulus of elasticity is preferred. The stresses in concrete can be found with Hooke's law:

$$\sigma = E \cdot \varepsilon \tag{3.3}$$

Eq. (3.3) shows this direct relation between the strain, the modulus of elasticity and the stresses. Concrete with a lower modulus of elasticity will see lower stresses from an imposed strain, where in the case of the jointless floor this imposed strain ε due to the shrinkage will provide tensile stresses. Hooke's law also shows that a reduced strain will result in reduced accommodating stresses, therefore the shrinkage size of the concrete mixture of importance. The total shrinkage size depends on several aspects as is described in the previous section, if the total shrinkage amount is less the total tensile stresses present will be less as well.

The crack-width in the concrete is also defined by the strain of the steel reinforcement bars at the crack, which is where the role of the bond strength of the concrete is found. The bond strength defines the transfer length that is required to transfer the tensile forces in the steel back in to the concrete, i.e. the anchorage length. A good bond between the concrete and the reinforcement allows for a faster reintroduction of the tensile stresses in the concrete, thus reducing the anchorage length. The reinforcement steel will see a lesser strain difference when the anchorage length is less, which in result provide lesser wide cracks. The formula to calculate the crack-width in Eq. (3.2) shows the bond strength, noted as τ_{bm} in the *fib*-model code, below the denominator which also shows that a higher bond strength will reduce the crack-width. The bond-strength of concrete is in general related to its tensile strength and the type of reinforcement used, which nowadays sees a standard ribbed profile to improve the bond between the concrete and the steel reinforcement.

3.4.2 Crack-width calculation from pure bending

For the crack-width calculation the stress in the reinforcement steel at the location of the crack must be known. For hybrid reinforced concrete the expressions and the approach are followed provided by the *CUR-Recommendation 111 Steel fibre reinforced concrete industrial floors on pile foundations – Design and construction*. In its annex the stress and strain diagrams for a hybrid reinforced structure are presented. In Figure 3.5 an edited stress diagram of this is shown where the residual tensile stress is taken as a constant value.
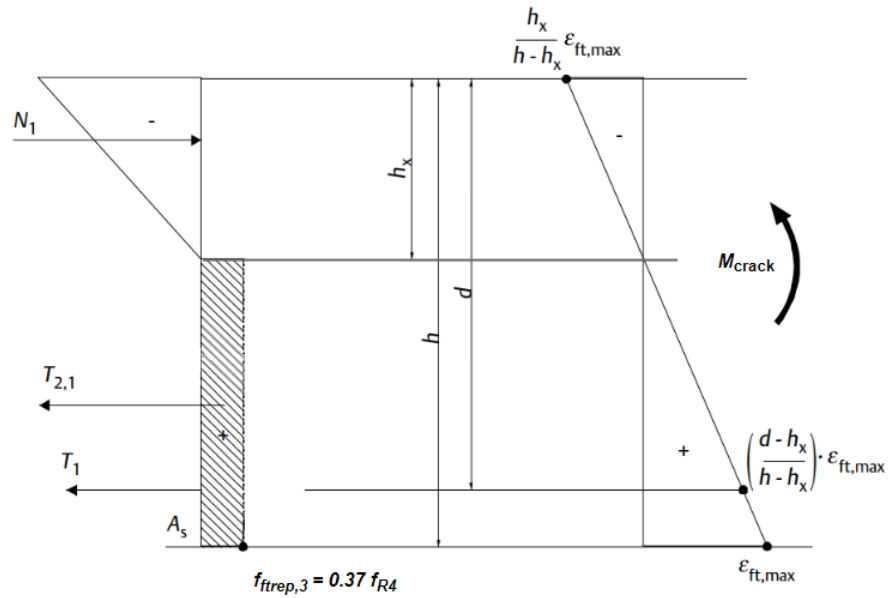
Figure 3.5 Stress and strain diagram used for the steel fibre reinforced concrete cross-section loaded in bending in serviceability limit state, figure adapted from (CURNET, 2007).

The equilibrium equations are based on the simplified stress-strain relation shown in Figure 3.6. N_1 is the compressive force, T_1 is the tensile reinforcement force and $T_{2,1}$ is the tensile force from the residual tensile stress due to the steel fibres. Here the conservative approach is made that the tensile stress in the tension zone is linear and has the value $f_{ftrep,3}$ for the entire tensile zone. As the cross-section is cracked the tension zone is in the descending branch shown in Figure 3.6 and the higher tensile residual stress $f_{ftrep,2}$ may be used at the point where the tension zone starts. This would result in an additional tensile force $T_{2,2}$, which is neglected here. As a result the force T_1 will increase to make horizontal equilibrium and as of that a slightly higher steel stress σ_s will be found. The residual tensile stress $f_{ftrep,3}$ has previously been denoted as σ_{r4}.

The tensile strengths mentioned above are calculated from the mean values from bending tests obtained for f_{R1} and f_{R4}:

$$f_{ftrep,2} = \sigma_{r1} = 0.45 \cdot f_{R1} \tag{3.4}$$

$$f_{ftrep,3} = \sigma_{r4} = 0.37 \cdot f_{R4} \tag{3.5}$$

The residual flexural tensile stresses f_{R1} and f_{R4} are obtained from experiments based on a notched beam loaded in bending.
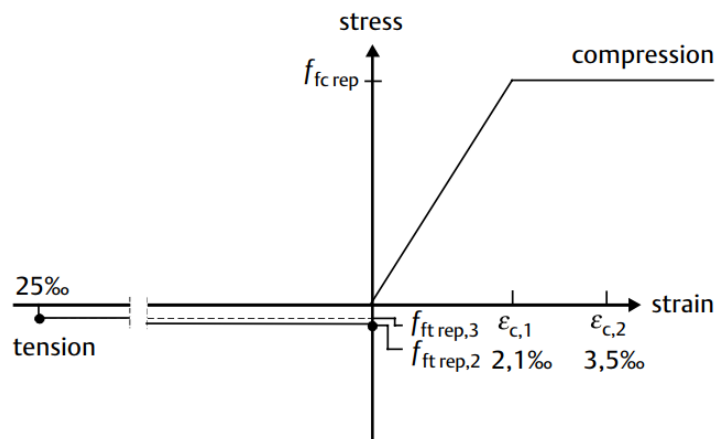

Figure 3.6 Simplified stress-strain relation of steel fibre reinforced concrete to be used in SLS design (CURNET, 2007).

33

Through horizontal forces equilibrium and bending moments equilibrium the system of two equations can be solved to compute the force T_1 and find the steel stress in a cracked cross-section. The cross-section is said to crack at the cracking bending moment M_{crack} which is calculated with the flexural tensile strength $f_{ctm,fl}$:

$$M_{crack} = \frac{1}{6} \cdot b \cdot h^2 \cdot f_{ctm,fl} \tag{3.6}$$

with
$$f_{ctm,fl} = \left(1.6 - \frac{h}{1000}\right) \cdot f_{ctm} \tag{3.7}$$

Where h is the thickness of the concrete floor in mm and f_{ctm} the concrete tensile strength in MPa. The cross-sections are considered per meter width so $b = 1000$ mm.

As the bending moment is set to be the cracking moment, bending moment equilibrium follows as:

$$M_{crack} = \frac{2}{3} h_x N_1 + \frac{1}{2}\ h - h_x\ T_{2.1} + (d - h_x)T_1 \tag{3.8}$$

Horizontal forces equilibrium must also be satisfied:

$$\Sigma H = 0 \rightarrow\ N_1 = T_1 + T_{2.1} \tag{3.9}$$

To calculate the crack-width the height of the concrete compression zone h_x and the steel stress σ_s need to be known. By solving the system of two equilibrium equations, the height concrete compressive zone can be found, after which the tensile force component T_1 can be found which divided by the reinforcement area results in the tensile steel stress σ_s. The height of the concrete compressive zone is also required to find the effective reinforcement ratio for the tensile bar $\rho_{s,ef}$. In Appendix B the crack-width calculation done according to Eq. (3.2) and the approach to solve the system of equation described above is further elaborated.

The formulation given to calculate the crack-width in Eq. (3.2) represents the crack-width at the level of the reinforcement for members subjected to bending. The crack-width will generally be larger at the extreme tensile fibre, the top surface of the jointless floor in this case. The crack-width at the extreme tensile fibre can found by multiplying the crack-width w_d with the factor shown in Eq. (3.10). The crack-width at the top surface of the jointless floor can be found with:

$$w_{opp} = w_d\ \left(\frac{h - h_x}{d - h_x}\right) \tag{3.10}$$

Where d is the effective height of the concrete cross-section and h_x the height of the concrete compressive zone.

This thesis is about the introduction of alkali-activated concrete and geopolymer concrete and its implementation in industrial jointless concrete ground floor. This material is interesting as it has the potential to be beneficial considering the concrete properties that have been described in section 3.4.1. In the next chapter this cement free concrete and its structural properties relevant towards the control of cracking are introduced.

4   ALKALI-ACTIVATED CONCRETE

Alkali-activated concrete (AAC) is a relatively new concrete for the modern world, even though it has been around for more than 70 years. Alkali-activated concrete is a concrete where the binding material is realised without cement and with cement being the component of concrete that is responsible for the most CO_2 emission, alkali-activated binders gained more interest in the last decade. This chapter will answer why this relatively new material should be implemented more broadly in The Netherlands. A brief history is given about alkali-activated concrete and the chemistry behind it. Comparisons are made of material and structural properties between AAC and traditional concrete and it is discussed in what way AAC can be interesting for the industrial floor industry.

4.1 Introduction alkali-activated concrete

Concrete is a composite material that in the most traditional way consists of the aggregates and the binder. Aggregates are granular materials like sand and gravel which in combination with a binder, which if realised with cement and water, becomes the material well known as concrete. Cement reacts with water, creating the binding material due to the hydration process that occurs. With alkali-activated concrete the binder is realised without cement. Instead, it is realised by the combination of an alkaline activator which is dissolved in water and solid pozzolanic precursors.

4.1.1 Alkali-activated binding material

The binder material is realised not due to hydration as with traditional concrete but by the chemical process polymerisation. The polymerisation of the pozzolanic materials, which are materials that are rich in alumina and silica, is activated in the alkaline environment created by the alkali activator. With this polymerisation a network is created of aluminosilicate polymers which is the alkali-activated material and the binder of an alkali-activated concrete. The final product is a sodium-alumino-silicate-hydrate (N-A-S-H) gel binder which is often referred to as 'geopolymer'. Calcium rich precursors are also suitable where an calcium-(alumino)-silicate-hydrate (C-A-S-H) gel is the main product in the binder, which is rather similar to the binder obtained from ordinary Portland cement (OPC). A common precursor that is calcium rich is blast furnace slag (BFS) which also contains alumina and silica in its chemical composition. Fly ash (FA) is the other most seen precursor which can be either be high- and low-calcium fly ash (Garcia-Lodeiro, Palomo, & Fernández-Jiménez, 2015b).

To activate the aluminosilicate materials alkaline activators such as sodium hydroxide (NaOH), sodium silicate (Na_2SiO_3), potassium hydroxide (KOH) and potassium silicate (K_2SiO_3) can be used. These alkaline activators are dissolved in water. The first two mentioned activators are the most common activators seen with alkali-activated concrete.

An overview of the components of the alkali-activated system is shown in Figure 4.1. One prominent feature of these alkali-activated material components is that both natural materials

(like clay) and industrial by-products (like slag and fly ash) can be used as the prime materials for the concrete (Garcia-Lodeiro, Palomo, & Fernández-Jiménez, 2015b). This is one of the beneficial aspects of alkali-activated concrete.
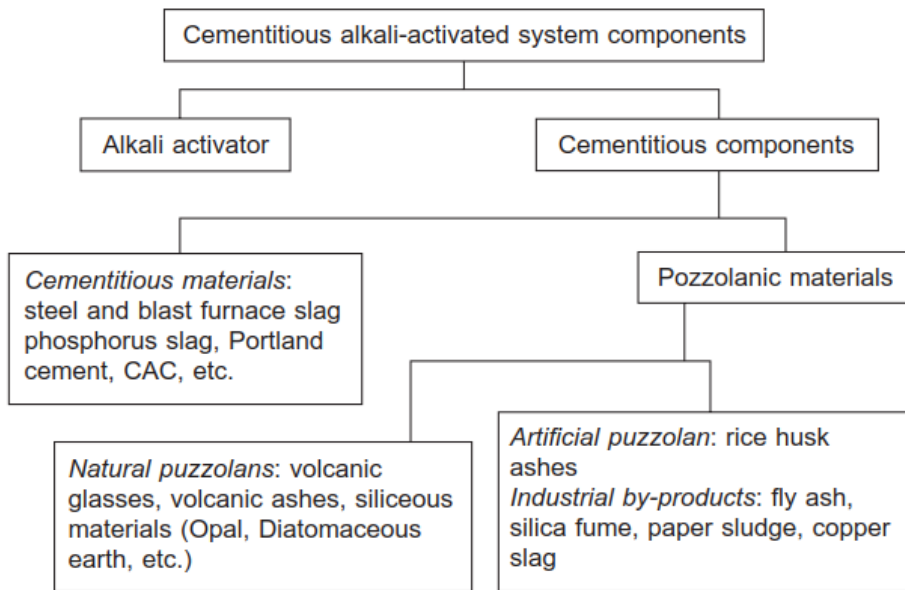
Figure 4.1 An overview of the alkali-activated system components (Garcia-Lodeiro, Palomo, & Fernández-Jiménez, 2015b).

The above systems shows many different components that are suitable to create an alkali-activated concrete and this results in a wide variety of binders. Because of this a plethora of terms and names for very similar alkali-activated materials exists. The product of the alkali-activated binder is dependent on the composition of the raw materials and its activator. Figure 4.2 illustrates the typical composition of the most used raw materials. A distinction has been made by Garcia-Lodeiro et al. (2015a) between the alkaline cements which is shown in Table 4-1.
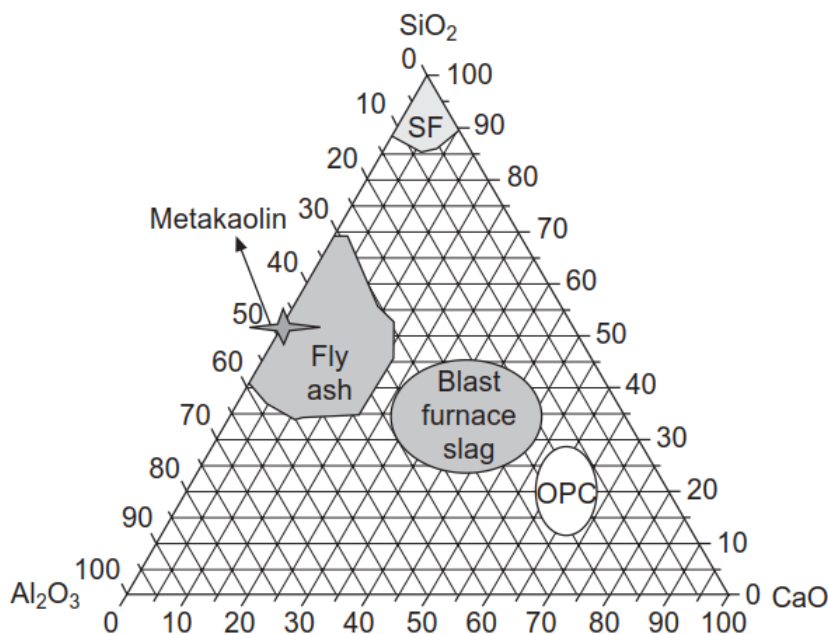
Figure 4.2 Usual range of composition of the raw materials used to manufacture alkaline cements on a CaO-SiO$_2$-Al$_2$O$_3$ diagram (Garcia-Lodeiro, Palomo, & Fernández-Jiménez, 2015b).

The table below shows this division that is made between the alkaline binder materials into the two main categories. The first type is where a calcium-rich precursor (e.g. BFS) is activated by a mild alkaline solution where C-A-S-H is the main product. The second type is categorised by the activation of a low-calcium precursor (e.g. metakaolin or silica fume) with a medium to high alkaline solution. Silica fume is shown in the top of the diagram from Figure 4.2, as SF, which shows that silica fume has a maximum calcium content CaO of 10%, making it a low-calcium precursor. The main product of low-calcium precursors are zeolites which because of their polymeric structure have been named 'geopolymers' by the French material scientist Davidovits in 1979 (Davidovits, 1991).

Table 4-1 Products precipitating in different types of binder (Garcia-Lodeiro, Palomo, & Fernández-Jiménez, 2015a).

Binder type		OPC	Alkaline cement	
			$(Na,K)_2O\text{-}CaO\text{-}Al_2O_3\text{-}SiO_2\text{-}H_2O$	$(Na,K)_2O\text{-}Al_2O_3\text{-}SiO_2\text{-}H_2O$
Reaction product	Primary	C-S-H	C-A-S-H	N-A-S-H
	Secondary	$Ca(OH)_2$ AF_m AF_t	Hydrotalcite $[Mg_6Al_2CO_3(OH)_{16}\cdot4H_2O]$ C_4AH_{13} $CASH_8$ C_4AcH_{11} $C_8Ac_2H_{24}$	Zeolites: hydroxysodalite, zeolite P, Na-chabazite, zeolite Y, faujasite
$C = CaO, S = SiO_2, A = Al_2O_3, N = Na_2O, H = H_2O, c = CO_2$				

In the RILEM State of the Art report 'Alkali-Activated Materials' by Provis and Van Deventer (2014) a simplified classification is made. In this RILEM report it is stated that the geopolymers are viewed in many instances as a subset of alkali-activated materials. This classification is shown in Figure 4.3.
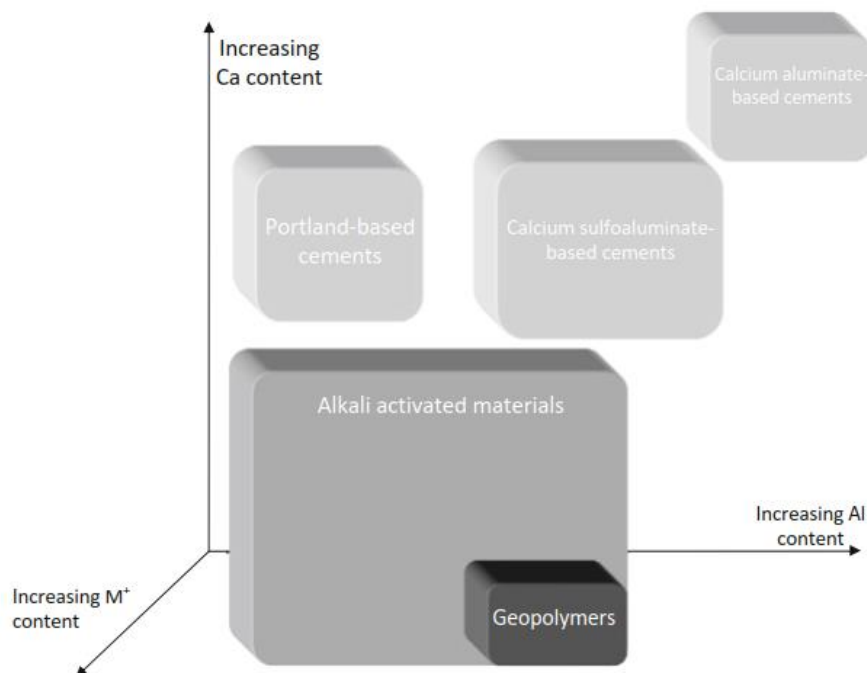

Figure 4.3 Classification of AAMs, with comparisons to OPC and other calcium based binders. Shading indicates an approximate of alkali content; darker shading corresponds to concentrations of Na and/or K (Provis & Van Deventer, 2014, p. 8).

Davidovits is in disagreement with this classification and has given several presentations to address why geopolymers are not the same as alkali-activated materials and therefore not a subset of them. Geopolymers should be separate from this classification according to Davidovits as he states that the polymerisation chemistry is very different from the alkali-activation of calcium-rich precursors and the hydration chemistry. However the term geopolymer is generally accepted as the term that is used for the complete range of alkali-activated materials and the reason people often use the term geopolymer concrete where the correct term may be alkali-activated concrete. In the current and the following chapters the term geopolymer concrete (GPC) will be used several times. In such cases the term is used as the concrete that is being discussed in the section, graph or table will be in reference to an earlier mentioned actual geopolymer concrete.

4.2 History

In the last decades there has been a lot of discussion, from scientific and historical perspectives, about the possible role of alkali-activated cements in ancient Egyptian and Roman structures. A brief history is given about this possible implementation of the alkali-activation chemistry from very long ago and the actual development the alkali-activation technology has seen in the last century.

4.2.1 Alkali-activation in ancient cements

There are potential connections between modern alkali-activated binders and ancient Roman concrete. Of interest are the Roman concretes which were based on the activation of pozzolanic materials, like volcanic ash from the region of southern Italy, with calcium compounds, particularly lime (Gotti, et al., 2008). Here the elevated pH generated by the reaction of the lime initiated the reaction of the pozzolanic material, which is similar to AAM. Some Roman structures have remained in service for over 2,000 years within harsh environments, i.e. seawater immersion and seismic activities. Nowadays modern concrete degrades mainly due to the corrosion of the reinforcing steel, a form of decay which the Roman unreinforced structures did not undergo.

Early Roman mortars appear to be predominantly based on the development of strength and hardness by carbonation of lime, until through either experimentation or implementation they discovered that the formation of aluminosilicate binding phases by including volcanic silica-containing ash and/or fired clay gave improvements to their mixtures. The addition of silica-containing materials changes the mineralogical composition which gave an increase in durability. The mineralogical composition of ancient binders appear to be lower in Ca and richer in alkalis Si and Al compared to modern Portland cements (Glukhovsky, 1994).

Modern cements that are used to repair ancient structures rarely prove to be as durable as the ancient cements when exposed to identical conditions. This may indicate that higher aluminosilicate with a lower calcium content could provide long term advantages in terms of binder stability. Where CSH is the major constituent of both ancient cements and OPC, it is not necessarily responsible for the durability. From the analysis of certain ancient materials and modern cements it can be implicated that aluminosilicate-based binders provide favourable chemical durability as opposed to calcium silicate-based binders (Provis & Van Deventer, 2014, pp. 21-23).

4.2.2 Modern development of alkali-activated materials

In the 1950s there was a lack of Portland cement in the former Soviet Union, during this time Professor V.D. Glukhovsky began to investigate the binders of the ancient Roman and Egyptian structures. He discovered the possibility to produce binders using low calcium or calcium-free aluminosilicate and solutions containing alkali metals in 1957. From the 1960s onwards this work of Glukhovsky has been involved in a lot of applications in Ukraine. Construction of apartment buildings, railway sleepers, road sections, pre-cast slabs and blocks were constructed in former Soviet Union using alkali-activated blast furnace slag. The materials of these original structures have shown to have high durability and compact microstructure (Xu, Provis, van Deventer, & Krivenko, 2008). Prior to 1989 more than 3,000,000 m³ of alkali-activated concrete has been poured in the former Soviet Union. Such a large volume of material production demonstrates the viability of this technology as many of these aged structures have good durability properties. Properties like frost-resistance, impermeability and strength increases were found to be improved on several AAM concretes that were put into service since 1962 (Wang, Pu, Scrivener, & Pratt, 1995).

Table 4-2 Case studies in the former Soviet Union: strength and frost-resistance results (Wang, Pu, Scrivener, & Pratt, 1995).

Application	Service years	Aggregate type	Original strength: MPa	After service		Strength increase: %
				Frost-resistance cycles	Strength: MPa	
Canal surface (under water)	11	Secondary sand rock	15	900	42·6	184
Canal surface (in air)	11	Secondary sand rock	15	900	40·0	167
Water pond	9	Sea sand	25	700	59·5	138
Pile	9	Sea sand	30	600	71·8	139
Road surface	8	Sea sand	16	250	47·6	198
Dam	8	Sea sand	30	570	62·0	107
Pipe	7	River sand	30	—	83·0	177
Floor member	2	Carbonate	90	1115	101·0	11
Floor member	2	Granite	96	1115	122·0	27
Floor member	2	Carbonate	70	1000	110·0	57

As described above, alkali-activated concrete has seen its implementation in concrete structures for several decades already. High-rise residential buildings with cast in-situ structural elements, office - and retailed buildings, storage houses with precast beams and columns have all been realised in Eastern Europe already in AAC in the previous century. Most of these structural implementation have shown good results considering structural performance, durability aspects and even cost savings (Provis & Van Deventer, 2014, pp. 309-315).

Two other promising examples are alkali-activated concrete roads that were cast on site in the city of Magnitogorsk, Russia, and in the city of Ternopol, Ukraine, both in 1984. The road constructed in Russia was a heavy-duty road for a quarry where the vehicle loads of 60 – 80 tons were common. Such axle loads are similar to the nowadays forklift-truck loads seen in modern warehouses. The alkali-activated material for the concrete was realised with blast furnace slag and Na_2CO_3 dissolved in water. The concrete for the road construction had a design strength of 30 MPa and a steel reinforcing mesh was applied. After 15 years in service inspections were made in 1999. A considerable compressive strength increase was measured to an average of 86 MPa and little water absorption and carbonation depths were measured. There was no evidence of reinforcement corrosion or freeze-thaw scaling, in spite of the exposure to freeze-thaw loads for several months per year.

In Ukraine the cast-in-situ road, and a concrete fountain, were also realised with alkali-activated blast furnace slag and constructed in 1984. Next to these structures were equivalent built Portland

cement concrete structures which were both inspected and compared in 1999. The road and fountain built using the alkali-activated BFS concrete were in very good working condition, while the equivalent structures directly next to it built with Portland cement concrete were seriously deteriorated (Provis & Van Deventer, 2014, pp. 315-316). The difference in degradation is clearly visible in Figure 4.4.

Figure 4.4 Comparison between cast-in-situ alkali-activated slag concrete (left side) and ordinary Portland cement concrete roads (right) in Ternopol, Ukraine (Provis & Van Deventer, 2014, p. 316).

Throughout the world the implementation of alkali-activated concrete, and geopolymer concrete, for structural components is seen more and more. Where Australia is one of the forerunners in this, as there the first modern structural components have been realised in geopolymer concrete. In 2012 a four-storey building for the University of Queensland has been constructed where the floors were made out of 33 precast geopolymer concrete elements, see Figure 4.5. Prior to construction of the building, a lot of experiments and tests have been conducted, which is still necessary. With this implementation modern geopolymer concrete has moved beyond an emerging technology into the space of a structural concrete that can be designed and used in structures (Bligh & Glasby, 2013). The applied proprietary geopolymer concrete is known as Earth Friendly Concrete (EFC).

Figure 4.5 The Global Change Institute building of the University of Queensland (left) and the assembly of that building showing the geopolymer concrete floor beams (right) (Bligh & Glasby, 2013).

The largest modern application of geopolymer concrete has been conducted in Australia as well. In 2014 for the Brisbane West Wellcamp Airport approximately 40,000 m^3 of geopolymer concrete was used for the turning node, apron and taxiway pavements. The concrete pavements have been realised with the same geopolymer concrete EFC as it was found to be well suited for this construction due to its high flexural tensile strength, low shrinkage and workability characteristics (Glasby, Day, Genrich, & Aldred, 2015).

Figure 4.6 Aerial photograph of the completed pavement works at the Brisbane West Wellcamp Airport site (Glasby, Day, Genrich, & Aldred, 2015).

The above mentioned implementations are prime examples that display that alkali-activated – and geopolymer concretes that have been placed into service, have been able to serve the purposes for which they have been designed, without evident problems to mechanical stability or durability aspects. Where the concrete structures made in the former Soviet Union provide valuable knowledge about the long-term effects of alkali-activated materials, these examples show that they are suitable to replace some of the Portland cement concrete structures in the future.

4.2.3 Alkali-activated concrete in The Netherlands

The Netherlands has seen its first structural implementations by now as well. The technology behind the ASCEM® cement, which uses alkaline activation of aluminosilicate materials in combination with the reuse of secondary raw materials, has been successfully tested in the late 1980s already (Buchwald, 2012). It was not commercialised at that time. Nowadays, other drivers such as CO_2 reduced cements have led to the reanimation of the research and it has been applied in the production of concrete pavement slabs and concrete sewer pipes, Figure 4.7.
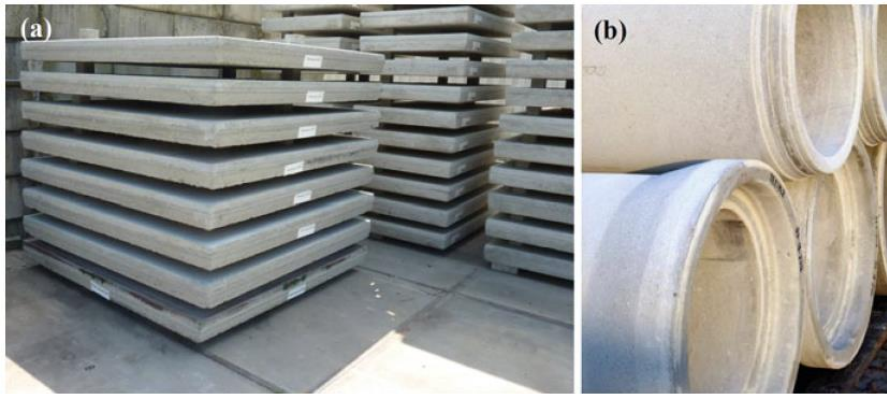
Figure 4.7 Storage of concrete products made with ASCEM® cement (Provis & Van Deventer, 2014, p. 326).

In the city of Hengelo a new office building has been realised for which the owner had high ambitions towards a sustainable building. So in 2016 the first building in The Netherlands was realised with structural components made with alkali-activated concrete, namely the hollow-core slabs used for the floor system of the five-storey building. Just like the building from the University of Queensland in Australia a lot of research was done before the hollow-core slabs could be made. Figure 4.8 shows the successful start of the production of a hollow-core slab in alkali-activated concrete after the initial tries failed (de Vries, 2017).

Figure 4.8 Production of the alkali-activated concrete hollow-core slab (left) and the office building in Hengelo in which these slabs have been applied (de Vries, 2017).

Another large implementation of alkali-activated concrete in The Netherlands is that of an actual industrial ground floor. In 2015 in the city of Gorinchem some 400 m^3 of alkali-activated concrete has been casted-in-situ for the construction of the floor of a powdered milk factory. This choice was made because alkali-activated can show a high resistance towards acids. The C-S-H gel in normal cement concrete does not withstand long-term exposure to acids and these acids could easily penetrate the pores filled with calcium-reaction products CaOH and CaCO$_3$. The C-(A)-S-H gel of alkali-activated concrete has a more dense structure, as of which the degradation of the concrete due to acids is significantly slower. Van Nieuwpoort Betonmortel, a supplier for durable and sustainable concrete, performed the research program for this alkali-activated concrete. Before the pour of the concrete the process of monolithic finishing of this alkali-activated concrete was realised, which showed that the usual tools were suited for this (Vermeulen & de Vries, 2015).

That such research is still necessary to perform, prior to the implementation of an AAC structurally, is one of the reasons that the number of structural implementations is still relatively low. As of yet the implementation of alkali-activated concretes requires more time and money for the research which is necessary to create a proper design for a concrete structure realised in an

alkali-activated concrete. A lot of research is done throughout the world and the first recommendations and design codes are being developed.

4.3 Structural and material properties

Before alkali-activated concrete sees practical applications it is essential to have a thorough understanding of the mechanical properties of it. For an industrial concrete ground floor the most important material properties have been given a brief introduction in paragraph 3.4.1 which will be further discussed here. The compressive strength is discussed as well as the relationship between the compressive strength and other mechanical properties of concrete are mostly codified in standards as empirical relationships involving the 28-day compressive strength of the material.

These standardised correlations are based on large volumes of data which have been generated from many thousands of, mostly Portland cement, concrete samples over a number of decades. However these well-known correlations are not completely in line with the prediction for the performance of alkali-activated concretes, as the physicochemical properties of the alkali-activated binder material and the interaction of it with the aggregates is notably different. Therefore it is important to develop a full understanding of the appropriate methods of testing and predicting the mechanical properties of alkali-activated concretes. The testing protocols that are used in Europe for the testing of mechanical strength properties of Portland cement-based materials are also suitable for alkali-activated materials (Provis & Van Deventer, 2014, pp. 170-171).

As the addition of steel fibres is an important design aspects for industrial concrete ground floors, its interaction with alkali-activated concrete is discussed as well. The following mechanical properties are discussed: compressive strength, tensile and flexural strength, modulus of elasticity, shrinkage, bond strength and steel fibres interaction.

4.3.1 Compressive strength

The compressive strength of concrete is used as the basis for the correlation with other material properties. Like with OPC concrete, AAC can see compressive strengths that range from very low to very high values. Concrete compressive strengths above 70 MPa have been reported for a lot of different AAC, were raw materials like blast furnace slag, fly ashes, phosphorus slag and metakaolin have been used.

In OPC concrete the development of strength can be correlated to the hydration grade which increases as the binder is formed, where AAC sees its development of strength by the formation of calciumsilicate and aluminosilicate components during the alkali-activation process. With AAM the development of the binder depends on a lot of factors where the chemical composition of the raw materials is one of them. As said calciumsilicate and aluminosilicate components are being formed during the alkali-activation, where mostly the latter is created within geopolymers and low-calcium precursors. The type and concentration of the alkaline activator is also important, high concentrations result in faster reactions. This can result in high early strength but it also has possible downsides like flash setting of the concrete mixture.

What often is applied is a mixture of the two most used precursors, BFS and FA, as AAC realised with only FA is characterised by low strength development. AAC realised with BFS shows a faster strength development and the addition of BFS to FA shows an improvement of the early strength of AAC (Kumar, Kumar, & S.P., 2010).
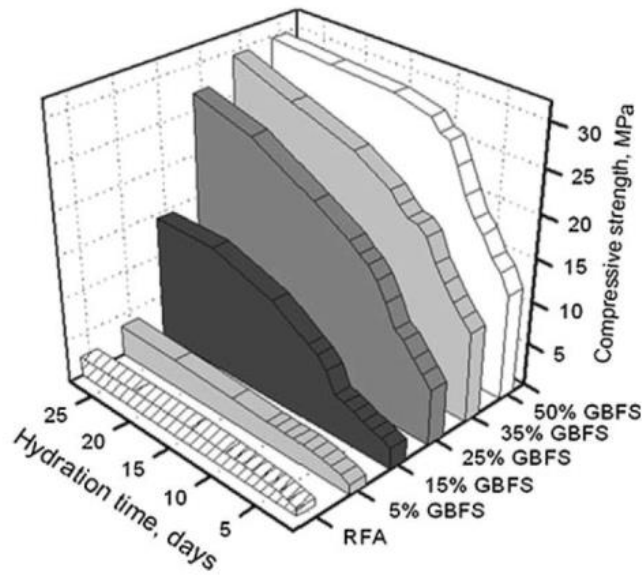
Figure 4.9 The effect of BFS on the compressive strength development in AAC, in relation to hydration time at 27⁰C (Kumar, Kumar, & S.P., 2010, p. 613).

As the compressive strength of concrete is highly dependent of its aggregates, the compressive strengths between OPC concrete and AAM concrete are comparable.

4.3.2 Tensile and flexural tensile strength

For alkali-activated concrete the tensile strength is also small compared to its compressive strength. In general alkali-activated concretes show relatively higher tensile and flexural tensile strengths than would be predicted from standards for OPC concretes of similar compressive strengths (Provis & Van Deventer, 2014; DELTA Concrete Consult, 2018). The standards used to predict the tensile and flexural strength vary slightly between the different national standards globally, in the graph of Figure 4.10 the relationship is shown computed from the American Concrete Institute standard.

Figure 4.10 Relationship between flexural and compressive strength of alkali-activated concretes synthesised from various precursors as marked, at ages between 4h and 1 year, with the relationship for OPC concretes as specified in ACI 318-02 shown for comparison (Provis & Van Deventer, 2014, p. 283).

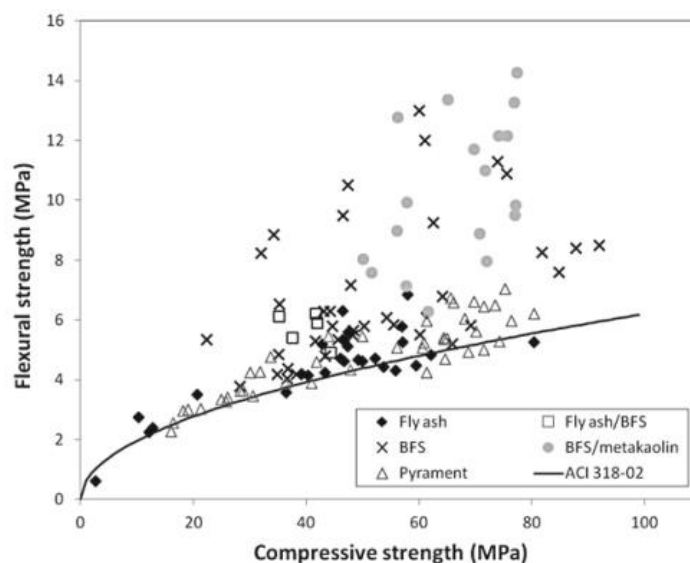Data from a variety of literature sources is displayed along the relationship and almost all of the data for AAM concretes show higher flexural strengths than the predicted relationship for OPC concretes.

The results of a higher tensile strength have been reported for several AAC realised solely with raw materials like slags (Rodriguez, Bernal, Mejía de Gutiérrez, & Puertas, 2008) and with blends of fly ash and slag (Sofi, van Deventer, Mendis, & Lukey, 2007). This increased tensile strength of alkali-activated binders are associated with a highly dense interfacial transition zone between matrix and aggregates when compared with conventional cements (Bernal, Mejía de Gutierrez, & Provis, 2012). Alkali-activated concretes see an average of 10-20% higher tensile strength to comparable OPC concretes with a similar compressive strength.

Usually concrete is not designed to resist tensional forces and a higher tensile strengths can easily be mistaken as a profitable benefit to concrete. The tensile strength is important to know in order to estimate when cracks will develop in the concrete. Where usually a lower concrete class is applied with industrial concrete ground floors, because this comes with a lower tensile strength, thus the cracking forces will be less resulting in thinner cracks. So the higher tensile strengths alkali-activated concretes show are far from beneficial for the jointless ground floors.

4.3.3 Modulus of elasticity

The modulus of elasticity is an important parameter to know when designing concrete structures, it provides an indication of the resistance against elastic deformation when loads are applied. Several studies have been performed regarding the modulus of elasticity of alkali-activated concretes and the results are different when different precursors are used for the binder. The elastic modulus of AAC can be comparable to that of OPC concrete with comparable compressive strength, but most reports show results that the modulus of elasticity is slightly lower. Similar behaviour for AAC is found that an increase of the compressive strength comes with an increase for the modulus of elasticity.

Alkali-activated concrete realised with BFS have been reported to have elastic moduli of around 30-35 GPa. Other reports show results for the elastic moduli between 28-50 GPa where AAC BFS is activated with an alkali-silicate and values between 12-42 GPa where the BFS is activated by an alkali-hydroxide. Alkali-activated concretes realised with fly ash and metakaolin have been reported with elastic moduli around 17-18 GPa, where the binder is realised of the zeolites N-A-S-H type gel instead of the C-A-S-H gel binder seen with calcium-rich precursors (Provis & Van Deventer, 2014, pp. 283-285). Overall most studies show elastic modulus between 10 and 40 GPa, which is comparable to that of OPC concrete. The wide spread shows that the modulus of elasticity can be somewhat controlled with the choice of different precursors and activators. Where, if desired, an approximate 10% lower modulus of elasticity can be reached in comparison to OPC concrete with similar compressive strengths (DELTA Concrete Consult, 2018).

Another important issue regarding AAC are reporting's of a decrease of the modulus of elasticity with increasing curing time (Wongpa, Kiattikomol, Jaturapitakkul, & Chindaprasirt, 2010; Prinsse, 2017). This decrease of stiffness is often accommodated with a decrease in strength properties as well. It is not quite clear yet as to why AAC can see this decrease of stiffness over time. A correlation is made that this loss is related to moisture loss. The research done by Prinsse (2017) showed that AAC samples that were wet-cured for 28 days had a decrease in modulus of elasticity when tested at a later hardening age, where an increase for the modulus of elasticity was measured for the same AAC where samples were wet-cured for this extended period. Bernal et al. (2015) also measured a degradation of the binding gel and therefore a decrease in strength and stiffness. This decrease is a result from a loss of alkalinity, where this loss of alkalinity can be contributed to carbonation effect and moisture loss.

The opposite it stated by some scientist who say that the storage of AAC in water is the culprit for this behaviour. When stored underwater the alkali of the activator within the concrete specimen can leach out of the mixture into the surrounding water reducing the alkali-activation and therefore reducing its stiffness and strength. The well-known curing conditions that are suitable for OPC concretes do not give equivalently good results for AAM, where early age immersion can lead to leaching of the alkali metal component of the activator hindering or halting the strength and microstructural development (Provis J. , 2013).

4.3.4 Shrinkage

There are a multitude of testing protocols that can be used in the assessment of the dimensional stability of hardened and fresh cement pastes and concretes. Some tests are intended to be specific to one form of shrinkage, through which drying and autogenous shrinkage are often isolated. Suggestions have been made that the C-A-S-H gel in alkali-activated BFS binders are more prone to shrinkage than the C-S-H gel formed through hydration of OPC. Where the shrinkage of alkali-activated fly ash materials can shrink very little or very significantly, depending on the mix design. Curing and mixture design are very important considering shrinkage, especially drying shrinkage. Where AAC with the addition of excess water or the exposure to drying conditions at early age can almost be guaranteed to lead to problems in terms of drying shrinkage, because the degree of chemical binding of water in the gel structure of AAM is much less than in OPC based materials (Provis & Van Deventer, 2014).

In an early report of Kukko and Mannonen (1982) the so-called F-concrete, an alkali-activated BFS concrete, showed a drying shrinkage at 50% RH that was around 10% lower than that of a Portland cement concrete of comparable strength grade, mix design and workability over a 2-year period. Häkkinen (1993) found for this same F-concrete indeed an initial lower shrinkage but found that the shrinkage of the AAC continued for an extended period and overtook the total extent of shrinkage compared to the OPC samples.

Melo Neto et al. (2008) tested parallel the drying – and autogenous shrinkage of an alkali-activated BFS mortar to determine the influence of each shrinkage mode. They showed that the ongoing shrinkage of alkali-activated BFS is highly dependent of the activator. They showed that the concentration of the activator plays an important role in autogenous and drying shrinkage, where an increase in activator amounts to an increase in total shrinkage. The formation of C-(A)-S-H plays a key-role in this as this formation is accommodated with an increase in volume which results in a decrease in porosity, hence the changes in shrinkage. Figure 4.11 shows the shrinkage graphs for different compositions of activators. The activator type used is sodium silicate where 2NS has the lowest silica modulus and 4NS has the highest silica modulus. It was found my Melo Neta et al. (2008) that the amount of silicate contained in the activator plays an important role in autogenous and drying shrinkage and that an increase in sodium silicate produces an increase in total shrinkage.
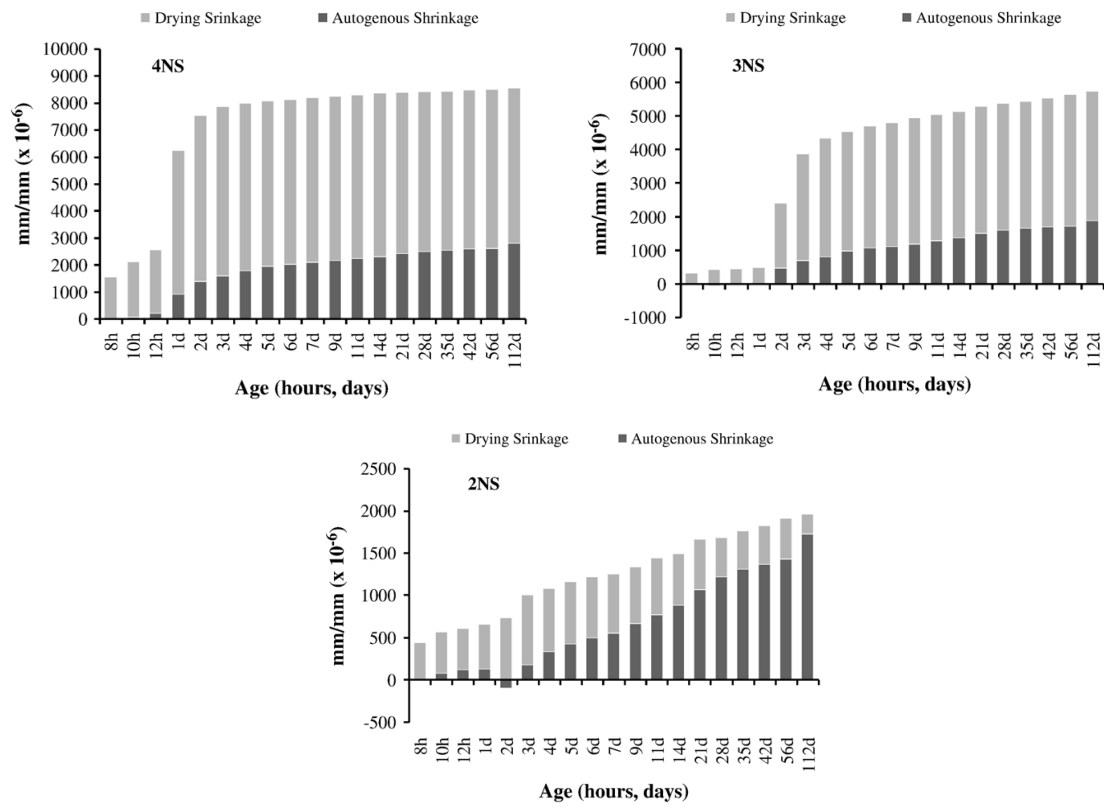
Figure 4.11 Comparative graphs for drying and autogenous shrinkage rate at multiple compositions of activators. Graphs taken from Melo Neto, Cincotto, & Repette (2008).

That the alkaline-activator plays a role with regard to shrinkage has been found by Wang et al. (1995) and Duran Atiş et al. (2009) as well. They noted that that the activation of BFS by either NaOH or Na_2CO_3 gave similar shrinkage properties to OPC, while waterglass activated BFS binders shrank more than OPC under drying conditions.

Aldin et al. (2017) tested the effect of curing age on the drying shrinkage of alkali-activated concrete. Prisms that were cured for several days showed much less shrinkage strain when compared to specimens that were cured for 1 day. The development of the drying shrinkage strain is shown in Figure 4.12. With curing a significant reduction of shrinkage strain in the early of age of the alkali-activated concrete can be achieved. This is correlated to the weight loss measured of the tested specimens.

Yong (2010) investigated this effect of curing duration and its influence on drying shrinkage. Specimens that were cured for a longer period of time prior to the measurements showed reduced drying shrinkage, visualised in Figure 4.13. The longer curing period provides a more mature binder which is more resistant to dimensional change, hence the shrinkage seen is less. The curing of concrete ground floors is important when they are realised with OPC concrete, these studies show that the curing is important as well when such floors were to be constructed with AAC.
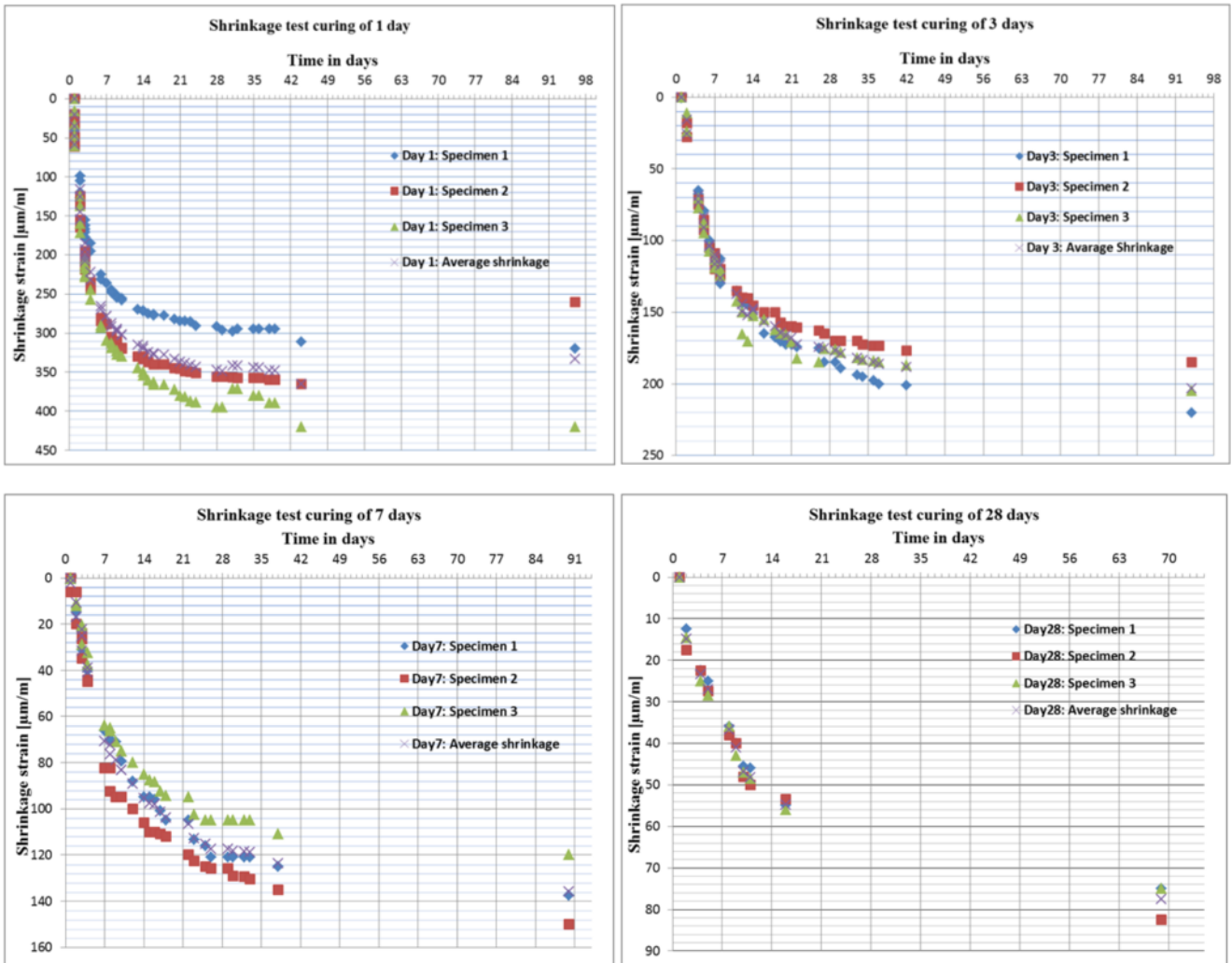
Figure 4.12 Drying shrinkage development for AAC specimens cured for different ages of 1 day, 3 days, 7 days and 28 days. Graphs taken from (Aldin, Guang, Luković, & Nederlković, 2017).
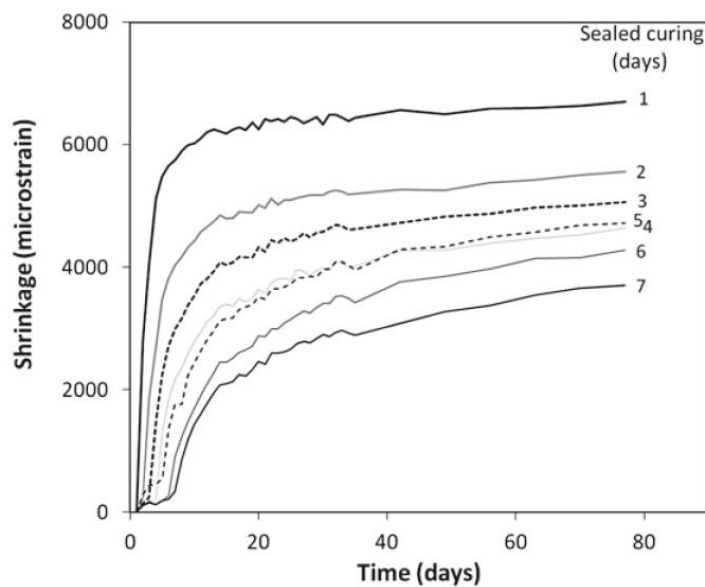
Figure 4.13 Shrinkage of 60% fly ash/40% BFS mortars activated with sodium silicate solution, cured in sealed bags for different periods as marked. Data from (Yong, 2010).

When alkali-activated fly ash-based concretes are heat-cured for a certain time they show very little drying shrinkage compared to ordinary Portland cement concrete (Wallah, 2009). Most of the water released during the chemical reaction may evaporate during the heat-curing process.

The amount of remaining water within the micro-pores of the hardened concrete is small that the drying shrinkage is low as well. As reduced drying shrinkage is preferable for the industrial ground floors, the realisation of a reduced shrinkage size through heat-curing of concrete is only practical with precast elements and therefore not suitable with cast-in-situ concrete ground floor.

In general most of the alkali-activated concretes show significant more shrinkage than ordinary concrete. This is especially the case for alkali silicate-activated BFS mortars and concretes, where up to four times higher drying shrinkage rates may occur compared to Portland cement concretes cured and stored under the same environmental conditions. Alkali silicate-activated is the case where for example the common activator sodium silicate, i.e. waterglass, is used. The effect of shrinkage reducing admixtures (SRA) on activated BFS systems has been studied by some because of this. Bakharev et al. (2000) reported that some of the standard shrinkage-reducing admixtures, along with air-entraining admixtures, could reduce drying shrinkage to less than that of a standard OPC mix realised without admixtures. Alkali-activated slag that were realised with other admixtures, like superplasticisers, showed an increase in shrinkage.

Palacios and Puertos (2007) found that shrinkage-reducing admixture based on polypropylene glycol in waterglass-activated slag mortars can reduce autogenous shrinkage by 85% and drying shrinkage by 50% . This beneficial effect on shrinkage is primarily due to the decline in the surface tension of the pore water and the change induced in the pore structure by the admixture. When the mortars were cured at RH = 99% the addition of SRA brought the shrinkage down to similar values for those found for OPC mortars, where cured at RH = 50% with the addition of SRA the alkali-activated slag mortars still showed shrinkage rates still twice as large. The shrinkage of Portland cement and the waterglass alkali-activated slag mortars with and without SRA, under both curing conditions are shown in Figure 4.14.
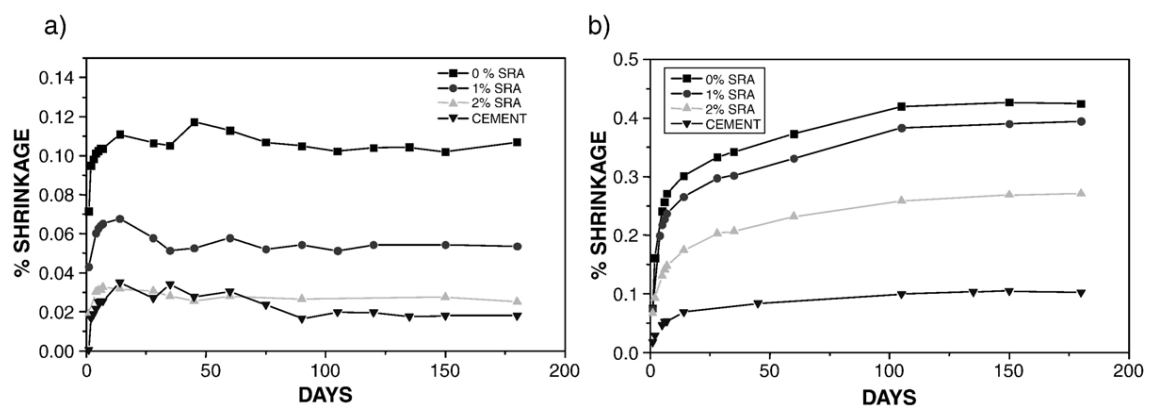
Figure 4.14 Shrinkage in waterglass-activated slag mortars, with and without SRA, under different curing conditions: a) RH =99% and b) RH =50% (Palacios & Puertas, 2007).

This shows that the addition of admixtures can be used to reduce the shrinkage of alkali-activated slag concretes, however the shrinkage values found aren't necessarily better compared to shrinkage values for OPC concrete. Another example is the addition of fibres other than steel fibres usually used in the industrial ground floor business, as Puertas et al. (2003) showed that polypropylene, glass or carbon fibres can give a reduction of up to 35% in drying shrinkage.

When less shrinkage is preferable, as is the case for industrial ground floors, alkali-activated binders that are realised with other precursors than solely slag are advised. Lee et al. (2014) measured that with the increase of slag, in an alkali-activated binder made of a blend with fly ash and slag, an increase of chemical and autogenous shrinkage was seen. The same principle held when the sodium silicate content increased.

Literature has shown that not all alkali-activated concretes or geopolymer concretes have higher shrinkage sizes when compared to traditional concrete. The Earth Friendly Concrete mentioned earlier is a geopolymer concrete that has been structurally implemented in Australia multiple times already. The geopolymer has a drying shrinkage that is much lower than for Portland cement based concretes, with typical 56 days shrinkage values of 300 μm or less as shown in Figure 4.15. The geopolymer concrete shows less drying shrinkage compared to a Portland cement based concrete even incorporating a shrinkage reducing admixture.

Figure 4.15 Drying shrinkage of geopolymer (EFC), 30% fly ash (Blended) and shrinkage reduced concretes (Eclipse). Graph taken from (Aldred & Day, 2012).
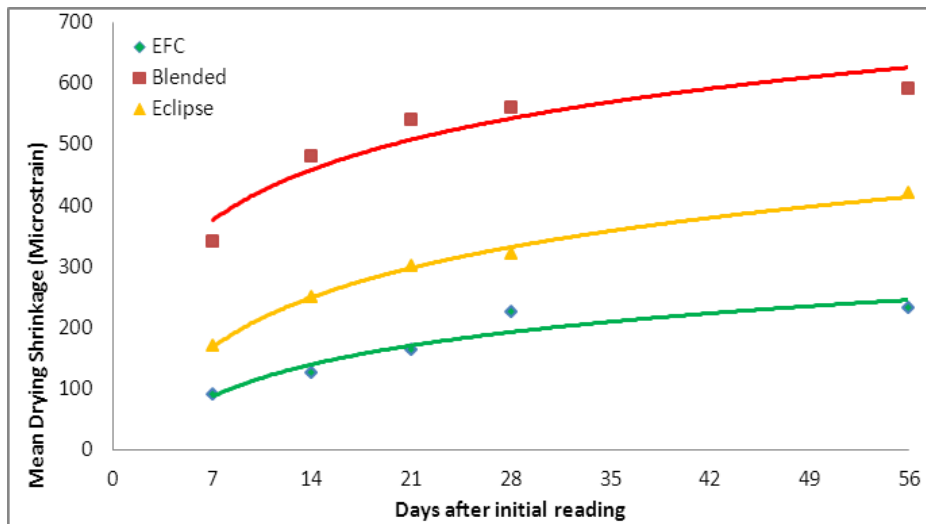
The geopolymer concrete EFC with the shrinkage size and development rate, shown in green in the above figure, will be the reduced shrinkage considered in this thesis. The geopolymer concrete has been structurally applied in several construction, both in precast and in-situ related works, and has therefore proven to be a suitable structural concrete realised without cement. Based on this reduced shrinkage size the study towards a reduced floor thickness and the optimisation of the jointless concrete ground floor is done in chapter 5.

4.3.5 Bond strength

Structural applications of reinforced concrete depend on the bond performance of the material to the reinforcement. With OPC concrete the relation between bond strength is usually computed through empirical equations. The widely accepted formulation of the fib model code states that the bond strength is proportional to the square root of the average compressive strength. For crack-width calculations the fib model code and the Eurocode 2 specify that the bond strength is directly related to the tensile strength of the concrete.

Fernandez-Jimenez et al. (2006) performed pull-out tests to determine the bond between an alkali-activated fly ash concrete and the reinforcing steel as well as with OPC concrete. They conclude that the characteristics of the fly ash AAC included excellent reinforcing steel bond strength. The matrix-steel bond in the AAC embedding 8-mm diameter was so strong that during the test the steel broke before slipping and before cracking the concrete. With 16-mm diameter steel bars failure occurred in the AAC due to matrix breakage, where in both cases of 8-mm and 16-mm diameter bars in the OPC concrete the bars slipped.

Songpiriyakij et al. (2011) tested several geopolymer pastes with varying amounts of binder materials and alkaline concentrations. The mixtures that were realised with silica fume and high NaOH concentrations showed the best bonding strengths of the pastes. Compared with the

control cement based concretes the geopolymer pastes showed slightly higher bonding strengths for round reinforcing bars where significantly higher values were found in the case of deformed bars, up to 1.6 times higher.

The higher bond strength of geopolymer concrete in comparison to OPC concrete has been found for fly ash based geopolymer concrete as well by Sarker (2010). He tested geopolymer concretes with compressive strengths within the ranges of 25 – 39 MPa and stated that the higher bond strength is found because of the higher splitting tensile strength geopolymer concrete shows, compared to OPC concrete of the same compressive strength. Stating that existing analytical expressions for bond strength of OPC concrete can be conservatively used for the calculation of bond strength of geopolymer concrete. Such results have been found by Castel (2017) as well who performed similar tests on ambient-cured alkali-activated blast furnace slag concrete and heat-cured alkali-activated fly ash concrete. For equivalent compressive strength, both fly ash and blast furnace slag AAC the bond strength was observed to be better than that of the OPC reference concrete. As a result he proposed a recalibrated correlation for the bond strength of AAC from the fib model code 2010 that is used for OPC concrete.
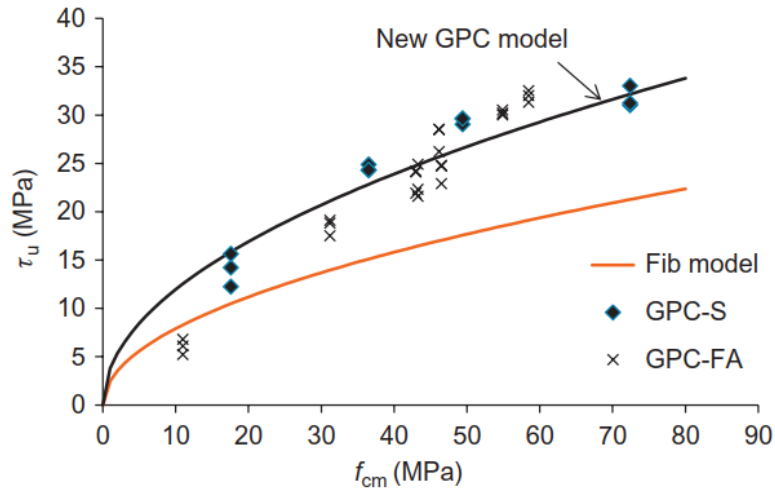
Figure 4.16 Comparison between the fib model predictions, the new model predictions, and experimental results for all GPCs (Castel, 2017).

The bond strength of OPC concrete with ribbed steel reinforcement can be calculated with the average compressive strength of the concrete. The fib model code provides the following equation:

$$\tau_{bmax} = 2.5 \cdot \sqrt{f_{cm}} \tag{4.1}$$

where τ_{bmax} is the ultimate bond strength and f_{cm} the average compressive strength. Castel found that following this equation the bond strength of GPC was underestimated, especially for compressive strengths greater than 30 MPa. As a result, the fib model was recalibrated providing a new equation that has the best correlation for GPC:

$$\tau_{u-GPC} = 3.83 \cdot \sqrt{f_{cm}} \tag{4.2}$$

where τ_{u-GPC} is the ultimate bond strength and f_{cm} the average compressive strength. The predictions by this new model are plotted in Figure 4.16.

In chapter 6 the bond strength and the concrete behaviour at cracked locations is further evaluated and the recalibrated bond strength model discussed here will be implemented for crack-width calculations.

In general the increased bond strength is related to the higher tensile strength alkali-activated concretes see in comparison to ordinary Portland cement concrete of similar compressive strength. Stated earlier this increased tensile strength of alkali-activated binders are associated with a highly dense interfacial transition zone between matrix and aggregates when compared with conventional cements, which also applies to the steel reinforcement bars. Regarding the reinforcement this highly dense matrix structure is also beneficial for the minimum cover that when considering durability aspects. The durability of alkali-activated materials is strongly dependent on the nano- and microstructure of the reaction products, which is depending on the types of precursors and type and concentration of activator (Bernal & Provis, 2014). The dense microstructure can provide certain impermeability such that the necessary concrete cover can be reduced when it is not limited by practical reasons.

4.3.6 Steel fibre interaction

That the addition of fibres in the concrete mixture is beneficial towards the mechanical and durability performance has been shown by several studies and the reason they are added in the industrial ground floor business has been addressed in section 2.5.3. Regarding the addition of steel fibres in alkali-activated concretes little research is done, especially when considering the steel fibres types that are used for hybrid reinforced concrete seen within the industrial concrete floors. Where steel fibres with end anchorages provide the best performance regarding the control of crack widths (ABT, 2015a). Steel fibres of longer length provide better anchorage and as such the longer the steel fibre the better the total performance. Practical reasons limit the steel fibres lengths to 50 mm with a reinforcement mesh size of 100 mm to prevent clustering of the steel fibres.

Aydin and Baradan (2013) performed tests on steel fibres with lengths of 6 mm and 13 mm without end anchorage with a tensile strength of the steel fibre of 2,250 MPa. Bernal et al. (2010) tested the performance of steel fibres with a length of 25 mm with a tensile strength of 800 MPa. Both studies showed that the addition of steel fibres improved the mechanical behaviour of the alkali-activated concrete.

The durability parameters, such as water absorption, abrasion resistance, resistance to chemical attack and resistance against chloride ions have been tested by Ganesan et al (2015) where the addition of fibres has been studied. Plain alkali-activated concrete and fibre reinforced both showed test results that provided superior durability characteristics than OPC concrete of similar strength grade.

At the time of writing this there are no actual tests performed regarding the interaction of AAC or GPC with steel fibres types seen in the ground floor industry, being steel fibres with a diameter of $d = 1$ mm and length $l = 40$ mm or longer with high tensile strengths up to 1,500 MPa and end anchorages. The assumption is made that the steel fibre interaction with the concrete will be the same as with OPC concrete, where one could expect that the residual flexural strengths in AAC/GPC may be better considering the dense micro-structure of AAC and GPC. Similar flexural residual strengths f_{Rj} are considered one can expect from OPC concrete with certain steel fibre contents.

The residual flexural strengths f_{Ri} are to be determined with three or four point bending test on notched beams, with a beam height of 125 mm at the notched cross-section. In accordance with NEN-EN 14651 these tests have to be performed and the steel fibre material properties can be determined. Values for the steel fibre residual flexural strengths, for concrete class C30/37, with a content of 35 kg/m³ range between $f_{R1} = 3.0 - 4.5$ MPa and $f_{R4} = 2.5 - 4.0$ MPa for common steel fibre types seen in industrial ground floors. A lower steel fibre content of 30 kg/m³ will see somewhat lower strength values, where higher contents of 45 kg/m³ are accommodated with

higher residual flexural strengths. When the residual flexural strengths between steel fibres contents of 25 and 45 kg/m³ are known, one can approximate quite accurately the residual flexural strengths with steel fibre contents in between 25 and 45 kg/m³ through linear interpolation.

The minimum preferable amount of steel fibres is said to be with a content of 30 kg/m³, one can expect slightly lower residual flexural strengths than seen with 35 kg/m³. Therefore, in chapter 5 where a reference floor is considered with a steel fibre content of 30 kg/m³, is said to have a residual flexural strength of f_{Rl} = 2.5 MPa. The residual flexural strengths f_{Rl} and f_{R4} can have around the same strength values and are for simplicity said to have the same value, so $f_{Rl} = f_{R4}$.

4.4 Concrete properties parameter range

Alkali-activated concrete and geopolymer concrete can be realised in a lot of different ways. As described, the type of precursors and the chemical activator specie and concentration can all vary, resulting in different mechanical properties. As the concrete can be realised in many different ways, the range of concrete properties achievable is quite large. The two tables below provide a good baseline for the range of mechanical properties that will be used in the next chapter. Where AAC and GPC tend to show a higher tensile strength, compared to similar compressive strength classes of OPC concrete, and with possible lower modulus of elasticity.

Table 4-3 shows the mechanical properties of the geopolymer concrete EFC. This concrete shows promising shrinkage results, with an average compressive strength of 55.6 MPa, coupled with a high tensile strengths of 6.0 MPa and a modulus of elasticity of 38.5 GPa. These values are set as the upper limit of the considered range for the parameter study in chapter 5.

Table 4-3 Mechanical properties of two geopolymer concretes EFC (Aldred & Day, 2012).

Mix	Compressive Strength (MPa)	Std Deviation	Tensile Strength (MPa)	Flexural Strength (MPa)	Shrinkage (microstrain)	Elastic Modulus (GPa)	Poisson's ratio
32 MPa	38.1	3.7	4.5	6.2	300	31.8	0.20
40 MPa	55.6	4.3	6.0	6.6	230	38.5	0.24

Table 4-4 shows the typical comparison that is found between OPC concrete and GPC. The third column, GPC-FA (cured 2 days), a fly ash based geopolymer concrete which has been heat cured for 2 days. It shows the increased tensile strength of 3.9 MPa and a quite low modulus of elasticity of 24.8 GPa compared to OPC40, an OPC concrete of similar compressive strength, with a tensile strength of 3.5 MPa and a modulus of elasticity of 32 GPa.

Table 4-4 Mechanical properties of OPC and GPC concretes (Castel, 2017).

	OPC40	GPC-FA (cured 2 days)	GPC-FA (cured 7 days)	GPC-S
Compressive strength, MPa	44	46.5	58.5	72.4
Elastic modulus, GPa	32.0	24.8	25.3	32.9
Tensile strength, MPa	3.5	3.9	4.4	N/A

For further study of the implementation of AAC and GPC, a range of mechanical concrete properties has been set. The range is based on the findings made in these first chapters and shown in Table 4-5. The upper limit is based on data found with certain alkali-activated concretes and geopolymer concretes. The lower limit is based on a low concrete class, C20/25, with a low tensile strength as this is preferable for the industrial jointless floor considering the control of cracking. The compressive strength range is set from 28 MPa to 55 MPa, the modulus of elasticity range from 25 GPa to 38.5 GPa, with tensile strengths ranging from 2.0 MPa to 6.0 MPa. The residual flexural strengths f_{R1} and f_{R4}, as a result of the steel fibres within the concrete mixture, are set to have the same range of 2.0 MPa to 6.0 MPa.

Table 4-5 Range of mechanical concrete properties

Parameter	Symbol	Range	Unit
Compressive strength	f_{cm}	28 - 55	N/mm²
Young's modulus	E_{cm}	25000 – 38500	N/mm²
Tensile strength	f_{ctm}	2 – 6	N/mm²
Residual tensile strength	$f_{R1} = f_{R4}$	2 – 6	N/mm²

In the next chapter it will be considered what a reduced drying shrinkage size can mean for a jointless concrete ground floor in terms of reduced thickness. After which a multiple amount of floor cross-sections are studied with the varying concrete properties ranging within the values set in Table 4-5.

5   OPTIMISATION OF A JOINTLESS CONCRETE GROUND FLOOR

Whether the implementation of alkali-activated concrete or geopolymer concrete can be beneficial will be examined in this chapter. Could a jointless concrete ground floor be utilised in such a way where the serviceability limit state isn't necessarily the governing design criteria and that perhaps for thinner floors the ultimate limit state unity checks may be governing instead of the control of cracking.

In 5.1 the design approach is described, what design assumptions are made and in what way the analysis is done. Section 5.2 discusses the consequences of a reduced floor thickness and to what extend the drying shrinkage has to be reduced to realise a less thick jointless concrete floor without disastrous consequences. Afterwards it is analysed what a theoretical minimal floor thickness is possible in section 5.3. In section 5.4 a more realistic reduced floor thickness is considered that could be realised in alkali-activated concrete or geopolymer concrete. One of the assumptions is that the floor cross-section cracks from pure bending only and the axial component from the shrinkage load is neglected. In section 5.5 this axial component will be considered and the crack-width of an AAC floor, reduced in thickness, is checked. The calculation is carried out to check whether the combination of the shrinkage load, its axial component and bending component, and the representative bending moment form external loads in SLS can be resisted in the cross-section.

5.1 Approach to a more fully utilised floor

The optimisation of a jointless concrete ground floor that is elastically supported, is done through the following way of thinking. To control the crack-widths is the governing aspect of the jointless floor, where these cracks arise due to the fact that the imposed load from drying shrinkage exceeds the bending cracking moment. The minimum concrete floor thickness realised with traditional OPC concrete is 160 mm, which has two reasons. One being that the thickness provides sufficient weight such that the warping effect won't lift the floor from the ground. And two, an important aspect considered for the design approach done in this thesis, is that the thickness ensures that cracks in the floor will only arise from pure bending and not from a uniform tension component within the floor. The thickness of 160 mm ensures that the development of the drying shrinkage strain at the bottom fibre of the floor occurs only at an old age, after 100 days, and at a very slow rate allowing for relaxation of the stress development. This ensures that a uniform tensile force component will not be developed that could force cracks in pure tension. When a floor cracks due to pure tension the crack-widths will be too large, with a factor 5 or even higher than cracks associated with bending. Such cracks require that the floor has to be repaired to ensure its future functionality and should therefore be prevented from happening.

A jointless thinner floor realised in a traditional concrete without a significant reduced drying shrinkage size would either have to be reinforced in with a high reinforcement ratio ($\omega_t \geq 1\%$) or see unacceptable crack-widths ($w_{max} \geq 0.3$ mm). As thinner ground floors also tend to have a higher final drying shrinkage size and a faster drying shrinkage development, a reduction in the drying shrinkage size is necessary if a jointless concrete ground floor is to be realised thinner. This will be further discussed in section 5.2.

The approach towards the optimisation of a concrete jointless ground floor has the following way of thinking:

> The control of cracking is governing, where the cracks arise due to pure bending from the restrained imposed deformation drying shrinkage.
>
> A concrete with a reduced final drying shrinkage strain size is associated with a slower development rate of its drying shrinkage strain in the first 100 days.
>
> A thinner jointless concrete floor has an average faster drying shrinkage development rate. Where the bottom fibre could undergo significant drying shrinkage risking crack formation due to uniform tension.
>
> If a jointless concrete ground floor is realised in a concrete with a reduced final drying shrinkage size and slower development rate it could be realised thinner. The two previous points will cancel each other out.
>
> A thinner floor can be realised which can still ensure that cracks only arise due to pure bending. As the floor is reduced in thickness the cracking moment will be less, resulting in lower steel stresses and as such less crack-widths.
>
> The thinner floor requires less concrete material and steel reinforcement could be saved as a result of the reduced steel stresses within the cracks.

This can conclude, that when the jointless concrete floor would be realised in a concrete that would show less drying shrinkage, savings could be made in concrete and steel material. To what thickness a jointless floor could be reduced, is considered in section 5.2. In section 5.3 and 5.4 a parameter study with the parameters and range of Table 4-5 in combination with different reinforcement bar diameters is done.

5.1.1 Design assumptions

For the theoretical approach towards the optimisation of the jointless concrete floor some assumptions have been made which are described here.

The floor is said to only crack due to pure bending, where the bending cracking moment M_{crack} will be reached, due to the restrained curvature caused by the non-uniform development of the drying shrinkage over the height of the cross-section.

The calculations are done with the average 28 days strengths of the concrete. Preferably the jointless concrete floor has a curing age of at least 14 days, after which drying shrinkage starts to develop. The concrete floor could crack before the 28 days strengths have been developed, but as early age cracking would develop under lower concrete tensile strengths the crack-widths would be less when compared to the calculated crack-widths from the 28 days strengths.

Average material properties are considered for the concrete and steel. The material factors γ are set to 1.0.

Long term aspects like creep, relaxation and the further development of the concrete strength past 28 days aren't considered.

The jointless concrete floor and its crack formation is considered to remain in the crack formation stage for the entire floor.

5.1.2 Setup of the parametric study

It is established that the concrete floor will crack in pure bending caused by the drying shrinkage gradient. The way the crack-width calculation is done, has been described in chapter 3.4 and is further elaborated in Appendix B. For the structural design process this calculation for the crack-widths has been combined with the calculation scheme for the ULS unity checks that were discussed in section 2.5.1 and Appendix A. In the combined spreadsheet all requirements will be checked once the remaining parameters are provided. The structural design is checked, where for the SLS the crack-width at the top surface is calculated. For the ULS the unity checks for flexure, from point loads and uniformly distributed loads, and punching shear are computed.

The design parameters to be specified determine the structural design of the hybrid reinforced floor cross-section. The concrete is defined by amount, as the thickness h which is depending on the drying shrinkage, and its strength and stiffness properties. The quantity of steel is defined by the diameter of the reinforcement bars of the top mesh and by the steel fibres content written in terms of its residual flexural strength. The input parameters to be defined are:

- Floor thickness h [mm]
- Concrete compressive strength f_{cm} [N/mm²]
- Concrete tensile strength f_{ctm} [N/mm²]
- Concrete modulus of elasticity E_{cm} [N/mm²]
- Reinforcement bar diameter ϕ [mm]
- Concrete cover c [mm]
- Residual flexural strength $f_{R1} = f_{R4}$ [N/mm²]

Once the above parameters are specified, the spreadsheet computes the crack-width associated with the bending cracking moment and finds what the unity checks are. For the SLS crack-width the bending cracking moment M_{crack} is calculated with the flexural tensile strength. ULS checks are done with the theoretical average strength values and not the characteristic or design strengths of the concrete and steel, so only the loads are multiplied with a load factor to compute the design loads. The output of the spreadsheet is the crack-width at the top surface of the floor and six unity checks:

- Crack-width w_{opp} [mm]
- UC 1: Flexure single point load   [-]
- UC 2: Flexure double point load   [-]
- UC 3: Punching shear single point load   [-]
- UC 4: Punching shear double point load   [-]
- UC 5: Flexure UDL A   [-]
- UC 6: Flexure UDL B   [-]

Whether for unity checks 1 to 4 the single or double point load has to be considered, depends on the spacing between the two adjacent point loads that are considered with back-to-back racking. When their base plates are close enough ($\leq 2h$) to each other the loads are considered as a single point load with an equivalent contact area. Otherwise they are considered separately as a double point load. Unity checks 5 and 6 check the uniformly distributed loads (UDL) in the patterns

where the maximum positive bending moment (A) and the maximum negative bending moment (B) occur.

As specified earlier, a certain range of parameters is studied, for which all possible variants have been calculated. For this the tool ABT Flow Simulator has been used. The tool is provided with the input parameters and their range which then computes all the possible variants and provides the output data specified above. In sections 5.3 and 5.4 the range of parameters studied are specified and the output data is analysed. The tool calculates all possible variants where each parameter with a certain value is considered. When increasing the number of parameters or their bandwidth, the total number of possible variants can grow exponentially and with that the calculation time as well.

The total amount of parameters considered, their range and step size defines the total amount of variants calculated. To reduce the total amount of variants, and with that reduce calculation time, the assumptions mentioned in 5.1.1 are followed. A further reduction for the calculation time has been realised by fixing the centre-to-centre distance of the top reinforcement mesh to 100 mm, thus reducing the total amount of parameters and possible variants that have to be calculated.

Once the complete calculation of all variants was finished, the complete data has been analysed with the program Power BI. With Power BI the complete data input and output has been analysed where the influence of the input parameters can be compared with the output. Here the bandwidth of the output is specified such that the floors with certain inputs that do not meet certain requirements aren't represented in the analysed data. An example of this is a variant calculated where a small reinforcement bar diameter ($\phi \leq 6$ mm) is applied in concrete floor cross-section with a high tensile strength ($f_{ctm} \geq 5.0$ MPa). If this floor were to crack in bending the steel would immediately yield. Such non-realisable floor cross-sections have been filtered out of the analysed data.

Filters are applied on the output such that only suitable cross-sections are analysed. The reason some solutions aren't analysed as they're not considered as suitable are:

- The crack-width w_{opp} exceeds the set limit $w_{opp} > 0.12$ mm
- The ULS unity checks are above 1.0
- The minimum or maximum required reinforcement isn't met
- The SLS bending moments from the external loads can provide localised cracks within the stabilised cracking stage
- Bending hardening behaviour were to occur when high residual flexural strengths are considered with low concrete tensile strengths

The reasoning to the set crack-width limit of $w_{opp} \leq 0.12$ mm is defined in the next section.

5.1.3 Reference floor and crack-width

The reference concrete ground floor is based on the standard minimum applied floor dimensions mentioned in section 2.5.2 and the floor cross-section is shown in Figure 5.1 below. The floor is 160 mm thick and hybrid reinforced, with a top reinforcement mesh of ϕ7-100 mm with a concrete cover of 30 mm and a steel fibre content of 30 kg/m³
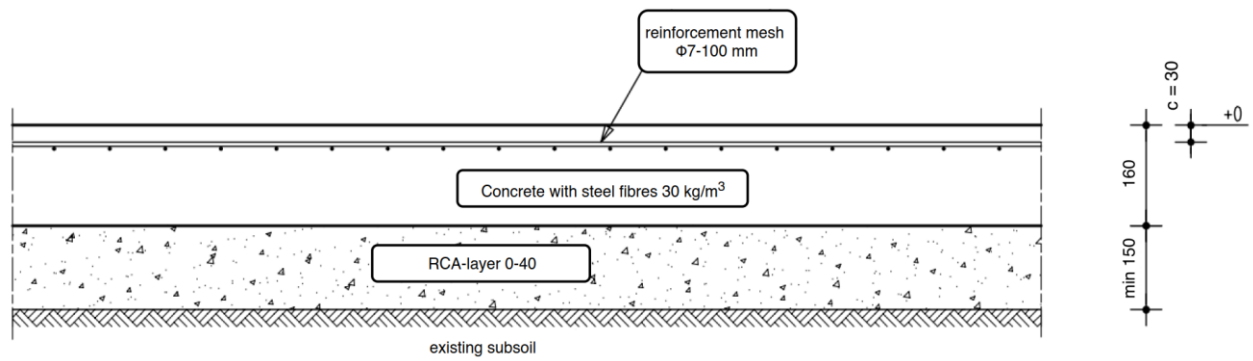
Figure 5.1 Reference jointless concrete floor with a thickness of 160 mm, a top reinforcement mesh of ϕ7-100 mm with a concrete cover of 30 mm and a steel fibre content of 30 kg/m³ added to the concrete mixture. The floor is realised on an RCA-layer that meets the requirements.

For the optimisation of the structure the average structural properties of the concrete and steel are considered. Often industrial ground floors are realised in a concrete class of around C30/37. The reference average concrete parameters that are used are based on this concrete class. The minimum amount of steel fibres used is 30 kg/m³, in most cases the content used in the concrete mixture is 35 kg/m³ and sometimes higher, up to 45 kg/m³. As 30 kg/m³ can be relatively low, the reference residual flexural strength f_{R4} is set to 2.5 MPa.

The crack-width findings are based on the findings related to the reference floor of which its input parameters are listed in Table 5-1 below.

Table 5-1 Reference concrete ground floor properties.

Floor property	Symbol	Value	Unit
Thickness	h	160	mm
Compressive strength	f_{cm}	38	N/mm²
Young's modulus	E_{cm}	33000	N/mm²
Tensile strength	f_{ctm}	3	N/mm²
Reinforcement bar diameter	ϕ	7	mm
Concrete cover	c	30	mm
Residual tensile strength	f_{R4}	2.5	N/mm²

The floor with above parameters has a crack-width w_m = 0.078 mm at the location of the crack around the steel reinforcement bar, at the extreme tensile fibre the crack-width is larger. At the top surface of the floor the crack-width w_{opp} = 0.114 mm. This is much less than the typical required maximum crack-width of $w_d \leq 0.3$ mm, however in reality within the hybrid reinforced floor there will be fluctuation in the steel fibre-concentrations and tensile strengths. As a result, there can be a spread in the crack-width, so the crack-widths seen in reality could be larger, up to 0.3 mm. In practice such steel fibre contents with a top reinforcement mesh are applied and similar lower crack-widths of around w_{opp} = 0.1 mm will be calculated. However, as explained the real behaviour of the floor can fluctuate somewhat and with these minimum amounts of steel it can be ensured that the spread of the crack-width is limited. Such that the maximum possible crack-width remains below the required $w_d \leq 0.3$ mm.

As mentioned the parameters above will be used as the reference floor for the approach towards a more optimised jointless concrete ground floor. The calculated crack-width of w_{opp} = 0.114 mm will be taken as the reference crack width. Therefore, for this chapter the maximum calculated crack-width to be allowed, will be set to $w_{opp} \leq 0.12$ mm. This will ensure that all the different calculated floor cross-sections will have a small crack-width that will allow for a spread in crack-

59

width to occur, where the maximum crack-widths will still remain below the actual maximum allowable crack-width of $w_d \leq 0.3$ mm.

5.2 Floor thickness reduction

The first key aspect for a jointless concrete ground floor to consider when optimising it, is to look at its drying shrinkage size and development rate. The thickness of the concrete floor and the steel within it are dimensioned towards this material property and its effect on the floor. As explained before the drying process of the concrete floor occurs only, if properly made on a suitable subsoil, through the top surface of the floor. Non-uniform shrinkage occurs over the height of the floor cross-section, resulting in a curvature.

This curvature results in bending moments and the upwards curling effect of the floor, for which the thickness of 160 mm is applied to ensure two things. First, to ensure that cracks only form from bending moments because the drying shrinkage reduction of the bottom section of the floor does not occur in the early age, i.e. the first 100 days, of the floor. After 100 days a shrinkage reduction can develop at the bottom, this process can take years and it assumed that the crack formation is stabilised by then. This means that no cracks shall arise due to pure tension in the floor. Second, the minimum thickness ensures that the upwards curling is restrained, by the self-weight of the floor, such that the floor won't lift itself from the ground. Initially this second phenomenon only happens at the free edges, but once the jointless floor is cracked at the top surface, the mid-section of the floor can undergo this curling effect as well.

5.2.1 Drying shrinkage size and its development rate

The rate at which a ground floor would see pure tension and upwards curling due to drying shrinkage, depends on the rate at which the drying shrinkage occurs. If the top part of the floor dries faster, it will curl more and the bottom part of floor will start to shrink faster as well. The opposite happens when the floor dries at a slower rate, ensuring no initial cracks occur in pure tension and that the floor won't lift itself up from the ground. With normal concrete the drying shrinkage rate is depending on multiple factors, like the cement type, the concrete class, the relative humidity of the environment and the thickness of the floor. The latter is one of importance as this determines the notional size h_o of the cross-section. The drying shrinkage and its development are increased with a lower notional size, which is determined by the area of the concrete cross-section A_c and the perimeter u of this cross-section that is in contact with the atmosphere:

$$h_0 = \frac{2A_c}{u} \tag{5.1}$$

Where the perimeter u for a ground floor is just the top surface, so the notional size becomes $h_o = 2h$. That a thinner floor shows a faster shrinkage development rate is visualised in Figure 5.2 where the developing drying shrinkage strain over time is shown for 6 different floor thicknesses. The graphs are computed in accordance with the Eurocode 2 for a CEM III blast furnace slag type cement for an indoor climate with a relative humidity of 50%. The reduction of a floor thickness is coupled with an increase of the final drying shrinkage strain size and with a faster development of the initial drying shrinkage strain. In other words, the drying shrinkage development rate is higher with thinner floors. It should be noted that these graphs are based on the average drying shrinkage strain of the entire cross-section. In reality, initially only the top part of the cross-section undergoes drying shrinkage. However, a faster average shrinkage development is also associated with a faster shrinkage development of the bottom section of the floor.
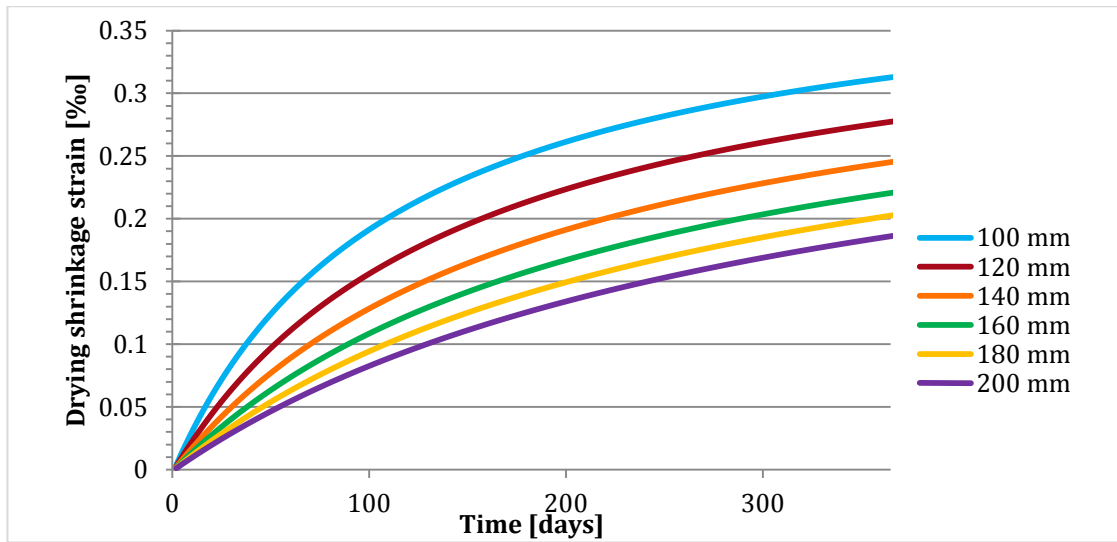
Figure 5.2 Average drying shrinkage strain over a year time for different floor thicknesses. Drying shrinkage curves are based on a CEM-III blast furnace cement concrete at a relative humidity RH of 50%.

The floor of 160 mm thickness shows an initial shrinkage development rate of $1.1 \cdot 10^{-6}$ ε/day, computed from Figure 5.2 over the first 100 days. The floors of 140 mm and 100 mm thickness show a drying shrinkage development rate of $1.3 \cdot 10^{-6}$ ε/day and $2.0 \cdot 10^{-6}$ ε/day, respectively. Compared to thickness of 160 mm, the floor of 140 mm has a reduction in thickness of 12.5% and has a strain development rate which has an increase of approximately 19%. Where the floor of 100 mm, compared to the 160 mm floor, sees an increase of 80% of the early drying shrinkage development rate, while its reduction in thickness is 37.5%. These numbers show that a reduction in thickness is associated with a faster shrinkage strain development.

In Figure 5.3 the reduction in thickness is shown next to the increase of the drying shrinkage development rate for several thicknesses, in reference to floor of 160 mm thickness. This figure shows that reducing the thickness by half of the reference height, to 80 mm, an increase is seen of the early drying shrinkage development of 130%, compared to the reference floor. The increase of the floor thickness is linked with a decrease of the shrinkage development, the differences in shrinkage development rates are not as big.
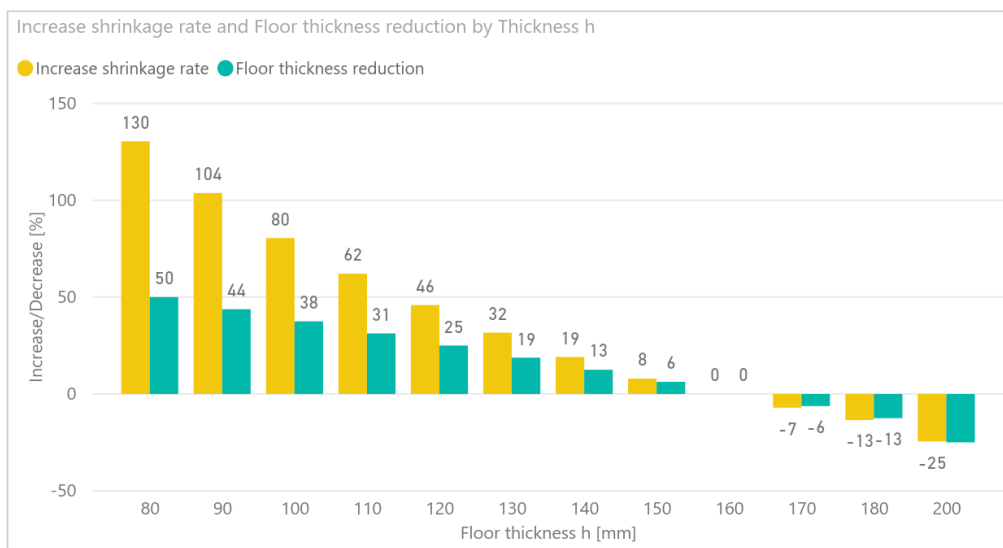

Figure 5.3 Increase of the average drying shrinkage development rate (of the first 100 days) compared to the decrease in floor thickness relative to the thickness of 160 mm and its corresponding drying shrinkage rate.

61

5.2.2 Reduced floor thickness

For a floor to be reduced with a certain thickness, a decrease of its concrete shrinkage development rate has to be realised. If the final shrinkage strain size of a concrete is higher, its initial development is faster and when the final shrinkage strain size is lower, the initial development of the shrinkage strain is slower. Drying shrinkage curves, from shrinkage prisms, of a traditional OPC based concrete and the geopolymer concrete EFC are shown in Figure 5.4. The final drying shrinkage strain sizes for the OPC based concrete and the geopolymer concrete EFC are 0.5‰ and 0.3‰, respectively. With the reduced final shrinkage size and its accompanied reduced shrinkage development rate, thinner floors can be realised.
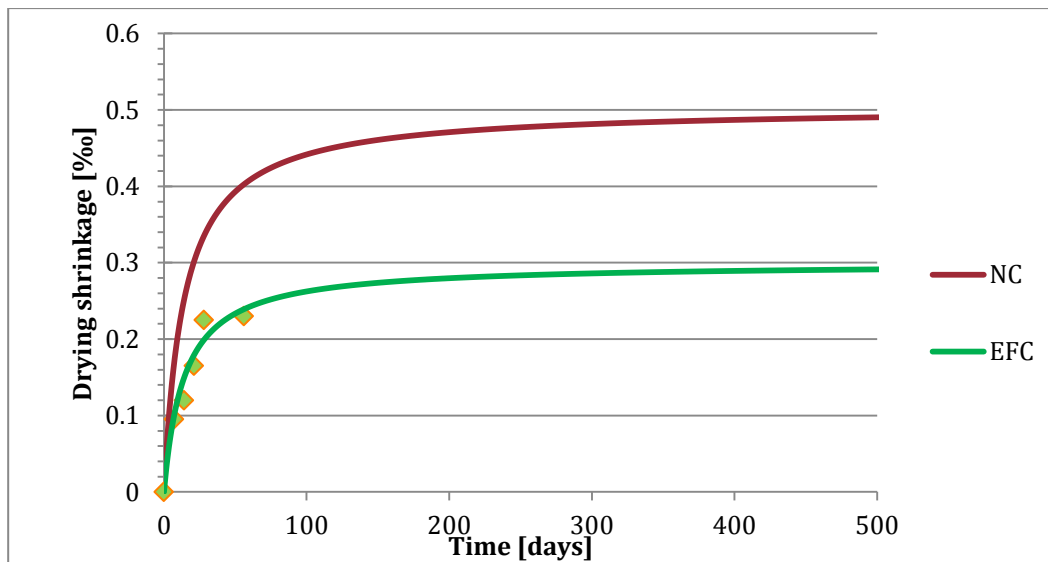
Figure 5.4 Drying shrinkage strain curves over time from shrinkage tests for a normal concrete (NC) realised with Ordinary Portland Cement and the geopolymer concrete EFC. The final drying shrinkage strain size of NC is close to 0.5‰ and that of EFC to 0.3‰.

The slower development rate of the drying shrinkage is clear when the difference in the early strain rates is seen, which are shown in Table 5-2. The development of the drying shrinkage is in the first 7 days 43% slower for the geopolymer concrete EFC. Looking at the drying shrinkage rate spread out over the first 28 days the development rate for EFC is 33% slower. That the initial slope of the curve, i.e. the early drying shrinkage development rate, is lower for EFC is better visible in Figure 5.5.

Table 5-2 Drying shrinkage strain rates at different time intervals measured for normal concrete (NC) and the geopolymer concrete EFC.

	NC	EFC	
t [days]	$\varepsilon_{cd}(t)$ [‰]		Difference [%]
0	0	0	–
7	0.167	0.095	43
14	0.251	0.120	52
21	0.301	0.165	45
28	0.335	0.225	33
56	0.403	0.230	43

Figure 5.5 Early drying shrinkage strain development of OPC concrete (NC) and geopolymer concrete (EFC).

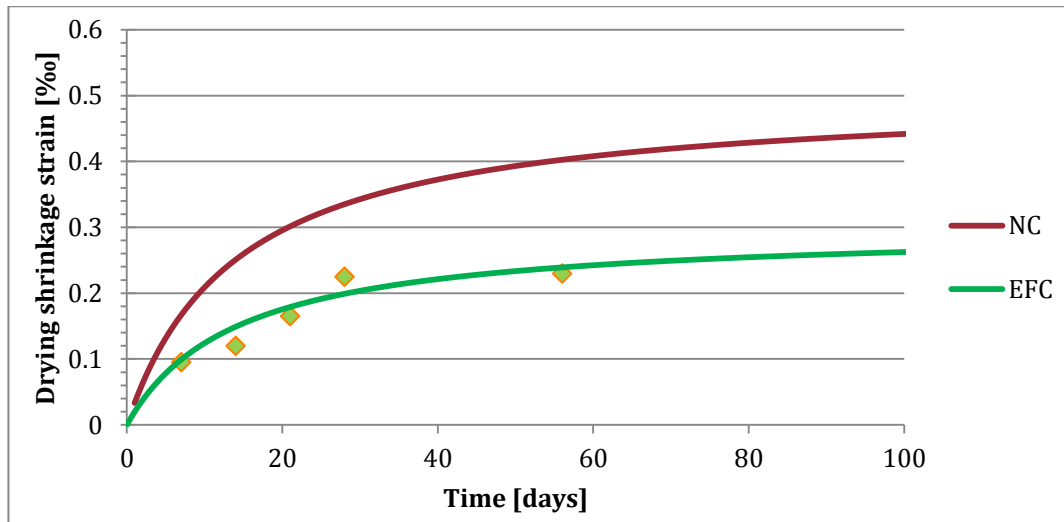The difference in the development of the shrinkage reduction from Table 5-2 are considered and compared with the increase of the shrinkage development thinner floors would see. Figure 5.6 shows the same principal as was visualised in Figure 5.3, where the increase of the drying shrinkage development rate for floor thicknesses from 120 to 135 mm are shown. The increase of the shrinkage development is again relative to the drying shrinkage development of a floor with a thickness of 160 mm.
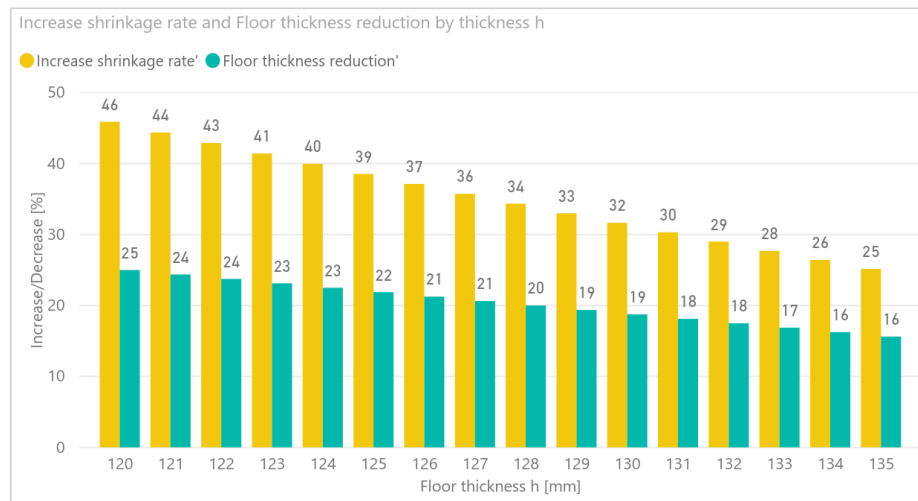
Figure 5.6 Floor thicknesses ranging between 120 – 135 mm and their corresponding increase of the drying shrinkage development rate, relative to a floor of 160 mm thickness.

For a suitable thickness reduction the lowest difference in shrinkage development from Table 5-2 is considered, which is 33%. According to Figure 5.6 a floor with a thickness of 129 mm would see a faster development of its drying shrinkage with 33%. Were one to realise the concrete floor with a thickness of 129 mm, in an alkali-activated – or geopolymer concrete, that follows the reduced shrinkage curve of EFC in Figure 5.5. The reduction in floor thickness is associated with a 33% faster shrinkage development, where the applied concrete is associated with a 33% slower shrinkage development. Thus it can be said that these two differences will cancel each other out. It is therefore considered that the reduced floor with a thickness of 129 mm, realised in a shrinkage reduced AAC, has a similar shrinkage development of the reference floor realised in OPC concrete. Accordingly, the design method from the reference floor is considered applicable for this thinner floor as well, such that the crack formation occurs due to pure bending only.

Table 5-2 shows higher difference in shrinkage strains which will be more beneficial and allow for a thinner floor. However, for a conservative approach the lowest value of 33% is considered. In section 5.4 this thinner cross-section is considered for the realistic optimisation of the jointless floor realised in AAC. Instead of 129 mm, the practical size of 130 mm is considered as the suitable reduced floor thickness.

5.3 Minimum floor thickness

Before this thickness of 130 mm is considered, it is examined what possible minimum floor thickness could be achieved, where the heavy points loads or the heavy uniformly distributed loads can still be carried and the crack-widths don't exceed the limit of w_{opp} = 0.12 mm. As described in section 5.1.2 a set of parameters has been studied, which ones and what their range is, is shown in Table 5-3 below.

Table 5-3 Range of properties for a concrete floor with thicknesses ranging from 70 to 100 mm thickness.

Parameter	Symbol	Range	Unit
Thickness	h	70 - 100	mm
Compressive strength	f_{cm}	35 - 55	N/mm²
Young's modulus	E_{cm}	25000 – 38500	N/mm²
Tensile strength	f_{ctm}	2 – 6	N/mm²
Residual tensile strength	f_{R1}	2 – 6	N/mm²
Concrete cover	c	20 – 30	mm
Bar diameter	ϕ	6 – 9	mm

In this first study the floor thickness h isn't fixed. The range considered for the minimum possible floor thicknesses is between 70 to 100 mm thickness, see Table 5-3. As explained all possible cross-section variants have been computed and after filtering non-compliant and non-suitable cross-sections they have been analysed.

In Figure 5.7 the first visualisation of the processed data is depicted. In the figure the coloured bars that are shown are based on variants that are in compliance with the set boundaries. The reasons some variants won't be analysed have been mentioned in section 5.1.2. The final boundary conditions for each variant are that the calculated crack-width is w_{opp} ≤ 0.12 mm and that all the unity checks are ≤ 1.0. The crack-widths, unity checks and computed averages shown in the coming figures are based only on suitable variants that meet the set boundaries. In some of the coming figures some boxes for certain parameters are checked, if such a box is checked, the shown suitable variants are in compliance with that checked parameter.

For example, in Figure 5.9 the boxes for the reinforcement bar diameter is checked at ϕ = 7 mm and for the concrete cover at c = 30 mm. The graph therefore only displays values based on the possible variants, where initially all boundaries conditions are met, but now the variants shown are also in compliance with the checked parameters. Such that, in this case, only suitable variants with a reinforcement bar of 7 mm with a concrete cover of 30 mm are shown, since these are specified by the checked box. In Figure 5.7 no parameter boxes have been checked so the bar diagrams are based on all the suitable variants within the entire parameter range.

The coming figures, in this and the next section, follow the visualisation principle as described here. The figures display the (average) crack-width w_{opp} or the unity check values on the vertical y-axis. The unit and range displayed on the horizontal x-axis can differ.

In Figure 5.7 the parameters and their range considered are shown on the right. As no boxes are checked, the bar diagrams on the left are based on all the suitable cross-section variants with the shown parameters. The bar diagram in the top left shows the average crack-width w_{opp} for different thicknesses coupled with a certain concrete tensile strength f_{ctm}. The bar diagram in the bottom left shows the six average unity checks for different floor thicknesses. Unity check 1 and 2 are the flexure checks for the back-to-back point loads, unity check 3 and 4 are the punching shear checks and unity check 5 and 6 are the flexure unity checks if the floor were loaded by a uniformly distributed load. For example, in the top left bar diagram, the floor with a thickness of 85 mm and a tensile strength of 6.0 MPa (the grey bar) shows to have an average crack-width of w_{opp} = 0.10 mm. The bottom bar diagram depicts that the highest average unity check for this floor thickness of 85 mm is UC1 = 0.88. The average values in this case are computed from all suitable variants.

In the top left diagram the floor thickness of 85 mm only shows solutions, i.e. visible bars, for tensile strengths $f_{ctm} \geq 3.0$ MPa. This means that there is no suitable variant for a floor with a thickness of 85 mm with a tensile strength of 2.0 MPa that fulfils all the requirements, it is therefore not visualised. The thicknesses 95 mm and 100 mm do show a solution with a tensile strength of 2.0 MPa, from this it is concluded that floors thinner than 95 mm with a low tensile strength of 2.0 MPa aren't possible. For such variants the ULS unity checks for flexure would most likely be the requirement that won't be met.
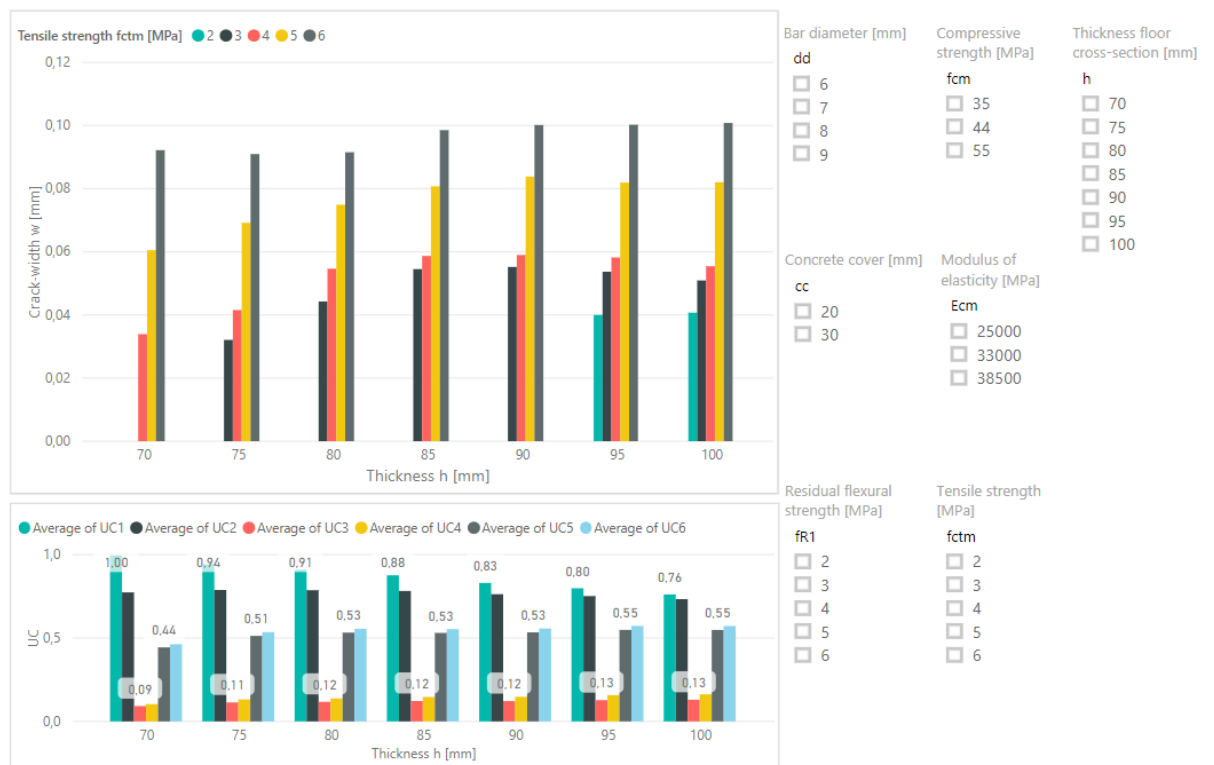
Figure 5.7 Suitable floor thicknesses in certain tensile strengths. Shown possible variants suitable for all UC's ≤ 1.0 and w_{max} ≤ 0.12 mm. Top left: average found crack-widths of the suitable options for different floor thicknesses with certain tensile strengths. Bottom left: average of the ULS unity checks 1-6 for different floor thicknesses. Right: parameters with their range; none are selected so all possible variants are shown in the two left figures.

In Figure 5.7 the influence of the thickness and the tensile strength can be seen. In the top left diagram the benefit of lower tensile strengths concerning the crack-widths can be seen. The average found crack-widths for the higher tensile strengths are higher for each thickness, a reduced crack-width can be seen at each thickness when the tensile strength is lowered. The

governing unity check UC1 can be seen to increase with reduced floor thicknesses, reaching the maximum of 1.0 at the floor thickness of 70 mm.

Within the considered range for the floor thickness of 70-100 mm there are a multiple of suitable solutions. As shown in the figure above there are some variants that meet all the requirements for the floor thickness of 70 mm. Figure 5.8 below shows the same principal as Figure 5.7, but now on the right the parameter for the thickness of 70 mm is checked. This results in the bar diagrams changing, where only variants are shown with the thickness of 70 mm that meet all the other requirements. On the right the remaining parameters are ones that could realise a suitable variant, as the thickness is fixed to 70 mm the bar diagram in the left only shows these solutions with different tensile strengths. What needs to be noted, is that the other parameters shown on the right, besides the tensile strength f_{ctm}, only have one remaining value left. For example, the only reinforcement bar diameter shown is $\phi = 9$ mm. The other bar diameters 6 – 8 mm aren't shown as there are no suitable variants where a floor with a thickness of 70 mm is realised with a bar diameter lower than 9 mm that meets the requirements. Suitable variants with a thickness of 70 mm are only realisable with the remaining shown parameter values.

For this case this means that the floor of 70 mm thickness is only realisable with a compressive strength of $f_{cm} = 55.0$ MPa, a modulus of elasticity $E_{cm} = 25.0$ GPa, a reinforcement mesh of $\phi9$-100 mm with the reduced concrete cover of $c = 20$ mm and a residual flexural strength of $f_{R1} = 6.0$ MPa. The remaining parameter with multiple solutions is the tensile strength f_{ctm}. The crack-width w_{opp} is found to be 0.03 mm, 0.06 mm and 0.09 mm for tensile strengths f_{ctm} of 4.0, 5.0 and 6.0 MPa, respectively. The governing unity check is UC1 = 1.0 for all three variants.

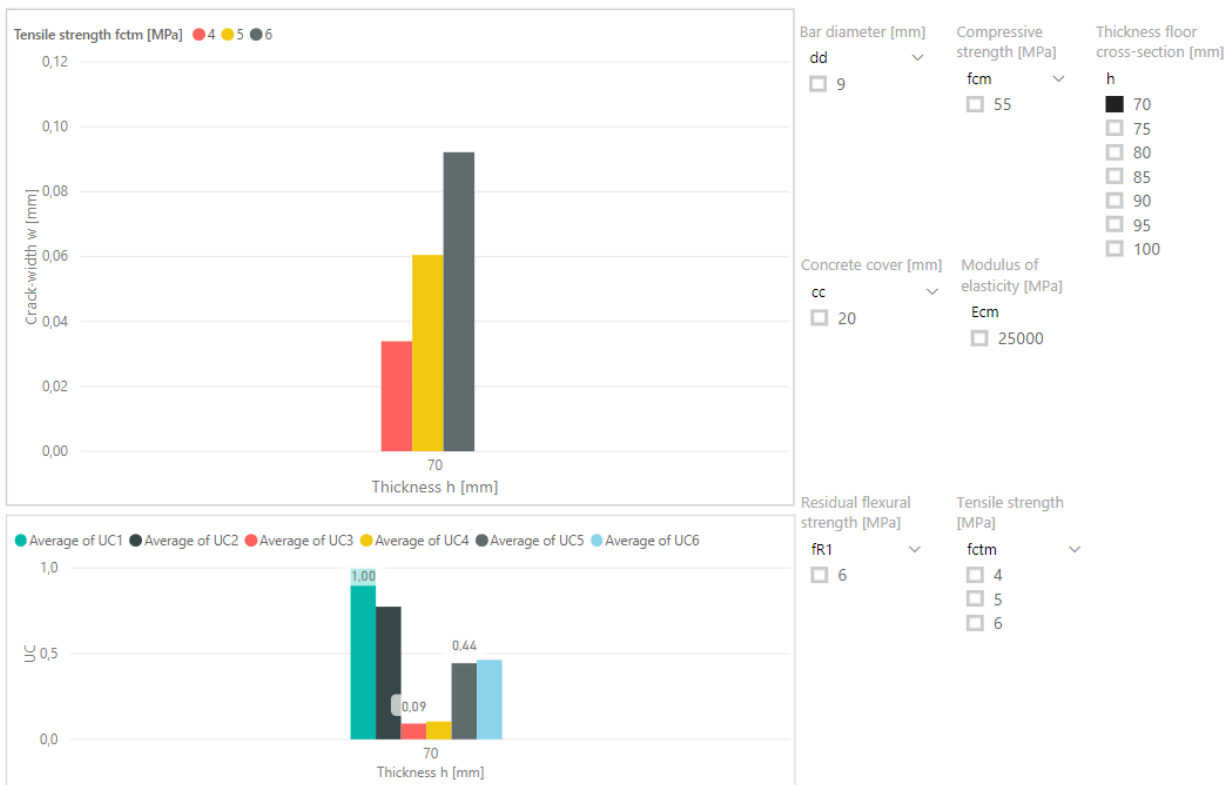**Figure 5.8 Average crack-widths and unity checks for the floor with a thickness of 70 mm.**

Theoretically a floor can thus be realised with a thin cross-section of 70 mm. However, the necessary concrete parameters are somewhat contradicting, the required reinforcement ($\phi9$-100 mm) and the residual flexural strength ($f_{R1} = 6.0$ MPa) are high that this cross-section isn't considered as optimal or practically realistic.

Selecting the standard applied top reinforcement mesh of ϕ7-100 mm with the practical minimum concrete cover of c = 30 mm, the minimum possible thickness becomes 90 mm, see Figure 5.9. For this to be realised, a concrete tensile strength of f_{ctm} = 4.0 - 5.0 MPa is required with a the highest flexural residual strength of f_{R1} = 6.0 MPa. The latter follows when the box of 90 mm is checked as well which is not visualised here.

Figure 5.9 Suitable floor thicknesses with a top reinforcement mesh of ϕ7-100 mm with a concrete cover c = 30 mm, shown in accordance with suitable tensile strengths. Shown possible variants suitable for all UC's ≤ 1.0 and w_max < 0.12 mm. Top left: max crack-width of the suitable options for different floor thicknesses with a certain tensile strength. Bottom left: average of the ULS unity checks 1-6 for different floor thicknesses. Right: selected parameters bar diameter dd 7 mm and concrete cover c 30 mm; only the possible solutions in accordance with these settings are visible in the diagrams.

In all the solutions found, with these minimum thicknesses, one finds that the governing design aspect is no longer necessary the SLS crack-width control. The flexure unity checks in ULS become the governing aspect one has to consider with these very thin floor cross-sections.

These floors are still be able to carry the heavy point loads or heavy bulk loads. However, for such thin floors to be realised, the drying shrinkage has to be close to zero, as is shown in the previous section. Reducing the floor thickness to 90 mm is coupled with a drying shrinkage development that is 104% faster compared to the shrinkage development of a floor of 160 mm thickness. One has to reduce the shrinkage size of the concrete to almost zero or such a thin floor would crack from pure tension.

This shows that, theoretically, with a non-shrinking concrete one could make a jointless concrete floor really thin with high amounts of steel and be able to put fully loaded warehouse racking's on top of it. Maybe in the future this might be possible but for now this is purely theoretical.

5.4 Reduced floor thickness in alkali-activated concrete

In this section the same design approach is followed as done for the minimum possible floor thickness. Now the reduced floor thickness of h = 130 mm, discussed in section 5.2.2, is considered. In section 5.2.2 it is shown that this reduced thickness is considered suitable with a reduced final shrinkage size of 0.3 ‰, such that the assumptions holds that the floor will only crack from bending. This floor thickness will be studied in the same manner as is done for the minimum floor thickness, now the thickness is fixed to 130 mm. This eliminates one variable parameter, which made it possible to reduce the step size for some parameters without increasing the amount of total variants that have to be computed. The step size of the tensile strength f_{ctm} and residual flexural strength f_{R1} was 1.0 in the previous analysis, here their step size is reduced to 0.5. The parameters and their range are shown in Table 5-4.

Table 5-4 Range of properties for the concrete floor with a reduced thickness of 130 mm.

Parameter	Symbol	Range	Unit
Thickness	h	130	mm
Compressive strength	f_{cm}	28 - 55	N/mm²
Young's modulus	E_{cm}	25000 – 38500	N/mm²
Tensile strength	f_{ctm}	2 – 6	N/mm²
Residual tensile strength	f_{R1}	2 – 6	N/mm²
Concrete cover	c	20 – 30	mm
Bar diameter	ϕ	5 – 8	mm

The same method is followed, so all variants are computed, analysed and the data is depicted with the help of similar figures. All possible variants, around 13,000, have been calculated and after filtering around 3,000 variants remain suitable within the set criteria. The remaining ~3000 suitable variants that are studied in this approach consist only of cross-sections that have a crack-width of $w_{opp} \leq 0.12$ mm and all ULS unity checks are UC ≤ 1.0. The other criteria, from section 5.1.2, like minimum required reinforcement and no bending hardening steel fibre behaviour allowed, are also met. All shown results are for floor cross-sections with a thickness of h = 130 mm.

5.4.1 Parameter influence

The concrete material parameters and their influence on the crack-width and the ULS unity checks is studied within the following figures. Figure 5.10 to Figure 5.14 show the influence on the average crack-widths and the average of the ULS unity checks considered for the compressive strength f_{cm}, the modulus of elasticity E_{cm}, the tensile strength f_{ctm} and the residual flexural strength f_{R1}, respectively. In these four following figures the top bar diagram shows the average crack-width computed from all the suitable variants with the corresponding parameter and value displayed on the horizontal axis. The bottom diagram displays the average values of the six ULS unity checks computed for all suitable variants with the corresponding parameter and value displayed on the horizontal axis. In section 5.1.2 on page 57 it is listed what each unity check is.

Figure 5.10 Top: average crack-widths for different compressive strengths f_{cm}. Bottom: Average values for the ULS unity checks for different compressive strengths f_{cm}. Compressive strength f_{cm} values of 28, 38, 44 and 55 MPa.

The influence of concrete compressive strength f_{cm}, Figure 5.10, is found to be little concerning the average crack-widths found. The increase of the compressive strength is coupled with a very small increase of the crack-width. The crack-widths and unity checks 1, 2, 5 and 6 are accommodated with bending on which the concrete compressive strength doesn't have such a big influence. Looking at the unity checks 3 and 4, which consider punching shear, one sees that the increase of the compressive strength lowers the unity check. This is expected as the shear strength is related to the compressive strength.
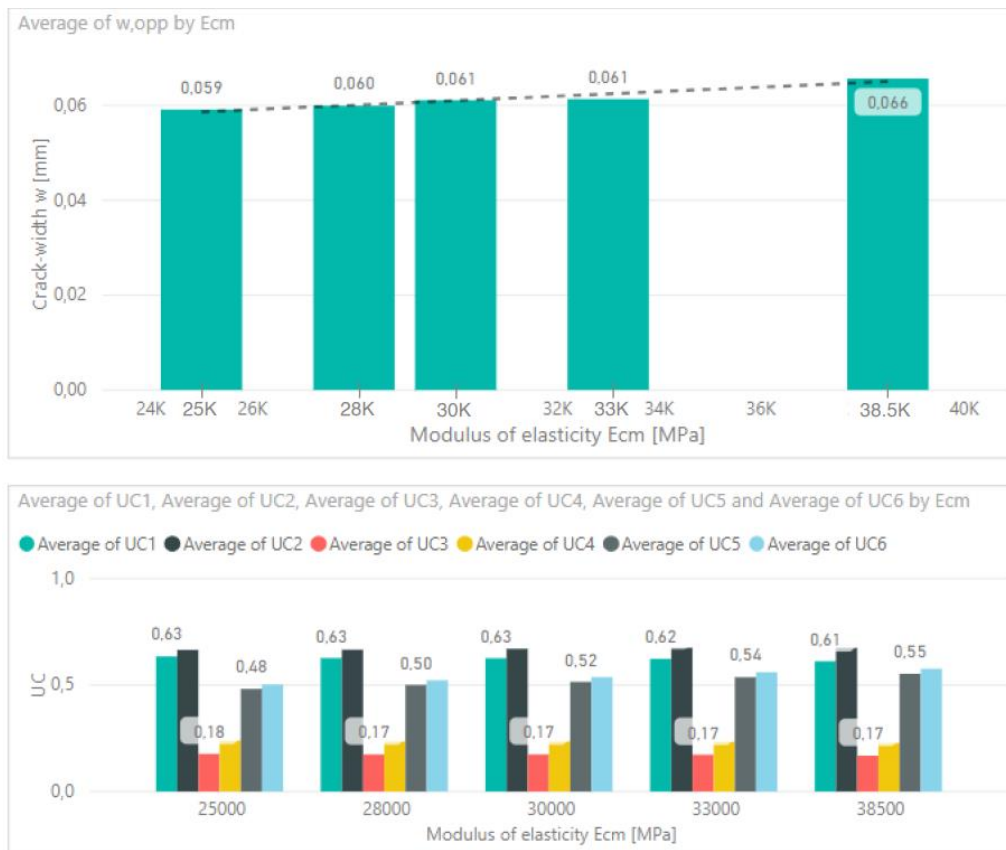
Figure 5.11 Top: average crack-widths for different modulus of elasticity E_{cm}. Bottom: Average values for the ULS unity checks for different modulus of elasticity E_{cm}. Modulus of elasticity E_{cm} values of 25, 28, 30, 33 and 38.5 GPa.

Figure 5.12 Top: average crack-widths for different tensile strengths f_{ctm}. Bottom: Average values for the ULS unity checks for different tensile strengths f_{ctm}. Tensile strength f_{ctm} values of 2-6 MPa.
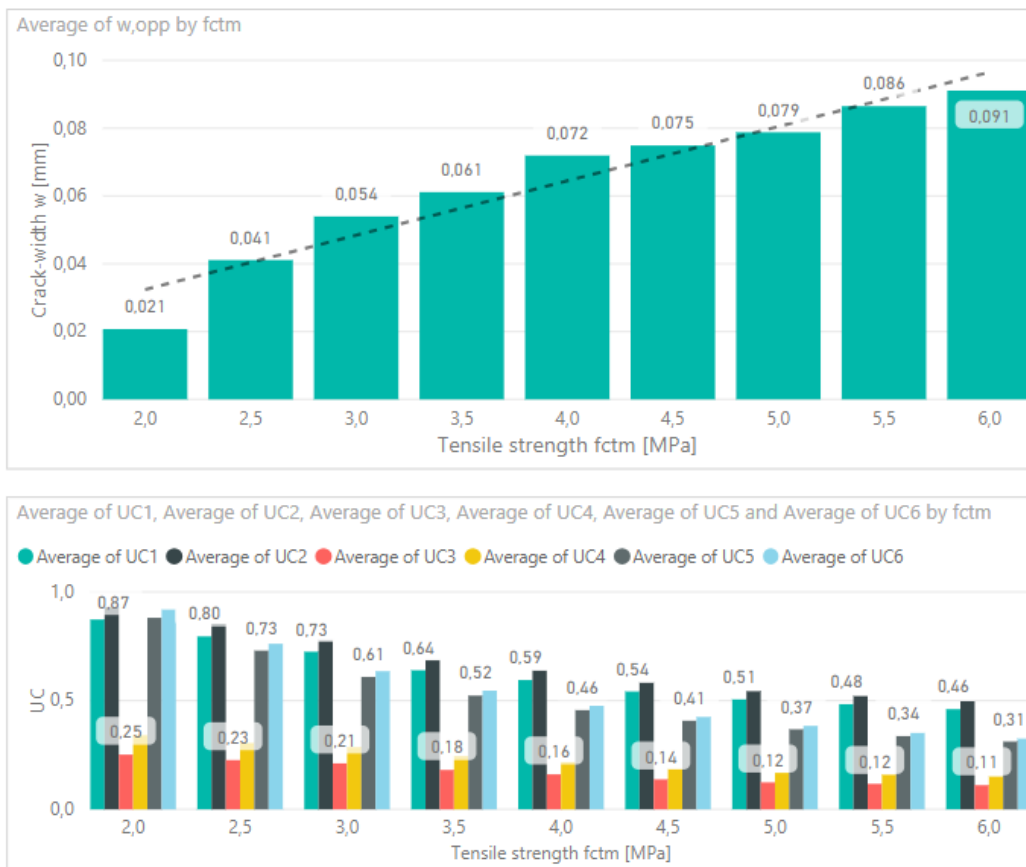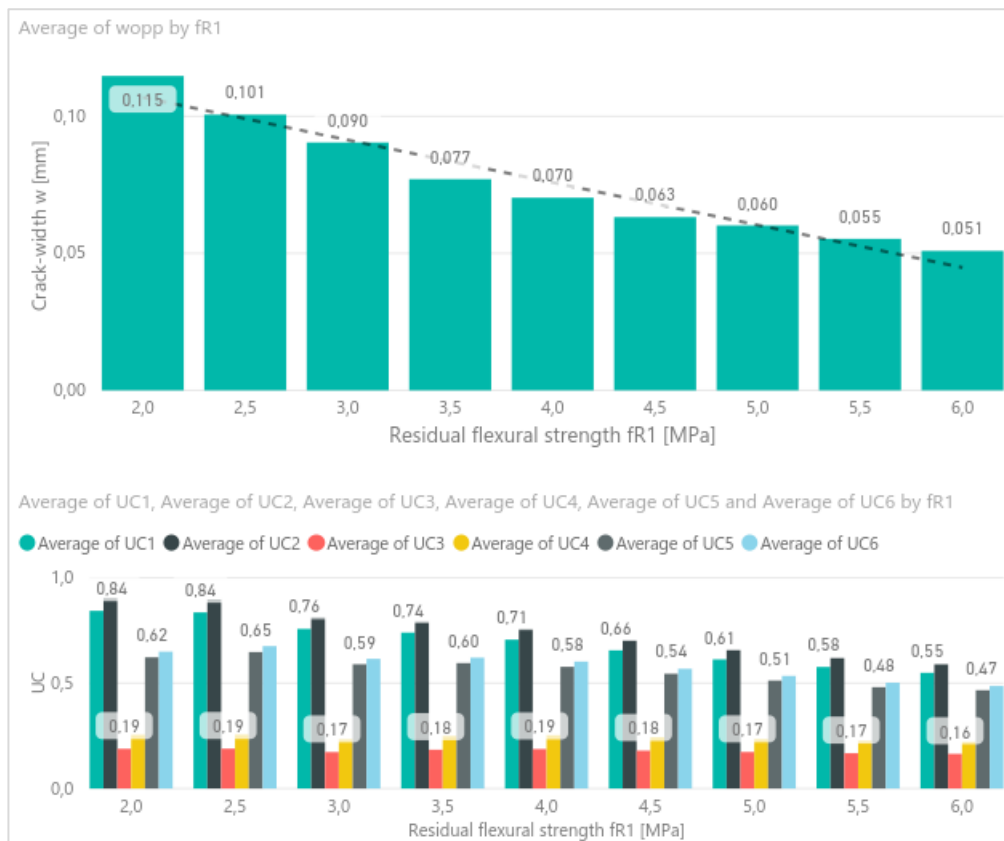
Figure 5.13 Top: average crack-widths for different flexural residual strengths f_{R1}. Bottom: Average values for the ULS unity checks for different flexural residual strengths f_{R1}. Flexural residual strengths f_{R1} values of 2-6 MPa.

In Figure 5.11 the modulus of elasticity E_{cm} and its influence is visualised. Here, similar to the compressive strength, a small influence is seen concerning both the crack-widths and the unity checks. A small decrease in the crack-widths is found with lower values for the modulus of elasticity. As alkali-activated concrete tends to show a lower modulus of elasticity, in comparison to OPC concrete with the same compressive strength, a small benefit is made here concerning the crack-widths.

When looking at the concrete tensile strength f_{ctm}, the influence on the crack-widths and the unity checks are clear. Figure 5.12 shows a trend line that, compared to the previous two concrete material parameters, isn't as flat. It can clearly visible why the lower tensile strengths are preferable when crack-width control is governing in a concrete structure. The average found crack-widths w_{opp} increase with a higher tensile strength f_{ctm}. The lowest tensile strength considered f_{ctm} = 2.0 MPa has an average crack-width found at w_{opp} = 0.02 mm where the tensile strength of f_{ctm} = 6.0 MPa has an average crack-width of w_{opp} = 0.09 mm. The average crack-widths are based on cross-sections that only have crack-widths between 0.01 mm < w_{opp} < 0.12 mm, where this minimum value of 0.01 mm comes from is discussed in section 5.4.2. The high tensile strength of f_{ctm} = 6.0 MPa has an average crack-width that is relatively close to maximum set crack-width.

The influence of the tensile strength f_{ctm} in Figure 5.12 is also visible on the unity checks related to flexure. Flexure is depending on the fictive flexural tensile strength $f_{ctm,fl}$ which is directly calculated from the tensile strength f_{ctm}. An opposite trend line can be seen for the flexure unity checks, lower the unity checks are found are for higher tensile strengths, as these have a higher flexural tensile strength. Alkali-activated concrete usually shows up to 10-20% higher tensile strengths compared to OPC concrete of the same compressive strength, considering the crack-width control this is unfavourable.

The increased calculated crack-widths one will find with the increased tensile strengths of AAC can be rectified with a slight increase of the residual flexural strength f_{R1}. Figure 5.13 displays a trend line opposite for the crack-widths compared to the one seen in Figure 5.12. It speaks for itself that the increase of the residual flexural strength reduces the crack-widths as the tensile forces in the reinforcement will be reduced. A reduction for all the unity checks with higher residual flexural strengths are also found.

Figure 5.14 shows the average crack-widths for different tensile strengths with different bar diameters ϕ for the reinforcement. The same trend line of increase in crack-width with higher tensile strengths can be seen. Here an increase of the reinforcement bar diameter shows the expected opposite behaviour where bigger bars are coupled with less wide crack-widths. The tensile strengths f_{ctm} of 4.0 and 4.5 MPa show this clearly, where the average crack-widths w_{opp} are the lowest with a reinforcement bar of ϕ = 8 mm and the highest with ϕ = 5 mm.
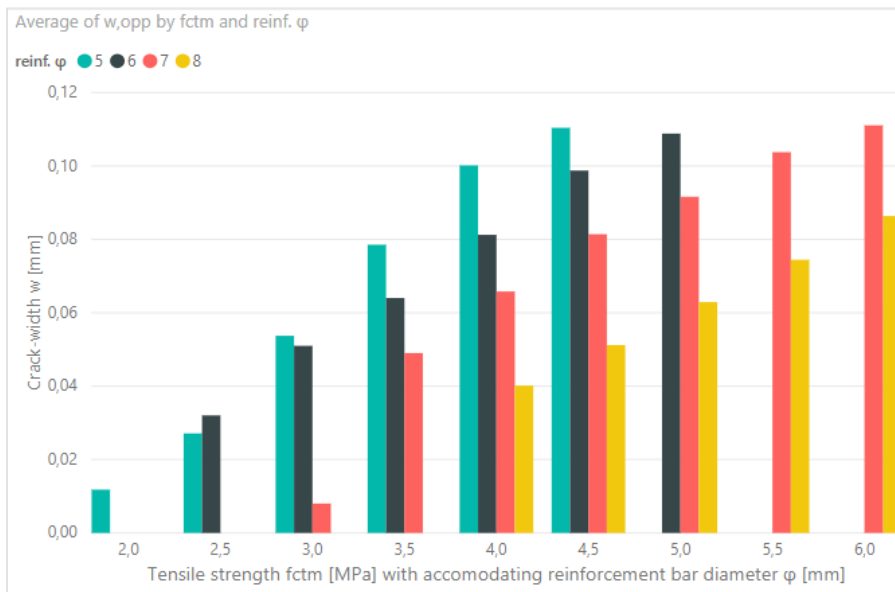
Figure 5.14 Average crack-widths over different tensile strengths with accommodating bar diameters ϕ in mm.

The minimum considered reinforcement bar of ϕ = 5 mm is only applicable up to a tensile strength of f_{ctm} = 4.5 MPa, see Figure 5.14. At higher tensile strengths the steel stress will be too high, because after the bending cracking moment has been reached the yielding stress will be reached. Therefore it is not shown as a suitable option for tensile strengths f_{ctm} > 4.5 MPa. Bar diameters of 7 and 8 mm are not applicable at the lower tensile strengths, as these can result in high local hogging bending moments from the external loads that the stabilized cracking stage can be reached. This is not allowed in the applied design method and thus such results are excluded.

In the following graph, Figure 5.15, the average crack-widths w_{opp} for different tensile strengths in combination with a certain residual flexural strength f_{R1} are shown. For example, the third column shows the average crack-widths for the cross-section with a tensile strength of f_{ctm} = 3.0 MPa with flexural residual strengths ranging from f_{R1} = 2.5 – 6.0 MPa, where in the final column of f_{ctm} = 6.0 MPa only the flexural residual strengths f_{R1} = 4.5 – 6.0 MPa seem to be suitable.
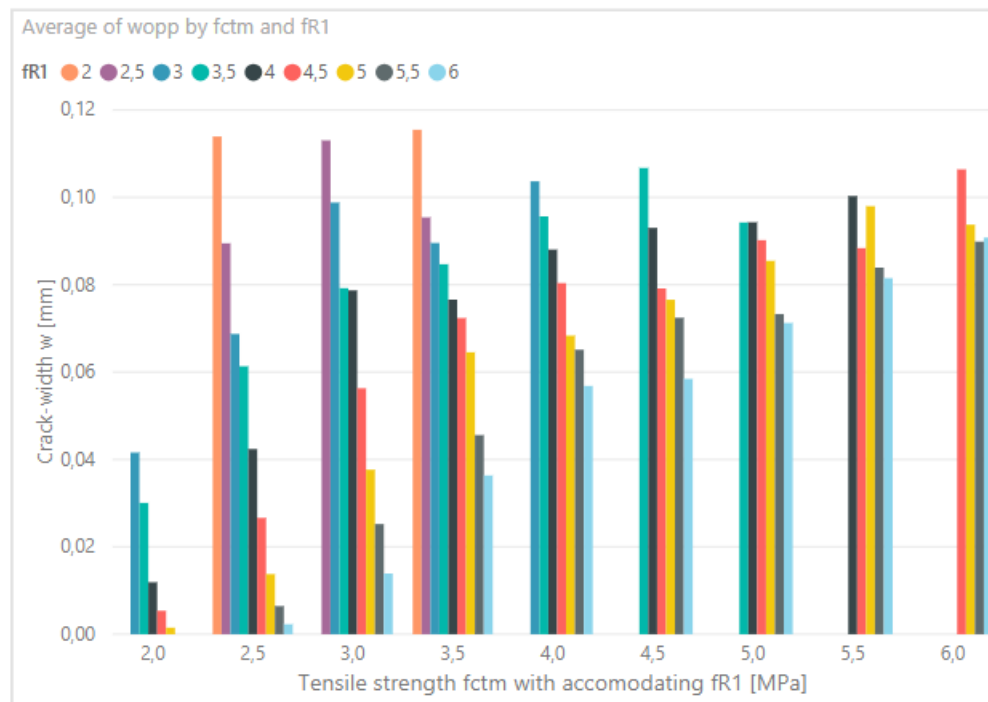
Figure 5.15 Average crack-widths for different tensile strengths with different flexural residual strengths. Note: this graph shows the average values where variants with crack-widths below 0.01 mm are also considered.

Figure 5.15 also shows suitable cross-section options where the crack-widths are nearly non-existent, most visible for low tensile strengths with high flexural residual strengths. Such specific cases where only micro-cracks will occur is theoretically possible, this will occur when steel fibre bending-hardening behaviour occurs. Bending hardening behaviour is feasible with steel fibres in higher dosages, up to 60-70 kg/m³, twice as much than usual. However, exceptional concrete mixtures are required to allow in-situ casting of such mixtures for a jointless floor, which are as of today not realistic yet. Besides that, deconcentration of steel fibres will be expected to occur in a way that crack formation takes place in the less dense concentrated areas. The actual crack-widths won't be as the calculated micro-cracks. Therefore, in the earlier and following analyses the crack-widths computed where w_{opp} < 0.01 mm, as a result of a low tensile strength accompanied with a much higher flexural residual strength, are disregarded.

5.4.2 Optimised ground floor in alkali-activated concrete

An optimised concrete ground floor with the reduced thickness of 130 mm can be further optimised when the amount of steel material needed is reduced. This can be realised by either a finer top reinforcement mesh by reducing the reinforcement bar diameter or by reducing steel fibre content added, resulting in lower residual flexural tensile strengths f_{Ri}. Less steel within the concrete floor cross-section will be correlated with increased crack-widths, this can be seen back in Figure 5.14 and Figure 5.15. In the following section it is analysed what possibilities there are when one were to realise the floor with the minimum considered reinforcement bar diameter. Possible floor cross-sections realised in alkali-activated concrete are considered. The concrete material parameters used will be in line with the properties found and discussed in chapter 4.

5.4.2.1 Minimum reinforcement bar

Floors with a thickness of 130 mm can be realised with a top reinforcement mesh of φ5-100 mm. Figure 5.16 shows that this can only be realised by providing enough steel fibres such that the flexural residual strength f_{R1} is higher than the accommodating tensile strength f_{ctm}. The graph shows the maximum found crack-widths of the suitable solutions with a practical minimum concrete cover of c = 30 mm. The maximum possible tensile strength suitable with a bar diameter of 5 mm is f_{ctm} = 4.0 MPa, where a residual flexural strength of f_{R1} = 6.0 MPa is required.

Figure 5.16 Top: crack-widths for different tensile strengths (x-axis) with different residual tensile strengths (coloured bars). Suitable options shown for a reinforcement mesh of φ5-100 mm with a concrete cover of 30 mm. Bottom: maximum ULS unity checks for different tensile strengths.

The yellow bars in the top diagram of Figure 5.16 represent the lowest suitable residual flexural strengths of f_{R1} = 3.5 MPa, further analysis showed these are only possible when realised with a modulus of elasticity E_{cm} ≤ 30,000 MPa. Cross-sections with a modulus of elasticity of E_{cm} = 38,500 MPa were only applicable with minimum flexural strengths of f_{R1} ≥ 4.0 MPa and

associated with slightly larger crack-widths. The compressive strength f_{cm} showed very little influence as discussed before.

Reducing the concrete cover is beneficial considering the flexure components as the internal lever arm and the effective depth of the concrete will increase. The following Figure 5.17 shows the suitable options when the minimum allowable concrete cover according to the Eurocode of $c = 20$ mm is applied. Compared to Figure 5.16, with $c = 30$ mm, an increased number of possible variants are suitable. Each tensile strength considered is realisable with an additional lower residual flexural strength. The maximum suitable tensile strength now is still $f_{ctm} = 4.0$ MPa.

What can be seen in both these graphs is that the lower tensile strengths have a reduced crack-width, such that the unity checks, for tensile strengths $f_{ctm} = 2.0$ and 2.5 MPa, are governing. The low tensile strength and fine reinforcement mesh result in a cross-section where the control of cracking isn't governing anymore but the ULS flexure checks are. Such low tensile strengths are for AAC likely not realistic to achieve.
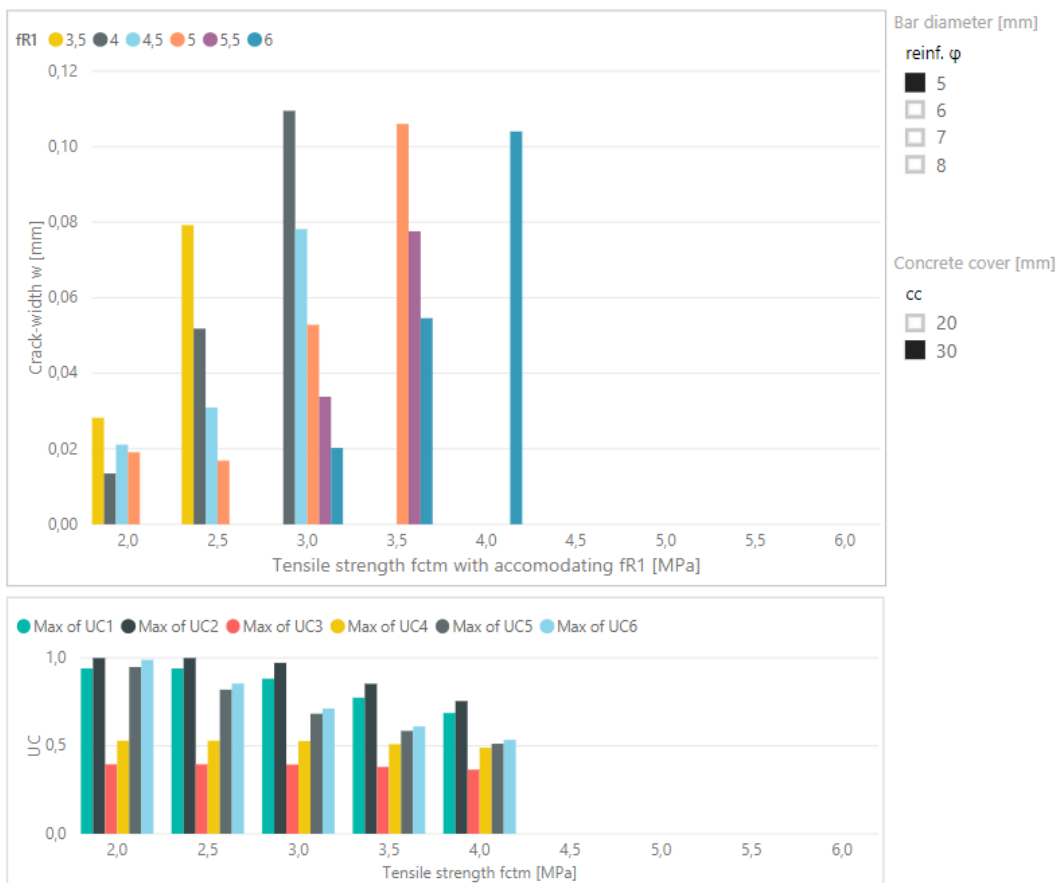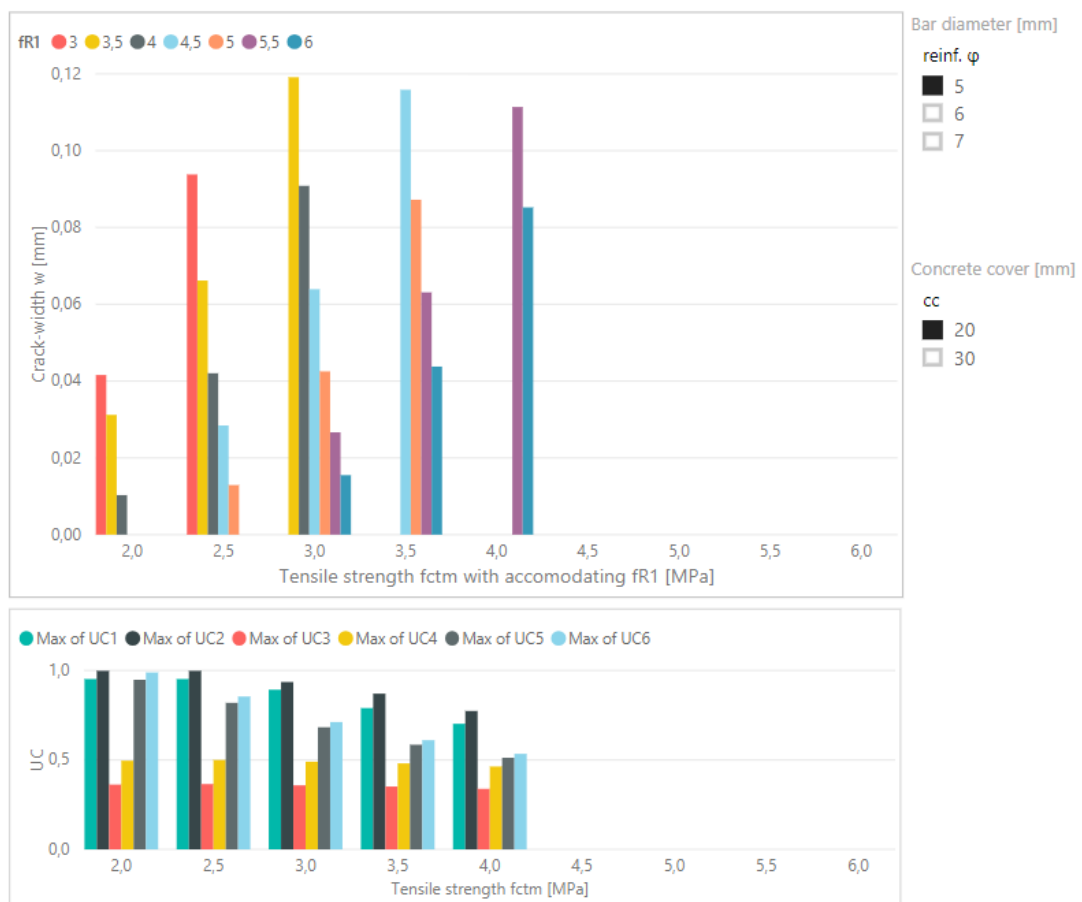

Figure 5.17 Top: crack-widths over different tensile strengths (x-axis) with different residual tensile strengths (coloured bars). Options shown for a reinforcement mesh of ϕ5-100 mm with concrete cover 20 mm. Bottom: maximum ULS unity checks for different tensile strengths.

5.4.2.2 The industrial jointless concrete ground floor realised in alkali-activated concrete

The possibilities of the reduced floor thickness $h = 130$ mm are considered when the concrete floor is realised with alkali-activated concrete. An alkali-activated concrete with an average compressive strength of $f_{cm} = 38$ MPa is chosen, based on the usually seen concrete class C30/37 for industrial concrete ground floors. In chapter 4 the concrete material properties of AAC and GPC have been discussed in relation to OPC concrete. AAC tends to have higher tensile strengths, a lower modulus of elasticity and due to its dense microstructure concrete covers can be reduced.

Therefore, the AAC considered here has the compressive strength f_{cm} = 38 MPa, with a tensile strength f_{ctm} = 4.0 MPa and a modulus of elasticity E_{cm} = 28 GPa where the top reinforcement mesh is applied with a concrete cover of c = 20 mm. The remaining variables for the floor cross-section are the steel reinforcement bar diameter ϕ and the steel fibre content expressed in the residual flexural strength f_{Rl}. The possible solutions with these set concrete material parameters are shown in Figure 5.18.

Figure 5.18 Top: maximum crack-widths for different reinforcement bar diameters (x-axis) and residual flexural strength f_{Rl} (coloured bars). Bottom: maximum ULS unity checks for different bar diameters. Shown for an alkali-activated concrete with compressive strength f_{cm} = 38 MPa, tensile strength f_{ctm} = 4.0 MPa and modulus of elasticity E_{cm} = 28 GPa. Reduced concrete cover of c = 20 mm applied.

This diagram shows that the AAC is realisable with reinforcement bar diameters from ϕ = 5 - 7 mm. The increased bar diameter ϕ = 8 mm isn't considered as this could result in a cross-section where external loads in SLS would cause high hogging bending moments through the redistribution of the bending moments, such that the floor would exceed the crack formation stage and locally the stabilised cracking stage will be reached. For this design approach this isn't allowed and therefore no suitable options are shown. Besides that, this study is about the optimisation of the floor, so a coarser reinforcement mesh isn't preferred.

For the concrete floor to be realised in the considered AAC with the minimum reinforcement bar diameter ϕ = 5 mm, residual tensile strengths have to be realised of f_{Rl} ≥ 5.5 MPa. Where this is most certainly possible for concrete with a tensile strength of f_{ctm} = 4.0 MPa, one will have to apply steel fibres contents higher than the common 35 kg/m³. This may become impractical when one has to cast this in-situ. With special multiple anchored steel fibres these high residual flexural strengths are conceivable with lower steel fibre contents, but such steel fibres are high-priced. Therefore is the floor realised with a top reinforcement mesh of ϕ5-100 mm considered as not optimal.

When the reinforcement bar diameter of ϕ = 6 mm is considered one can see that the suitable solutions are increased, realisable with practical residual flexural strengths. The maximum found ULS unity checks are well below its limit value of UC ≤ 1.0, this means that the SLS crack-width control for these floors remains the governing design aspect. The optimal jointless concrete ground floor is the one where the least steel material is required, which in this case is with a steel fibre content coupled with the residual flexural strength f_{R1} = 4.0 MPa. In Figure 5.18 this is shown in the top graph for the grey bar with a crack-width that is just within the limit set crack-width w_{opp} ≤ 0.12 mm.

This optimal jointless floor cross-section has a surface crack-width of w_{opp} = 0.118 mm. In Table 5-5 the AAC and steel parameters for the optimal jointless floor are listed. Table 5-6 shows the calculated crack-width at the top surface w_{opp} and the ULS unity checks.

Table 5-5 Optimised alkali-activated concrete ground floor properties.

AAC concrete floor	Symbol	Value	Unit
Thickness	h	130	mm
Compressive strength	f_{cm}	38	N/mm²
Young's modulus	E_{cm}	28000	N/mm²
Tensile strength	f_{ctm}	4.0	N/mm²
Residual tensile strength	f_{R1}	4.0	N/mm²
Concrete cover	c	20	mm
Bar diameter	ϕ	6	mm

Table 5-6 Crack-width and unity checks of the optimised AAC floor.

Check	Symbol	Value
Crack-width	w_{opp}	0.118 mm
Flexure single point load	UC1	0.70
Flexure double point load	UC2	0.74
Punching shear single point load	UC3	0.18
Punching shear double point load	UC4	0.24
Flexure UDL A	UC5	0.44
Flexure UDL B	UC6	0.46

The found crack-width w_{opp} = 0.118 mm for this AAC floor cross-section is small enough, below the limit w_{max} ≤ 0.12 mm, to ensure that a practical fluctuation in tensile strengths and steel fibre concentrations is possible. One might see increased crack-widths, but they will remain below the durability criteria of w_d ≤ 0.3 mm. The highest ULS unity check follows from $UC2$ = 0.74, where the back-to-back point loads act as separate points close to each other.

If the practical concrete cover c = 30 mm has to be applied, the floor is still realisable in the considered AAC with the parameters listed in Table 5-5, only the steel fibre residual flexural strength has to be increased slightly to f_{R1} = 4.5 MPa and the crack-width w_{opp} and the ULS unity checks are fulfilled. The associated crack-width and unity checks barely deviate from the values presented in Table 5-6.

The reduced shrinkage curve from section 5.2.1 that is studied, is based on the geopolymer concrete EFC. Were one to realise a jointless concrete floor with its reduced thickness in this geopolymer concrete there will be multiple solutions possible, see Figure 5.19. The concrete material properties of EFC are listed in Table 4-3 on page 53.
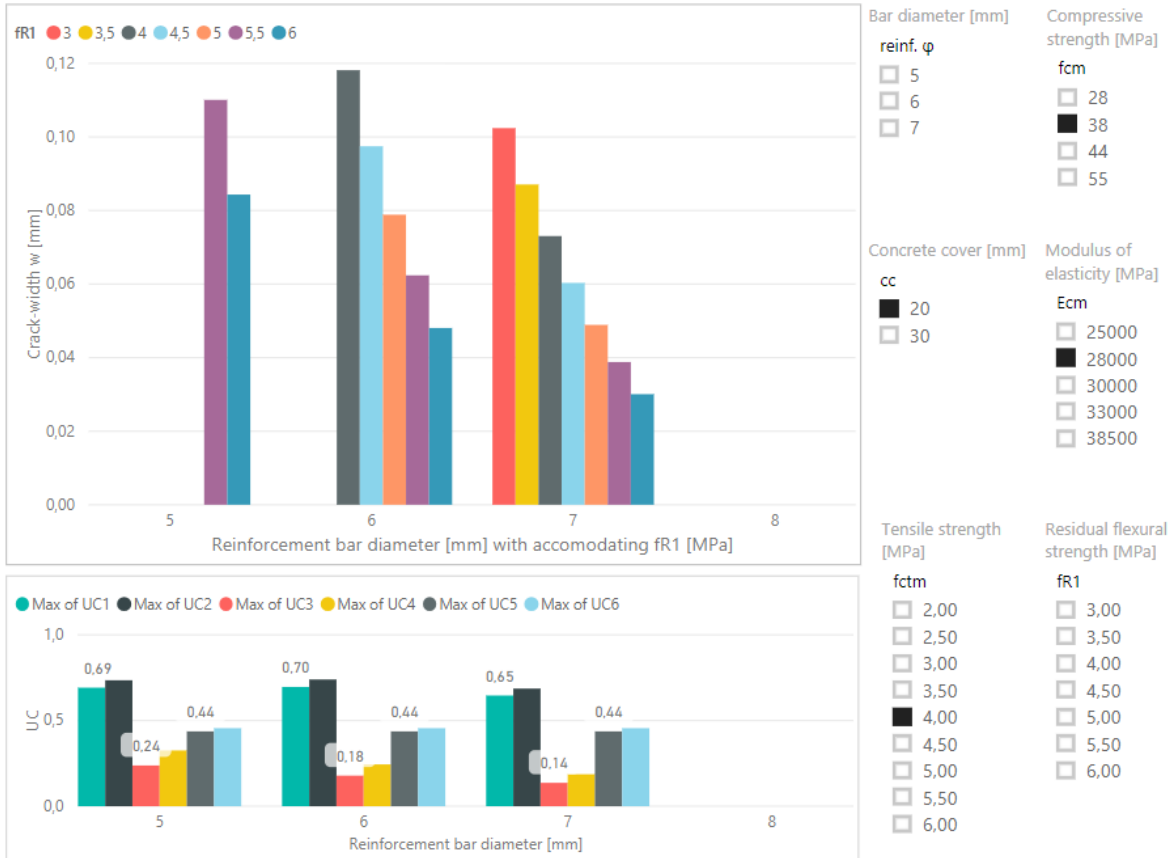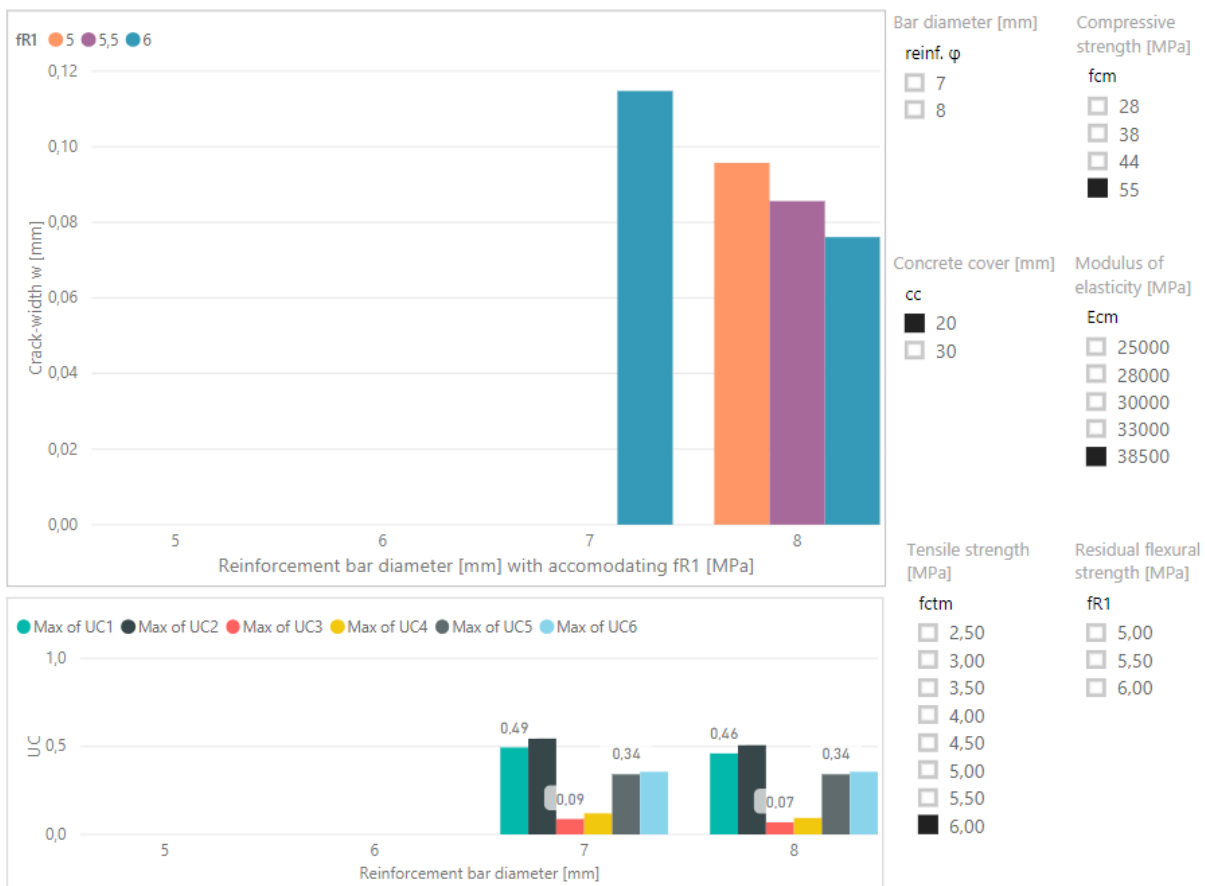
Figure 5.19 Top: maximum crack-widths for different reinforcement bar diameters (x-axis) and residual flexural strength f_{R_1} (coloured bars). Bottom: maximum ULS unity checks for different bar diameters. Shown for the geopolymer concrete EFC. Compressive strength f_{cm} = 55 MPa, tensile strength f_{ctm} = 6.0 MPa and modulus of elasticity E_{cm} = 38.5 GPa.

The geopolymer concrete EFC has a high tensile strength of f_{ctm} = 6.0 MPa. As can be seen in the graphs above, a cross-section with such a high tensile strength is still realisable for a jointless concrete floor. However, a reduction in the amount of steel material required won't be possible. For a top reinforcement mesh of ϕ7-100 mm with a reduced concrete cover of c = 20 mm a residual flexural strength of f_{R_1} = 6.0 MPa is required. A lower steel fibre content is possible when the reinforcement bar diameter is increased to ϕ = 8 mm. In both cases the crack-width control will be governing as the ULS unity checks are all below UC < 0.5.

In the design method it was stated that all the calculations for this theoretical analysis have been done with the average materials strength properties. In practice, the ULS requirements have to be calculated with the design strengths where the characteristic strength will be divided by its material factor. The calculations were redone for the optimised floor of Table 5-5. The material factors were set from γ_i = 1.0, to γ_c = 1.5 and γ_s = 1.15. All the ULS unity checks still fulfilled the requirements, the shear resistance and flexure check from a UDL load did increase significantly.

5.5 Combined axial and bending load

In the previous sections all cross-section crack-width calculations have been performed for pure bending only. It has been assumed that during crack formation the bottom fibre of the floor cross-section doesn't see a shrinkage reduction and as of that an average shrinkage component of the shrinkage gradient has been considered negligible. However, an average reduction component will be present and contribute to the development of stresses, especially once the bottom fibre starts to develop its shrinkage reduction after a certain time. The latter is considered

here in compliance with the CUR-Recommendation 36. When dimensioning the elastically supported jointless floor the CUR-Recommendation 36 provides the design method, where the shrinkage load is taken into account in the form of a combination of an average shrinkage with a linear gradient or a fully uniform developed shrinkage reduction. A floor cross-section realised in AAC with a thickness of 130 mm is checked here in accordance with this recommendation. Before long-term effects weren't taken into account, this will be done for this check.

A floor cross-section realised in AAC with the parameters shown in Table 5-5 is considered. The floor has a thickness of 130 mm, this thickness in AAC is only possible with a reduced shrinkage size, the maximum shrinkage strain of 0.3 ‰ from section 5.2 is followed. The AAC has an average concrete strength of f_{cm} = 38 MPa, tensile strength of f_{ctm} = 4.0 MPa and a modulus of elasticity E_{cm} = 28 GPa. The floor is reinforced with a top reinforcement mesh of ɸ6-100 mm with a concrete cover of c = 20 mm and has a steel fibre content resulting in the residual flexural strengths f_{R1} = f_{R4} = 4.0 MPa. The jointless floor will be considered to be loaded by a bulk load with a uniformly distributed load of q = 75 kN/m².

The requirement to be met for combined loading is:

$$\frac{M_{rep} + M_{shrinkage}}{M_{wmax}} + \frac{N_{shrinkage}}{bhf_{ft,rep1}} \leq 1 \tag{5.2}$$

The first term in Eq. (5.2) considers the bending component. The representative bending moment M_{rep} follows from the prescribed load, the bending moment from the shrinkage gradient is $M_{shrinkage}$. The bending moment M_{wmax} is the moment at which the limit value of the crack-width is present in the outer tension fibre of a steel fibre reinforced cross-section, which here would be the top surface with the limit value of the crack-width at w_{max} = 0.3 mm. In the second term the axial component is considered, where $N_{shrinkage}$ is the axial force from the shrinkage load and $f_{ftrep,1}$ is the representative value of the long-term tensile strength of steel fibre concrete.

The floor cross-section is checked after one year, as crack formation can be considered to be stable after approximately a year. The CUR-Recommendation 36 recommends to account for the shrinkage in the following two ways:

- At the top surface a shrinkage reduction of 0.9 ε_{cs} is present and at the bottom side a shrinkage reduction of 0.6 ε_{cs} is present, or
- A uniform acting shrinkage reduction over the floor thickness of 1.0 ε_{cs}.
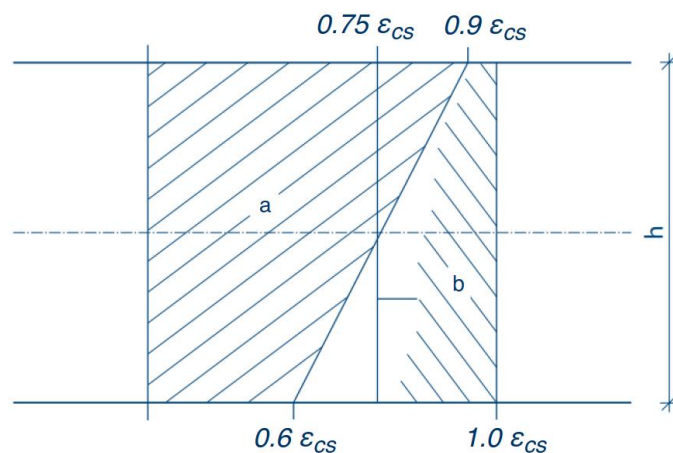

Figure 5.20 Shrinkage deformations that have to be accounted for in accordance with the CUR-Recommendation. ε_{cs} is the calculated shrinkage strain size. a: variant 1 with the maximum shrinkage gradient. b: variant 2 with a fully developed shrinkage. Graph edited from (CURNET, 2011).

The shrinkage size ε_{cs} and creep coefficient φ should be calculated in accordance with section 3.1.4 of NEN-EN 1992-1-1:2005. However, the empirical expressions provided here are suitable for OPC concrete and not necessarily for AAC or GPC. Such expressions don't exist yet for an AAC, therefore the expressions provided by the Eurocode are used in a way where they would approximate the shrinkage size and creep coefficient for the AAC.

The reduced shrinkage curve for EFC from Figure 5.4 can be closely approximated with an OPC concrete drying in a relative humidity of RH = 77%. The same final shrinkage size, for the shrinkage prism, of 0.3 ‰ and an almost similar early shrinkage development is found this way. Therefore, the expressions in NEN-EN 1992-1-1:2005 are used for an OPC concrete with a relative humidity of RH = 77%. This reconstructs the shrinkage curve well for an AAC, with the reduced shrinkage size, in an indoor environment with RH = 50%. The shrinkage reduction calculated after a year at t = 365 days and with the thickness h = 130 mm is ε_{cs} = 0.16 ‰.

The creep coefficient φ is computed with the same approach, where for OPC concrete the creep coefficient φ = 1.33 is found. Alkali-activated concrete tends to have lower creep values, long-term experiments on the creep of AAC are scarce as of yet. Short-term experiments show trends where the creep values are lower compared to OPC concrete. Here, the assumption is made that the AAC considered creeps around 20% less and the creep coefficient used here for the AAC is φ = 0.8 · 1.33 = 1.06. The relaxation coefficient follows to be k_ϕ = 0.62. The calculated bending moments and axial force from the imposed shrinkage load may be reduced with the relaxation coefficient. This is computed by calculating the forces with the fictive modulus of elasticity $E_{c,eff}$:

$$E_{c,eff} = E_c \cdot k_\phi = 28000 \cdot 0.62 = 17235 \; N/mm^2 \tag{5.3}$$

With the fictive modulus of elasticity $E_{c,eff}$, the axial force $N_{shrinkage}$ and bending moment $M_{shrinkage}$ can be computed for the two variants. As a uniformly distributed load is considered the theory of Hetényi is used with this fictive modulus of elasticity $E_{c,eff}$ to calculate the representative hogging bending moment M_{rep}. The tensile stresses are considered to be maximum at the top surface, so the maximum hogging bending moment is considered and follows to be M_{rep} = 5.92 kNm. In Appendix D this calculation is shown where M_{rep} is denoted as $M_{n,max}$. The bending moment M_{wmax} calculation is also shown in this appendix and is found at $M_{w,max}$ = 17.35 kNm.

The representative value for the long-term tensile strength of steel fibre concrete $f_{ftrep,1}$ can be computed from $f^f_{ct,L}$, the limit of proportionality, which here is assumed to be the value of flexural tensile strength of a notched bending test. The limit of proportion $f^f_{ct,L}$, according to NEN-EN 14651, is based on the maximum load value F_L. For bending-softening behaviour, which is the behaviour accepted for the jointless floor, it is assumed that this maximum load F_L takes place once the flexural tensile strength is reached. The value for axial tensile strength is found by multiplying the flexural tensile strength by a factor 0.6. So, for this example $f_{ftrep,1}$ follows from a beam with a notch of 125 mm and a tensile strength of f_{ctm} = 4.0 MPa:

$$f_{trep,1} = 0.6 \cdot f^f_{ct,L} = 0.6 \cdot \left(1.6 - \left(\frac{125}{1000} \right) \right) \cdot f_{ctm} = 3.54 \; N/mm^2 \tag{5.4}$$

The values above are estimations made which could differ with certain steel fibre contents or with AAC. The real values have to be found by performing bending tests on steel fibre concrete in accordance with NEN-EN 14651.

5.5.1 Variant 1

First the unity check is performed where the shrinkage gradient is present and where the shrinkage restrainment leads to an axial force and a bending moment. The bending moment follows from the restrained curvature:

$$\kappa_s = \frac{0.3 \cdot \varepsilon_{cs}}{h} \tag{5.5}$$

And becomes:

$$M_{shrinkage} = E_{c,eff} \cdot I \cdot \kappa_s = 1.17 \cdot 10^6 \ Nmm/m \tag{5.6}$$

The axial force follows from the average shrinkage reduction of $0.75 \ \varepsilon_{cs}$:

$$N_{shrinkage} = 0.75 \cdot \varepsilon_{cs} \cdot E_{c,eff} \cdot h = 269 \cdot 10^3 \ N/m \tag{5.7}$$

Which correlates to a constant tensile stress over the entire cross-section of 2.07 N/mm².

The SLS unity check from Eq. (5.2) follows (bending moments with tension at the top side are shown in kNm and with a positive sign):

$$\frac{5.92 + 1.17}{17.35} + \frac{2.07}{3.54} = 0.99 \tag{5.8}$$

It seems the floor barely fulfils the SLS unity check. Following the CUR-Recommendation, where the bottom fibre of the floor shows significant amounts of shrinkage, a significant axial component in the UC can be found, the second term in Eq. (5.8). When the bottom fibre shrinks in such a manner, the axial component that develops is of importance and as of that the unity check for the crack-width requirement follows to be close to 1.0. Thus, one can expect to see crack-widths at the top surface of the floor reaching the maximum allowable crack-width of 0.3 mm according to Eq. (5.8). Were the floor to develop a uniform shrinkage over its height the axial component increases which is considered in variant 2.

5.5.2 Variant 2

The second recommendation to be checked, follows the shrinkage to be fully developed forming a uniform shrinkage reduction over the height of the floor thickness. The shrinkage load in this case will only induce an axial load and no longer a bending moment.

The axial force to be considered in variant 2, with a uniform shrinkage over the height of the floor, is:

$$N_{shrinkage} = \varepsilon_{cs} E_{c,eff} \ h = 358 \cdot 10^3 \ N/m \tag{5.9}$$

Which introduces a tensile stress of 2.76 N/mm².

The SLS unity check from Eq. (5.2) follows to be:

$$\frac{5.92}{17.35} + \frac{2.76}{3.54} = 1.12 \tag{5.10}$$

So, the assumptions were made that the drying shrinkage at the bottom fibre won't occur to its final shrinkage size. If however, the shrinkage at the bottom fibre were to fully develop, one can see that the SLS unity check isn't met.

If in a case the jointless concrete floor with the concrete and reinforcement properties of this example is already realised and one finds crack-widths that exceed the maximum allowable crack-width of w_{max} = 0.3 mm, because the bottom part of the floor saw a shrinkage reduction as well, one should have to repair the floor. A solution to prevent the crack-width from being exceeded, is to reduce the allowable maximum uniformly distributed load, which would reduce the representative bending moment M_{rep}. A reduction of this bending moment in Eq. (5.10) to M_{rep} = 3.75 kNm follows from a maximum allowable uniformly distributed load of q = 47.5 kN/m². In this case the unity check of variant 1 becomes UC = 0.87 and of variant 2 the unity check is exactly UC = 1.0.

5.6 Results

Thin jointless concrete ground floors can be realised, down to thicknesses of 70 to 90 mm, such that the SLS and ULS unity checks are still met. This does however requires a concrete that shows close to no drying shrinkage at all. In practice such floors won't crack from a restrained drying shrinkage curvature but would most likely warp and crack from the imposed loads caused by temperature changes. At floor thicknesses ranging from 70 to 100 mm thick, the control of cracking is no longer necessarily the governing design criteria for the jointless concrete ground floor. For such low thicknesses the requirements regarding the ULS unity checks become governing. The double point loads or uniformly distributed loads require certain flexural tensile strength and a redistribution of the bending moments, that the floor must be realised with a vast amount reinforcement ($\omega_t > 0.5\%$). The top reinforcement mesh has to be accommodated with a significant amount of steel fibres to ensure a high residual flexural strength, necessary to provide the required ultimate design bending moment of the floor cross-section. The flexural tensile strength $f_{ctm,fl}$ and ultimate design moment M_{Rd} are depending on the thickness h and therefore the ULS unity checks become of more significance with lower thickness h values.

With alkali-activated concrete a reduced final drying shrinkage size can be realised. A reduced final drying shrinkage size of 0.3‰ is possible. This lower final drying shrinkage size is coupled with an initial development rate of the drying shrinkage that is slower. It is found that this can be translated to a thinner floor cross-section down to a reduced thickness of 130 mm. At this thickness it is assumed that the bottom part of the concrete floor won't undergo any drying shrinkage in the early age of the concrete floor, thus ensuring that there won't be an uniform tension component present in the floor until a couple of years. This ensures that the cracks that will arise in the floor will arise only from bending. As the control of cracking is crucial, cracks may not be formed from pure tension, as these result in crack-widths that can be several times larger and would result in a damaged jointless floor that needs repairing.

The studied reduced thickness of 130 mm show that the parameters compressive strength f_{cm} and modulus of elasticity E_{cm} of the concrete aren't that much of a significance concerning the crack-widths and ULS unity checks. When taking long-term properties into account, the modulus of elasticity is a more important material property. The calculations done in section 5.5 show that the axial component from the average or fully developed shrinkage load is quite significant. The developed tensile stresses from the shrinkage load will be reduced with a lower modulus of elasticity. Section 5.4 shows that the tensile strength f_{ctm} and the residual flexural strength f_{R1} are significant concerning the crack-widths and the flexure ULS unity checks. As expected, one will find the lowest crack-widths w_{opp} with low tensile strengths coupled with high residual flexural strengths.

It is found that, for an AAC with a compressive strength of f_{cm} = 38 MPa with matching concrete properties, one can reduce the amount of required steel within the jointless floor compared to the

reference floor realised in OPC concrete. Even though alkali-activated concrete has a disadvantageous higher tensile strengths compared to OPC concrete, concerning the crack-widths. The reduced floor thickness is coupled with a reduced bending cracking moment M_{crack}, for which the thickness h is squared in the calculation, thus resulting in lower tensile stresses within the reinforcement and thus reducing the found crack-widths.

The alkali-activated concrete with a compressive strength of $f_{cm} = 38$ MPa is considered with the matching tensile strength of $f_{ctm} = 4.0$ MPa and modulus of elasticity of $E_{cm} = 28$ GPa. It is found that one can realise such a jointless floor, with a reduced thickness of $h = 130$ mm, with less required steel, either by a lower reinforcement ratio or by a lower steel fibre content. The floor is realisable with a reduced top reinforcement mesh of ϕ6-100 mm with a concrete cover of $c = 20$ mm and residual flexural strength of $f_{R1} = 4.0$ MPa, which is achievable with steel fibre contents between 30 to 40 kg/m³.

The design approach followed in sections 5.1 to 5.4 assumes that the development of the drying shrinkage reduction at the bottom fibre of the floor is close to non-existent, especially in the early age of the floor. The CUR-Recommendation 36, for the design of elastically supported ground floors, states that the floor has to be checked where the bottom fibre does see a shrinkage reduction. Following the design method provided by this recommendation, one will find that the axial component of the shrinkage load is quite significant in the SLS unity check.

If the drying shrinkage were to fully develop at the bottom fibre, the floor won't fulfil the SLS unity check anymore, as is found in the calculation for variant 2. The external loads must be lowered to ensure that the unity check remains below 1.0 so the crack-widths won't exceed $w_{max} = 0.3$ mm. One can expect higher representative bending moments when a fully loaded back-to-back racking is considered. A double point load of 95 kN can therefore result in a SLS unity check above 1.0, also when the shrinkage reduction at the bottom fibre is considered to be the at a maximum of 0.6 ε_{cs}, being variant 1.

This further shows that the shrinkage development that is considered at the bottom fibre of the concrete floor is important. If one assumes that the bottom shrinkage reduction is close to non-existent and the average axial shrinkage component is neglected, one can design floor cross-sections with a fine top reinforcement mesh. If in practice the bottom part of the concrete floor sees a significant shrinkage reduction, the average shrinkage component will result in axial tensile stresses which can cause the crack-widths to exceed the limit of $w_{max} = 0.3$ mm.

The floor cross-section considered in AAC, realised with the properties listed in Table 5-7, is realisable with the reduced thickness of 130 mm, a top reinforcement mesh of ϕ6-100 mm and a steel fibre content of around 35 kg/m³. The floor is in accordance with the CUR-Recommendation 36 and will fulfil the SLS and ULS unity checks, when the external uniformly distributed load is limited to $q = 47.5$ kN/m². The governing design criteria is still to control the crack-widths, which with this floor will remain below the maximum allowable crack-width $w_d \leq 0.3$ mm.

Table 5-7 Optimised alkali-activated concrete jointless ground floor properties

AAC floor properties	Symbol	Value	Unit
Thickness	h	130	mm
Compressive strength	f_{cm}	38	N/mm²
Young's modulus	E_{cm}	28000	N/mm²
Tensile strength	f_{ctm}	4.0	N/mm²
Residual tensile strength	f_{R1}	4.0	N/mm²
Concrete cover	c	20	mm
Bar diameter	ϕ	6	mm

The optimised jointless concrete ground floor realised in AAC, with the properties of Table 5-7, requires less material compared to the reference floor of which the floor properties are listed in Table 5-8.

Table 5-8 Reference OPC concrete jointless ground floor properties

OPC floor properties	Symbol	Value	Unit
Thickness	h	160	mm
Compressive strength	f_{cm}	38	N/mm²
Young's modulus	E_{cm}	33000	N/mm²
Tensile strength	f_{ctm}	3.0	N/mm²
Residual tensile strength	f_{R1}	2.5	N/mm²
Concrete cover	c	30	mm
Bar diameter	ϕ	7	mm

The minimum floor thickness is reduced from 160 mm to 130 mm. The minimum bar diameter for the top reinforcement mesh is reduced from 7 mm to 6 mm. The steel fibre content was minimally 30 kg/m³, which now is estimated at minimally 35 kg/m³. Per square meter industrial floor this results in a reduction of 19% in concrete material, 26% in reinforcement steel and 5% in steel fibres required.

6

BOND-SLIP CRACK-WIDTH CALCULATION

Bond is the term used to denote the interaction and transfer of force between reinforcement and concrete. The bond influences crack-widths and the spacing, i.e. the anchorage length, of transverse cracks. In chapter 3 the bond strength τ_{bm} of concrete is mentioned as one of the important material properties concerning the control of cracking. In the previous chapter the crack-width calculations have been done, in accordance with the Eurocode 2 and the fib Model Code 2010, where a constant bond stress is assumed and the steel and concrete stresses are simplified by linearization adjacent to cracks, i.e. in the discontinuity area. In reality the steel, concrete and bond stresses in the discontinuity area are non-linear, which can be computed with bond-slip relations. Crack-width calculations here are further studied by studying crack formation in a tensile member that remains in the crack formation stage. The findings can be translated to the crack formation by bending of a jointless concrete floor. For these floors the remaining important material property to be considered, the bond strength, is studied in this chapter, both for OPC concrete and AAC.

The simplified crack-width relations are introduced of which its results will be compared to crack-width computations done by bond-slip models. Which are introduced in section 6.2, these models are used to study the non-linear behaviour of the materials. The latter is done with theoretical bond-slip calculations and with finite element analysis (FEA) in DIANA, which will be compared with each other. The improved bond-slip relation for AAC is further studied and its influence on crack-width calculations is presented.

6.1 Simplified direct method

The mean bond stress that is assumed in the simplified method of the crack-width calculation, is independent of the magnitude of the slip between steel and concrete and linearly related to tensile strength f_{ctm}. In Figure 6.1 the transmission of forces in a disturbed area adjacent to a crack is shown. The crack-width expressions and relations applied in chapter 5 are based on this simplified linearization.

The maximum found crack-widths and the associated stresses are studied. Crack-widths are at a maximum in the crack formation stage just before, at another location, a new crack arises. For a tensile member in the crack formation stage the following expressions are used.

The maximum steel stress in a crack in the crack formation stage σ_{sr} is:

$$\sigma_{sr} = \frac{f_{ctm}}{\rho_{s,ef}}(1 + \alpha_e \rho_{s,ef})$$

(6.1)

where $\rho_{s,ef}$ is the effective reinforcement ratio and α_e is the modular ratio, $\alpha_e = E_s/E_c$. Outside of the discontinuity area the strains of the steel and concrete are equal and the steel stress in the undisturbed area is directly proportional to the concrete stress:

$$\sigma_{se} = \alpha_e f_{ctm}$$

(6.2)

The discontinuity area is twice the length of the transfer length l_t:

$$l_t = \frac{1}{4}\frac{f_{ctm}}{\tau_{bm}}\frac{\phi}{\rho_{s,ef}}$$

(6.3)

The fib Model Code 2010 expression has an additional term $k \cdot c$ which takes the concrete cover into consideration that can be added to the transfer length. This additional term isn't considered here. The transfer length is also called the anchorage length.

The maximum crack-width in the crack formation stage can be calculated with:

$$w_{max} = \frac{1}{4}\frac{f_{ctm}}{\tau_{bm}}\frac{\phi}{\rho_{s,ef}}\frac{1}{E_s}\sigma_{sr}$$

(6.4)
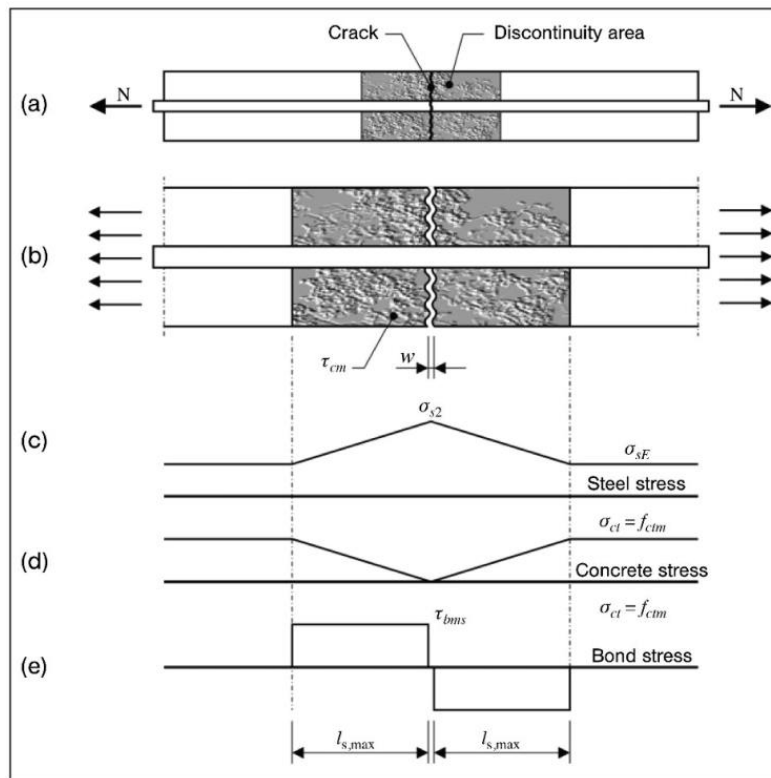
Figure 6.1 Simplified representation of the steel, concrete and bond stresses in disturbed area in the crack formation stage. (a) centrically reinforced tensile member with crack; (b) discontinuity area; (c) steel stress development in discontinuity area; (d) concrete stress development in discontinuity area; (e) development of bond stress in discontinuity area. Figure from (Fédération Internationale du Béton, 2013).

The maximum steel stress in the crack formation stage σ_{sr}, is found right before another crack is formed when the concrete tensile stress is reaching its tensile strength. The tensile member first cracks at $N_{cr,1}$, see Figure 6.2, after which the force N drops. Further increasing the load increases

the steel stress within the crack, upon reaching the maximum steel stress in a crack in the crack formation stage σ_{sr}, the concrete tensile stresses reach the tensile strength again and a new crack shall be formed at $N_{cr,2}$. It is just before that point that with Eq. (6.4) the maximum crack-widths are found in the crack formation stage. This is the point and stage at which the crack-widths computations in this chapter are performed and studied.

Figure 6.2 Load-strain graph for a centrically reinforced member subjected to tension (Walraven & Braam, 2015).

The bond stress τ_{bm} in Eq. (6.4), and in the following Eq. (6.6), is determined by the concrete tensile strength f_{ctm} and its value can be taken from Table 6-1. Shrinkage is considered a long-term effect, under long term or dynamic loads the bond stress decreases, and the bond stress τ_{bm} is thus estimated with:

$$\tau_{bm} = 1.6 \cdot f_{ctm} \tag{6.5}$$
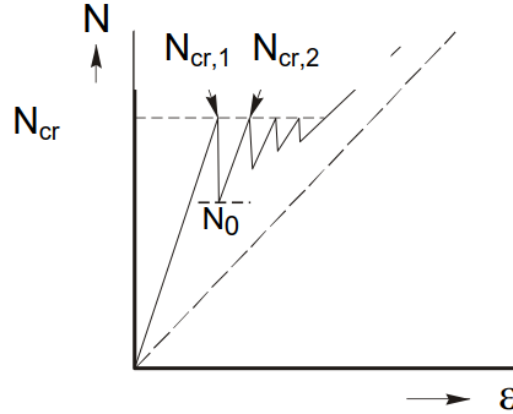
The other coefficients β and η_r shown in Table 6-1 are applied in the more general expression for the crack-width which can also calculate crack-widths in the stabilized cracking stage:

$$w_d = \frac{1}{2} \frac{\phi_s}{\rho_{s,eff}} \frac{f_{ctm}}{\tau_{bm}} \frac{1}{E_s} (\sigma_s - \beta\sigma_{sr} + \eta_r \varepsilon_{cs} E_s) \tag{6.6}$$

The expression in Eq. (6.6) is almost the same expression introduced in Eq. (3.2) from section 3.4, where in Eq. (3.2) only the extra term f_{Ftsm} is present taking the residual tensile strength from the steel fibres into account.

Table 6-1 Values for β, η$_r$ and τ$_{bm}$ for various conditions.

	Crack formation stage	Stabilized cracking stage
Short term loading	$\beta = 0.6$ $\eta_r = 0$ $\tau_{bm} = 2.0\,f_{ctm}$	$\beta = 0.6$ $\eta_r = 0$ $\tau_{bm} = 2.0\,f_{ctm}$
Long term or dynamic loading	$\beta = 0.6$ $\eta_r = 0$ $\tau_{bm} = 1.6\,f_{ctm}$	$\beta = 0.4$ $\eta_r = 1$ $\tau_{bm} = 2.0\,f_{ctm}$

The crack-width expression for the maximum crack-width in the crack formation stage of a tensile member in Eq. (6.4) is used and will be compared with the non-linear crack-width calculations introduced next. In this chapter the process of the crack-width calculation for the different methods is explained with the following theoretical example. A concrete tensile member of 100 mm width and height, reinforced with a $\phi = 10$ mm ribbed reinforcement bar and the

concrete has a compressive strength of f_{cm} = 38.0 MPa, a modulus of elasticity E_{cm} = 30.0 GPa and a tensile strength f_{ctm} = 3.0 MPa.

Using Eq. (6.1) to (6.5) the following values are found. The maximum steel stress in the crack formation stage follows at σ_{sr} = 402.0 MPa, the steel stress in the undisturbed area where the concrete and steel strain are equal is σ_{se} = 20.0 MPa. The constant bond stress assumed in this case will be τ_{bm} = 1.6 · 3.0 = 4.8 MPa. A transfer length l_t = 199 mm follows with a maximum crack-width in the crack formation stage of w_{max} = 0.40 mm.

6.2 Bond-slip models

In cracked cross-sections the tension forces are transferred across the crack by the reinforcing steel. Adjacent to cracks in the discontinuity area the displacements of the steel u_s and the concrete u_c are different. Due to their relative displacement $s = u_s – u_c$ bond stresses are generated between the concrete and the reinforcing steel. This relative displacement is called the slip s. The bond stresses gradually transfer the steel force to the concrete, for which the ribs of the reinforcement bars are of importance.

The slip s is the displacement difference between the concrete and the reinforcement bar. The maximum slip is at the location of the crack and slowly decreases over the anchorage length. Slip between the reinforcement bar and the concrete occurs at both sides of the crack, so the crack-width is two times the slip value found at the location of the crack. With bond slip models more accurate crack-width calculations can be done, where the bond stress over the anchorage length is non-linear. If the bond between the steel and concrete is better, the anchorage length will be shorter. A shorter anchorage length is associated with a lower maximum bond stress found at the crack location. As the slip value is directly related to the bond stress value, a lower maximum bond stress results in a lower slip and thus a smaller crack-width.

The magnitude of the bond stresses depends predominantly on the slip s, but is also influenced by the surface of the reinforcing steel, the concrete strength f_{cm} and the confinement from the concrete. The top reinforcement mesh for a jointless floor is considered to be under good bond conditions and confined. There are several bond-slip models that express the magnitude of the bond stress τ_b. The bond-slip relationship of the fib Model Code for Concrete Strucutres 2010 and the Shima bond-slip relationship are the models considered here. The fib relationship is a well-known one and the Shima relationship is one that is quite easily applicable and thus often applied for FEA in DIANA. Therefore these two bond-slip relationships are chosen as the considered models.

6.2.1 fib Model Code for Concrete Structures 2010 bond-slip relationship

The bond stress-slip relationship presented covers anchorage of ribbed reinforcing bars. This relation has a different formulation depending on the slip value. The following expression define the fib bond-slip relation, which will result in the bond-slip curve presented in Figure 6.3:

$$\tau_{bm} = \tau_{bmax} \left(\frac{s}{s1}\right)^{\alpha} \qquad\qquad for\ 0\ \leq s \leq s1 \qquad\qquad (6.7)$$

$$\tau_{bm} = \tau_{bmax} \qquad\qquad for\ s1\ \leq s \leq s2 \qquad\qquad (6.8)$$

$$\tau_{bm} = \tau_{bmax} - (\tau_{bmax} - \tau_{bf}) \left(\frac{s - s2}{s3 - s2}\right) \qquad\qquad for\ s2\ \leq s \leq s3 \qquad\qquad (6.9)$$

$$\tau_{bm} = \tau_{bf} \qquad\qquad for\ s3\ < s \qquad\qquad (6.10)$$

where the parameters are given in Table 6-2.

The grey Pull-out line from Figure 6.3 presents the bond-slip curve for a confined bar with good bonding conditions, the reinforcements bars considered for the tensile members follow this relation. The ascending part, defined by Eq. (6.7), refers to the stage in which the ribs penetrate in the mortar matrix, characterised by local crushing and micro cracking. The sustained plateau occurs only for confined concrete, during which advanced crushing and shearing off of the concrete between the ribs takes place. At the descending branch the concrete corbels between the ribs are sheared off resulting in the reduction of the bond resistance.

The parameters that are applicable here for the expressions of Eq. (6.7) to (6.10) are listed in Table 6-2 in column 1 for good bond conditions. The value for s_1 = 1.0 mm and since the crack-width w_d is two times the slip s value, the expression in Eq. (6.7) representing the ascending branch of the bond-slip relation, must be considered for crack-widths of $w_d \leq 2.0$ mm.
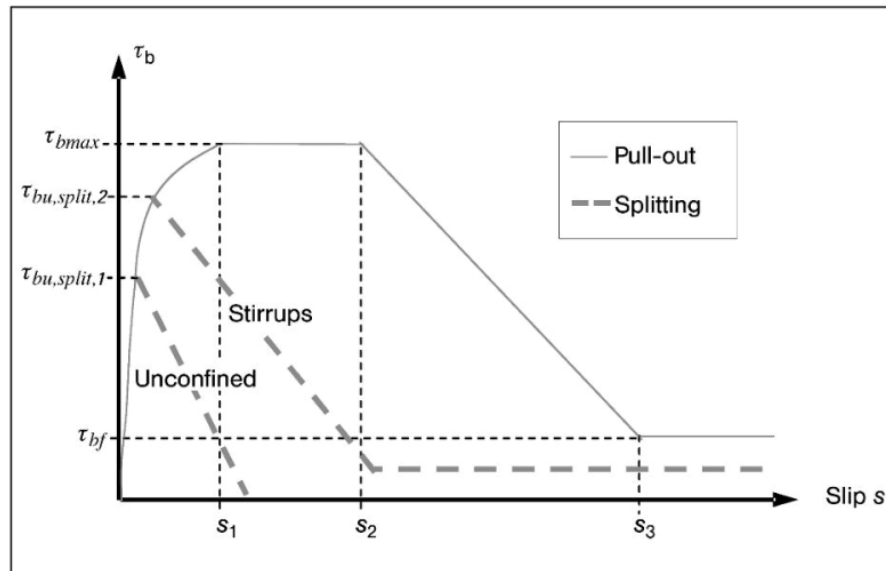

Figure 6.3 Bond stress-slip relationship, for confined and unconfined concrete. The grey Pull-out curve applies for the confined top reinforcement of the jointless floor and the tensile member that are considered. Graph from (Fédération Internationale du Béton, 2013, p. 154).

Table 6-2 Parameters defining the mean bond stress-slip relationship of ribbed bars (Fédération Internationale du Béton, 2013). c_{clear} is the clear distance between ribs.

	1	2	3	4	5	6
	Pull-out (PO)		**Splitting (SP)**			
	$\varepsilon_s < \varepsilon_{s,y}$		$\varepsilon_s < \varepsilon_{s,y}$			
	Good bond cond.	**All other bond cond.**	**Good bond cond.**		**All other bond cond.**	
			Unconfined	**Stirrups**	**Unconfined**	**Stirrups**
τ_{bmax}	$2.5\sqrt{f_{cm}}$	$1.25\sqrt{f_{cm}}$	$2.5\sqrt{f_{cm}}$	$2.5\sqrt{f_{cm}}$	$1.25\sqrt{f_{cm}}$	$1.25\sqrt{f_{cm}}$
$\tau_{bu,split}$	—	—	$7.0\cdot\left(\dfrac{f_{cm}}{25}\right)^{0.25}$	$8.0\cdot\left(\dfrac{f_{cm}}{25}\right)^{0.25}$	$5.0\cdot\left(\dfrac{f_{cm}}{25}\right)^{0.25}$	$5.5\cdot\left(\dfrac{f_{cm}}{25}\right)^{0.25}$
s_1	1.0 mm	1.8 mm	$s(\tau_{bu,split})$	$s(\tau_{bu,split})$	$s(\tau_{bu,split})$	$s(\tau_{bu,split})$
s_2	2.0 mm	3.6 mm	s_1	s_1	s_1	s_1
s_3	c_{clear}[1)]	c_{clear}[1)]	$1.2s_1$	$0.5c_{clear}$[1)]	$1.2s_1$	$0.5c_{clear}$[1)]
a	0.4	0.4	0.4	0.4	0.4	0.4
τ_{bf}	$0.40\tau_{max}$	$0.40\tau_{max}$	0	$0.4\tau_{bu,split}$	0	$0.4\tau_{bu,split}$

The ascending part of the bond-slip model depends on the ultimate bond strength τ_{bmax}, which according to the fib model relation is calculated from the average compressive strength f_{cm}, as is shown in Table 6-2. For crack-width control only the ascending branch is considered, for which the expression in Eq. (6.7) can be rewritten as:

$$\tau_{bm} = 2.5\sqrt{f_{cm}}\left(\frac{s}{1.0}\right)^{0.4} \tag{6.11}$$

Where s is the slip between the reinforcement bar and the concrete.

6.2.1.1 Improved fib bond stress-slip relationship for alkali-activated concrete

In section 4.3.5 it has been mentioned that alkali-activated concrete has a bond strength between the concrete and reinforcing bars that is significantly greater that the fib model predicts. A recalibrated model has been provided by Castel (2017) for the ultimate bond strength that has a better prediction for geopolymer concrete. Castel speaks of geopolymer concrete but in that study the calcium rich blast furnace slag has been used as a precursor, and thus C-(A)-S-H will be one of the reaction products, so one could argue that he actually tested alkali-activated concrete. From here on the terms used by Castel will be followed by using the abbreviation GPC, but his findings are also applicable for AAC. The recalibrated model provides the following expression for the ultimate bond strength $\tau_{u\text{-}GPC}$ for GPC:

$$\tau_{u-GPC} = 3.83\sqrt{f_{cm}} \tag{6.12}$$

For geopolymer – and alkali-activated concrete the ascending branch of the bond-slip relation can be written:

$$\tau_{bm,GPC} = 3.83\sqrt{f_{cm}}\left(\frac{s}{1.0}\right)^{0.4} \tag{6.13}$$

In Figure 6.4 the bond-slip curves are plotted for OPC concrete and GPC both having an average concrete compressive strength $f_{cm} = 38$ MPa. The influence of the improved ultimate bond strength τ_{bmax} is clearly visible. The bond stress at lower slip values is increased as well the bond stress at the sustained plateau and the final horizontal branch.
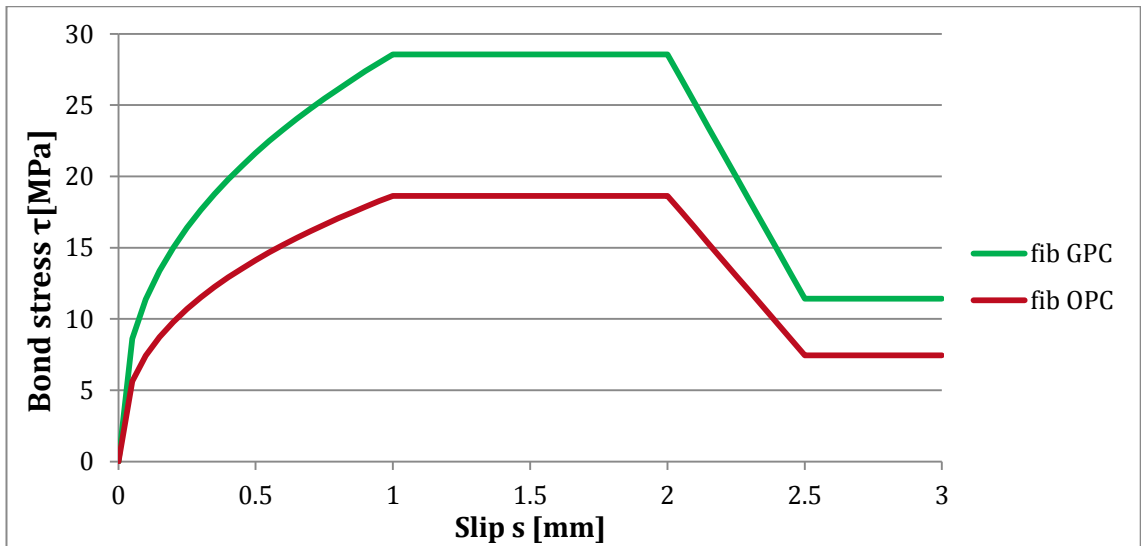
Figure 6.4 Bond-slip curves for OPC concrete and GPC. Based on the same concrete strength with f_{cm} = 38 MPa.

In section 6.5 the influence is studied of this improved bond strength for AAC and GPC concerning the crack-widths of a tensile member. The findings apply for the jointless concrete ground floor realised in AAC or GPC as well.

6.2.2 Shima bond-slip relation

In 1987 Shima et al. investigated the bond between steel and concrete. A constitutive model for bond behaviour has been formulated, the model includes the effects of the bar diameter and the concrete strength (Shima, Chou, & Okamura, 1987). Test results and bond-slip curves calculated by the Shima relationship are shown in Figure 6.5.
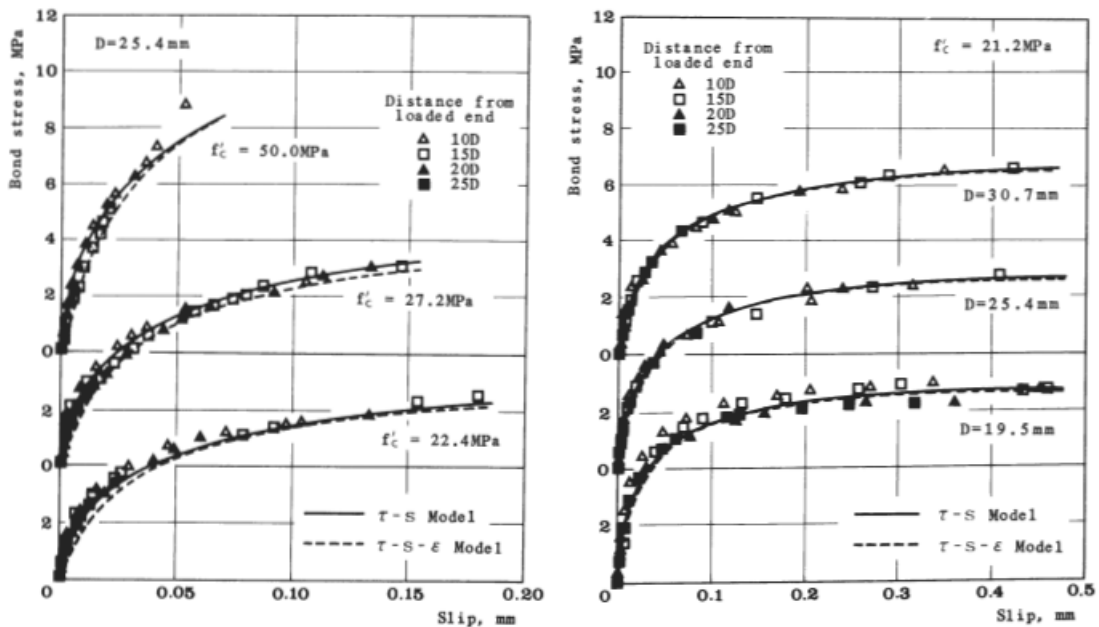
Figure 6.5 Bond-slip relationships with test results and predictions with the Shima relationship. Left: showing the effect of concrete strength. Right: showing the effect of bar diameter. Graphs taken from (Shima, Chou, & Okamura, 1987).

91

The bond-slip relationship Shima formulated agrees well with the experimental pull-out results under various values of the concrete strength and bar diameter. The Shima bond-slip relationship considering the effect of the bar diameter and the concrete strength is represented as:

$$\tau = 0.9 \ f_{cm}^{\frac{2}{3}}(1 - e^{-40s^{0.6}}) \tag{6.14}$$

where $\quad s = S/D$

In the above expression τ is the bond stress, f_{cm} the concrete strength, S is the slip and D the bar diameter. The bond-slip relation in accordance with Eq. (6.14) for a concrete strength of 28 and 38 MPa with bar diameters 8 and 16 mm are plotted in Figure 6.6.
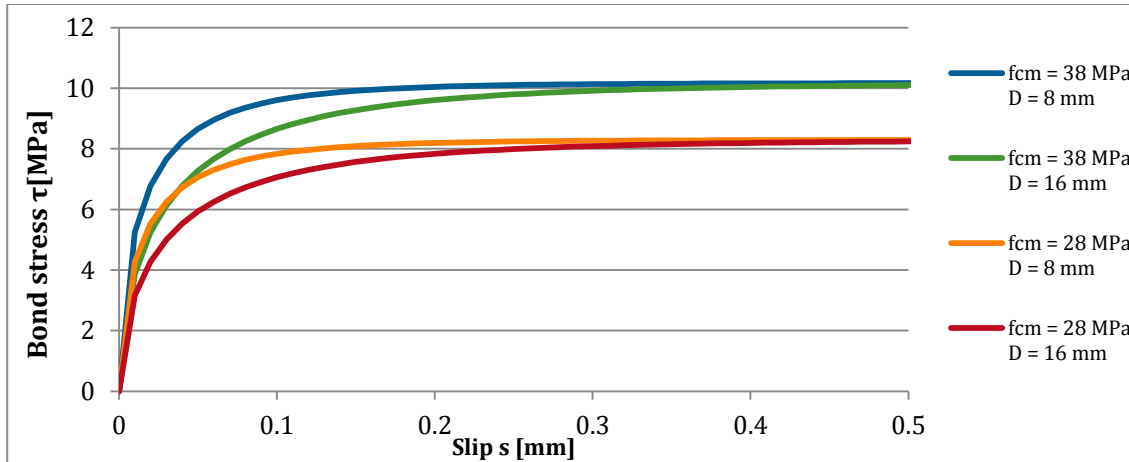

Figure 6.6 Bond-slip relationships for different concrete strengths and bar diameter.

This graph shows that smaller bar diameters reach the ultimate bond strength at lower slip values for the same compressive strength. This supports the well-known behaviour that smaller crack-widths are found when crack-widths are compared for similar reinforcement ratios but with different bar diameters. At lower slip values ($s \leq 0.2$ mm) smaller bar diameters provide higher bond stresses, according to the Shima bond-slip relation, and one can find lower crack-widths as a results.

6.3 Analytical and finite element analysis calculations

The mentioned bond-slip models of the fib Model Code 2010 and the Shima relation can be used to calculate crack-widths in a more accurate way compared to the simplified approach explained in section 6.1. The non-linear behaviour can be computed with analytical manners and with finite element analysis models. The former is done with Microsoft Excel spreadsheets and the latter with the FEA software program DIANA. In the following sections the spreadsheet's work process is explained and the tensile member that has been modelled in DIANA is introduced. The crack-width findings between the two will be evaluated and compared. Concrete tensile members are considered with a width and height of 100 mm and a length of 1000 mm, reinforced with one ribbed reinforcement bar.

There is some doubt around DIANA's accuracy for its crack-width calculations. Calculations in DIANA have been performed to study the non-linear behaviour and to compare it with theoretical computations, to try and shed some light on the idea whether this doubt is valid and if so for what reason.

6.3.1 Analytical crack-width calculation

The analytical calculation method that has been used is described here. The non-linear behaviour of the material in the discontinuity area for a cracked tensile member is studied with the fib and Shima bond-slip models. The non-linear behaviour is studied when the maximum crack-width within the crack formation stage is reached. The associated maximum steel stress σ_{sr} within the tensile member must be known. For the analytical manner this is calculated with the expression from Eq. (6.1). The following remaining properties must be specified in the Excel spreadsheet for the analytical calculation to be able to run.

The concrete compressive strength $f_{cm,}$ concrete tensile strength f_{ctm}, the moduli of elasticity for the concrete E_{cm} and the steel E_s and the steel reinforcement bar diameter ϕ are the input. The steel stress σ_{sr} is calculated beforehand, for the tensile member considered now this is done with Eq. (6.1). For bending the steel stress σ_s can be computed with manners described in chapter 3.4.2.

With the above parameters known and the expressions from section 6.1 the maximum steel stress of σ_{sr} and the steel stress at the undisturbed area σ_{se} are calculated. Through bond the difference in the steel stress, $\Delta\sigma_s = \sigma_{sr} - \sigma_{se,}$ will be reintroduced into the concrete over the transfer length l_t.

The analytical model starts its calculation from the equilibrium point where the strain of the concrete and the steel are the same, where the steel stress is $\sigma_{s,o} = \sigma_{se}$ and the concrete stress is equal to $\sigma_{c,o} = f_{ctm}$. The stress in the reinforcement increases to the maximum steel stress σ_{sr} at the crack location. Therefore, the steel stress is stepwise increased with a fraction $\Delta\sigma_{s,i}$ of $\Delta\sigma_s$. As the total force within the tensile member remains the same over all cross-sections, through equilibrium a new lower concrete stress $\sigma_{c,i}$ in the "second" cross-section is found. The "first" cross-section is considered where the slip is zero and the "final" cross-section is at the crack location. The new stresses $\sigma_{s,1}$ and $\sigma_{c,1}$ in this "second" cross-section are associated with new steel and concrete strains, which are no longer the same, so a strain difference $\Delta\varepsilon_1$ is formed. The difference in strain $\Delta\varepsilon_i$ results in the slip value s_i. This value s_i, is found when the strain difference $\Delta\varepsilon_i$ is multiplied with a length l_i, $s_i = \Delta\varepsilon_i \cdot l_i$. The length l_i is iteratively computed as this determines the slip s_i and from the slip value the bond stress $\tau_{b,i}$ is computed. The bond stress τ_b is calculated with either the fib bond-slip Eq. (6.11) or the Shima bond-slip Eq. (6.14). The length l_i of the first step is found iteratively when equilibrium is found between the steel stress increase $\Delta\sigma_{s,i}$ and the stress increase introduced by bond, as these two must be equal to each other. The latter is the second term in Eq. (6.15). The first analytical step is computed when the following expression is satisfied:

$$\Delta\sigma_{s,i} = \frac{\tau_{b,i} \cdot \pi \cdot \phi \cdot l_i}{A_s} \tag{6.15}$$

The slip values s_i add up for each step as the total slip increases over the transfer length with each step. The process is continued until all steps are computed and the steel stress $\sigma_{s,i}$ is increased to σ_{sr}. The summation of the slip values s_i is the total slip s and the slip value of the final step. This is the total slip between the reinforcement bar and the concrete at the crack location, on one side adjacent to the crack. The crack-width is computed by multiplying the slip s with two to find the maximum crack-width w_{max}. The summation of the lengths l_i is the anchorage length.

The coming figures show the computed data of the example tensile member. Reinforced with a $\phi = 10$ mm reinforcement bar and a concrete with a compressive strength of $f_{cm} = 38.0$ MPa, a modulus of elasticity $E_{cm} = 30.0$ GPa and a tensile strength $f_{ctm} = 3.0$ MPa. First the fib bond-slip model is applied in the example.

The maximum steel is the input at $\sigma_{sr} = 402.0$ MPa, the steel stress in the undisturbed area where the concrete and steel strain are equal follows as $\sigma_{se} = 20.0$ MPa. Figure 6.7 shows the strain values

in the discontinuity area adjacent to one side of the crack, computed with the analytical method and the fib bond-slip model from Eq. (6.11). At a distance of 0 mm the strains are equal, as explained this is where the model starts its stepwise calculation. With increased distance the steel strain gradually increases as the concrete strain decreases. The total distance covered in these graphs is the transfer length l_t, i.e. the anchorage length, and is l_t = 243.8 mm for this example. At this distance the crack is located and the concrete is strain is thus zero.
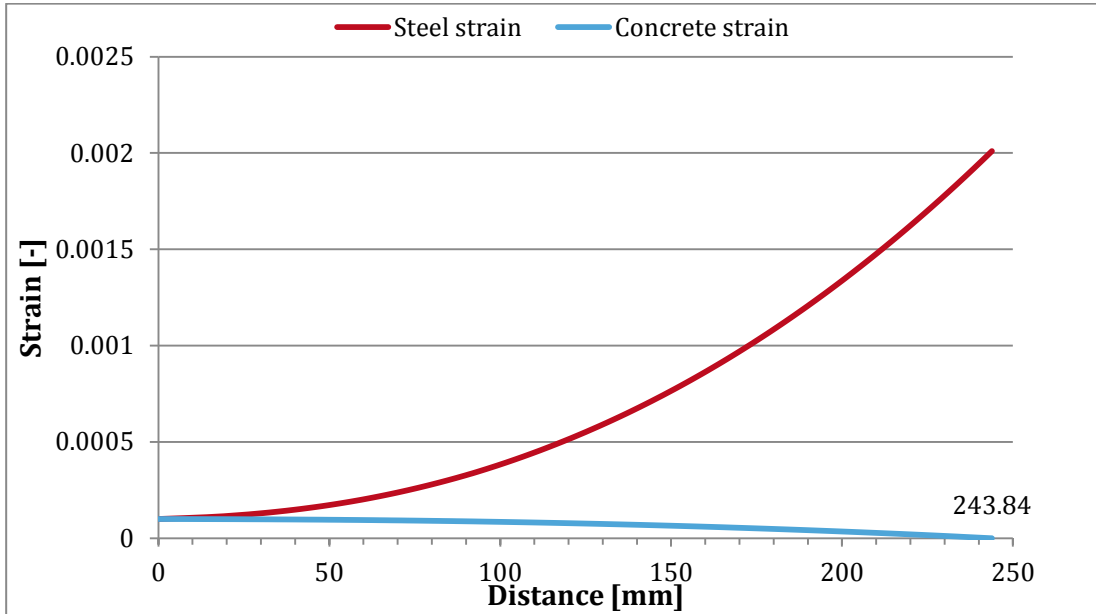
Figure 6.7 Strain progression of the concrete ε_c and steel ε_s within the discontinuity area adjacent to one side of the crack. Strains are equal at L = 0 mm and at the crack location, L = 243.8 mm, the concrete strain is zero. The distance 234.8 mm is the total anchorage length. Computed with the fib bond-slip model.
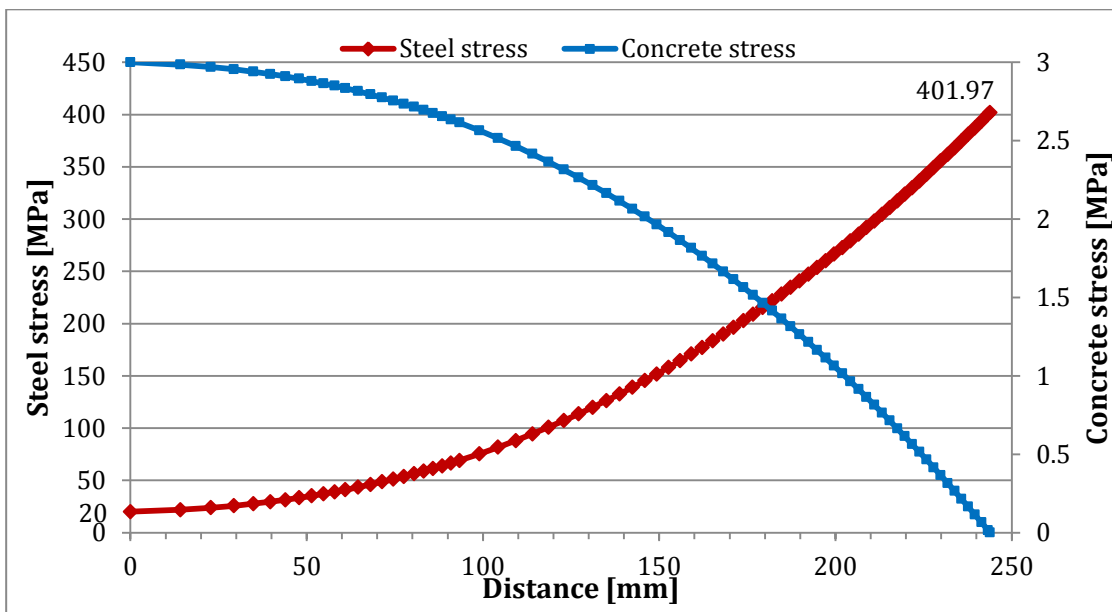
Figure 6.8 Non-linear steel stress σ_s and concrete steel σ_c over the transfer length. The maximum steel stress is σ_{sr} = 402.0 MPa at the crack location where L = 244 mm, at L = 0 mm the steel stress is equal to σ_{se} = 20.0 MPa. At L = 0 the concrete stress is equal to the tensile strength f_{ctm} and at the crack location the concrete stress is zero. Computed with the fib bond-slip model.

Figure 6.8 displays the associated steel and concrete stresses. The non-linear progression of the stresses is clearly visible, where the maximum steel stress σ_{sr} is reached at the crack location where the concrete stress is zero.

The increase of the slip s is visible in the graph of Figure 6.9. The increase of the slip is related to the increase of the difference between the strains of the concrete and steel from Figure 6.7. The slip between the steel reinforcement bar and the concrete at the crack location is s = 0.23 mm, this slip behaviour occurs, adjacent on the other side of the crack as well, so the total slip between the reinforcement bar and the concrete in the discontinuity area is two times this value. The maximum crack-width value for the crack formation stage w_{max} = 0.46 mm is found.

Figure 6.9 Build-up of the slip s over the transfer length. The maximum slip at L = 244 mm, the crack location, is s = 0.23 mm. Computed with the fib bond-slip model.

In Figure 6.10 the development of the bond stress τ_b over the transfer length is computed. The non-linear development is related to the development of the slip s values. For this case the maximum bond stress at the crack location is found at τ_b = 8.6 MPa, which for the fib bond-slip relation translates to the slip found s = 0.23 mm. There where the strains are equal and no slip between the reinforcement bar and concrete occurs there are no bond stresses generated.

Figure 6.10 Development of bond stresses over the transfer length. The maximum bond stress is found at L = 243 mm, the crack location, and is τ_b = 8.6 MPa. Computed with the fib bond-slip model.

In the next four figures, the graphs display the results for the same example but computed with the Shima bond-slip relation. The non-linear strain and stress development of the steel and concrete are very similar as with the fib bond-slip model. The Shima model predicts higher bond stresses at low slip values compared to the fib model. Because of that the Shima model computes a smaller crack-width and a smaller anchorage length. The different bond stress development can be seen in Figure 6.14. The anchorage length l_t = 174.2 mm and the crack-width found is w_{max} = 0.34 mm.
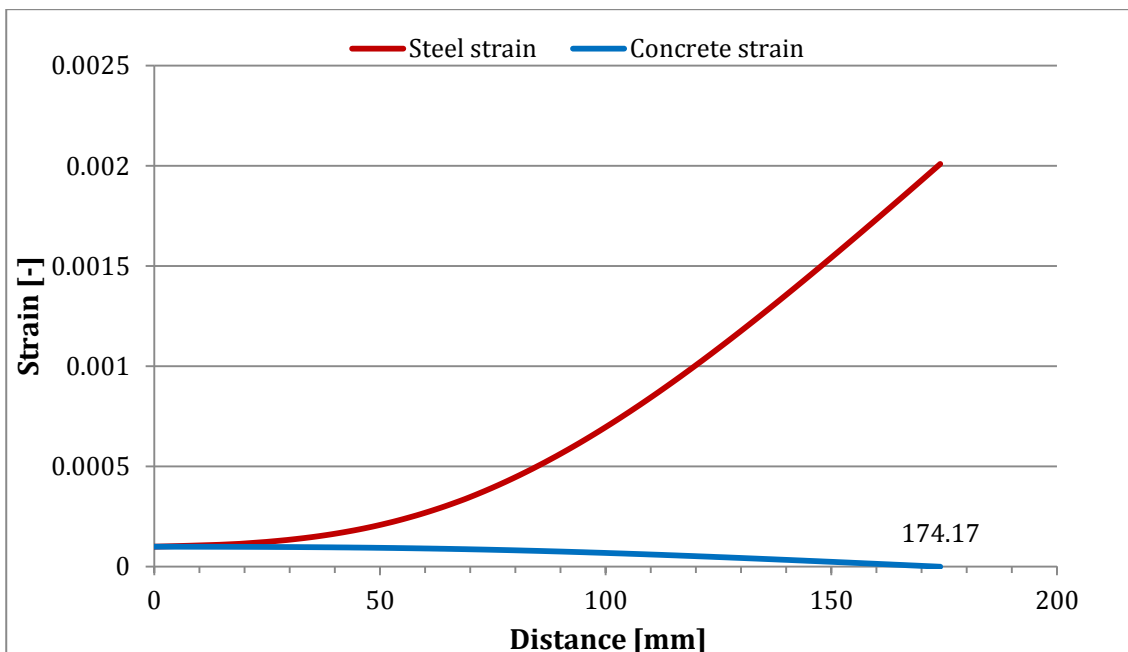
Figure 6.11 Strain progression of the concrete ε_c and steel ε_s within the discontinuity area adjacent to one side of the crack. Strains are equal at L = 0 mm and at the crack location, L = 174.2 mm, the concrete strain is zero. The distance 174.2 mm is the total anchorage length. Computed with the Shima bond-slip model.
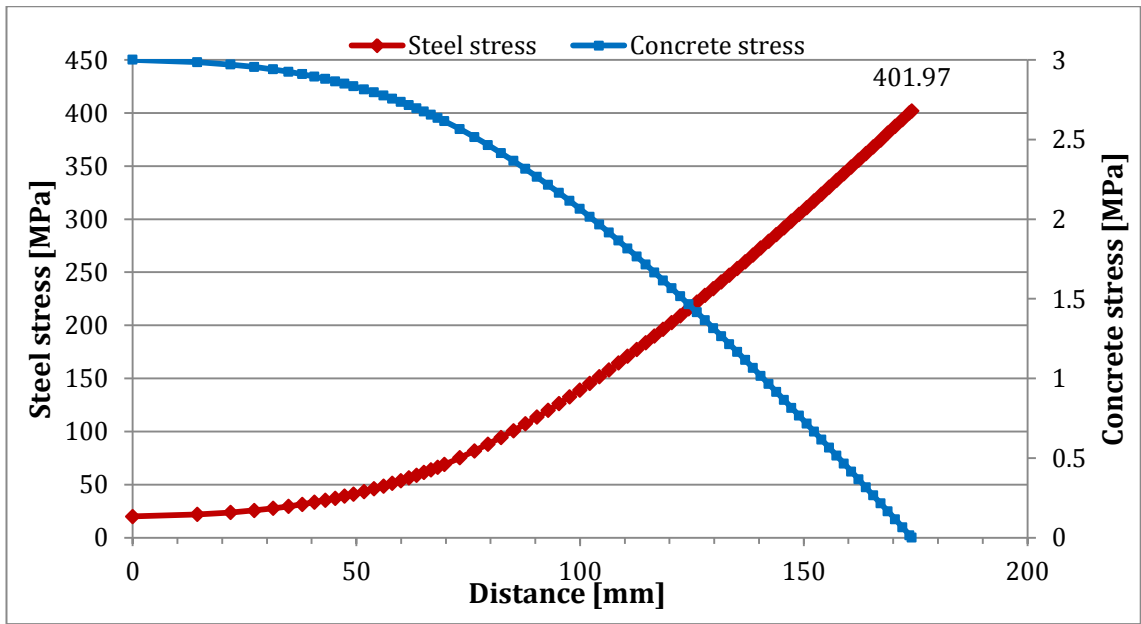
Figure 6.12 Non-linear steel stress σ_s and concrete steel σ_c over the transfer length. The maximum steel stress is σ_{sr} = 402.0 MPa at the crack location where L = 174 mm, at L = 0 mm the steel stress is equal to σ_{se} = 20.0 MPa. At L = 0 the concrete stress is equal to the tensile strength f_{ctm} and at the crack location the concrete stress is zero. Computed with the Shima bond-slip model.
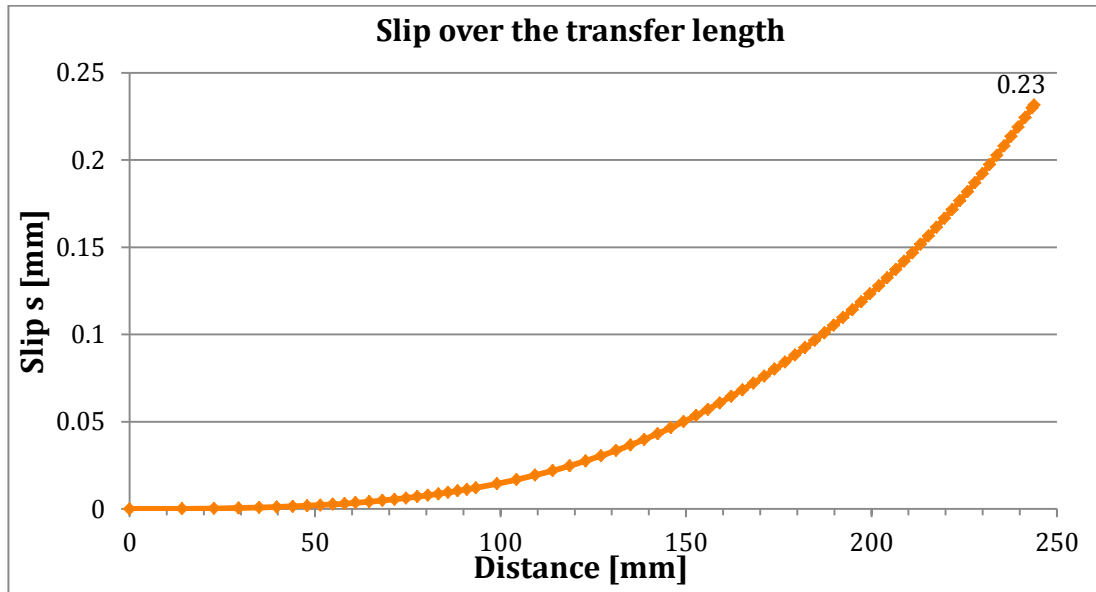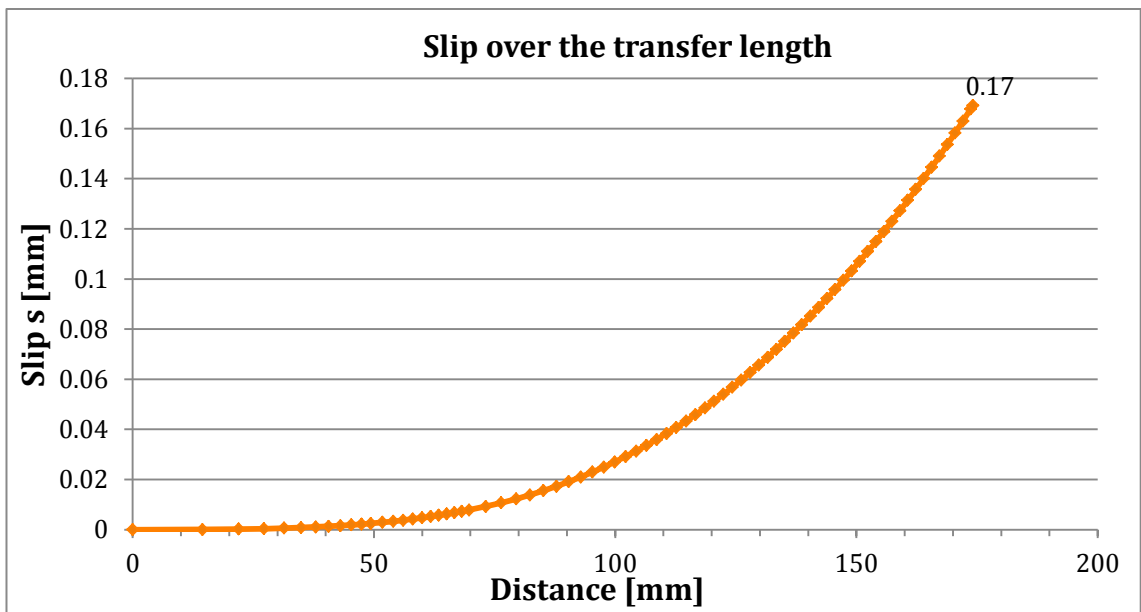

Figure 6.13 Build-up of the slip s over the transfer length. The maximum slip at L = 174 mm, the crack location, is s = 0.17 mm. Computed with the Shima bond-slip model.
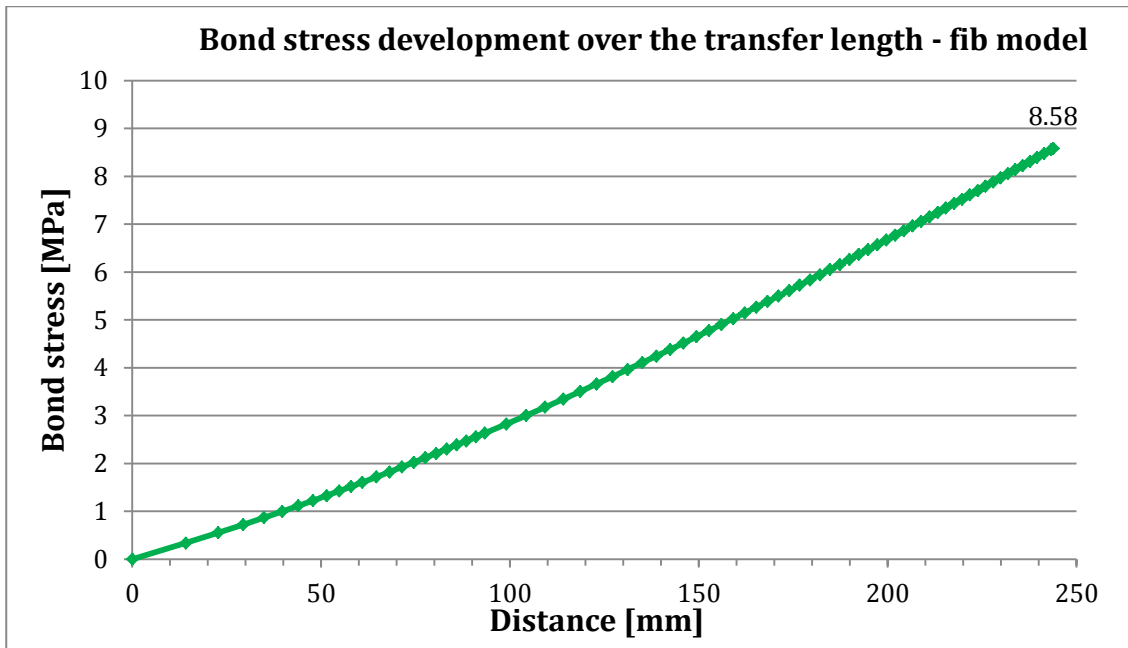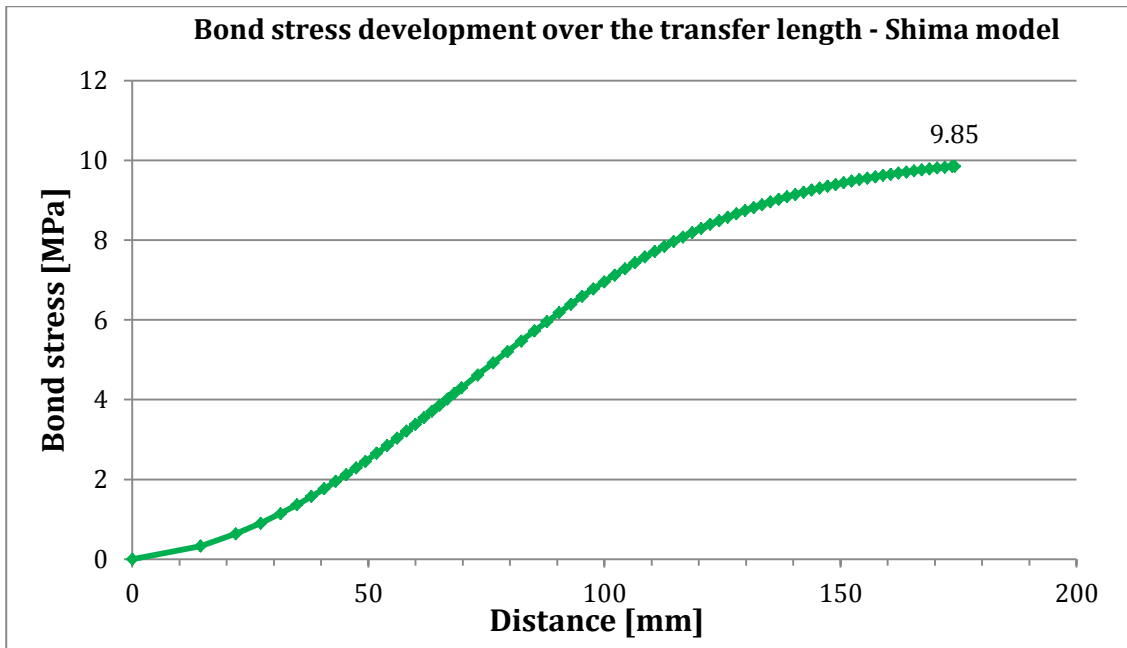
Figure 6.14 Development of bond stresses over the transfer length. The maximum bond stress is found at L = 174 mm, the crack location, and is τ_b = 9.9 MPa. Computed with the Shima bond-slip model.

A multiple number of analytical bond-slip calculations is done this way. In the next sections not all associated graphs are reported, but for some cases just the output value. The computed output values of significance are the total slip s, the maximum bond stress at the crack location and the anchorage length l_t.

6.3.2 DIANA model

The reinforced tensile member has been modelled in DIANA to study the non-linear behaviour and make comparisons of the output with the theory. A structural two dimensional model with regular plane stress elements has been made. The cracking behaviour has been studied with discrete cracking interfaces in the geometry. The reinforcement bar is modelled as a wire with bond-slip interfaces, both with the fib and Shima bond-slip models. The mid sections of the outer edges are clamped, where the remainder of the edge is connected via tying's to the clamped node at the mid-section. The member is loaded on the right by a prescribed deformation to force stresses and crack formation into the model.

The complete model and its geometry is shown in Figure 6.15. A multiple amount of discrete cracking interfaces has been applied so the formation of multiple cracks is possible. The first crack is modelled to appear exactly in the middle of the tensile member, which is forced by providing this discrete interface with the lowest concrete tensile strength. In the example a concrete with a tensile strength of f_{ctm} = 3.0 MPa is considered, the interface at the middle here is therefore modelled with a tensile strength of f_{ctm} = 2.9 MPa. Realistically, a concrete tensile member will crack at the location where the lowest tensile strength is found, which is here forced to occur at the interface located in the middle part of the member. The other discrete interfaces have a tensile strength of f_{ctm} = 3.0 MPa. This same approach has been done with other DIANA models when alkali-activated concrete with higher tensile strengths were considered.

The prescribed displacement forces the first crack at mid interface after which tensile force will drop. Further increasing the load factor increases the stresses in the member again, up to the point where the concrete tensile strength is reached again and a new crack will form. Just before the second crack forms in the model, the steel stress in reinforcement bar is at its maximum and

the crack-width in the open discrete interface will be at its maximum. This is point at which the non-linear behaviour of the model is studied and compared with the theoretical non-linear behaviour computed with the analytical manner.

Displacement controlled structural nonlinear analyses have been done. The Newton-Raphson method has been applied with the maximum number of iterations at 50. The convergence norm that had to be satisfied was either the displacement norm or the force norm with a tolerance of 0.01. If no convergence was found the analysis was terminated. Larger load steps were applied during linear material behaviour and small load steps have been applied before and after the tensile stresses were reaching the tensile strength of the concrete.
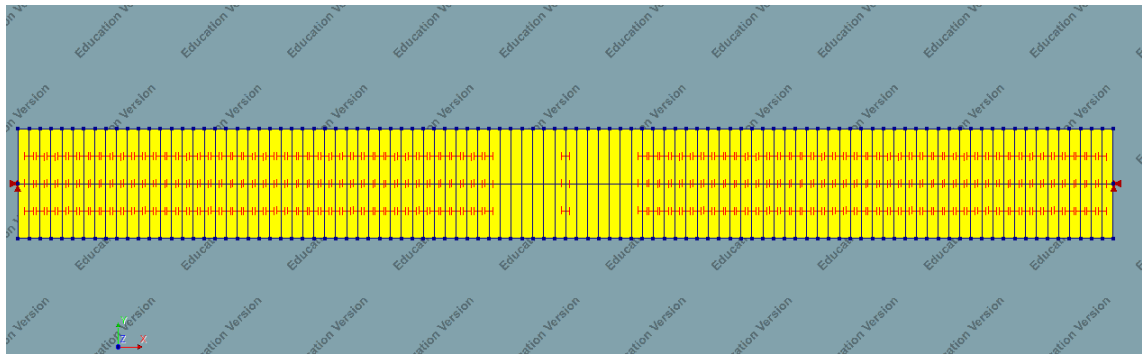
Figure 6.15 The geometry of the 2D tensile member. Length = 1000 mm, height = 100 mm and thickness = 100 mm. The horizontal line through the middle represents the reinforcement wire. The vertical lines with red tags are discrete interfaces, of which the middle has a slightly reduced tensile strength. The outer vertical edges are clamped.

The mesh for the model that worked best is shown in Figure 6.16. Different mesh sizes and element types, being linear and quadratic, were applied. The mesh used consists of elements sizes 5 mm and 1 mm, the larger value is applied over the vast majority of the model where the small mesh is applied around the mid-section where the first crack occurs. With this small mesh size DIANA was able to compute the most accurate steel stresses within the crack.
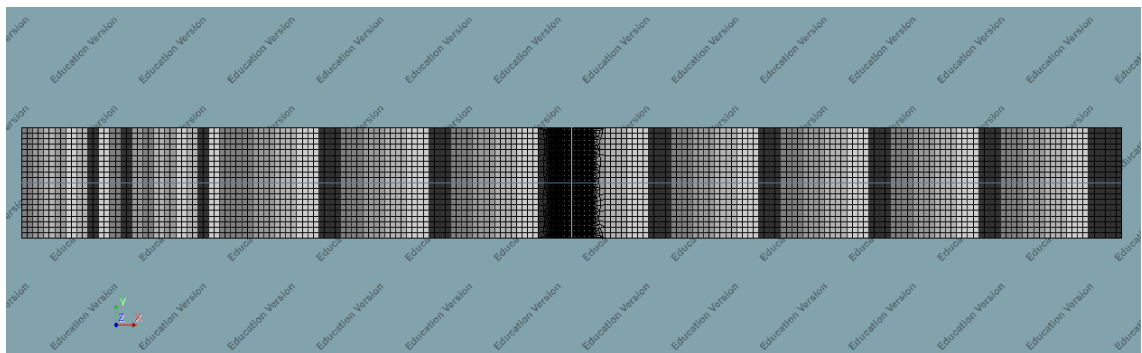
Figure 6.16 The mesh of the 2D tensile member. A very fine mesh, element size 1 mm, is applied at the first crack location at the middle of the member is applied. Other mesh elements size is 5 mm.

Overall linear elements have been applied. Quadratic elements, both with mid node calculation by linear interpolation and on shape, have been computed as well. The corresponding results showed a limited increase in accuracy, but required a much longer calculation time to converge. The same principle was found with increased dummy stiffness values for the discrete interfaces and the bond-slip interface. For which normally high normal- and shear stiffness modulus values are applied. Models with even higher dummy stiffness values computed steel stresses that were a bit more in line with the theory but were also coupled with a much longer computing time.

The maximum crack-width within the crack formation stage is found right before the second crack occurs. The next two graphs can be compared with the load-strain graph in Figure 6.2.

99

Here, in Figure 6.17, the reaction force N from the right support is displayed on the vertical axis. The first crack occurs just above the 30000 N, which in this case is $N_{cr,1}$ and at a load factor of 1.00. The load step that is analysed is the one at $N_{cr,2}$, right before the second crack is formed and before the force N drops again. In this example the second crack is formed at a load-factor 4.4 which is at load step 59. The crack-width is thus studied at load step 58, where the concrete tensile stress reaches the tensile strength to its nearest and the maximum crack-width is found. Figure 6.18 displays the same increase of the load factor but with the tensile stress development of the undisturbed concrete on the vertical axis.
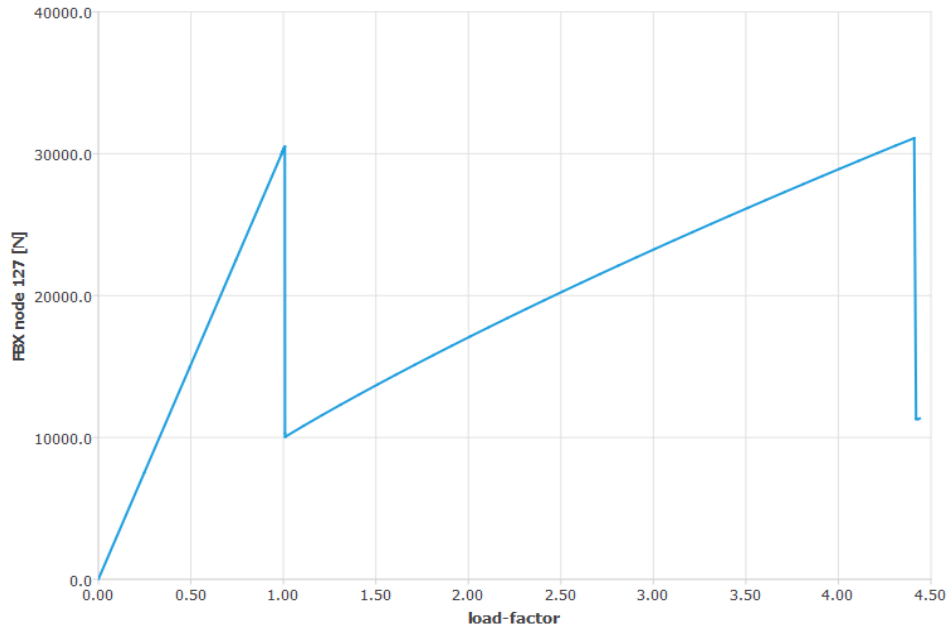
Figure 6.17 Load-displacement diagram. The load-factor is related to the prescribed displacement. The second crack is formed at load-factor 4.4.
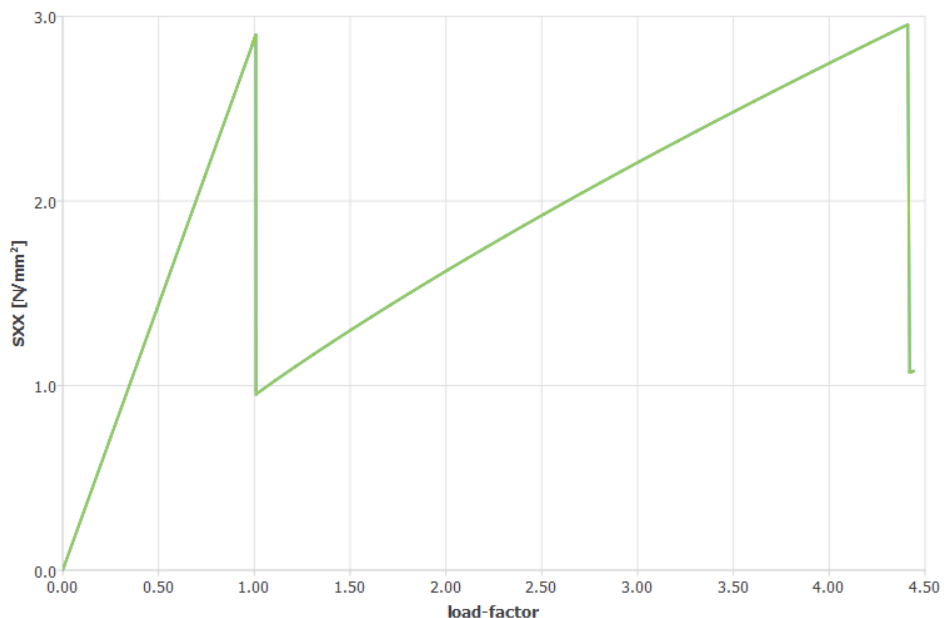
Figure 6.18 Concrete stress SXX development with increasing displacement. The load-factor is related to the prescribed displacement.

The above and following figures are associated to the same example tensile member as before. Reinforced with a $\phi = 10$ mm reinforcement bar and a concrete with a compressive strength of $f_{cm} = 38.0$ MPa, a modulus of elasticity $E_{cm} = 30.0$ GPa and a tensile strength $f_{ctm} = 3.0$ MPa. The fib bond-slip model is applied in the example.
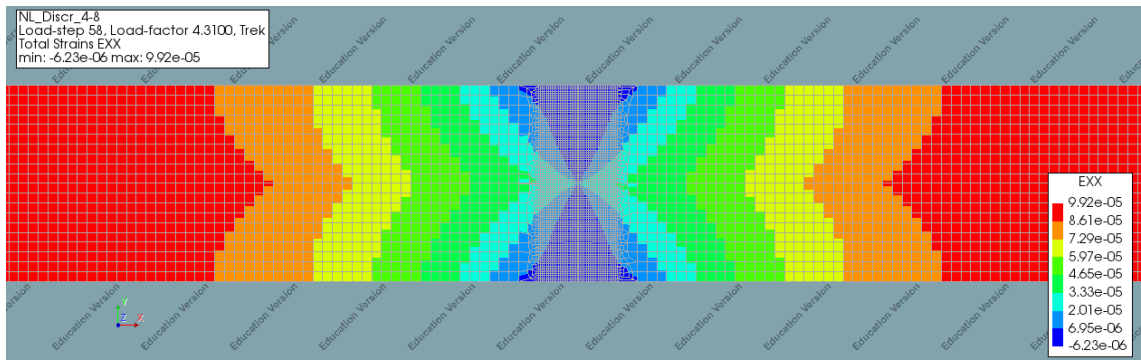
Figure 6.19 Concrete element strains, EXX, in the discontinuity area right before a new crack is formed.
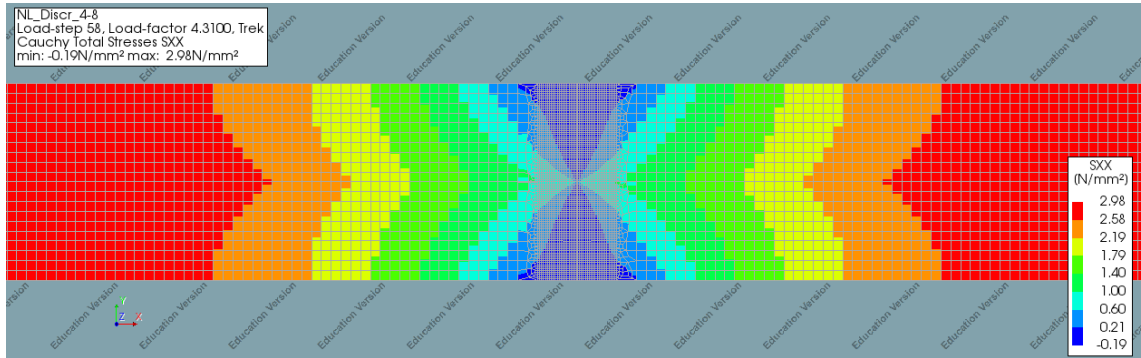
Figure 6.20 Concrete element stresses, SXX in MPa, in the discontinuity area right before a new crack is formed.
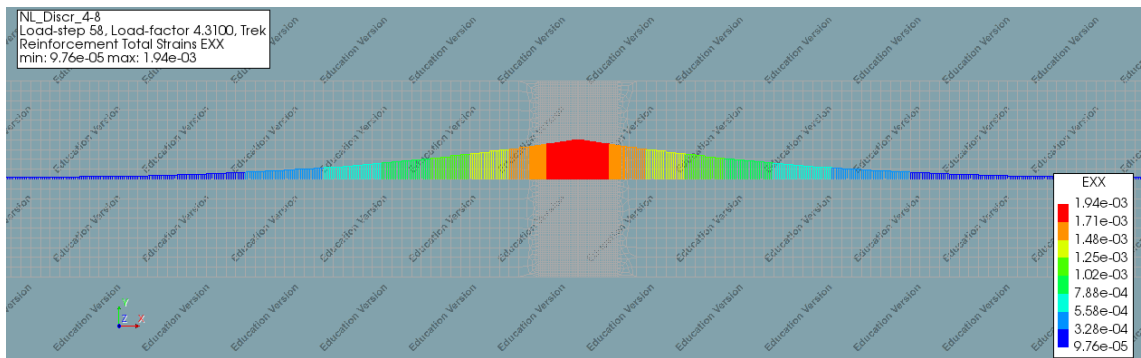
Figure 6.21 Reinforcement steel strain, EXX, development in the discontinuity area right before a new crack is formed.
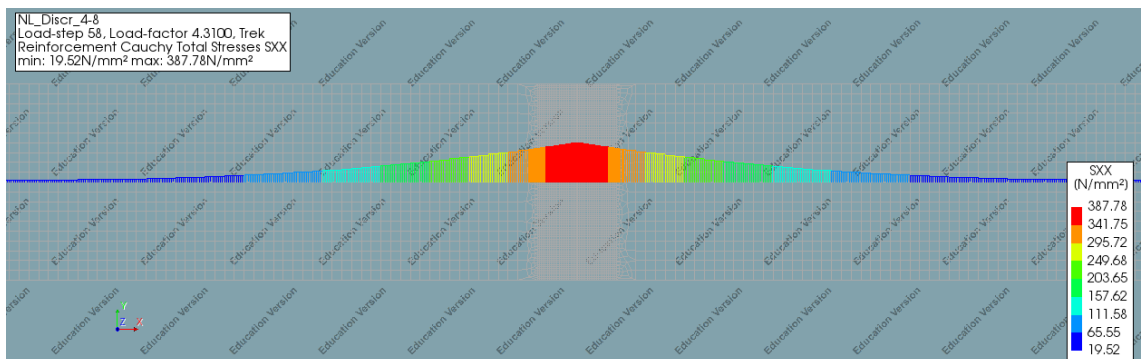
Figure 6.22 Reinforcement steel stress, SXX in MPa, development in the discontinuity area right before a new crack is formed.
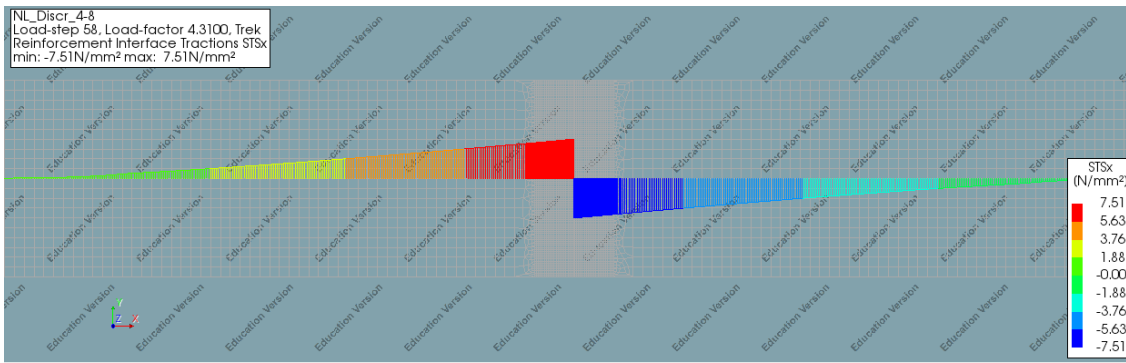
Figure 6.23 Reinforcement interface traction, STSx in MPa, in the discontinuity area right before a new crack is formed. Interface tractions are the same as the bond stresses.
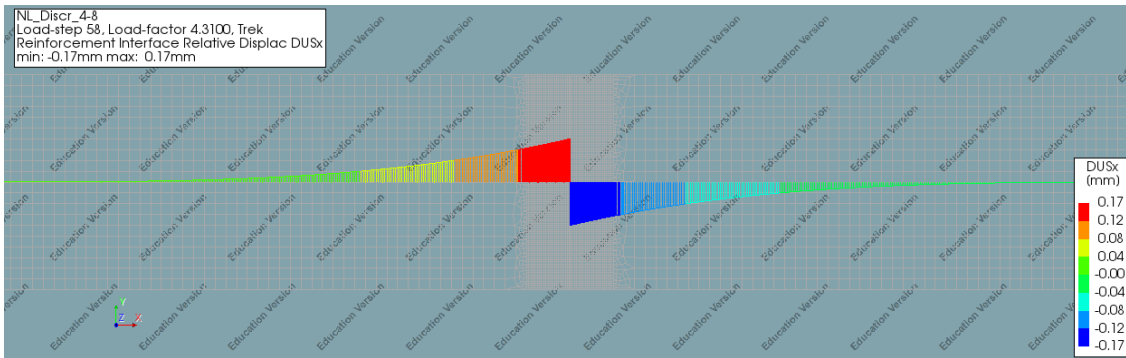
Figure 6.24 Reinforcement interface relative displacement, DUSx in mm, in the discontinuity area right before a new crack is formed. The interface relative displacement is the same as the slip.
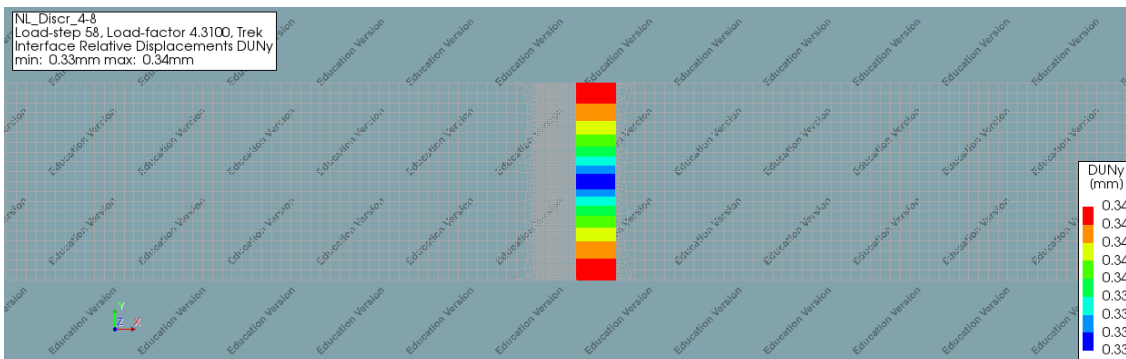
Figure 6.25 Crack-width opening, DUNy in mm, of the initial crack right before a new crack is formed.

In the previous figures, that display the graphical DIANA output, some output values are seen that slightly differ from the theoretical values calculated. A small difference is found in Figure 6.20, the tensile stress of the concrete σ_c = 2.98 MPa at which the crack-width is studied, it is not exactly the tensile strength of f_{ctm} = 3.0 MPa.

The maximum steel stress, in Figure 6.22, is found at σ_s = 387.8 MPa, which is at 97% of the value for the theoretical maximum steel stress of σ_{sr} = 400.2 MPa. The fact that a fraction of the tensile stress in the concrete is lower and that the concrete elements directly adjacent to the steel within the crack carry a tiny tensile stress, instead of being zero, explains this small difference in the maximum steel stress found. The fine mesh allows for the steel stress σ_s to be this close to σ_{sr}.

More significant differences are found, compared to the analytical calculated values, for the bond stress development and the associated slip values along the transfer length in Figure 6.23 up to Figure 6.25. The DIANA calculation finds a maximum bond stress at the crack location of τ_b = 7.5 MPa with a total slip of s = 0.17 mm, resulting in the maximum crack-width of w_{max} = 0.34 mm.

6.4 Comparison (non-) linear crack-width calculations

In sections 6.1 to 6.3 the methods for the linear and non-linear crack-width calculation have been explained. In this section the results are compared considering the different bond stress-slip models and the way they have been computed. Initially the different bond-stress behaviour is studied and the differences of the computed crack-widths between them are explained. Then the differences between the analytical non-linear crack-width calculations are compared with the FEA results computed in DIANA.

The comparisons are made from results of calculations done on the example concrete, which from now on is labelled as OPC38, and the geopolymer concrete EFC which is labelled as GPC55. Their concrete material properties are shown in Table 6-3.

Table 6-3 Concrete material properties of the concretes OPC38 and GPC55.

Property	OPC38	GPC55	Unit
Compressive strength f_{cm}	38.0	55.6	MPa
Tensile strength f_{ctm}	3.0	6.0	MPa
Young's modulus E_{cm}	30.0	38.5	GPa

6.4.1 Bond stress differences

The bond-slip models that have been introduced have different bond stress-slip developments. For the simplified method the bond stress in the discontinuity area is assumed to be constant and for shrinkage induced loads equal to 1.6 times the tensile strength f_{ctm}. In Figure 6.26 and Figure 6.27 the bond stress τ_b is shown constant for all slip values, plotted in green and labelled as EC2. For OPC38 the constant bond stress is $\tau_b = 4.8$ MPa and for GPC55 it is $\tau_b = 9.6$ MPa.

The fib bond-slip model has an ascending branch up to 1 mm slip, where the bond stress increase for the Shima bond-slip model stagnates around a slip of 0.5 mm. As the crack-widths considered for the jointless floor must remain below the maximum allowable crack-width of $w_d = 0.3$ mm, the horizontal axis for the bond-slip graphs are limited to the maximum associated slip $s = 0.15$ mm.

A clear difference is found between the two bond-slip models when the fib bond-slip relation is plotted together with the Shima bond-slip relation. The Shima relation computes higher bond stresses at lower slip values, especially with lower bar diameters when the initial bond stress development would be even higher.
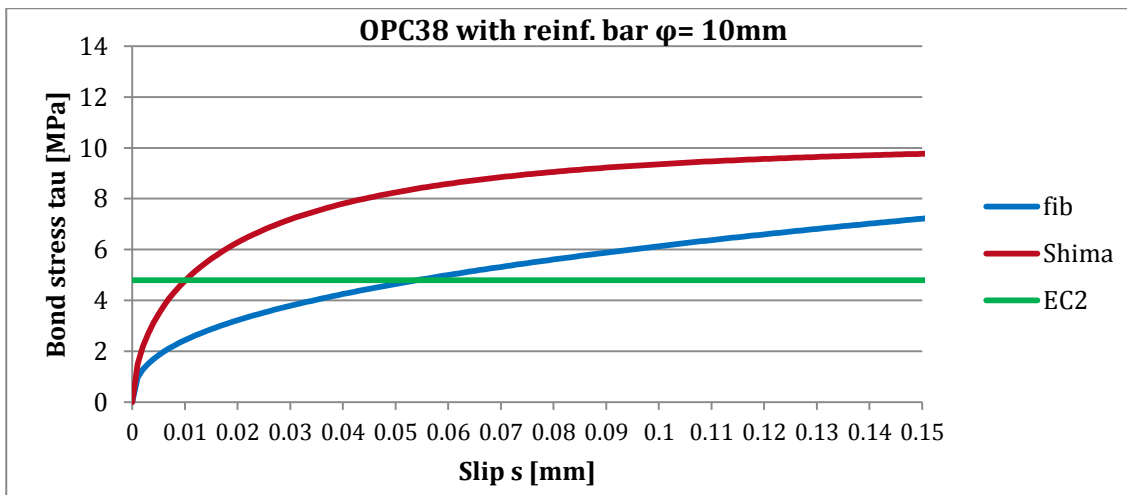
Figure 6.26 Bond stress-slip development for OPC38 with different bond-slip models.

For a ribbed reinforcement bar to be pulled out of the concrete work is required, according to the Shima relation the work required is higher when compared to the fib relation. This means that with the Shima model the steel stress will be reintroduced into the concrete over a shorter distance, a shorter anchorage length is the result. This shorter anchorage length and increase of required work for slip to occur, results in a reduced total slip value. Thus the Shima bond-slip relation computes lower crack-widths when compared to the fib bond-slip relation.

In chapter 3 section 3.4.1 it was mentioned that the bond strength is one of the important concrete parameters for crack-width control, as the bond strength defines the strain difference that occurs between the steel and the concrete. The above explains why this is, with a better bond strength the bond stresses developed at lower slips values will be higher and thus reduce the total slip, i.e. the total strain difference between the steel and concrete is lower. Therefore, an improved bond strength results in lower crack-widths.

The results computed with the simplified method, the analytical method and the FEA in DIANA ,for the OPC38 tensile member reinforced with a bar of φ = 10 mm, are shown in the following tables. The results with the fib bond-slip relation are shown in Table 6-4 and the results computed with the Shima relation in Table 6-5. The maximum steel stress σ_{sr} for the simplified and analytical method are part of the input, the DIANA steel stress displayed is the computed steel stress. The steel stresses found of around 400 MPa are relatively high and not preferable in practice considering the SLS. However, for this theoretical study these high steel stresses aren't an issue.

The crack-widths from the Shima model are, for both methods, lower compared to the crack-widths computed with the fib model. DIANA computes lower crack-widths compared to the analytical method. DIANA finds a lower maximum bond stress at the crack location and thus a lower crack-width. This is further assessed in section 6.4.2.

Table 6-4 Steel and bond stress at crack location and the computed crack-widths for concrete OPC38 with a reinforced bar diameter of ϕ = 10 mm. Non-linear behaviour computed with the fib bond-slip relation.

Method	Steel stress σ_{sr} [MPa]	Max bond stress τ_b [MPa]	Crack-width w [mm]
Simplified	400.2	Constant 4.8	0.40
Analytical – fib	400.2	8.52	0.45
DIANA - fib	387.8	7.5	0.34

Table 6-5 Steel and bond stress at crack location and the computed crack-widths for concrete OPC38 with a reinforced bar diameter of ϕ = 10 mm. Non-linear behaviour computed with the Shima bond-slip relation.

Method	Steel stress σ_{sr} [MPa]	Max bond stress τ_b [MPa]	Crack-width w [mm]
Simplified	400.2	Constant 4.8	0.40
Analytical – Shima	400.2	9.83	0.33
DIANA – Shima	384.3	9.49	0.22

The well-known fib Model Code 2010 provides the accepted simplified method to calculate the crack-widths in a direct manner. This same well-known work provides the fib bond-slip relation, which is able to imitate the material behaviour in a more realistic manner and thus computes crack-widths more precise when compared to the direct simplified manner. Comparing the two, in Table 6-4, the bond-slip manner finds for this example a slightly larger crack-width. The analytical manner finds a crack-width w = 0.45 mm compared to w = 0.40 mm found with the simplified method, the difference is 12.5%. The Shima relation computes lower crack-widths as expected when compared to the fib-relation, see Table 6-5.

The same difference between the fib- and Shima relation is found for higher concrete strength grades with a higher compressive strength. The plotted bond stress-slip for GPC55 in Figure 6.27 shows that the difference in bond stress is similar at low slip values for the Shima relation compared to the fib relation. This Shima bond-slip relation is defined by the compressive strength and the bar diameter where the fib bond-slip relation is defined just by the compressive strength. The difference between the bond stress for GPC55 would be higher when the Shima relation were plotted with a reduced bar diameter for the displayed slip values.
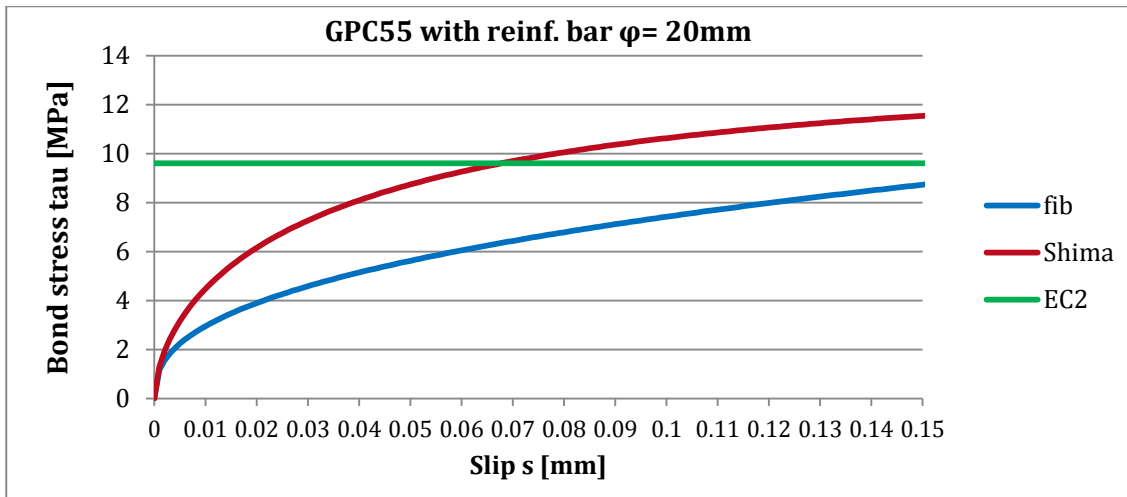
Figure 6.27 Bond stress-slip development for GPC55 with different bond-slip models.

What is more compelling in this bond stress-slip graph, is that when one were to calculate the crack-width for such a high tensile strength concrete only with the simplified method, one would overestimate the bond stress when assuming the constant value. The simplified method is derived from the fib Model Code 2010 and when compared to the fib bond-slip relation of this same fib Model Code 2010, one can find a significant difference between the computed crack-widths. The constant assumed bond stress EC2 has a bond stress that is higher for all slip values, at least for the considered slip values $s \leq 0.15$ mm, compared to the fib bond stress-slip relation. In Figure 6.27 the fib relation, the blue line, remains below the bond stress EC2, the green line, for all displayed slip values.

The results for GPC55 are given in Table 6-6 and Table 6-7. The principle explained above is seen when the calculated crack-width of the simplified method $w = 0.11$ mm is compared to the more accurately calculated crack-width $w = 0.26$ mm. A quite big difference is found here, where for OPC38 the difference was just 12.5%, here the difference for GPC55 is 236%.

Comparing the Shima computed crack-widths to the fib computed crack-widths, lower values are found again. For GPC55 DIANA computes lower maximum bond stresses at the crack location as well and finds lower crack-widths.

Table 6-6 Steel and bond stress at crack location and crack-widths for concrete GPC55 with a reinforced bar diameter of $\phi = 20$ mm. Non-linear behaviour computed with the fib bond-slip relation.

Method	Steel stress σ_{sr} [MPa]	Max bond stress τ_b [MPa]	Crack-width w [mm]
Simplified	222.16	Constant 9.6	0.11
Analytical – fib	222.16	8.27	0.26
DIANA - fib	220.01	7.31	0.20

Table 6-7 Steel and bond stress at crack location and crack-widths for concrete GPC55 with a reinforced bar diameter of $\phi = 20$ mm. Non-linear behaviour computed with the Shima bond-slip relation.

Method	Steel stress σ_{sr} [MPa]	Max bond stress τ_b [MPa]	Crack-width w [mm]
Simplified	222.16	Constant 9.6	0.11
Analytical – Shima	222.16	10.59	0.20
DIANA - Shima	218.97	9.63	0.14

6.4.2 Comparison of non-linear behaviour

When comparing the analytical computed results with the DIANA results the crack-widths found are lower. Where DIANA is able to compute the maximum steel stress in the crack formation stage quite accurately, the associated crack-widths found aren't in line with the theoretical values. The non-linear material behaviour of the concrete and steel within the discontinuity area is compared between the analytical method and the FEA done in DIANA. The results that are being compared here are computed as explained in section 6.3.1 and 6.3.2.

The steel and concrete stresses, as well as the strains, computed with DIANA are almost the same when compared to the theoretical values computed analytically. In the next section the DIANA output and the analytical output are plotted on the same graphs for the comparison between the two. The results computed in the analytical way according to section 6.3.1 are labelled as Theory and the DIANA output computed in accordance with section 6.3.2 is labelled as DIANA in the coming figures.

For the following graphs the distance along the left side of the discontinuity area is plotted on the horizontal axis. The crack-location studied is in the middle of the tensile member, which is of 1000 mm total length, thus the stresses and strains at the location of the crack are displayed at the distance L = 500 mm in the following figures.

6.4.2.1 Stress and strain comparison

The steel stress development over the discontinuity area for OPC38 is plotted in Figure 6.28, the results are computed with the fib bond-slip model. The theoretical found anchorage length is $l_t = 243$ mm. As the crack is located at L = 500 mm, the steel stress is equal to σ_{se} at L = 500 - 243 = 257 mm. The maximum steel stress is found at the crack-width location (L = 500 mm) and is equal to $\sigma_{sr} = 400.2$ MPa. The DIANA output has the maximum steel stress at the same location at a value of $\sigma_{sr} = 387.8$ MPa. The stress development of the two methods is almost equal, so DIANA is able to compute the steel stress quite accurately.
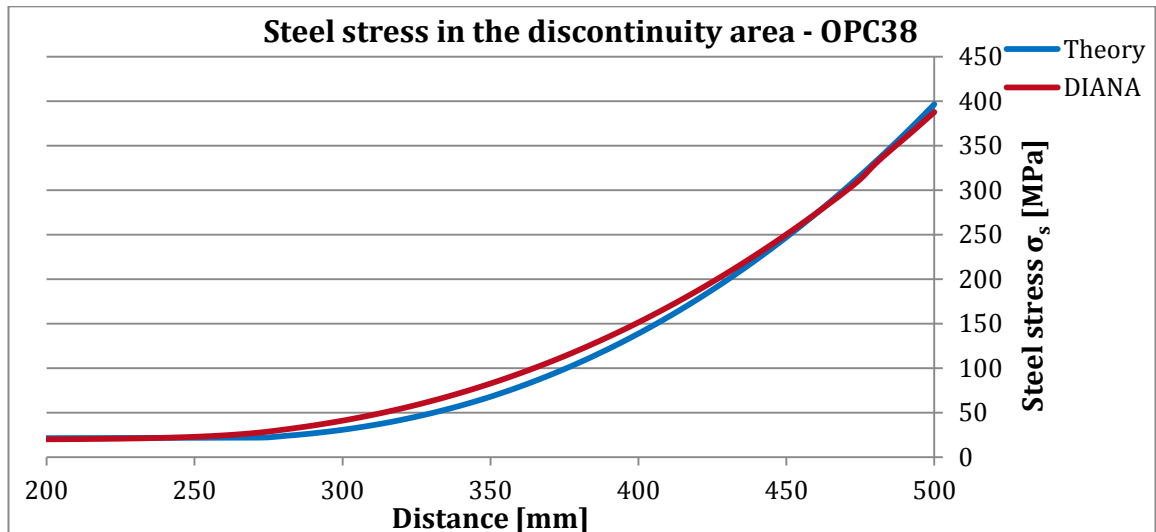
Figure 6.28 Steel stress σ_s development within the discontinuity area plotted from the analytical method and from the DIANA output. Theoretical maximum stress $\sigma_{sr} = 400.2$ MPa and DIANA maximum steel stress $\sigma_s = 387.8$ MPa. The steel stress where no slip occurs from theory is $\sigma_{se} = 20.0$ MPa and in DIANA the steel stress found is $\sigma_{se} = 19.5$ MPa.

Figure 6.29 plots the strain progression of the steel and concrete within the discontinuity area. The strains area equal, or really close to equal, for L ≤ 257 mm which is outside the disturbed area where no slip occurs. A small difference between steel strain is seen which is similar to small

difference to the steel stress from Figure 6.28. The concrete strains are computed accurately with DIANA with close to no difference. However, as the steel stress and the strains seem to be computed closely to the theoretical values with DIANA, the computed crack-widths are for all studied cases underestimated. Figure 6.30 displays the slip development over the transfer length and it is clearly visible that the analytically computed slip values increases more, further towards the crack location, resulting in a higher total slip and thus a larger crack-width. These differences in slip values are found when the bond stress development is plotted next to each other.
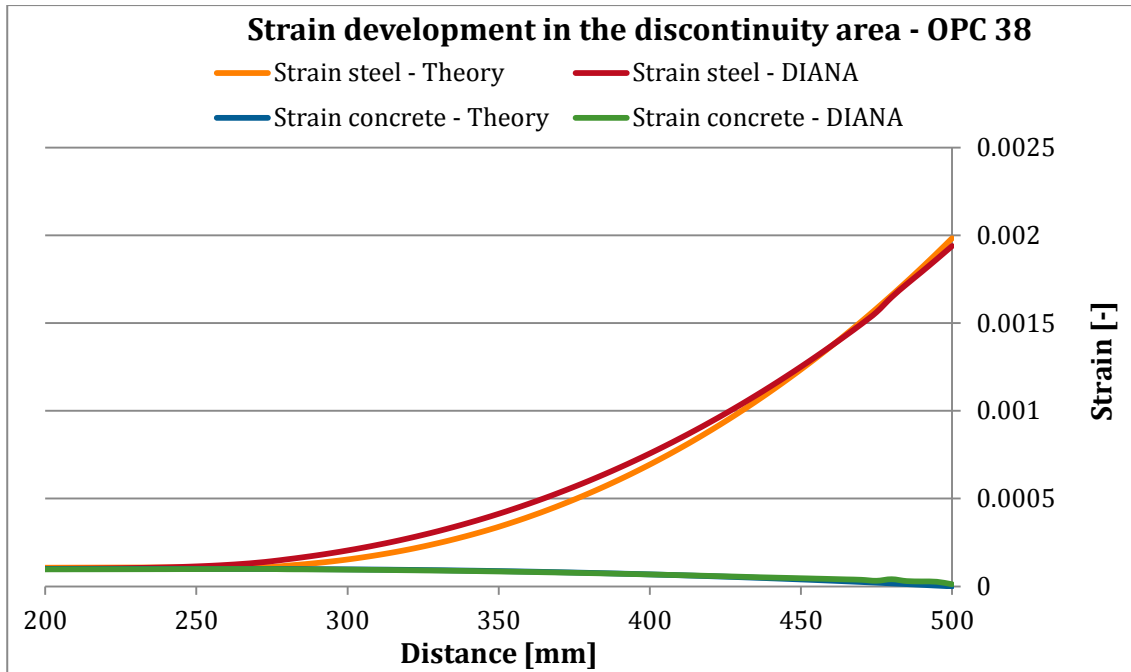
Figure 6.29 Steel and concrete strain progression in the discontinuity area. Plotted from the analytical method and the DIANA output.
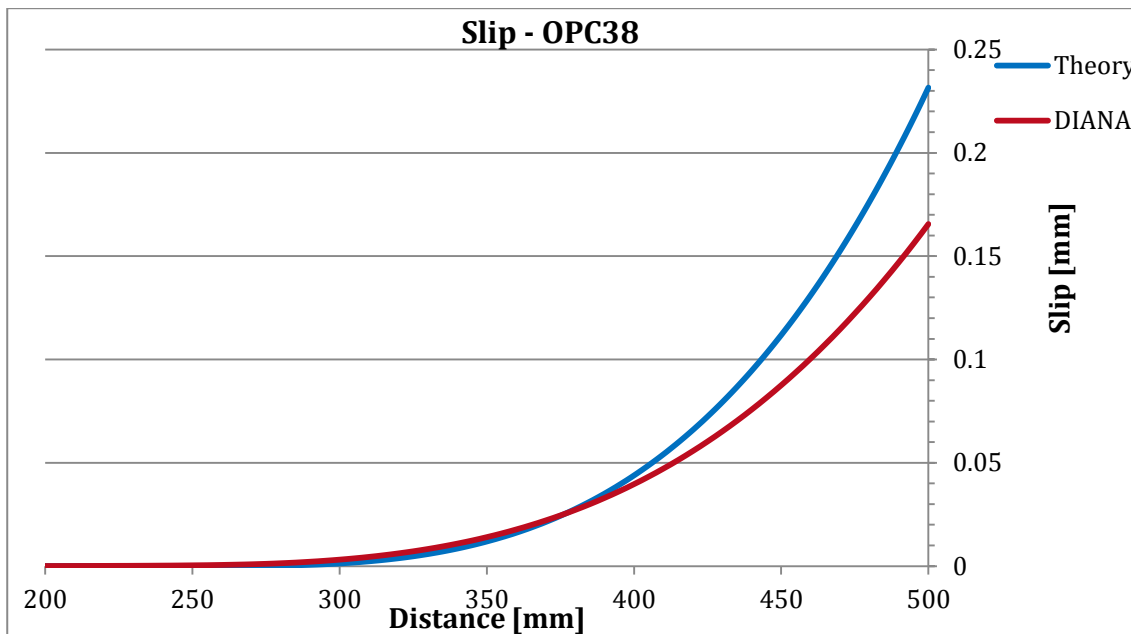
Figure 6.30 Slip development in the discontinuity area. Plotted from the analytical method and the DIANA output.

6.4.2.2 Bond stress differences

The difference in the computed crack-widths between the theoretical and DIANA bond-slip models is found in the development of the bond stress along the transfer length. In the following figures the non-linear bond stress τ_b development in the discontinuity area, left of the crack, is plotted. The development is shown for the theoretical analytically computed output and the DIANA computed output. The results are shown for the OPC38 and GPC55 with both the fib and Shima bond-slip models.

In the following figures it can be seen that the bond stress development computed with DIANA is somewhat accurate when compared to the theoretical computed bond stress development. The non-linear behaviour and the bond stress development approaches the theoretical behaviour, the bond increase witnessed follows the same sort of shape. This demonstrates that the tensile member in DIANA behaves according to the theory, but computes different actual values.

Figure 6.31 and Figure 6.32 display the bond stress development for OPC38 and GPC55 computed with the fib bond-slip model. The first thing to be noticed is that the DIANA result has a lower bond stress value at the crack location and the total slip value is related to this bond stress. This is the reason why the crack-width values computed by DIANA are lower compared to the theoretical crack-widths.

For both OPC38 and GPC55 the total transfer length in DIANA is longer. The FEA computes a longer distance to reintroduce the tensile stresses into the concrete. It can be seen that the bond stress starts to increase at a further distance away from the crack. The model uses a longer distance to reintroduce the stresses and therefore the build-up of the bond stress is lower, the result is a lower average bond-stress compared to the theory and a lower maximum bond stress at the location of the crack.

Figure 6.31 Bond stress development for OPC38 in the discontinuity area computed with the fib bond-slip model. Max bond stress theory τ_b = 8.52 MPa; max bond stress DIANA τ_b = 7.51 MPa.

The maximum bond stress found with the analytical method is τ_b = 8.52 MPa, which for the fib-model results in a crack-width of w = 0.45 mm. The DIANA output finds a maximum bond stress at the crack location of τ_b = 7.51 MPa which results in a crack-width of w = 0.34 mm.

The same behaviour is found for GPC55 displayed in Figure 6.32. The maximum bond stress found with the analytical method is τ_b = 8.27 MPa, which for the fib-model results in a crack-width of w = 0.26 mm. The DIANA output finds a maximum bond stress at the crack location of τ_b = 7.31 MPa which results in a crack-width of w = 0.20 mm.
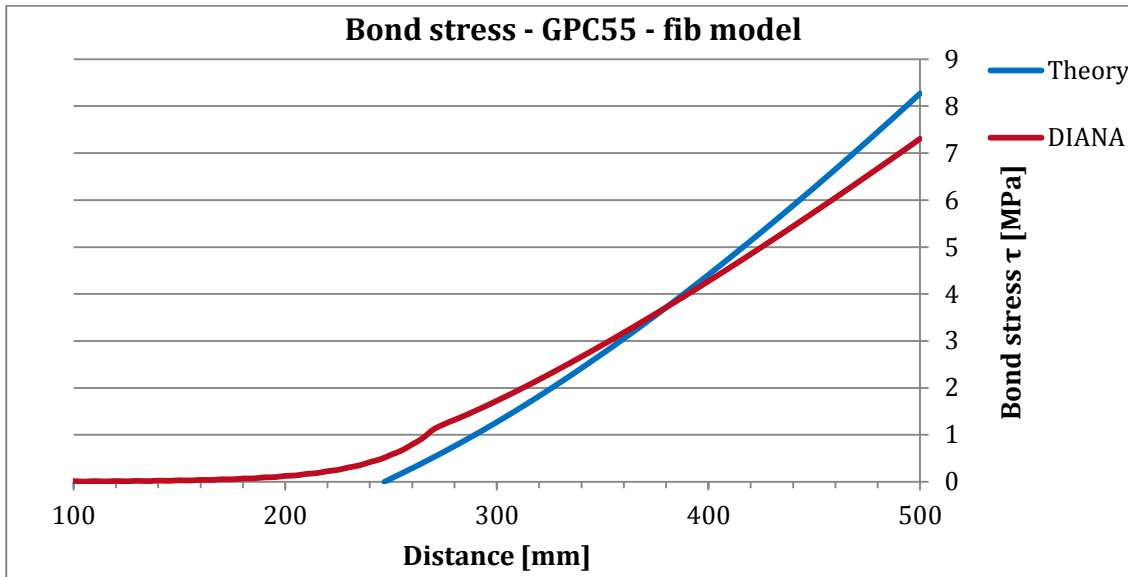
Figure 6.32 Bond stress development for GPC55 in the discontinuity area computed with the fib bond-slip model. Max bond stress theory τ_b = 8.27 MPa; max bond stress DIANA τ_b = 7.31 MPa.

Figure 6.33 and Figure 6.34 display the bond stress development for OPC38 and GPC55 computed with the Shima bond-slip model. The same sinus-like shape is computed with DIANA showing the bond-slip behaviour is modelled correctly, but the actual bond stress values differ. Just like with the fib bond-slip model DIANA requires a longer distance to reintroduce the tensile stresses into the concrete. The difference in bond stress between theory and DIANA is less with the Shima bond-slip model, the difference in computed crack-width is still quite significant.

The maximum bond stresses for OPC38 found with the analytical method is τ_b = 9.83 MPa, which for the Shima-model results in a crack-width of w = 0.33 mm. The DIANA output finds a maximum bond stress at the crack location of τ_b = 9.49 MPa which results in a crack-width of w = 0.22 mm.
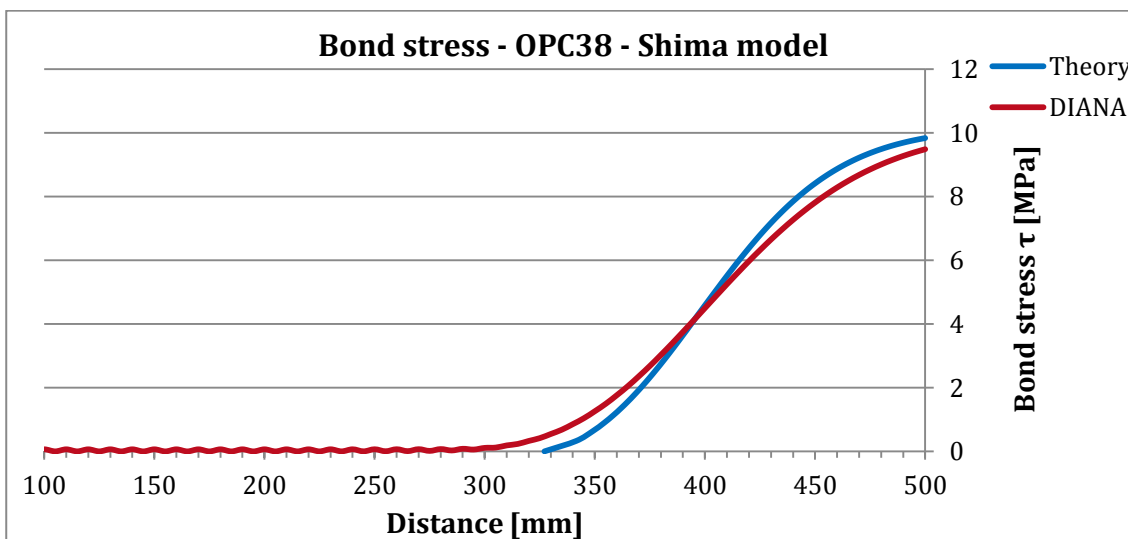
Figure 6.33 Bond stress development for OPC38 in the discontinuity area computed with the Shima bond-slip model. Max bond stress theory τ_b = 9.83 MPa; max bond stress DIANA τ_b = 9.49 MPa.

The maximum bond stresses for GPC55 found with the analytical method is τ_b = 10.44 MPa, which for the Shima-model results in a crack-width of w = 0.19 mm. The DIANA output finds a maximum bond stress at the crack location of τ_b = 9.63 MPa which results in a crack-width of w = 0.14 mm.

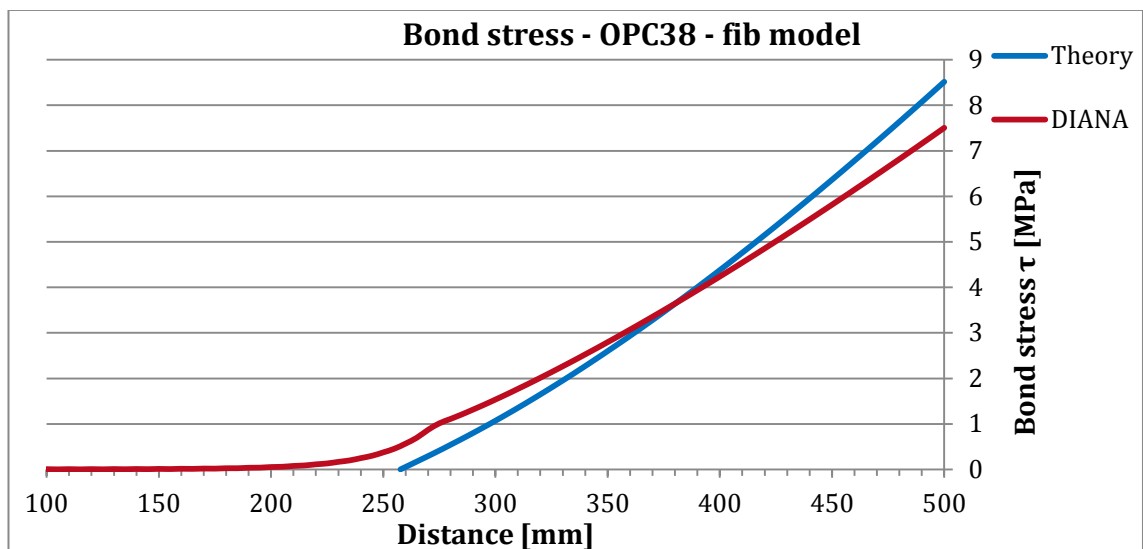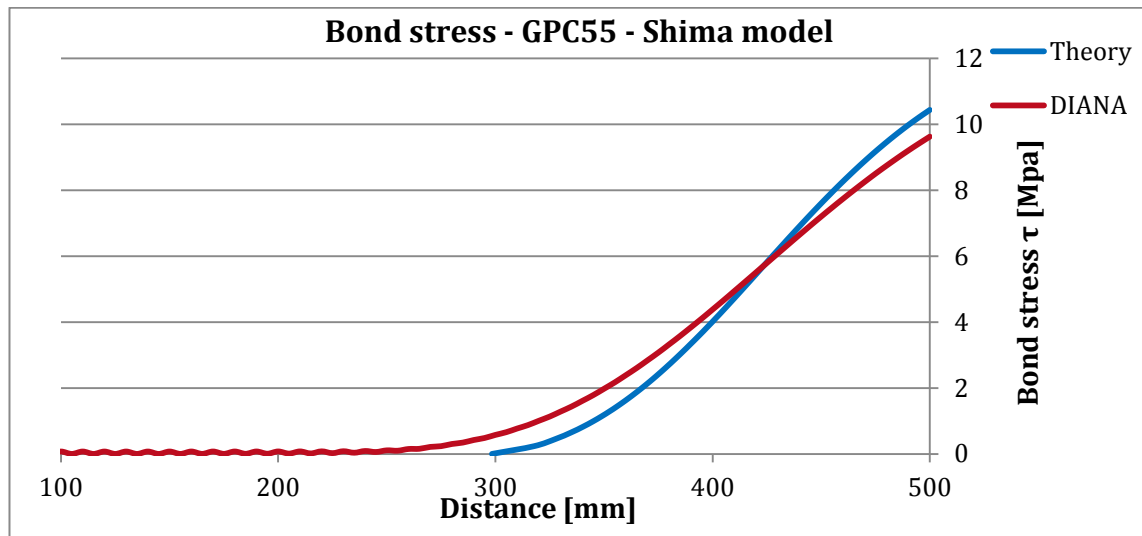**Figure 6.34 Bond stress development for GPC55 in the discontinuity area computed with the Shima bond-slip model. Max bond stress theory τ_b = 10.44 MPa; max bond stress DIANA τ_b = 9.63 MPa.**

With the Shima model DIANA computes the bond-slip behaviour a bit more accurate, the difference in crack-width is still present. In section 6.2.2 it was explained that the bond stress increase for the Shima bond-slip relation stagnates at quite a low slip value. Thus the small difference in bond stresses found with the Shima model still result in quite significant crack-width differences.

Above the computed results of OPC38 and GPC55 have been shown for both the fib- and Shima bond-slip model. A multiple variety of tensile members have been studied, with adjusted concrete material parameters, other reinforcement bar diameters and different DIANA settings. For all studied cases similar differences in the behaviour, like the non-linear bond stress development displayed above, were found.

6.4.3 Findings of the comparisons

The linearization that is generally accepted can compute the crack-widths quite accurately for the lower tensile strength concretes. Initially the constant bond stress assumed overestimates the actual bond stress, but for small crack-widths the average found bond stress can be accurate. For concrete with higher tensile strengths, like alkali-activated concretes, this overestimation is more severe and one can calculate very low crack-widths which will underestimate the actual crack-width significantly.

Comparing the fib bond-slip relation with the Shima bond-slip relation one finds lower crack-width values computed with the Shima model. The Shima model predicts higher bond stresses for all lower slip values and is therefore able to reintroduce the tensile stresses over a shorter distance back into the concrete. A shorter anchorage length is found which is associated with lower crack-widths.

With the FEA done in DIANA the non-linear material behaviour can be simulated quite accurately. The steel stress in the discontinuity area computed in DIANA is close to the theoretical actual steel stress. With the fine mesh size around the studied crack location the

maximum steel stresses σ_{sr} were found with 97-99% accuracy for the fib bond-slip model and only slightly lower accuracies for the Shima bond-slip model, with 96-98% accuracy of the actual theoretical maximum steel stress σ_{sr}.

The tensile member in the FEA model computes a longer distance to reintroduce the tensile forces back into the concrete. The computed anchorage length is longer when compared to the actual anchorage length according to the bond-slip theory. The average bond stress found is therefore lower, resulting in a lower maximum bond stress found at the crack location. This lower maximum bond stress is associated with a lower slip value and thus a lower crack-width.

It is wise when one is modelling concrete structures with DIANA, and has to study the cracking behaviour of reinforced structures, to study and draw conclusions from the steel stresses at the cracked locations and not the computed crack-widths. The behaviour of crack formation has been studied for the crack formation stage only, if the structure were to reach the stabilised cracking stage one should expect to see an overestimation of the crack spacing.

Where DIANA is able to compute quite accurate steel stresses with the bond-slip models, the differences found in the bond stresses is still of significance, such that the computed crack-widths are underestimated. The analytical method described in section 6.3.1 is considered to be the most accurate of the two explained methods to compute the non-linear crack-width calculations. Therefore, in the next section, where the improved bond-slip behaviour of alkali-activated concrete and geopolymer concrete is considered, the crack-width calculations are only computed with the analytical method.

6.5 Improved AAC and GPC bond strength

Alkali-activated concrete and geopolymer concrete in general have a higher tensile strength compared to OPC concrete of the same strength grade. This is due to the fact that AAC and GPC have a denser microstructure, a highly dense interfacial transition zone between matrix and aggregates is present. The matrix to steel bond for AAC and GPC is also stronger compared to cement based matrixes. The widely accepted formulation where the bond strength is proportional to the square root of the average compressive strength, underestimates the bond strength for AAC and GPC. The improved bond strength relation presented by Castel (2017) and the new improved bond stress-slip associated with that, is shown in Figure 6.35.
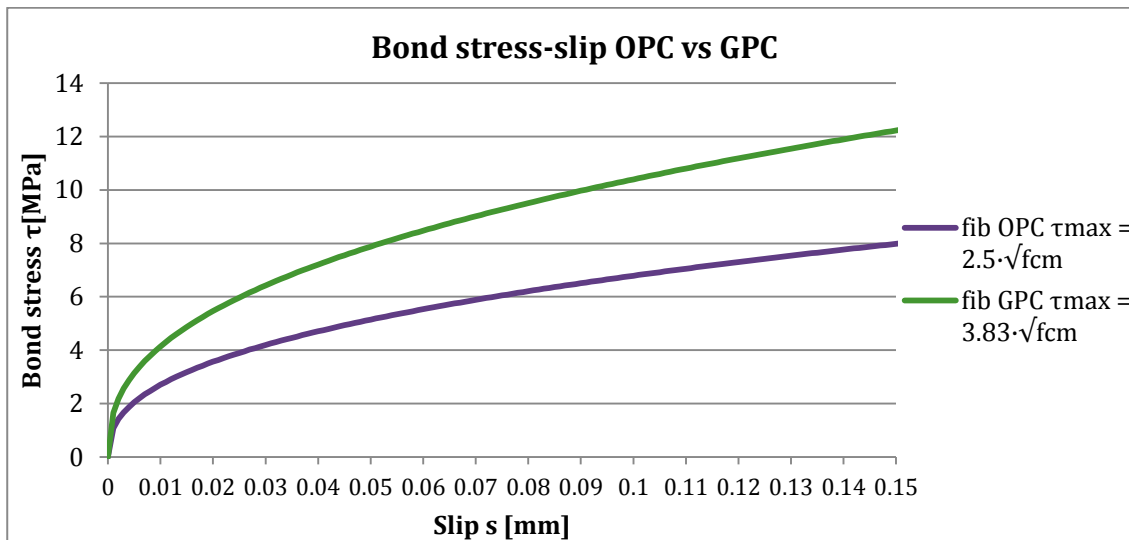
Figure 6.35 Bond stress-slip curves for the OPC based bond strength formulation and the improved GPC bond strength formulation. Plotted for a compressive strength of $f_{cm} = 46.5$ MPa.

The improved model provides a higher ultimate bond strength related to compressive strength, introduced in section 6.2.1.1 with Eq. (6.13). As the ascending part of the fib bond-slip relation is proportional to the ultimate bond strength the bond stresses found at lower slip values are higher.

6.5.1 Improved AAC and GPC bond-slip calculations

Bond-slip crack-width calculations have been done with the original and improved bond-slip relations, on multiple concrete types, listed in Table 6-8. The first two OPC40 and GPC-FA have the concrete properties that Castel (2017) tested, on which the improved geopolymer concrete relation is based. A concrete with a low tensile strength, LowTens, ideal for crack-width control and a high tensile strength concrete, HighTens, based on the geopolymer concrete EFC are also considered. Comparisons are made for the crack-width calculations of these concretes between the direct crack-width calculation, the original fib bond-slip relation and the improved fib bond-slip relation.

Table 6-8 Concrete class types considered for the linear and non-linear crack-width calculations. OPC40 and GPC-FA are the two concrete classes tested on their bond strength by Castel (2017). LowTens and HighTens are concrete types considered with a low tensile strength and a high tensile strength, respectively. Classes ordered on tensile strength. Values in MPa.

	LowTens	OPC40	GPC-FA	HighTens
Compressive strength f_{cm}	30	44	46.5	55.6
Tensile strength f_{ctm}	2	3.5	3.9	6
Young's modulus E_{cm}	25000	32000	24800	38500

The crack-width calculations are performed as described in section 6.3.1 for a tensile member with a width and height of 100 mm. The maximum crack-width for the crack formation stage is computed for each concrete with two different reinforcement bar diameters, ϕ = 12 mm and ϕ = 16 mm, with a steel modulus of elasticity E_s = 200 GPa. The concrete and steel parameters and the maximum steel stress in the crack formation stage σ_{sr} are the input required to compute the non-linear bond-slip calculations. The steel stress σ_{sr} is computed with Eq. (6.1). The simplified crack-width is calculated with Eq. (6.4) and its the anchorage length with Eq. (6.3).

The calculated crack-widths and anchorage lengths are listed in Table 6-9, where the tensile member is reinforced with a ribbed reinforcement bar of diameter ϕ = 12 mm.

Table 6-9 Crack-widths and anchorage lengths for different concrete types calculated for a tensile member with the maximum possible steel stress in the crack formation stage σ_{sr}. Crack-width and anchorage lengths calculated with different models named in the first column. Tensile concrete member of 0.1 x 0.1 m reinforced with a reinforcement bar of diameter ϕ = 12 mm.

Model		LowTens	OPC40	GPC-FA	HighTens	Unit
	Steel stress $\sigma_s = \sigma_{sr}$	192.8	331.3	376.3	561.7	MPa
Simplified	Crack-width w	0.160	0.275	0.312	0.446	mm
	Anchorage length l_t	166	166	166	166	mm
fib	Crack-width w	0.195	0.373	0.432	0.74	mm
$\tau_{bmax}=2.5\sqrt{f_{cm}}$	Anchorage length l_t	215	239	244	279	mm
fib	Crack-width w	0.143	0.277	0.319	0.545	mm
$\tau_{u\text{-}GPC}=3.83\sqrt{f_{cm}}$	Anchorage length l_t	158	177	180	205	mm

For all results in Table 6-9 it can be seen that the calculated crack-widths by the simplified method are underestimated, for the lower tensile strengths this difference is more or less

acceptable. For the higher tensile strengths, especially of the HighTens geopolymer concrete, the fib bond-slip model computes a significantly higher crack-width. The fact that the computed steel stress is above the yielding stress for standard reinforcement steel is ignored for the sake of this theoretical study. The anchorage lengths of the simplified row are also all shorter when compared to the fib bond-slip calculations. The fact that they are all 166 mm is because in Eq. (6.3) the only difference follows in the tensile strength f_{ctm}, which is divided by the bond strength τ_{bm}, which is directly calculated by the tensile strength. Thus a constant factor for the second term in Eq. (6.3) is found.

Dividing the crack-widths computed with the bond-slip model by the crack-widths computed with simplified method, gives a factor of increase between the two. These factors are 1.22, 1.36, 1.38 and 1.66 for the concrete types LowTens, OPC40, GPC-FA and HighTens, respectively. A similar development of increase is seen for the anchorage length as the tensile strength is increased.

The two lowest rows of Table 6-9 show the crack-widths and the anchorage lengths, considered with the same steel stress σ_{sr} from the first row, calculated with the improved bond-slip relation for AAC and GPC. For each concrete class considered a lower crack-width and anchorage length is found. Compared to the original fib bond-slip relation the calculated crack-widths for the concrete classes LowTens, OPC40, GPC-FA and HighTens are reduced by a factor of 0.733, 0.742, 0.738 and 0.736, respectively, when calculated with the improved GPC bond-slip relation.

The crack-widths and anchorage lengths have been calculated with a different reinforcement bar diameter as well. The calculated results computed with the simplified method, the original fib bond-slip relation and the GPC improved fib bond-slip relation are shown in Table 6-10. The ribbed reinforcement bar diameter has been increased to $\phi = 16$ mm.

Table 6-10 Crack-widths and anchorage lengths for different concrete types calculated for a tensile member at the maximum possible steel stress in the crack formation stage σ_{sr}. Crack-width and anchorage lengths calculated with different models named in the first column. Tensile concrete member of 0.1 x 0.1 m reinforced with a reinforcement bar of diameter $\phi = 16$ mm.

Model		LowTens	OPC40	GPA-FA	HighTens	Unit
	Steel stress $\sigma_s = \sigma_{sr}$	115.47	195.95	225.42	329.58	MPa
Simplified	Crack-width w	0.072	0.122	0.140	0.205	mm
	Anchorage length l_t	124	124	124	124	mm
fib	Crack-width w	0.111	0.208	0.246	0.409	mm
$\tau_{bmax}=2.5\sqrt{f_{cm}}$	Anchorage length l_t	203	226	231	264	mm
fib	Crack-width w	0.082	0.154	0.181	0.301	mm
$\tau_{u\text{-}GPC}=3.83\sqrt{f_{cm}}$	Anchorage length l_t	150	167	170	194	mm

As the concrete tensile member remains the same size, the maximum steel stress σ_{sr} is lowered because the reinforcement ratio is increased. This results in overall lower anchorage lengths and crack-widths values compared to the values in Table 6-9. Again, the simplified computed crack-widths are increasingly underestimated for higher tensile strengths. The factors of increase found are 1.54, 1.70, 1.76 and 2.00 for LowTens, OPC40, GPA-FA and HighTens, respectively.

Overall similar differences are found here when compared to the differences found between the values from Table 6-9. Similar factors between the calculated crack-widths are found comparing the original and improved bond-slip models. For LowTens, OPC40, GPC-FA and HighTens the factor difference between the crack-widths are 0.740, 0.736, 0.739 and 0.736, respectively, with the bigger bar diameter of $\phi = 16$ mm.

This displays the importance of the bond strength as a parameter for the control of cracking. Where it is generally accepted that the bond strength is directly computed from the tensile strength. However, the simplified method underestimates the crack-widths compared to the more accurate calculated crack-widths performed with the bond stress-slip relation. The latter being dependent of the bond strength. For alkali-activated concrete and geopolymer concrete this bond strength can be higher compared to OPC concrete. When following the recalibrated bond strength expression of Castel for AAC, computed crack-widths are reduced by a factor 0.74. This is beneficial considering the governing design aspect, the control of cracking, for the jointless floors.

6.5.2 Shima bond-slip comparisons

The same comparisons are made where the crack-width calculations are done with the simplified method and the Shima bond-slip relation. The Shima bond-slip relation has an increased bond stress-slip development at lower slip values which is somewhat similar to the improved geopolymer concrete bond stress-slip development. The comparisons are made on the same concrete types and reinforcement bars. The computed values are shown in Table 6-11, for $\phi = 12$ mm, and in Table 6-12 for $\phi = 16$ mm.

Table 6-11 Crack-widths and anchorage lengths for different concrete types calculated for a tensile member at the maximum possible steel stress in the crack formation stage σ_{sr}. Crack-width and anchorage lengths calculated with simplified method and the Shima bond-slip model. Tensile concrete member of 0.1 x 0.1 m reinforced with a reinforcement bar of diameter $\phi = 12$ mm.

Model		LowTens	OPC40	GPC-FA	HighTens	Unit
	Steel stress $\sigma_s = \sigma_{sr}$	192.8	331.3	376.3	561.7	MPa
Simplified	Crack-width w	0.160	0.275	0.312	0.446	mm
	Anchorage length l_{bt}	166	166	166	166	mm
Shima	Crack-width w	0.136	0.265	0.312	0.58	mm
	Anchorage length l_{bt}	163	174	177	205	mm

The Shima bond-slip model predicts the crack-widths closer related to the simplified method. The factors of increase for LowTens, OPC40, GPC-FA and HighTens are 0.85, 0.96, 1.00 and 1.30, respectively, when dividing the simplified crack-widths by the Shima computed crack-widths.

Table 6-12 Crack-widths and anchorage lengths for different concrete types calculated for a tensile member at the maximum possible steel stress in the crack formation stage σ_{sr}. Crack-width and anchorage lengths calculated with simplified method and the Shima bond-slip model. Tensile concrete member of 0.1 x 0.1 m reinforced with a reinforcement bar of diameter $\phi = 16$ mm.

Model		LowTens	OPC40	GPA-FA	HighTens	Unit
	Steel stress $\sigma_s = \sigma_{sr}$	115.47	195.95	225.42	329.58	MPa
Simplified	Crack-width w	0.072	0.122	0.140	0.205	mm
	Anchorage length l_{bt}	124	124	124	124	mm
Shima	Crack-width w	0.082	0.148	0.160	0.301	mm
	Anchorage length l_{bt}	173	180	181	202	mm

The factors of increase from Table 6-12 are 1.14, 1.21, 1.14 and 1.47 in the same order as the concrete classes specified. The crack-widths differ less when computed with the Shima bond-slip model. The difference in anchorage length is a bit more significant and increases with higher tensile strengths.

6.6 Results

The crack-width w can be calculated in a lot of different manners. The general method applied assumes linear stresses in the discontinuity area and assumes a constant bond stress τ_{bm}. For long term loading and cracks calculated in the crack formation stage, the bond stress τ_{bm} can then be computed with the expression:

$$\tau_{bm} = 1.6 \cdot f_{ctm} \tag{6.16}$$

This constant bond stress τ_{bm} is used to calculate the crack-width in the simplified manner. Crack-widths can be calculated in a more accurate way when bond-slip models are considered. With bond-slip models the non-linear bond stress-slip development can be computed. The bond-slip model of the well-known fib Model Code for Concrete Structures 2010 expresses the bond stress τ_{bm} in terms of the compressive strength f_{cm} and slip s as:

$$\tau_{bm} = 2.5\sqrt{f_{cm}} \left(\frac{s}{1.0}\right)^{0.4} \tag{6.17}$$

For alkali-activated concrete and geopolymer concrete the ultimate bond strength τ_{bmax} is higher and thus a new bond stress-slip relation is formulated which follows as:

$$\tau_{bm,GPC} = 3.83\sqrt{f_{cm}} \left(\frac{s}{1.0}\right)^{0.4} \tag{6.18}$$

Another bond-slip model is the Shima bond-slip model. In DIANA this model is often applied as this requires only the compressive strength f_{cm} and the reinforcement bar diameter ϕ as input. The Shima bond stress-slip relation is expressed as:

$$\tau = 0.9 \ f_{cm}^{\frac{2}{3}}(1 - e^{-40s^{0.6}}) \tag{6.19}$$

where $\quad s = S/D$ with S being the slip and D the bar diameter.

The fib bond-slip relation and the Shima bond-slip relation have been used to analyse the non-linear material behaviour of a cracked tensile member. The crack-widths and the development of stresses within the discontinuity area has been studied with theoretical models computed in an analytical way and with finite element analysis in DIANA. It turns out that the computed DIANA results all find lower crack-widths compared to the analytical computed crack-widths. The bond stress development within the discontinuity area in DIANA is lower and computes a longer anchorage length necessary to reintroduce the tensile forces back into the concrete. The longer anchorage length results in a lower average bond stress and lower maximum bond stress, the latter is related to the total relative displacement of the reinforcement. The total slip computed at the crack-width is found to be lower and thus a lower crack-width is computed in DIANA.

Were one to use DIANA for actual crack-width calculations, one would have to assume that the computed crack-widths are most likely underestimated and that the crack spacing can be overestimated once a fully developed crack pattern is realised. The steel stresses within the cracks are computed accurately and it is better to draw conclusions from concerning crack-widths based on the steel stresses in an around the cracks.

Further study of the crack-width calculations with (non-)linear material behaviour has therefore been done with the analytical method. The different bond stress-slip relations have been studied on several concrete classes. Below are the four bond stress expressions plotted for low slip values for three different concrete types. Plotted for the considered low tensile strength concrete in Figure 6.36. In Figure 6.37 for the concrete class C30/37 and in Figure 6.38 for the high tensile strength concrete based on the geopolymer concrete EFC.
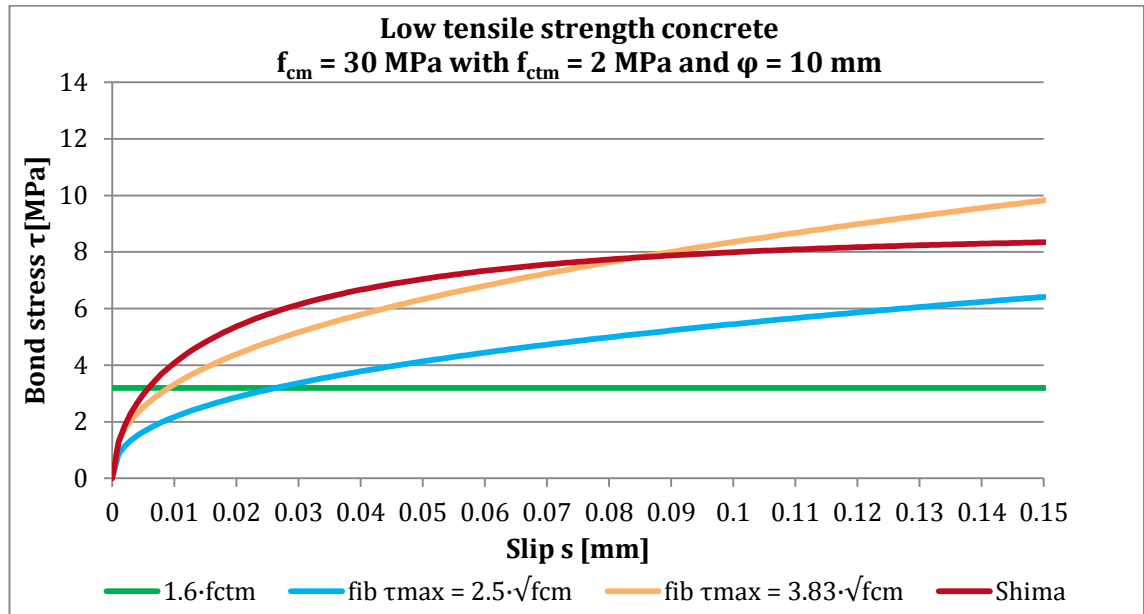
Figure 6.36 Bond stress-slip development at low slip values for different bond-slip models. Bond stresses displayed for low tensile strength concrete.
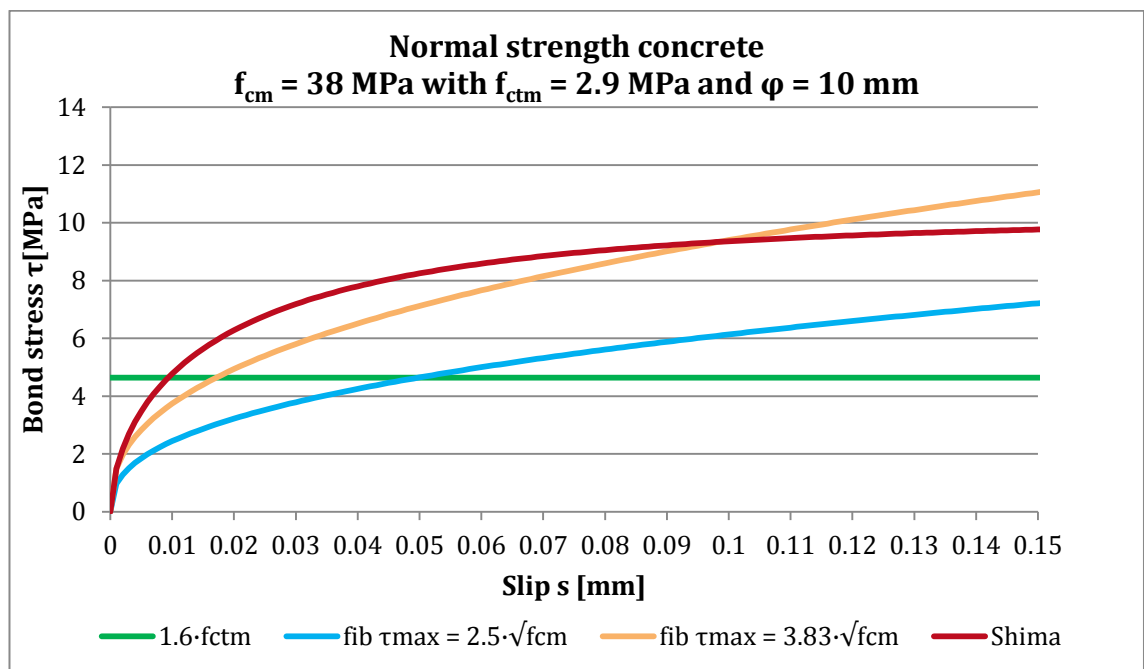
Figure 6.37 Bond stress-slip development at low slip values for different bond-slip models. Bond stresses displayed for concrete class C30/37.
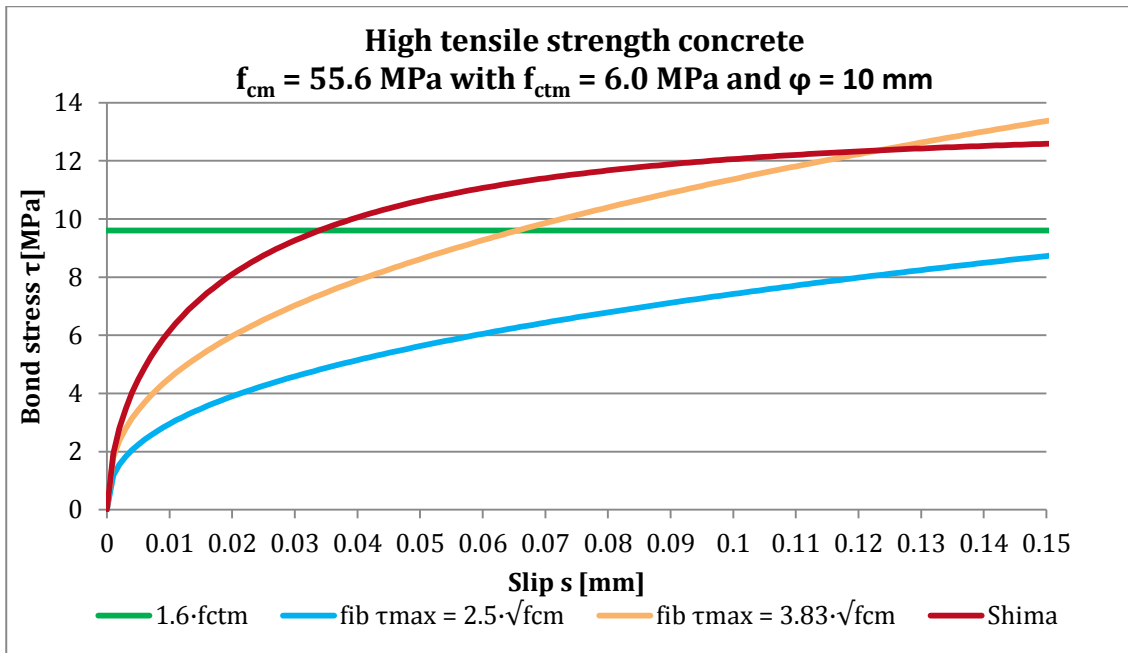
Figure 6.38 Bond stress-slip development at low slip values for different bond-slip models. Bond stresses displayed for high tensile strength concrete.

Comparisons have been made between the calculated results. The simplified crack-widths are all lower when compared to the crack-widths computed with the original fib bond-slip relation. The underestimation of the crack-width between the two methods increases with an increase of the tensile strength of the cracked concrete that is considered. This also applies for the anchorage length. This difference is clearly visible in Figure 6.38 where the constant assumed bond stress, the green line, is higher than the actual bond stress for all slip values, the blue line.

The computed crack-widths with the Shima bond-slip model are more in line with the simplified method, but also see an increase in the difference between the crack-widths and anchorage lengths for increasing tensile strengths. In the bond stress-slip graphs it can be seen that the Shima bond stress-slip relation predicts higher bond stresses for all low slip values compared to the original fib bond stress-slip relation. This results in the lower anchorage lengths and lower maximum crack-widths.

For alkali-activated concrete and geopolymer concrete the original fib bond stress-slip relation is recalibrated to be more in line with the bond stress-slip behaviour found for AAC and GPC. The improved bond stress behaviour results in computed crack-widths that are a factor 0.74 lower compared to the crack-widths computed with the original fib bond-slip model. This is beneficial when considering that the governing design aspect of jointless concrete floors is crack-width control.

7 DISCUSSION

In this chapter the findings are reviewed with respect to the research and sub-research questions.

This thesis is about the implementation of alkali-activated concrete (AAC) in concrete industrial jointless ground floors, of which the control of cracking is the governing design aspect. Calculations show that the current minimal applied floor thickness and applied reinforcement are sufficient enough to fulfil the ULS unity checks, even when quite heavy external loads are considered. The serviceability limit state (SLS), therefore, follows to be governing for this type of structure. In this thesis only the SLS crack-width control is studied, for which it is considered that the floor cross-sections only crack in bending. It is assumed that concrete ground floor is realised on the suitable subsoil such that settlements of the concrete structure do not exceed the set limits. User aspects, like flatness and levelness, are expected to be met by a proper execution of the floor. Crack-width control calculations are thus made for an indoor jointless floor that is constructed properly.

The most important concrete properties for the jointless floor are the shrinkage size, the tensile strength, the modulus of elasticity and the bond strength. The residual flexural strength, from the addition of steel fibres in the floor, is also of importance for the crack-width control. However, this property is mainly defined by the type and amount of steel fibres and thus not necessarily a concrete material property. It is shown that alkali-activated concrete has material properties, compared to OPC concrete, that are beneficial for the governing design aspect of the jointless floor. The control of cracking is important for the cracks that arise from imposed loads, of which only the predominant drying shrinkage is considered. Temperature changes are smaller imposed loads that will influence the behaviour of the floor, especially if outdoor floors are considered too. Nevertheless, for the indoor floors considered in this thesis only the predominant drying shrinkage is accounted for. A reduction of this drying shrinkage, which AAC can have, is essential for a thinner jointless floor to be realisable. This possibility to reduce the minimum floor thickness is crucial for a further optimisation of the jointless floor. The increased tensile strength that AAC has, is disadvantageous concerning the crack-width control. However, the beneficial reduced shrinkage size outweighs this "bad" tensile strength of AAC. A lower bending cracking moment is still found with the reduced thickness and a higher (flexural) tensile strength.

The optimisation process performed for the concrete jointless ground floor is accommodated with two aspects. First, the drying shrinkage determines the minimum required thickness for the floor. A lower final drying shrinkage size allows for a thinner cross-section. And second, the structural material properties of the concrete define the reinforcement mesh and steel fibre contents required to control the crack-widths.

For the first aspect, it is demonstrated in chapter 4 that alkali-activated concretes and geopolymer concretes exist that show significantly less shrinkage compared to concrete realised with OPC. The most common precursor blast furnace slag and activator sodium silicate seem to be related with higher shrinkage values when used in higher quantities. An alkali-activated concrete

produced with other low calcium precursors and an activator with little silicate can provide the desired reduced shrinkage size. Proper curing of the AAC is of importance as well as with longer curing ages the drying shrinkage strain developed will be reduced. In this thesis the shrinkage development curve of the geopolymer concrete EFC is considered for the optimisation of the concrete ground floor. The reduced suitable thickness of 130 mm that follows is applicable for this specific drying shrinkage size, if an alkali-activated concrete will be implemented with another drying shrinkage size the possible floor thickness reduction must be revaluated.

Where with OPC concrete the autogenous shrinkage is not an issue, since it is little and fully developed at an early stage. It will actually be beneficial for an OPC concrete jointless floor if crack formation were to occur from autogenous shrinkage in the very young phase. This will result in craquelure, which prevents new crack formation to occur from drying shrinkage at a later time. The many miniscule cracks will evenly widen a fraction, but remain very small. For AAC it is important to know what component of the total shrinkage is autogenous shrinkage. AAC can show higher autogenous shrinkage reductions developed over a longer period. Autogenous shrinkage develops, unlike the drying shrinkage, uniformly through the concrete cross-section. If its development is significantly higher ($\varepsilon_{ca} > 0.1\text{‰}$), the average shrinkage reduction over the height of the floor cross-section can cause crack formation from a pure tensile component to occur. This will result in crack-widths that will surely exceed the maximum allowable crack-width with the standard reinforcement. If the autogenous shrinkage of AAC is too high the jointless floor has to be reinforced to withstand crack formations for pure tension, requiring vast amounts or reinforcement. It is, therefore, not advised to realise a jointless floor in AAC if its autogenous shrinkage is significantly higher than what is seen for OPC based concretes.

The second aspect of the floor optimisation is performed with the parametric study in chapter 5. It follows that for crack-width control the concrete material properties compressive strength f_{cm} and modulus of elasticity E_{cm} aren't as influencing as the concrete tensile strength f_{ctm} and the residual flexural strength f_{R4} provided by the steel fibres. The computed crack-width calculations, for this specific part, assume a constant bond stress directly related to the tensile strength. One finds the lowest crack-widths when a jointless floor cracks in bending, from the restrained shrinkage gradient, and is realised with a low tensile strength concrete and a high residual flexural strength. With the reduced shrinkage size the minimum floor thickness is reduced. It is assumed that the associated average slower shrinkage development ensures that the thinner floor only cracks in bending and that the average shrinkage component is small and negligible. So the floor cracks at the bending cracking moment from pure bending. This bending moment depends on the flexural tensile strength $f_{ctm,fl}$ and the thickness h. As the thickness h is squared in the calculation of the bending cracking moment the reduction in thickness has more influence than the increase in tensile strength. A lower bending cracking moment is the result.

It follows that with the reduced floor thickness of 130 mm, realised in AAC with a relatively high tensile strength of $f_{ctm} = 4.0$ MPa, a smaller minimum bar diameter for the top reinforcement mesh is applicable, without increasing the steel fibre content above normal proportions. Currently, a jointless floor is realised with a minimum thickness of 160 mm, with a top reinforcement mesh of ϕ7-100 mm and a minimum steel fibre content of 30 kg/m³. A floor realised in AAC, with the considered reduced shrinkage size, can be realised with a thickness of 130 mm, a top reinforcement mesh of ϕ6-100 mm and a steel fibre content of 35 kg/m³. This new optimised jointless floor fulfils both the SLS and ULS unity checks.

For this it is assumed that the steel fibre interaction with AAC is similar to the interaction with OPC concrete. The residual flexural strengths considered are based on test results performed on OPC concrete notched beams. There are no results yet for long and end-anchored steel fibres applied in AAC notched beams. It is possible that the improved bond strength and higher tensile

strength of AAC is seen back into an improved steel fibre interaction. Such that higher residual flexural strengths can be found in AAC, compared to OPC concrete of similar strength grade, when the same amount of fibres are used. This could translate itself to a further optimisation of the jointless floor, in a manner that lower steel fibre contents or lower reinforcement ratios are possible.

The design approach for the parameter study neglects an average axial component of the shrinkage reduction and the crack-width calculations are performed for pure bending only. If the shrinkage development at the bottom of the floor is non-existent as it is considered, an average axial strain component will still be present. This axial component causes fictive uniform tensile stresses. In accordance with the CUR-Recommendation 36 a partially and a fully developed shrinkage reduction is considered. It follows that the axial component is a significant component of the unity check for combined loading. Theoretically this axial component can thus not just be neglected. The considered optimal jointless floor in AAC following from the parameter study does fulfil the unity check where this average axial component is not neglected, but it does require a reduction of the allowable external loads. If a jointless floor is designed while neglecting this axial component and in practice the crack-widths do exceed the maximum allowable crack-width, this phenomenon can be the reason.

Finally, for a further optimisation of the floor, the improved bond strength of AAC is studied in the previous chapter. This is done by looking into the cracking behaviour with more realistic bond-slip models. The non-linear behaviour of the concrete and steel within the discontinuity area is analysed with different bond-slip models. The bond-slip crack-width calculations find larger crack-widths compared to the simplified method, which is applied in chapter 5. The simplified method assumes linear stresses over the transfer length where in reality non-linear stresses occur, thus the bond-slip models compute more accurate results. Even though this study is done on a tensile member, the findings also apply to crack formation in bending. The reintroduction of the tensile forces from steel to concrete is not different. The applied concrete cover ensures that the concrete surrounding the reinforcement provides good bonding conditions. The computed crack-widths in chapter 5 all remain below the set crack-width of w_{max} = 0.12 mm. This leaves some tolerance for the crack-width to see an increase were they recalculated with the bond-slip method. However, when the improved bond-slip model for AAC and GPC is applied, this increase in computed crack-widths is nearly negligible, apart for the high tensile strength of f_{ctm} = 6.0 MPa.

Crack-width calculations are performed with finite element analysis as well, computed in DIANA. The non-linear behaviour of concrete and steel can be studied with DIANA excellently. The study done shows that the non-linear material behaviour of steel and concrete can be imitated well. But, one should not blatantly believe its output and see it as reality, it turns out that the doubt in this specific software, for its crack-width calculations, is valid. The DIANA model used is made to imitate the realistic behaviour of a tensile cracked concrete member to its best. With bond-slip models and a discrete interface, such that the cracked location can open up. However, all the DIANA bond-slip crack-width calculations performed underestimated the crack-widths compared to the theoretical results computed analytically. The study shows that the differences occur due to a different bond stress development over the anchorage length. Why this happens exactly is not understood. DIANA might not be able to compute exact zero slip values after the theoretical anchorage length is passed. Such that it still computes small slip values which, even for small slip values, are still associated with bond stresses. It is known that DIANA computes a maximum bond stress, at the crack location, that is lower and therefore a smaller crack-width is found.

8

CONCLUSIONS AND RECOMMENDATIONS

This chapter summarizes the findings presented in this thesis and the conclusions that are drawn from them. An answer to the main research question is formulated and recommendations for further research are provided.

8.1 Conclusions

The most useful jointless concrete floor is one that is hybrid reinforced, i.e. with a top reinforcement mesh applied in addition to steel fibres in the concrete mixture. When a jointless concrete floor with a large area is realised on a subsoil with a high friction it is fully restrained, apart from its free edges. The drying process results in a shrinkage gradient, which leads to tensile stresses at the top surface, causing the floor to crack in bending. The governing design aspect of a jointless floor is to control the crack-widths at the top surface. The maximum allowable crack-width is 0.3 mm for the cracks located at the top surface.

Alkali-activated concrete and geopolymer concrete show promising structural material behaviour and sustainable properties and are therefore studied for their implementation in elastically supported jointless ground floors. This relatively new concrete type is realised without cement, which results in a reduced CO_2 footprint. Since its binder is realised differently, the concrete material properties can differ from traditional concrete realised with Ordinary Portland Cement. The main research question to be answered is:

"To what extent can elastically supported jointless concrete ground floors be constructed in a more efficient way when realised in alkali-activated concrete compared to traditional concrete?"

For jointless floors the concrete properties that are of most importance when considering the minimum floor thickness and the control of cracking are:

- The shrinkage size ε_{cs};
- The tensile strength f_{ctm};
- The modulus of elasticity E_{cm}; and
- The bond strength τ_{bm}.

Alkali-activated concrete can have a reduced shrinkage size making it possible to realise the jointless concrete floors with thinner cross-sections. The tensile strength of AAC is higher, compared to traditional OPC concrete of similar strength grades. This results in higher tensile stresses that have to be carried by the reinforcement after crack formation, resulting in larger crack-widths. The modulus of elasticity for AAC is usually lower than traditional OPC concrete of similar strength grades, causing lower stresses to develop from internal and external loads. The bond strength of AAC is better between the concrete and the steel reinforcement, compared to traditional OPC concrete of similar strength grades, resulting in shorter anchorage lengths and smaller crack-widths.

Reduced floor thicknesses are possible in AAC and GPC with a reduced drying shrinkage size compared to the shrinkage size of a typical OPC based concrete. The reduced drying shrinkage size is essential to ensure that the smaller floor cross-section cracks in bending and not from a pure tensile component. A reduction of 40% for the final shrinkage size is realisable with alkali-activated concrete compared to a typical shrinkage size of an OPC based concrete. Even though AAC has a higher tensile strength, the reduced thickness results in a lower bending cracking moment and thus in lower steel reinforcement stresses within the cracks. It is, therefore, possible to realise a jointless floor with a finer top reinforcement mesh without significantly increasing the steel fibre content necessary to control the crack-widths.

Crack-widths calculated in a direct manner in accordance with the fib Model Code 2010 and the Eurocode 2, which assume constant bond stress behaviour in the discontinuity area, tend to underestimate the crack-widths. The bond stress is overestimated, especially for higher concrete tensile strengths ($f_{ctm} > 4.0$ MPa) at low slip values ($s < 0.15$ mm) or low crack-widths ($w_d < 0.3$ mm). Non-linear bond-slip calculations, which provide a more realistic approach, find larger crack-widths differentiations with increased tensile strengths compared to the direct simplified computed crack-widths.

Crack-width calculations performed with finite element analysis in DIANA using bond-slip relations underestimate the crack-widths compared to the analytically calculated crack-width values. The cracked tensile member models in DIANA all show a larger distance along the reinforcement bar where bond stresses are generated. This means that DIANA computes a larger anchorage length necessary to reintroduce the tensile forces back into the concrete compared to the analytically computed anchorage length. The increased anchorage length results in a lower maximum bond stress at the crack location, which translates to a lower slip value and thus an underestimated crack-width. DIANA is able to compute the steel reinforcement stresses within the discontinuity area accurately, with both the fib Model Code 2010 and Shima bond-slip relations.

The improved bond stress-slip relation for AAC and GPC results in smaller crack-widths and lower anchorage lengths. The increased maximum bond strength of AAC provides higher bond stresses at low slip values, reducing the maximum slip between the reinforcement bars and the concrete. With the improved bond-slip relation for alkali-activated concrete 26% smaller crack-widths are found compared to the bond-slip relation for traditional concrete. As a result, the control of cracking can be realised with a lower amount of steel in the jointless floor, either by applying a finer top reinforcement mesh or by applying lower steel fibre contents.

Jointless concrete ground floors with a reduced thickness and a finer top reinforcement mesh are realisable with AAC while fulfilling the SLS and ULS unity checks, provided that the shrinkage of AAC is less than that of traditional OPC based concrete. It is possible to realise an industrial jointless floor in alkali-activated concrete that per square meter floor can save in materials around 20% concrete and 30% steel, in reinforcement and fibres, compared to the standard industrial jointless floor realised in traditional concrete. From a sustainable point of view, the jointless floor realised in AAC is more efficient in two aspects. First, due to the improved material properties the just named reduction of materials is possible. And second, the floor is realised in a concrete that has a lower CO_2 footprint since the production of its materials are more sustainable.

8.2 Recommendations

In order to implement alkali-activated concrete as a replacement of traditional concrete for a jointless ground floor, knowledge of the material has to be sufficient. The development of its shrinkage, especially as a reduction of its drying shrinkage size, is essential for the floor thickness reduction to be realisable. Multiple studies have shown that blast furnace slag and sodium silicate in the activator are associated with increased shrinkage sizes, thus it is advised to use an AAC with low amounts of these two components, even though they are one of the most common precursor and activator. Curing of jointless floors realised with AAC is important, and it is therefore advised to apply the same curing age as applied for OPC concrete ground floors. The AAC ground floor is ideally cured by sealing the top surface, since this prevents the occurrence of early drying shrinkage. Typical curing compounds may not be as effective as for OPC concrete and it is discouraged to cure AAC by keeping the top surface wet at all times. Water curing can cause the dissolved alkalis to seep out of the concrete mixture, which results in a weakened end product.

When testing the shrinkage of alkali-activated concrete specimens, the separate proportions of the drying shrinkage and the autogenous shrinkage to the total shrinkage reduction have to be known. With OPC concrete, the autogenous shrinkage is little and develops at an early stage that it is not disadvantageous for the jointless floor. If the autogenous shrinkage reduction for AAC is larger and develops over a longer period, it can cause crack formation from pure tension, making the AAC unsuitable for the implementation in a jointless floor. Therefore, it is advised to measure the drying shrinkage and autogenous shrinkage separately over a longer time to be sure whether the AAC is actually applicable. It is also advised to perform pull-out tests on AAC to be able to show its increased bond strength, such that the floor crack-width calculations can be computed with an improved bond-slip model.

For further research, it is interesting to measure the shrinkage reduction of a jointless floor over its height in time, to study how close theory and practice are. With modern techniques, it is possible to measure this shrinkage development accurately. The actual strain developments can be measured exact by pouring fibre optic cables at several points and at different heights into a jointless floor structure. The measurements can be translated to the actual deformations and stresses present within the jointless concrete floor. This makes it possible to tell to what extent shrinkage has taken place in the bottom fibre of the floor and whether the neglect of an axial tensile component is acceptable or not.

Finally, awareness of the crack-width calculations performed with the simplified method or with DIANA is recommended. Both can provide results that underestimate the crack-widths, especially when dealing with concrete with higher tensile strengths, such as AAC. When DIANA is used, it is advised to draw conclusions from the steel stresses around the crack locations instead of from the computed crack-widths. It has been shown that the crack-widths computed by DIANA differ from the theory due to a different bond stress development. Effort should be put into finding a solution that solves the deviation for this bond stress-slip development within the discontinuity area as computed in DIANA. This leads to an increase in accuracy of computed crack-widths calculated with bond-slip models.

References

Abdul-Wahab, H., & Jaffer, A. (1983). Warping of reinforced Concrete Slabs Due to Shrinkage. *ACI Journal*, Proceedings V. 80, pp. 109-115.

ABT. (2015a). *Beton voor bedrijfsvloeren deel 1.* Retrieved from https://www.abt.eu/bestanden/Afbeeldingen/Organisatie/Kennisgebieden/2334-2/Beton_voor_bedrijfsvloeren_2015_ABT_1.pdf

ABT. (2015b). *Beton voor bedrijfsvloeren deel 2.* Retrieved from https://www.abt.eu/bestanden/Afbeeldingen/Organisatie/Kennisgebieden/2335-2/Beton_voor_bedrijfsvloeren_2015_ABT_2.pdf

ABT. (2015c). *Voegloze bedrijfsvloeren.* Retrieved from https://www.abt.eu/bestanden/Afbeeldingen/Organisatie/Kennisgebieden/2326-3/Voegloze_bedrijfsvloeren_ABT_2015.pdf

ABT. (2015d). *Granulaat werkvloer voor bedrijfsvloeren.* Retrieved from https://www.abt.eu/bestanden/Afbeeldingen/Organisatie/Kennisgebieden/2331-1/Granulaatwerkvloer_voor_bedrijfsvloeren_2015.pdf

Adyin, S., & Baradan, B. (2013). The effect of fiber properties on high performance alkali-activated slag/silica fume mortars. *Composites: Part B 45*, 63-69.

Aïtcin, P.-C. (2000). Cements of yesterday and today. *Cement and Concrete Research, 30*(9), 1349-1359.

Aldin, Z., Guang, Y., Luković, M., & Nederlković, M. (2017). *Optimization of a geopolymer mixture for a Reinforced cantilever concrete bench.* TU Delft.

Aldred, J., & Day, J. (2012). Is Geopolymer Concrete a Suitable Alternative To Traditional Concrete ? *37th Conference on Our World in Concrete & Structures*(August), 1-14.

Alhasani, M., & Zaraei, A. (1996). *Design of Industrial Floors Principles of Control of Warping.* Lund Institute of Technology, Division of Structural Engineering.

Bak, R. (2018). Logistiek vastgoed in cijfers 2017. *Statistiek van de Nederlandse markt voor distributiecentra en opslagruimten*. Nieuwegein: NVM Business.

Bakharev, T., Sanjayan, J., & Cheng, Y.-B. (2000). Effect of admixtures on properties of alkali-activated slag concrete. *Cement and Concrete Research 30*, 1367-1374.

Beckett, D. (2003). Strength and serviceability design of concrete industrial ground floors. *Proceedings of Industrial Colloquium Industrial Floors*, 601-612.

Bekaert. (2013). *Reinforcing your industrial floor.* Hendrik Thooft.

Bernal, A., & Provis, J. (2014). Durability of Alkali-Activated Materials: Progress and Perspectives. *Journal of American Cermaic Society 97(4)*, 997-1008.

Bernal, S., De Gutierrez, R., Delvasto, S., & Rodriguez, E. (2010). Performance of an alkali-activated slag concrete reinforced with steel fibers. *Construction and Building Materials 24*, 208-214.

Bernal, S., Mejía de Gutierrez, R., & Provis, J. (2012). Engineering and durability properties of concretes based on alkali-activated granulated blast furnace/metakaolin blends. *Construction and Building Materials 33*, 99-108.

Bernal, S., Provis, J., Mejía de Gutiérrez, R., & van Deventer, J. (2015). Accelerated carbonation testing of alkali-activated slag/metakaolin blended concretes: effect of exposure conditions. *Materials and Structures 48*, 653-669.

Bertens, S., & Geijtenbeek, B. (2017). *Ranking Logistics 2017.* Jones Lang LaSalle IP, Inc.

Beton & Staalbouw. (2015, September 1). *Journaal.* Retrieved from Beton & Staalbouw Platform over beton en staal in de bouw: http://www.betonenstaalbouw.nl/journaal-3/

BetonLexicon. (2018, October). *https://www.betonlexicon.nl/V/Voeg.* Retrieved from BetonLexicon: https://www.betonlexicon.nl/library/beton_lexicon_files/356.jpg

Bligh, R., & Glasby, T. (2013). Development of geopolymer precast floor panels for the Global Change Institute at University of Queensland. *Proceedings Concrete Institute of Australia Biennial Conference, Concrete.*

Bouquet, G., & Frénay, J. (1998). *Betonnen bedrijfsvloeren en bedrijfsverhardingen.* 's-Hertogenbosch: VNC.

Breugel, K., Braam, C., Van der Veen, C., & Walraven, J. (2016). Concrete Structures under Imposed Thermal and Shrinkage Deformations - Theory and Practice.

Buchwald, A. (2012). ASCEM® cement - a contribution towards conserving primary resources and reducing the output of CO2. *Cement International 10(5)*, 86-97.

Castel, A. (2017). Bond Between Steel Reinforcement and Geopolymer Concrete. In A. Nazari, & J. Sanjayan, *Handbook of Low Carbon Concrete* (pp. 375-387). Elsevier Inc.

CURNET. (2007). *CUR Recommendation 111 Steel fibre reinforced concrete industrial floors on pile foundations - Design and construction.* Gouda.

CURNET. (2011, december). CUR-Aanbeveling 36: 2011 (derde, herziene uitgave). *Ontwerpen van elastisch ondersteunde betonvloeren en -verhardingen.* Gouda: Stichting CURNET.

Davidovits, J. (1991). Geopolymers: inorganic polymeric new materials. *Journal of Thermal Analysis and calorimetry*, Vol 37, Edition 8, pp. 1633-1656.

de Vries, P. (2017). Geopolymeerbeton warm(te) aanbevolen. *Betoniek vakblak 1*, 18-25.

DELTA Concrete Consult. (2018, april). Kansen voor geopolymeerbeton in windturbinefundaties [Powerpoint presentation]. Retrieved from ABT.

Duran Atiş, C., Billim, C., Çelik, Ö., & Karahan, O. (2009). Influence of activator on the strength and drying shrinkage of alkali-activated slag mortar. *Construction and Building Materials 23(1)*, 548-555.

Duxson, P., Provis, J., Lukey, G., & van Deventer, J. (2007). The role of inorganic polymer technology in the development of 'green concrete'. *Cement and Concrete Research, 37*(12), 1590-1597.

Fédération Internationale du Béton. (2013). *fib Model Code for Concrete Structures 2010.* Lausanne, Switzerland: Ernst & Sohn.

Fernández-Jiménez, A., Palomo, A., & López-Hombrados, C. (2006). Engineering Properties of Alkali-Activated Fly Ash Concrete. *ACI Materials Journal 103(2)*, 106-112.

Ganesan, N., Abraham, R., & Deepa Raj, S. (2015). Durability characteristics of steel fibre reinforced geopolymer concrete. *Construction and Building Materials 93*, 471-476.

Garcia-Lodeiro, I., Palomo, A., & Fernández-Jiménez, A. (2015a). An overview of the chemistry of alkali-activated cement-based binders. In *Handbook of Alkali-Activated Cements, Mortars and Concretes* (pp. 19-47). Woodhead Publishing Limited.

Garcia-Lodeiro, I., Palomo, A., & Fernández-Jiménez, A. (2015b). Crucial insights on the mix design of alkali-activated cement-based binders. In *Handbook of Alkali-Activated Cements, Mortars and Concretes* (pp. 49-73). Woodhead Publishing Limited.

Glasby, T., Day, J., Genrich, R., & Aldred, J. (2015). EFC geopolymer concrete aircraft pavements at Brisbane West Wellcamp Airport. *Concrete*, 1-9.

Glukhovsky, V. (1994). Ancient, modern and future concretes. *Proceedings of the First International Conference on Alkaline Cements and Concretes, Kiev, Ukraine.* (pp. 1-9, vol. 1). VIPOL Stock Company.

Gotti, E., Oleson, J., Bottalico, L., Brandon, C., Cucitore, R., & Hohlfelder, R. (2008). A comparison of the chemical and engineering characteristics of ancient Roman hydraulic concrete with a modern reproduction of Vitruvian hydraulic concrete. *Archaeometry [50]*, 576-590.

Häkkinen, T. (1993). The influence of slag content on the microstructure, permeability and mechanical properties of concrete Part 1. *Cement and Concrete Research. Vol 23*, 407-421.

Hengelhoef Concrete Joints. (2018). *Cosinus Slide Joint*. Retrieved from https://www.hcjoints.be/nl/producten/Sinus-Slide-joints/1/Cosinus-Slide/26

Hetényi, M. (1971). *Beams on Elastic Foundation: theory with applications in the filds of civil and mechanical engineering.* Michigan: University of Michigan.

Kukko, H., & Mannonen, R. (1982). Chemical and mechanical properties of alkali-activated blast furnace slag (F-concrete). *Nordic Concrete Federation 1*, 1-16.

Kumar, S., Kumar, R., & S.P., M. (2010). Influence of granulated blast furnace slag on the reaction, structure and properties of fly ash based geopolymer. *Journal of Materials Science 45(3)*, 607-615.

Lee, N., Jang, H., & Lee, H. (2014). Shrinkage characteristics of alkali-activated fly ash/slag paste and mortar at early ages. *Cement & Concrete Composites 53*, 239-248.

Loonen, N. (2002). Vloeren op grondslag. *Praktijkhandboek Bouw- en Installatietechniek*(6), 1-2.

Loonen, N. (2018). Zettingen beheersen of voorkomen. *Civiele Techniek*(5), 32-35.

Melo Neto, A., Cincotto, M., & Repette, W. (2008). Drying and autogenous shrinkage of pastes and mortars with activated slag cement. *Cement and Concrete Research 38*, 565-574.

Meyerhof, G. (1962). Load-Carrying Capacity of Concrete Pavements. *Journal of the Soil Mechanics and Foundations Division*, Vol. 8, Issue 3, Pg. 89-116.

NEN. (2011). *NEN-EN 1991-1-1:2002+C1:2009+NB:2011*. NEN.

Palacios, M., & Puertas, F. (2007). Effect of shrinkage-reducing admixtures on the properties of alkali-activated slag mortars and pasted. *Cement and Concrete Research 37*, 691-702.

Prinsse, S. (2017). *Alkali-activated concrete: developtment of material properties (strength and stiffness) and flexural behaviour of reinforced beams over time.* TU Delft.

Provis, J. (2013). Alkali-activated binders and concretes: the path to standardization. *Geopolymer Binder Systems*, STP 1566, pp 185-195.

Provis, J., & Van Deventer, J.-T. (2014). Alkali Activated Materials : State-of-the-Art Report, RILEM TC 224-AAM. *NV - 1 0*. Dordrecht :: Springer,.

Puertas, F., Amat, T., Fernández-Jiménez, A., & Vázquez, T. (2003). Mechanical and durable behaviour of alkaline cement mortars reinforced with polypropylene fibres. *Cement and Concrete Research 33(12)*, 2031-2036.

Punt, N., & Meer, L. (2017). Puntlasten op vloeren vaak onderschat. *Cement*, 48-52.

Riemens, K. (2016). Modelling of young hardening underwater concrete with steelfibres in DIANA [PowerPoint slides]. Retrieved from ABT.

RILEM. (2003). Final recommendations of TC 162-TDF, Test and design of methods for steel fibre reinforced concrete, sigma-epsilon-design method. *Materials and Structures*, Vol 36, Issue 262, pp. 560-565.

Rodriguez, E., Bernal, S., Mejía de Gutiérrez, R., & Puertas, F. (2008). Alternative concrete based on alkali-activated slag. *Materiales de Construcción 58(291)*, 53-67.

Sarker, P. (2011). Bond strength of reinforcing steel embedded in fly ash-based geopolymer concrete. *Materials and Structures 44*, 1021-1030.

Shima, S., Chou, L.-L., & Okamura, H. (1987). *Micro and Macro Models for Bond in Reinforced Concrete.* Journal of the Faculty of Engineering, The University of Tokyo (B) Vol. 39 No. 2.

Sofi, M., van Deventer, J., Mendis, P., & Lukey, G. (2007). Engineering properties of inorganic polymer concretes (IPCs). *Cement and Concrete Research 37*, 251-257.

Songpiriyakij, S., Pulngern, T., Pungpremtrakul, P., & Jaturapitakkul, C. (2011). Anchorage of steel bars in concrete by geopolymer paste. *Materials and Design 32*, 3021-3028.

The Concrete Society. (2016). *TR 34: Concrete Industrial Ground Floors - Fourth Edition.* Camberley: The Concrete Society.

Vermeulen, E., & de Vries, P. (2015). De uitdagingen van geopolymeerbeton. *Betoniek 2*, 20-27.

VOBN. (2003). *Monolietvloeren Gietbouw in de utiliteitsbouw.* VOBN.

Wallah, S. (2009). Drying Shrinkage of Heat-Cured Fly Ash-Based Geopolymer Concrete. *Modern Applied Science, 3*(12), 14-21.

Walraven, J., & Braam, C. (2015). *Prestressed Concrete.* Delft University of Technology.

Wang, S.-D., Pu, X.-C., Scrivener, K., & Pratt, P. (1995). Alkali-activated slag cement and concrete: a review of properties and problems. *Advances in Cement Research, 7*(27), 93-102.

Westergaard, H. (1926). Stresses in concrete pavements computed by theoretical analysis. *Public Roads*, Vol. 7, No. 2.

Wongpa, J., Kiattikomol, K., Jaturapitakkul, C., & Chindaprasirt, P. (2010). Compressive strength, modulus of elasticity, and water permeability of inorganic polymer concrete. *Materials and Design 31(10)*, 4748-4754.

Xu, H., Provis, J., van Deventer, J., & Krivenko, P. (2008). Characterization of aged slag concretes. *ACI Materials Journal 105(2)*, 131-139.

Yong, C. (2010). *Shrinkage behaviour of geopolymers.* M.Eng.Sci. thesis, University of Melbourne.

Appendices

Appendix A.   STRUCTURAL PROPERTIES AND DESIGN CALCULATIONS

Introduction

This appendix covers the calculations of the material properties and the structural strength requirements. The chosen reference concrete is of class C30/37. The yellow boxes in the figure below are the adjustable parameters. The minimum recommended thickness of 150 mm is chosen. Normally only a top reinforcement net of ϕ7-100 mm is applied with a steel fibre dosage with minimum residual flexural strengths of 4.4 MPa and 4.0 MPa for f_{R1} and f_{R4}, respectively. In this example lower values are chosen of ϕ6-100, with f_{R1} = 3.0 MPa and f_{R4} = 3.0 MPa to show that the ultimate limit state strength requirements aren't the normative requirements.

Concrete

Class	C30/37	
f_{ck}	30 MPa	
f_{cm}	38 MPa	$= f_{ck} + 8$
f_{ctm}	2.9 MPa	$= 0.3 f_{ck}^{(0.67)}$
E_{cm}	32.8 GPa	$= 22 (f_{cm}/10)^{0.3}$
γ_c	1.5	

Flexural tensile strength

$f_{ctd,fl}$	2.79992 MPa	$= f_{ctm} \times (1.6 - h/1000)/\gamma_m$

Steel fibres - mean axial tensile strengths

f_{R1}	3 MPa	f_{R1}	= the residual flexural strength at CMOD 0.5
f_{R4}	3 MPa	f_{R4}	= the residual flexural strength at CMOD 3.5

σ_{r1}	1.35 MPa	σ_{r1}	$= 0.45 f_{R1}$
σ_{r4}	1.11 MPa	σ_{r4}	$= 0.37 f_{R4}$

Bending moment capacities

Cracking moment plain concrete

M_{cr}	10499.7 Nmm/m'	$= f_{ctd,fl}(h^2/6)$
	10.4997 kNm/m'	

Floor

h	150 mm	
k	0.06 N/mm³	

Base plate racking

x	150 mm
y	125 mm

Equivalent radius

a	77 mm

Reinforcement

ϕ	6 mm
c.t.c.	100 mm
c	30 mm
E_s	200000 MPa
f_{yk}	435 MPa
f_{yd}	435 MPa
γ_s	1.15

d	117 mm
	$= h - c - \frac{1}{2} \cdot \phi$

Shear

V_{max}	5.28 MPa	$= 0.5 k_2 f_{cd}$
k_2	0.5	$= 0.6 (1 - f_{ck}/250)$
$V_{Rd,c,min}$	0.54 MPa	$= 0.5 k_s f_{cd} f_{ck}^{0.5}$
k_s	2.0	$= 1 + (200/d)^{0.5} \le 2$
$V_{Rd,c}$	0.54 MPa	$= \frac{0.18k_s}{\gamma_c}(100\rho_l f_{ck})^{0.33} \ge 0.035 k_s^{1.5} f_{ck}^{0.5}$
ρ_l	0.0024	$= A_{ss}/bd$
V_f	0.18 MPa	$= [0.12 (f_{r1} + f_{r2} + f_{r3} + f_{r4})/4]/2$

Ultimate moment capacity

Fibre reinforcement only

$M_{R,d}$	8068.5 Nmm/m'	$M_u = \frac{h^2}{\gamma_m}(0.29\sigma_{r4} + 0.16\sigma_{r1})$
	8.1 kNm/m'	
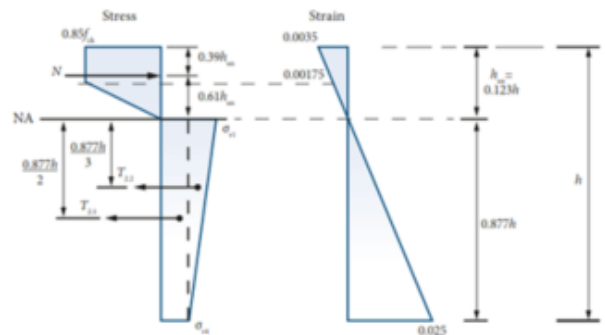
Fibre reinforced + steel bar reinforcement
Where As ≥ 0.15% of gross cross-sectional area

As	283 mm²/m'	
ω	0.19 %	Green = OK

x_u (=h_{ux})	15.1 mm	Solved through equilibrium from:
		$0.64 h_{ux} f_{cd} = (h - h_{ux})[\sigma_{r4} + 0.5(\sigma_{r1} - \sigma_{r4})] + A_s f_{yk}$

only valid if xu < 0.3d

0.3d	35.1 mm	Green = OK

$M_{R,d}$	1.2E+07 Nmm/m'	$M_u = [0.5(\sigma_{r1} - \sigma_{r4})(h - h_{ux})(0.28 h_{ux} + 0.33h)]/\gamma_m$
	11.9 kNm/m'	$+ [\sigma_{r4}(h - h_{ux})(0.11 h_{ux} + 0.5h)]/\gamma_m$
		$+ [A_s f_{yk}(d - 0.39 h_{ux})]/\gamma_s$
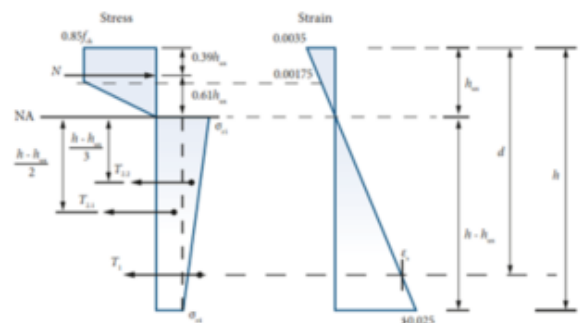
Bending moment capacity

The figure below is an example of a typical hybrid reinforced concrete floor, where steel fibres are distributed throughout the entire floor, the steel reinforcement is only located at the top and the floor is supported by a RCA-layer. The hogging (negative) bending moment capacity will be a lot higher than the sagging (positive) bending moment due to the top reinforcement. On the previous page the calculations are shown for the bending moment capacities which have been done in Excel. These simplified methods are provided in the Fourth Edition of the Technical Report 34: Concrete Industrial ground floors. The methods apply where the steel fibre tensile stresses reduce as the strain increases, so called strain softening. Strain hardening can occur as well which can be reached with a higher fibre dosage, for concrete industrial ground floors such a high dosages aren't commonly seen or applied.
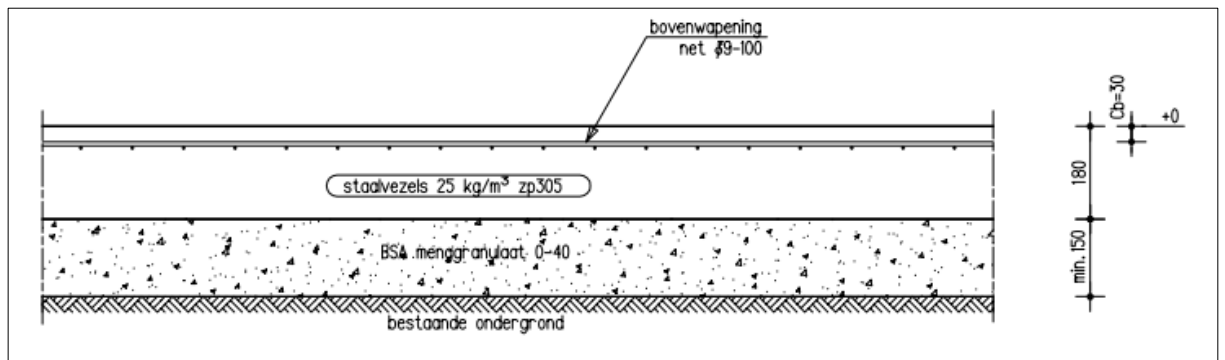
Figure A-1 Detail drawing of a typical hybrid reinforced concrete floor.

The ultimate moment capacity for the fibre only section, sagging moment, is calculated as it's done for traditionally reinforced section where failure occurs when the extreme compressive strain in the concrete is reached. Simultaneously the fibre tensile part is reaching the limiting tensile strain. The positive ultimate moment capacity per meter width $M_{R,d} = M_p = 8.1$ kNm/m'.

The ultimate moment capacity is calculated with the following calculation steps which are computed from the stress diagram in Figure A-2.

$$N \geq T_{2.1} + T_{2.2}$$

$$N = 0.123h * 0.75 * 0.85 * f_{ck} = 0.078h * f_{ck}$$

$$T_{2.1} = 0.88h * \sigma_{r4}$$

$$T_{2.2} = 0.44h * (\sigma_{r1} - \sigma_{r4})$$

Calculating the bending moment about the centroid of compression zone N:

$$M_{Rd} = \left[T_{2.1} \left(\frac{0.877h}{2} + 0.075h \right) + T_{2.2} (\frac{0.877h}{3} + 0.075h) \right] / \gamma_m \qquad (A.1)$$

Which can be simplified to:

$$M_{R,d} = \frac{h^2}{\gamma_m} (0.029\sigma_{r4} + 0.16\sigma_{r1}) \qquad (A.2)$$

135
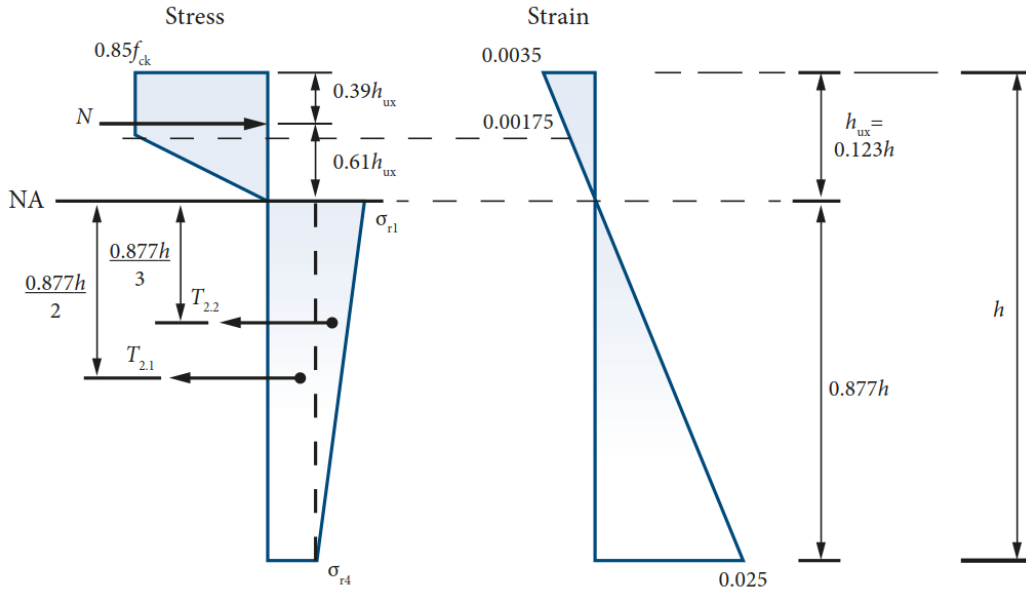
Figure A-2 Stress and strain block for fibre reinforced concrete (The Concrete Society, 2016).

The negative ultimate bending moment capacity, where tension is at the top fibres of the cross-section, can be calculated through the stress diagram shown in Figure A-3. Note that the figure shows an example where the tensile forces and the reinforcement are situated in the bottom part of the floor. This does not change the calculations for the bending moment capacity.

Where steel fibres are combined with steel reinforcement in a section where the area of reinforcement is $A_s \geq 0.15\%$ of the gross cross-sectional area the neutral axis depth h_{ux}, also known as the concrete compressive zone x_u, needs to be found based on equilibrium between the compressive and tensile forces. In the figures h_{ux} is used where in these calculations the notation x_u is used for the neutral axis depth. Assumption that are made to compute this are that the reinforcement is yielding and that the extreme fibre tensile stress is σ_{r4}. The latter one is a slightly conservative assumption as in reality the stress will be slightly higher.

The bending moment capacity and neutral axis depths can be found through the following steps:

$$N = 0.75x_u * 0.85f_{ck}$$

$$T_{2.1} = (h - x_u)\sigma_{r4}$$

$$T_{2.2} = 0.5(h - x_u) * (\sigma_{r1} - \sigma_{r4})$$

$$T_1 = A_s E_s (\frac{d - x_u}{x_u})0.0035$$

Through equilibrium the following equation is computed which can be rewritten to find x_u:

$$0.64x_u f_{ck} = h - x_u [\sigma_{r4} + 0.5(\sigma_{r1} - \sigma_{r4})] + A_s f_{yk}$$

$$x_u = \frac{h\sigma_{r4} + 0.5h\ \sigma_{r1} - \sigma_{r4} + A_s f_{yk}}{0.64f_{ck} + \sigma_{r4} + 0.5\ \sigma_{r1} - \sigma_{r4}} \tag{A.3}$$

Calculating the bending moment about the centroid of compression zone N:

$$M_{Rd} = \frac{[0.5 \; \sigma_{r1} - \sigma_{r4} \quad h - x_u \quad 0.28x_u + 0.33h \;]}{\gamma_m}$$
$$+ \frac{[\sigma_{r4} \quad h - x_u \quad 0.11x_u + 0.5h \;]}{\gamma_m} + \frac{[A_s f_{yk} \quad d - 0.39x_u \;]}{\gamma_s}$$

<div align="right">(A.4)</div>

The above equation is valid when $x_u \leq 0.3d$ to ensure the ductility of the floor so the yield line theory is valid and applicable.

The negative bending moment capacity for the assumed floor is $M_{R,d} = M_n = 11.9$ kNm/m'.
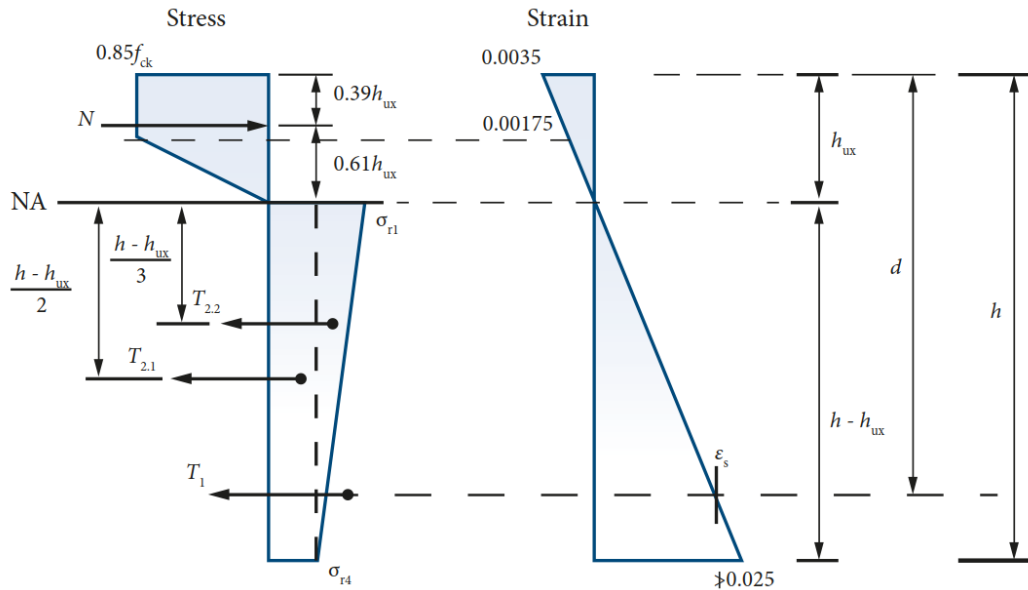
Figure A-3 Stress and strain block for fibre and steel reinforced concrete (The Concrete Society, 2016).

Yield line theory

In 1962 Meyerhof obtained design formulae for point loads for internal, edge and corner loads. With an ulitmate strength analysis of slabs based on plastic analysis, the yield line theory, he formulated his equations (Meyerhof, 1962).

For a single point load the maximum positive bending moment, tension at the bottom of the slab, is directly under the point load. When the the flexural stresses at the bottom reach the flexural strength of the concrete the slab will start to yield. This yielding will lead to radial cracks in the bottom of the slab. With proper ductility and an increase of the load the moments will be redistributed and the circumferential moments will increase where tensile stresses at the top of the slab occur. If the negative circumferential bending moments reach the negative ultimate bending moment capacity failure is considered. A full yield line pattern and a cracking pattern like in Figure A-4 will be reached.
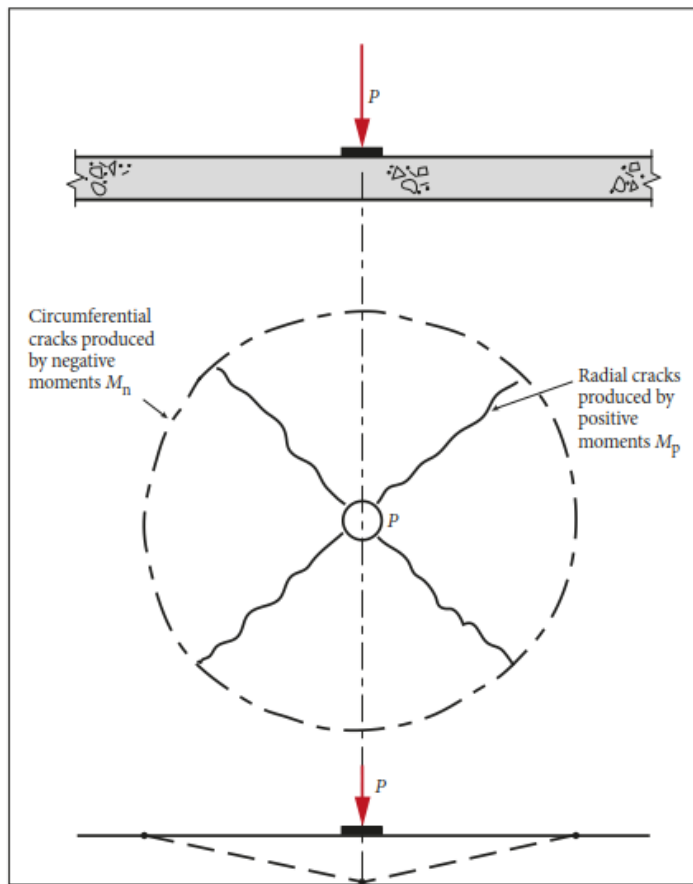
Figure A-4 Radial and circumferential cracking pattern for a concrete floor on subgrade (The Concrete Society, 2016).

The circumferential cracks will appear some distance away from the location of the point load. This distance can be found with the so-called radius of relative stiffness l which has been introduced by Westergaard and can be determined as (Westergaard, 1926):

$$l = \left(\frac{E_{cm} h^3}{12 \; 1 - \nu^2 \; k} \right)^{0.25}$$ (A.5)

For the case of a single point load the maximum positive bending moment is directly under said point load, the circumferential moment remains positive but decreases with distance. At a distance of 1.0 l from the load the bending moment is zero, which with a further distance becomes negative and has its maximum negative bending moment at a distance 2.0 l. The bending moment approaches a zero value again at the distance 3.0 l from the load. With the radius of relative stiffness the influence of additional loads can be found. If a second load is located within the radius of relative stiffness the result will be an increase in the positive bending moment below the loads. When the secondary load is located between 1.0 l and 3.0 l the positive bending moment below the first load will see a decrease.
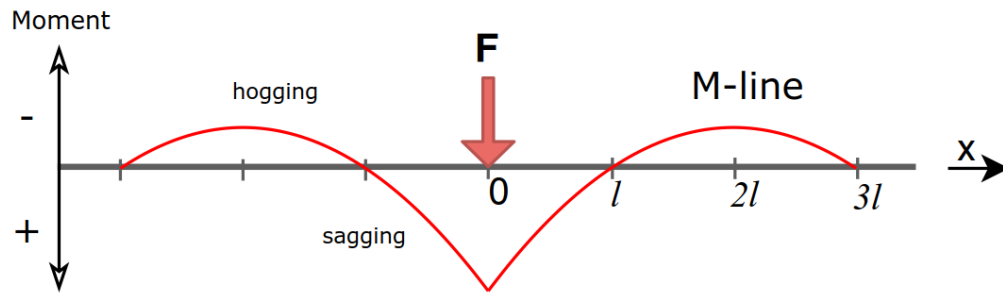
Figure A-5 Schematic of the distribution of the bending moment from a point load on an elastic founded slab.

The design equations for point loads that Meyerhof designed are different depending on the load locations. Meyerhof formulated his design equations for internal, edge and corner loads. For each location a pair of equations is given, a theoretical point load, like a singularity, and a patch load. The definition is dependant on the equivalent radius of contact area of the load a and the radius of relevant stiffness l. The theoretical point load is considered when the contact area is zero and the ratio $a/l = 0$. Patch loads are considered when this ratio is $a/l \geq 0.2$. It has been shown by later studies that linear interpolation is applicable for values of a/l between 0 and 0.2 (Beckett, 2003).

The three load locations are schematised in Figure A-6. When the center of a load is located at a distance of more than $(a + l)$ from a free edge or a joint in can be considered as an internal load. Edge loads are considered when the center of the load is a distance a from a free edge or joint. In case the center of the load has two edges or joints at a distance a beside it, it is considered a corner load. This thesis considers jointless floors so the edge load or corner load will only be situated at the free edges of the floor.
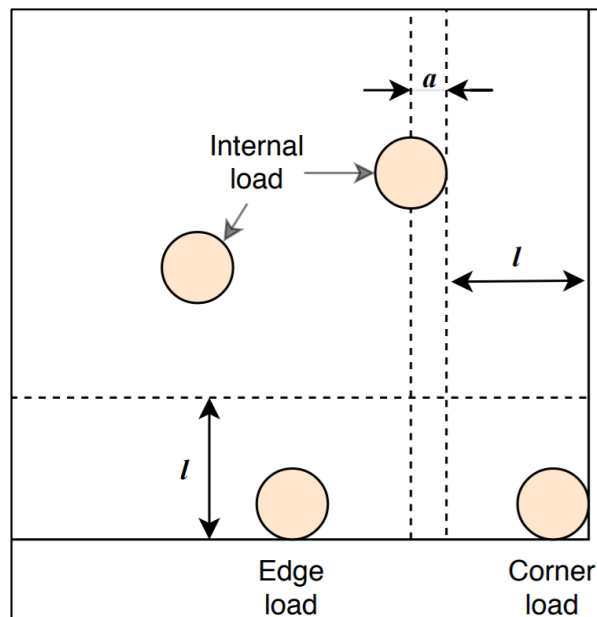
Figure A-6 Load locations defined with by the radius of relative stiffness l and the equivalent radius of contact area of the load a.

Flexure

On the next page the calculations for the back-to-back racking loads are shown.

A back-to-back racking with a distance between the base plates of 300 mm is considered. The base plate widths are assumed at 150 and 125 mm, which gives an equivalent radius of contact area a = 77 mm. The double point loads may be considered as a single load due to the fact that the distance between the point loads is less than double the thickness of the floor. Figure A-7 shows the schematization of this concept. The two point loads may be considered as one single point load with an equivalent total contact area where the grey part may be contributed as well. From this total contact area a new equivalent radius of contact area of the load can be computed.

The design equation for a single internal point load is as followed:

$$ P_{u,0.2} = \frac{4\,\pi\,(M_p + M_n)}{1 - \left(\frac{a}{3l}\right)} \tag{A.6} $$

With the earlier calculated sagging and hogging bending moment capacities for the hybrid reinforced concrete floor the failure load is found at $P_{u,0.2}$ = 275 kN. Considering the double point load in ULS for a CC1 building the ultimate load is F_{Ed} = 257 kN. This results in a unity check of UC = 0.93.

The design failure load for the edge and corner load locations are 134 kN and 65 kN, respectively. This shows a benefit of the jointless floor system, as loads that are located near joints have a failure load that is almost twice as low. For an industrial warehouse it is possible with proper care to position the static loads away from the joints, this will however not be the case for the dynamic loads.
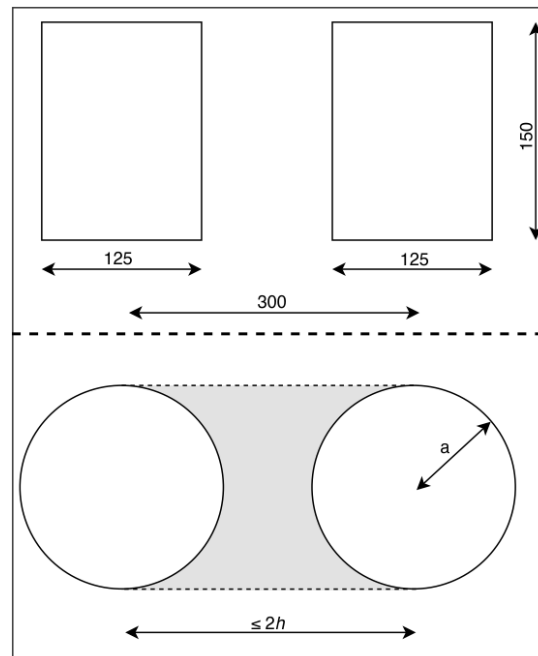
Figure A-7 Schematization for the equivalent contact area for two adjacent point loads.

140

Radius of relative stiffness I and contact area a	
Poisson's ratio	
v	0.2
I	633 mm $= [(E_{cm} h^3) / (12 (1 - v^2) k)]^{0.25}$
Equivalent radius of single load	
a_{single}	77 mm
Adjacant double point load	
Distance apart back-to-back	
$l_{spacing}$	300 mm
Considered as one load?	
$l_{spacing} \leq 2h$	300 mm Green = Yes
Equivalent contact area	
$A_{base\ plates}$	90000 mm^2
a_{double}	169 mm

Hybrid concrete floor

Steel fibres with top reinforcement

Sagging bending moment capacity

M_p 8.1 kNm

Hogging bending moment capacity

M_n 11.9 kNm

ULS load F_{ed}			
Single point load		CC1	Double load ULS
F	95 kN	F_{Ed}	=2·95·1.35 257 kN

Meyerhof: design load single point loads	
Theoretical point load	a/l =0
Patch load	a/l ≥ 0.2
Linear interpolation	0 < a/l < 0.2
a/l 0.27 ⟶ Patch load	

Internal design load

Theoretical load	Patch load
$P_{u,0} = 2\pi (M_p + M_n)$	$P_{u,0.2} = 4\pi (M_p + M_n) / [1 - (a/3l)]$
$P_{u,0} =$ 125 kN	$P_{u,0.2} =$ 275 kN

Edge design load

Theoretical load	Patch load
$P_{u,0} = [\pi (M_p + M_n)/2] + 2M_n$	$P_{u,0.2} = [\pi (M_p + M_n) + 4 M_n]/\left[1 - \frac{2a}{3l}\right]$
$P_{u,0} =$ 55 kN	$P_{u,0.2} =$ 134 kN

Corner design load

Theoretical load	Patch load
$P_{u,0} = 2M_n$	$P_{u,0.2} = 4M_n / [1 - (a/l)]$
$P_{u,0} =$ 24 kN	$P_{u,0.2} =$ 65 kN

Considering single point loads or double point loads where their distance is further apart similar results are found. Meyerhof formulated design equations for multiple loads, i.e. dual and quadruple point loads. The same principal holds that linear interpolation is suitable for values of a/l between 0 and 0.2.

On the next page in the bottom right the dual and quadruple design equation are shown and in the bottom left the linear interpolation results. Similar conclusions can be drawn from the calculations. Internal single point loads have a failure load which is approximately 2 and 4 times higher than the corresponding edge and corner failure load, respectively. The internal dual design load, which could be considered as the normative load situation, in this case has a failure load of $P_{u,a/l} = 232$ kN. This gives a unity check of UC = 1.11. This is the situation where failure would occur in this extreme case.

This shows that for a pretty thin concrete floor for flexural failure to occur very high point loads need to act on the floor. That is if with proper ductility the yield line patterns can be reached through the redistribution of the bending moments in the circumferential area of the point loads.

Radius of relative stiffness I and contact area a	
Poisson's ratio	
v	0.2

$$I = 633 \text{ mm} = [(E_{cm}\, h^3) / (12\,(1 - v^2)\,k)]^{0.25}$$

Equivalent radius of single load	
a_{single}	77 mm

Adjacant double point load	
Distance apart back-to-back	
$I_{spacing}$	400 mm
Considered as one load?	
$I_{spacing} \leq 2h$	300 mm Green = Yes
	Red = No
Equivalent radius of single load ←	
a_{single}	77 mm

Hybrid concrete floor	
Steel fibres with top reinforcement	
Sagging bending moment capacity	
M_p	8.1 kNm
Hogging bending moment capacity	
M_n	11.9 kNm

Linear interpolation single design loads.	
Internal design load	
$P_{u,a/l}$	208 kN
Edge design load	
$P_{u,a/l}$	95 kN
Corner design load	
$P_{u,a/l}$	42 kN
Internal design dual load	
$P_{u,a/l}$	232 kN
Internal design quadruple load	
$P_{u,a/l}$	256 kN

ULS load F_{ed}			
Single point load		CC1	Double load ULS
F	95 kN	F_{Ed}	= 2·95·1.3 257 kN

Meyerhof: design load single point loads	
Theoretical point load	a/l = 0
Patch load	a/l ≥ 0.2
Linear interpolation	0 < a/l < 0.2
a/l 0.12 ⟶ Linear interpolation	

Internal design load

Theoretical load	Patch load
$P_{u,0} = 2\pi\,(M_p + M_n)$	$P_{u,0.2} = 4\pi\,(M_p + M_n) / [1 - (a/3l)]$
$P_{u,0} =$ 125 kN	$P_{u,0.2} =$ 261 kN

Edge design load

Theoretical load	Patch load
$P_{u,0} = [\pi\,(M_p + M_n)/2] + 2M_n$	$P_{u,0.2} = [\pi\,(M_p + M_n) + 4M_n]/\left[1 - \frac{2a}{3l}\right]$
$P_{u,0} =$ 55 kN	$P_{u,0.2} =$ 120 kN

Corner design load

Theoretical load	Patch load
$P_{u,0} = 2M_n$	$P_{u,0.2} = 4M_n / [1 - (a/l)]$
$P_{u,0} =$ 24 kN	$P_{u,0.2} =$ 54 kN

Meyerhof multiple internal point loads.	
Design load dual point loads	

Theoretical load	Patch load
$P_{u,0} = [2\pi + (1.8\,x\,/l)][M_p + M_n]$	$P_{u,0.2} = \left[\dfrac{4\pi}{1-(a/3l)} + \dfrac{1.8x}{1-(a/2)}\right][M_p + M_n]$
$P_{u,0} =$ 148 kN	$P_{u,0.2} =$ 286 kN

Design load quadruple point loads

Theoretical load	Patch load
$P_{u,0} = \left[2\pi + \dfrac{1.8\,(x + y)}{l}\right][M_p + M_n]$	$P_{u,0.2} = \left[\dfrac{4\pi}{1-(a/3l)} + \dfrac{1.8(x + y)}{1-(a/2)}\right][M_p + M_n]$
$P_{u,0} =$ 171 kN	$P_{u,0.2} =$ 310 kN

142

Theory of Westergaard

The flexural tensile stresses in a concrete slab due to a point load can be calculated with the formulas of Westergaard. These are based on an infinite long thin plate founded on a Winkler-foundation. Similar like Meyerhof there are equations for the different load locations, i.e. the internal, edge and corner load locations.

Over the years the theory and formulas of Westergaard have been reviewed, therefore there are different notations to be found for the calculations of the stresses. The Dutch CUR-Recommendation 36 for the design of elastic supported concrete floors is considered here with the following formulas (CURNET, 2011).

In the recommendation the equivalent radius of the contact surface area a is considered in the middle of the concrete floor:

$$a = a_c + 0{,}5h + h_d \tag{A.7}$$

Here a_c is the equivalent radius of the contact area at the surface, which earlier in this annex was noted as a. The notation h_d is the thickness of a finishing layer on the concrete floor. Monolithically finished floors have no additional finishing layer and the value of h_d is considered as zero.

Besides the radius of relative stiffness l, Westergaard gives the relation for the equivalent radius of the resisting section b:

$$b = \begin{cases} \sqrt{1.6a^2 + h^2} - 0.675\ h, & a < 1.724h \\ a, & otherwise \end{cases} \tag{A.8}$$

In the following formulas for the internal and edge conditions the maximum stress is calculated at the bottom side of the floor. For the corner condition the maximum stress calculated is situated at the top side of the floor. The formulas provided here are simplified approximations where the Poisson ratio is taken into account as $\nu = 0.15$ for the concrete.

Internal stress
$$\sigma_m \approx \frac{0.55F}{h^2}\ [\ln\left(\frac{l}{b}\right) + 0.62] + \frac{0.05F}{h^2}\left(\frac{b}{l}\right)^2 \tag{A.9}$$

Edge stress
$$\sigma_e \approx \frac{0.35F}{h^2}\ [\ln\left(\frac{Eh^3}{100ka^4}\right) + 2.07 + 1.53(\frac{a}{l})] \tag{A.10}$$

Corner stress
$$\sigma_c = \frac{3F}{h^2}\ [1.0 - \left(\frac{a\sqrt{\pi}}{l}\right)^{0.72}] \tag{A.11}$$

The stresses in the outer concrete fibres according to Westergaard are computed for the same floor shown on the following page. All the tensile stresses are relatively high exceeding the tensile strength f_{ctm} of all the concrete classes. This does not necessarily mean that the concrete floor fails, but that cracks will occur. Westergaard's theory is applicable in the case that cracking should be fully prevented. In this example cracks do appear, which is in line with the yield line theory where along the yield lines the bending moment capacity has to be The same conclusions from the yield line theory that can be drawn from the calculated tensile stresses, is that the internal tensile stresses are the lowest showing the same benefit of the jointless floor concept.

Theory of Westergaard	

radius of relative stiffness l		thickness floor	
l	630 mm	h	150 mm
equivalent radius of contact area		E-modulus concrete	
a	$= a_c + 0.5h$	E	32837 MPa
a	152 mm	Poisson ratio	
		v	0.15
equivalent radius of resisting section		Subgrade	
b	143 mm	k	0.06 N/mm^3

Stresses single load

$F_{Ed} = F \cdot 1.35$ 128 kN

Internal stress - tensile stress at bottom fibre

$\sigma_m =$ 6.6 MPa
$$\sigma_m \approx \frac{0{,}55F}{h^2} \left[\ln\left(\frac{l}{b}\right) + 0{,}62\right] + \frac{0{,}05F}{h^2}\left(\frac{b}{l}\right)^2$$

Edge stress - tensile stress at bottom fibre

$\sigma_e =$ 11.9 MPa
$$\sigma_e \approx \frac{0{,}35F}{h^2} \left[\ln\left(\frac{Eh^3}{100ka^4}\right) + 2{,}07 + 1{,}53\left(\frac{a}{l}\right)\right]$$

Corner stress - tensile stress at top fibre

$\sigma_c =$ 7.8 MPa
$$\sigma_c = \frac{3F}{h^2} \left[1{,}0 - \left(\frac{a\sqrt{\pi}}{l}\right)^{0{,}72}\right]$$

Punching shear

As the dominant design loads are point loads for industrial ground floors the ultimate strength mode of failure punching shear needs to be considered. The punching shear capacity is determined by checking the shear capacity at the critical perimeter. The critical perimeter is distanced *2d*, where *d* is the effective depth, from the face of the of the contact area, see Figure A-8.

As the concrete floor is in direct contact with the subgrade a proportion of the load within the punching shear parameter can be considered to be applied directly to the subgrade. This proportion can be deducted from the imposed shear load. Figure A-8 illustrates the ground pressure below a concentrated point load, the sum of the ground pressure within the critical perimeter is the said proportion that may be deducted from the shear load. For a single internal patch load, where $a/l < 0.2$, the total reaction R_p within the critical perimeter can be calculated with:

$$R_p = 1.4 \left(\frac{d}{l}\right)^2 P + 0.47 \; x + y \; \frac{dP}{l^2} \tag{A.12}$$

Where P is the point load and *x* and *y* are the effective dimensions of the base plate.
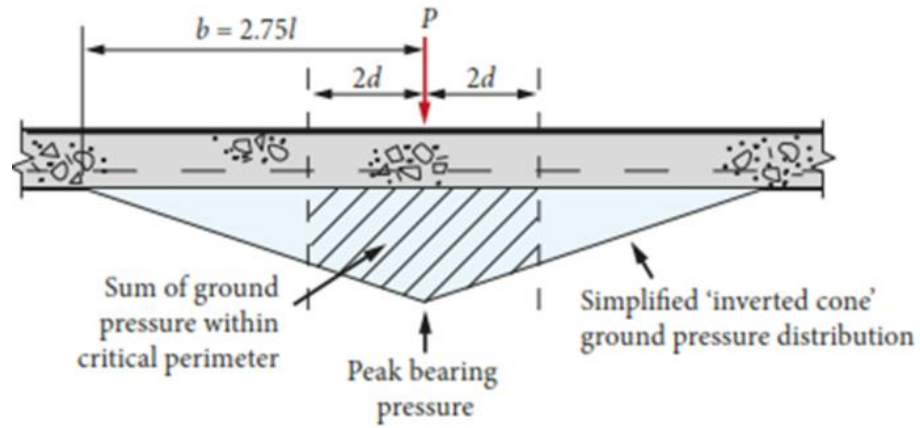
Figure A-8 Ground-pressure below an internal load (The Concrete Society, 2016).

The load capacity depends on the shear capacity at the face of the loaded area. For traditional concrete the average shear stress, according to the Eurocode 2, is given by:

$$v_{Rd,c} = \frac{0.18 k_s}{\gamma_c} \, 100 \rho f_{ck}^{\,0.33} \geq 0.035 \, k_s^{1.5} f_{ck}^{0.5} \tag{A.13}$$

The reinforcement net has the same diameter in both directions, so $\rho = \rho_x$. The factor k_s is found with:

$$k_s = 1 + \left(\frac{200}{d}\right)^{0.5} \leq 2.0$$

The concrete floor is hybrid reinforcemed, several studies that the presence of steel fibres will increase the shear capacity in a concrete section, mainly in addition with the presence of conventional reinforcement (RILEM, 2003). For steel-fibre only reinforced slabs the punching shear capacity can show an increase as well with fibres dosages that are higher than the typical fibre dosage seen in industrial concrete floors.

The RILEM suggest that this increase is equal to 0.12 times of the residual flexural strength, where the mean flexural strength is taken. The Concrete Society suggest for the industrial floors to take a conservative approach to only take 50% of this increase into account. The increase in shear strength is therefore given by:

$$v_f = \left[\frac{0.12 \, f_{r1} + f_{r2} + f_{r3} + f_{r4}}{4}\right] / 2 = 0.015 \, f_{r1} + f_{r2} + f_{r3} + f_{r4} \tag{A.14}$$

So the total slab load capacity P_p will therefore be:

$$P_p = (v_{Rd,c} + v_f) \, u_1 d \tag{A.15}$$

Where u_1 is the length of the perimeter at the distance $2d$ from the loaded area. The outline of this critical perimeter is shown as the dotted line u_1 in Figure A-9 for internal single and double point loads, where for the latter the center of the base plates is distanced less than $2h$. In that case the double loads can be considered as a single point load where the contact area may be added up.
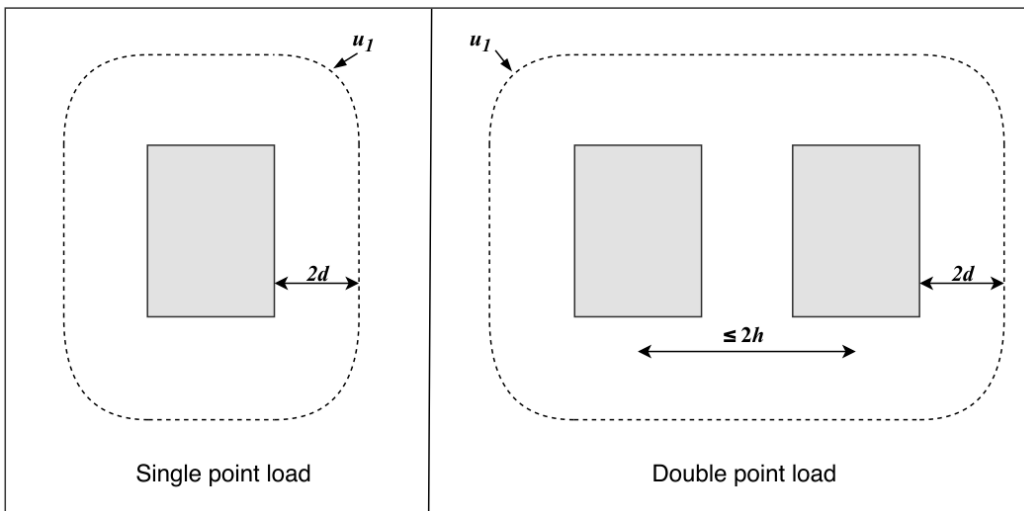
Figure A-9 Critical perimeter for punching shear for internal single and double point loads.

For single and double point loads the punching shear checks are computed below. The unity check is found by dividing the design load P_{Ed} by the shear load capacity P_p. The singular point load shows a unity check of UC = 0.69, the double point load where the critical perimeter is increased and the ULS load is twice as high a unity check of UC = 0.95 is found.

This proves that the hybrid reinforced concrete floor with a thickness of 150 mm will pass the punching shear ultimate strength check as well.

Punching shear	
F=	95 kN
P= 1.35*F	128250 N
Double load	
P= 1.35*2*F	256500 N

Effective depth and radius of relative stiffness	
d	117 mm
l	633 mm

Base plate	
x	150 mm
y	125 mm

Ground reaction

$$R_p = 1.4 \left(\frac{d}{l}\right)^2 P + 0.47(x+y)\frac{dP}{l^2}$$

R_{cp} (single load)	10982 N
R_{cp} (double load)	21963 N

Shear

V_{max}	5.28 MPa	$= 0.5k_2 f_{cd}$
k_2	0.5	$= 0.6 (1 - f_{ck}/250)$
$V_{Rd,c,m}$	0.54 MPa	$= 0.5k_2 f_{cd}\, f_{ck}^{0.5}$
k_s	2.0	$= 1 + (200/d)^{0.5} \le 2$
$V_{Rd,c}$	0.54 MPa	$= \frac{0.18k}{\gamma_c}(100\rho_l f_{ck})^{0.33} \ge 0.035 k_s^{1.5} f_{ck}^{0.5}$
ρ_l	0.0024	$= A_{sx}/bd$
V_f	0.18 MPa	$= [0.12 (f_{r1} + f_{r2}+f_{r3} +f_{r4})/4]/2$

Punching shear capacity				
Singe load		**Double load**		
Critical perimeter		Critical perimeter		
u_1	2020 mm	u_1	2920 mm	
Load capacity		Load capacity		
P_p	170711 N	$P_p = (v_{Rd,c} + v_f)\, u_1 d$	P_p	246761 N	$P_p = (v_{Rd,c}+v_f)\, u_1 d$
Design load		Design load		
P_{Ed}	117268 N	$P_{Ed} = P - R_{cp}$	P_{Ed}	234537 N	$P_{Ed} = P - R_{cp}$
UC	0.69	UC	0.95	

Uniformly distributed loads

Floors that will be loaded by uniformly distributed loads can be calculated based on the theory for beams on elastic foundation by Hetényi. This analysis uses a global safety factor of 1.5 which means an additional safety factor for the loads isn't required (Hetényi, 1971). The bending moments in the ground-supported floors incorporate the term λ:

$$\lambda = \left(\frac{3k}{E_{cm}h^3}\right)^{0.25} \tag{A.16}$$

Where the factor λ is has a dimension of (length)$^{-1}$, the term $(1/\lambda)$ is known as the characteristic length.

A typical example of an uniformly distributed load is block stacking, the two governing situations are considered where the extreme hogging and sagging bending moments will occur. This maximum positive bending moment is found when the breadth of the load is $\pi/2\lambda$ as shown in Figure A-10(a) and the maximum negative bending moment is induced between a pair of loads with each a breadth of π/λ distanced $\pi/2\lambda$ apart, Figure A-10(b). This distance is called the critical aisle width.
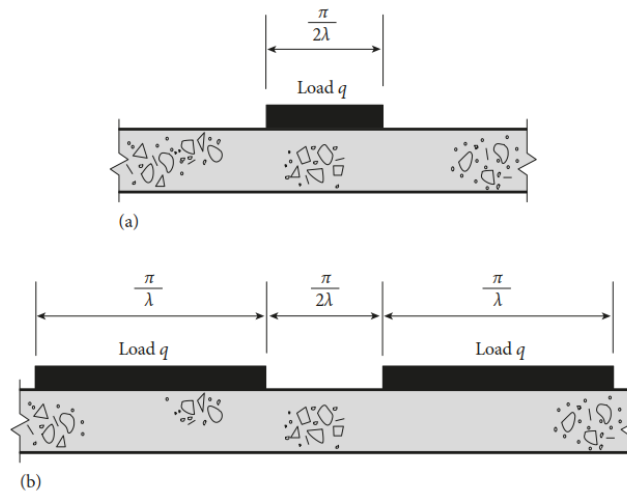
Figure A-10 Loading patterns for uniformly distributed loads *q* causing (a) the maximum positive bending moment and (b) the maximum negative bending moment (The Concrete Society, 2016).

The design formulas for the two normative situations are shown in the calculation scheme on the next page. The calculations are made for uniformly distributed loads on a jointless floor, so there are only loads present in the middle sections of the floor. The provided formulas are designed for the free edges, for the middle sections these formulas must be divided by *(1-v²)*. The example is calculated with the same floor properties of this annex and a conservative assumption for *q* = 75 kN/m².
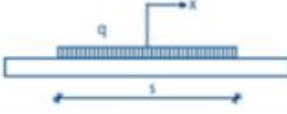
The analysis of Hetényi is based on elastic distributed of the bending moment so the cracking moment M_{cr} of the concrete must be considered (The Concrete Society, 2016). This depends on the design flexural tensile strength and can be found with:

$$M_{cr} = f_{ctd,fl}\left(\frac{h^2}{6}\right) \tag{A.17}$$

With $f_{ctd,fl} = \frac{f_{ctm}\left(1.6 - \frac{h}{1000}\right)}{\gamma_m}$

It can be found that the extreme hogging and sagging bending moments remain below this cracking bending moment. The floor can resist the considered relatively high uniformly distributed load.

Theory of Hetényi

λ	0.00113 1/mm	$\lambda = [k/(4EI)]^{0.25} = [3k/(Eh^3)]^{0.25}$
λ	1.13 1/m'	
Characterisic length		
$1/\lambda$	886 mm	

Floor

E-modulus $E_{cm} =$	32837 MPa	
	$E_{cm} =$	3.3E+07 kN/m^2
Thickness	$h =$	150 mm
	$h =$	0.15 m
Subgrade	$k =$	0.06 N/mm^3
	$k =$	60000 kN/m^3

Uniformly distributed load
$q =$ 75 kN/m^2

Maximum bending moments due to UDL

Positive (sagging) bending moment

a	0.70 -	$a = \pi/4\lambda$
$B\lambda a$	0.32 -	$B\lambda_x = e^{-\lambda x}.\sin\lambda x$
$M_{p,max}$	9.49 kNm	$M = [q/2\lambda^2].B\lambda_a$
	9.70 kNm	$M_{p,max} = M/(1-v^2)$

Situation a:

Cracking moment

f_{ctm}	=	2.90 MPa
$f_{ctd,fl}$	=	2.80 MPa

$$f_{ctd,fl} = f_{ctm} \times (1.6 - h/1000)/\gamma_m$$

M_{cr}	=	10500 Nmm/m'
		10.50 kNm/m'

$$M_{un} = f_{ctd,fl}(h^2/6)$$

Negative (hogging) bending moment

a	0.70 -	$a = \pi/4\lambda$
b	3.48 -	$b = 5a$
$B\lambda a$	0.32 -	$B\lambda_x = e^{-\lambda x}.\sin\lambda x$
$B\lambda b$	-0.01 -	
$M_{n,max}$	-9.90 kNm	$M = [-q/2\lambda^2].(B\lambda_a - B\lambda_b)$
	-10.12 kNm	$M_{n,max} = M/(1-v^2)$

Situation b:

Unity checks

Situation a
UC	0.92	$UC = M_{p,max}/M_{cr}$

Situation b
UC	0.96	$UC = |M_{n,max}/M_{cr}|$

Concluding

This annex shows that with relatively high variable loads the ultimate limit state strength checks are satisfied for a relatively thin concrete floor. Where the reinforcement and fibres dosages are below the minimum that is normally applied in concrete industrial floors. The serviceability limit state and its control of cracking are normative in the design for the concrete floors that elastically supported.

ULS checks for ABT minimum floor dimensions from section 2.5.2

In the following pages the Excel sheets and the calculations are shown like they are previously described but for a concrete floor that meets the nowadays standards of ABT. The same concrete class C30/37 is considered, a thickness of $h = 170$ mm with a steel reinforcement net of ϕ7-100 mm with a steel fibre content that will provide the minimum required residual flexural tensile strengths of $f_{R1} = 4.4$ MPa and $f_{R4} = 4.0$ MPa. The same minimal cover of 30 mm is taken.

Concrete

Class C30/37		
f_{ck}	30 MPa	
f_{cm}	38 MPa	$= f_{ck} + 8$
f_{ctm}	2.9 MPa	$= 0.3 f_{ck}^{(0.67)}$
E_{cm}	30.0 GPa	$= 22 (f_{cm}/10)^{0.3}$
γ_c	1.5	

Flexural tensile strength

$f_{ctd,fl}$	2.781 MPa	$= f_{ctm} \times (1.6 - h/1000)/\gamma_m$

Steel fibres - mean axial tensile strengths

f_{R1}	4.4 MPa	f_{R1}	= the residual flexural strength at CMOD 0.5
f_{R4}	4 MPa	f_{R4}	= the residual flexural strength at CMOD 3.5

σ_{r1}	1.98 MPa	σ_{r1}	$= 0.45 f_{R1}$
σ_{r4}	1.48 MPa	σ_{r4}	$= 0.37 f_{R4}$

Bending moment capacities

Cracking moment plain concrete

M_{cr}	11864 Nmm/m'	$= f_{ctd,fl} (h^2/6)$
	11.86 kNm/m'	

Ultimate moment capacity

Fibre reinforcement only

$M_{R,d}$	12732 Nmm/m'	$M_u = \dfrac{h^2}{\gamma_m}(0.29\sigma_{r4} + 0.16\sigma_{r1})$
	12.7 kNm/m'	

Floor

h	160 mm	
k	0.06 N/mm³	

Base plate racking

x	150 mm
y	125 mm

Equivalent radius

a	77 mm

Reinforcement

ϕ	7 mm
c.t.c.	100 mm
c	30 mm
E_s	200000 MPa
f_{yk}	500 MPa
f_{yd}	435 MPa
γ_s	1.15

d	126.5 mm
	$= h - c - \frac{1}{2}\cdot\phi$

Shear

V_{max}	5.28 MPa	$= 0.5 k_2 f_{cd}$
k_2	0.5	$= 0.6 (1 - f_{ck}/250)$
$V_{Rd,c,min}$	0.54 MPa	$= 0.5 k_s f_{cd} f_{ck}^{0.5}$
k_s	2.0	$= 1 + (200/d)^{0.5} \le 2$
$V_{Rd,c}$	0.54 MPa	$= \dfrac{0.18 k_s}{\gamma_c}(100\rho_l f_{ck})^{0.33} \ge 0.035 k_s^{1.5} f_{ck}^{0.5}$
ρ_l	0.003	$= A_{ss}/bd$
V_f	0.252 MPa	$= [0.12(f_{r1}+f_{r2}+f_{r3}+f_{r4})/4]/2$
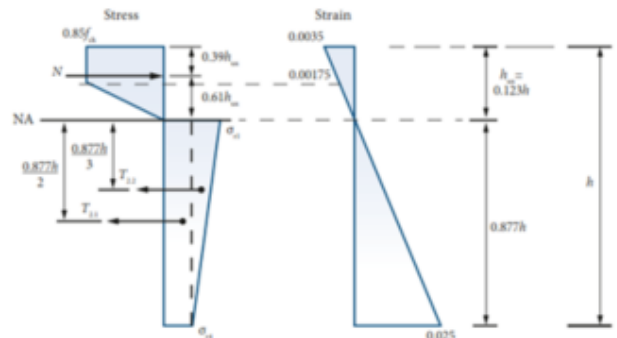
Fibre reinforced + steel bar reinforcement

Where As ≥ 0.15% of gross cross-sectional area

As	385 mm²/m'	
ω	0.24 %	Green = OK

x_u (=h_{u}	22.4 mm	Solved through equilibrium from:
		$0.64 h_{us} f_{cd} = (h - h_{us})[\sigma_{r4} + 0.5(\sigma_{r1} - \sigma_{r4})] + A_s f_{yk}$

only valid if xu < 0.3d

0.3d	37.95 mm	Green = OK

		$M_u = [0.5(\sigma_{r1} - \sigma_{r4})(h - h_{us})(0.28 h_{us} + 0.33h)]/\gamma_m$
$M_{R,d}$	2E+07 Nmm/m'	$+ [\sigma_{r4}(h - h_{us})(0.11 h_{us} + 0.5h)]/\gamma_m$
	19.72 kNm/m'	$+ [A_s f_{yk}(d - 0.39 h_{us})]/\gamma_s$
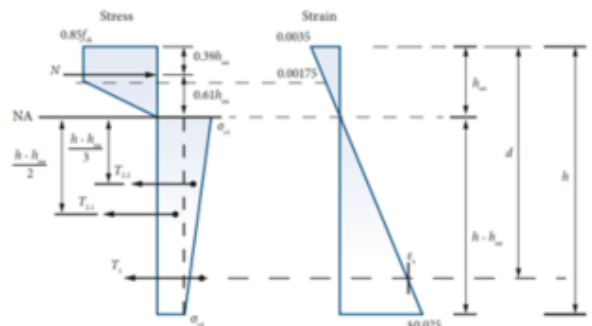
Meyerhof: Double point load considered as a single load.

Radius of relative stiffness l and contact area a
Poisson's ratio
v 0.2
l 649 mm $= [(E_{cm} h^3) / (12 (1 - v^2) k)]^{0.25}$

Equivalent radius of single load
a_{single} 77 mm

Adjacant double point load
Distance apart back-to-back
$l_{spacing}$ 300 mm
Considered as one load?
$l_{spacing} \leq 2h$ 320 mm   Green = Yes
Equivalent contact area
$A_{base\ plates}$ 90000 mm^2
a_{double} 169 mm

Hybrid concrete floor
Steel fibres with top reinforcement
Sagging bending moment capacity
M_p 12.7 kNm
Hogging bending moment capacity
M_n 19.7 kNm

ULS load F_{ed}		
Single point load	CC1	Double load ULS
F 95 kN	F_{Ed}	=2·95·1.35 257 kN

Meyerhof: design load single point loads	
Theoretical point load	a/l =0
Patch load	a/l ≥ 0.2
Linear interpolation	0 < a/l < 0.2
a/l 0.26 $\longrightarrow$ Patch load	

Internal design load

Theoretical load	Patch load
$P_{u,0} = 2\pi (M_p + M_n)$	$P_{u,0.2} = 4\pi (M_p + M_n) / [1 - (a/3l)]$
$P_{u,0} =$ 204 kN	$P_{u,0.2} =$ 447 kN

Edge design load

Theoretical load	Patch load
$P_{u,0} = [\pi (M_p + M_n)/2] + 2M_n$	$P_{u,0.2} = [\pi (M_p + M_n) + 4 M_n]/\left[1 - \frac{2a}{3l}\right]$
$P_{u,0} =$ 90 kN	$P_{u,0.2} =$ 219 kN

Corner design load

Theoretical load	Patch load
$P_{u,0} = 2M_n$	$P_{u,0.2} = 4M_n / [1 - (a/l)]$
$P_{u,0} =$ 39 kN	$P_{u,0.2} =$ 107 kN

The above calculations show an internal design load of 447 kN, similar with the previous results the design edge load of 219 kN is about twice as low. These higher design loads than in the previous example can be contributed to the cause that the sagging and hogging bending moment capacities are increased. The concrete compressive zone x_u is still within the limit of 0.3d to ensure enough ductility such that the redistribution of the bending moments is possible.

If the spacing between the base plates of the back-to-back racking's is above 2h they'll be considered as single separate point loads. The ultimate internal design loads found are 335 kN and 373 kN, which is well above the ULS load of 257 kN meaning no flexural failure will occur.

Computing the flexural tensile stresses with the theory of Westergaard it can be found that the tensile strength of the concrete will be exceeded, cracks will still occur. Structural engineers will know that the cracking of structural concrete is inevitable and necessary for the reinforcement and steel fibres to be utilised.

The two final checks for punching shear and the extreme bending moments due to uniformly distributed loads both show unity checks that are below 1.0.

The calculations are made for a concrete floor with the minimum acceptable dimensions applied in The Netherlands, considering the thickness, the reinforcement and the steel fibre content. The loads applied are of the highest kind seen in The Netherlands nowadays. All ULS design checks are fulfilled, confirming that the SLS design criteria can be considered as normative.

Meyerhof: Double point load flexure

Radius of relative stiffness l and contact area a	
Poisson's ratio	
v	0.2
l	649 mm $= [(E_{cm} h^3) / (12 (1 - v^2) k)]^{0.25}$

Equivalent radius of single load	
a_{single}	77 mm

Adjacant double point load	
Distance apart back-to-back	
$l_{spacing}$	400 mm
Considered as one load?	
$l_{spacing} \leq 2h$	320 mm Green = Yes
	Red = No
Equivalent radius of single load $\leftarrow$	
a_{single}	77 mm

Hybrid concrete floor
Steel fibres with top reinforcement
Sagging bending moment capacity
M_p 12.7 kNm
Hogging bending moment capacity
M_n 19.7 kNm

Linear interpolation single design loads.
Internal design load
$P_{u,a/l}$ 335 kN
Edge design load
$P_{u,a/l}$ 153 kN
Corner design load
$P_{u,a/l}$ 69 kN

Internal design dual load
$P_{u,a/l}$ 373 kN
Internal design quadruple load
$P_{u,a/l}$ 410 kN

ULS load F_{ed}		
Single point load	CC1	Double load ULS
F 95 kN	F_{Ed}	$=2 \cdot 95 \cdot 1.3$ 257 kN

Meyerhof: design load single point loads	
Theoretical point load	a/l =0
Patch load	a/l ≥ 0.2
Linear interpolation	0 < a/l < 0.2
a/l 0.12 $\longrightarrow$	Linear interpolation

Internal design load	
Theoretical load	Patch load
$P_{u,0} = 2\pi (M_p + M_n)$	$P_{u,0.2} = 4\pi (M_p + M_n) / [1 - (a/3l)]$
$P_{u,0} =$ 204 kN	$P_{u,0.2} =$ 425 kN

Edge design load	
Theoretical load	Patch load
$P_{u,0} = [\pi (M_p + M_n)/2] + 2M_n$	$P_{u,0.2} = [\pi (M_p + M_n) + 4 M_n]/\left[1 - \frac{2a}{3l}\right]$
$P_{u,0} =$ 90 kN	$P_{u,0.2} =$ 196 kN

Corner design load	
Theoretical load	Patch load
$P_{u,0} = 2M_n$	$P_{u,0.2} = 4M_n / [1 - (a/l)]$
$P_{u,0} =$ 39 kN	$P_{u,0.2} =$ 90 kN

Meyerhof multiple internal point loads.	
Design load dual point loads	
Theoretical load	Patch load
$P_{u,0} = [2\pi + (1.8 \, x \,/l)][M_p + M_n]$	$P_{u,0.2} = \left[\frac{4\pi}{1-(a/3l)} + \frac{1.8x}{l-(a/2)}\right][M_p + M_n]$
$P_{u,0} =$ 240 kN	$P_{u,0.2} =$ 463 kN

Design load quadruple point loads	
Theoretical load	Patch load
$P_{u,0} = \left[2\pi + \frac{1.8 \, (x + y)}{l}\right][M_p + M_n]$	$P_{u,0.2} = \left[\frac{4\pi}{1-(a/3l)} + \frac{1.8(x + y)}{l-(a/2)}\right][M_p + M_n]$
$P_{u,0} =$ 276 kN	$P_{u,0.2} =$ 501 kN

Westergaard

Theory of Westergaard	
radius of relative stiffness l	thickness floor
l 661 mm	h 160 mm
equivalent radius of contact area	E-modulus concrete
a $= a_c + 0.5h$	E 32837 MPa
a 249 mm	Poisson ratio
	v 0.15
equivalent radius of resisting section	Subgrade
b 246 mm	k 0.06 N/mm^3

Stresses single load	
$F_{Ed} = F \cdot 1.35$ 128 kN	
Internal stress - tensile stress at bottom fibre	
$\sigma_m =$ 5.9 MPa	$\sigma_m \approx \dfrac{0{,}55F}{h^2}\left[\ln\left(\dfrac{l}{b}\right)+0{,}62\right]+\dfrac{0{,}05F}{h^2}\left(\dfrac{b}{l}\right)^2$
Edge stress - tensile stress at bottom fibre	
$\sigma_e =$ 10.6 MPa	$\sigma_e \approx \dfrac{0{,}35F}{h^2}\left[\ln\left(\dfrac{Eh^3}{100ka^4}\right)+2{,}07+1{,}53\left(\dfrac{a}{l}\right)\right]$
Corner stress - tensile stress at top fibre	
$\sigma_c =$ 7.0 MPa	$\sigma_c = \dfrac{3F}{h^2}\left[1{,}0-\left(\dfrac{a\sqrt{\pi}}{l}\right)^{0{,}72}\right]$

Stresses double load	
$F_{Ed} = 2 \cdot F \cdot 1.35$ 257 kN	
Internal stress - tensile stress at bottom fiber	
$\sigma_m =$ 8.9 MPa	$\sigma_m \approx \dfrac{0{,}55F}{h^2}\left[\ln\left(\dfrac{l}{b}\right)+0{,}62\right]+\dfrac{0{,}05F}{h^2}\left(\dfrac{b}{l}\right)^2$
Edge stress - tensile stress at bottom fiber	
$\sigma_e =$ 15.5 MPa	$\sigma_e \approx \dfrac{0{,}35F}{h^2}\left[\ln\left(\dfrac{Eh^3}{100ka^4}\right)+2{,}07+1{,}53\left(\dfrac{a}{l}\right)\right]$
Corner stress - tensile stress at top fiber	
$\sigma_c =$ 7.6 MPa	$\sigma_c = \dfrac{3F}{h^2}\left[1{,}0-\left(\dfrac{a\sqrt{\pi}}{l}\right)^{0{,}72}\right]$

Punching shear and UDL

Punching shear		
F=		95 kN
P= 1.35*F		1E+05 N
Double load		
P= 1.35*2*F		3E+05 N

Effective depth and radius of relative stiffness		
d	126.5 mm	
l	664 mm	

Base plate		
x		150 mm
y		125 mm

Ground reaction

$$R_p = 1{,}4 \left(\frac{d}{l}\right)^2 P + 0{,}47(x+y)\frac{dP}{l^2}$$

R_{cp} (single load)	11267 N
R_{cp} (double load)	22534 N
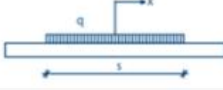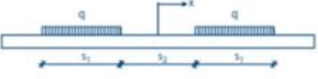
Shear

v_{max}	5.28 MPa	$= 0.5k_2 f_{cd}$
k_2	0.5	$= 0.6\,(1 - f_{ck}/250)$
$v_{Rd,c,m}$	0.54 MPa	$= 0.5k_2 f_{cd}\ f_{ck}^{0.5}$
k_s	2.0	$= 1 + (200/d)^{0.5} \le 2$
$v_{Rd,c}$	0.54 MPa	$= \frac{0.18k}{\gamma_c}(100\rho_l f_{ck})^{0.33} \ge 0.035k_s^{1.5}f_{ck}^{0.5}$
ρ_l	0.0030	$= A_{sx}/bd$
v_f	0.252 MPa	$= [0.12\,(f_{r1}+f_{r2}+f_{r3}+f_{r4})/4]/2$

Punching shear capacity

Singe load		Double load	
Critical perimeter		Critical perimeter	
u_1 2140 mm		u_1 3040 mm	
Load capacity		Load capacity	
P_p 214967 N	$P_p = (v_{Rd,c} + v_f)\,u_1 d$	P_p 305389 N	$P_p = (v_{Rd,c} + v_f)\,u_1 d$
Design load		Design load	
P_{Ed} 116983 N	$P_{Ed} = P - R_{cp}$	P_{Ed} 233966 N	$P_{Ed} = P - R_{cp}$
UC **0.54**		UC **0.77**	

Theory of Hetényi

λ	0.00108 1/mm	$\lambda = [k/(4EI)]^{0.25} = [3k/(Eh^3)]^{0.25}$
λ	1.08 1/m'	
Characterisic length		
$1/\lambda$	930 mm	

Floor

E-modulus E_{cm} =	32837 MPa	
E_{cm} =	3.3E+07 kN/m^2	
Thickness h =	160 mm	
h =	0.16 m	
Subgrade k =	0.06 N/mm^3	
k =	60000 kN/m^3	

Uniformly distributed load

q =	75 kN/m^2

Maximum bending moments due to UDL

Positive (sagging) bending moment

a	0.73 -	$a = \pi/4\lambda$
$B\lambda a$	0.32 -	$B\lambda_x = e^{-\lambda x}.\sin\lambda\,x$
$M_{p,max}$	10.45 kNm	$M = [q/2\lambda^2].B\lambda_a$
	10.69 kNm	$M_{p,max} = M/(1-v^2)$

Situation a:

Cracking moment

f_{ctm}	=	2.90 MPa
$f_{ctd,fl}$	=	2.78 MPa

$$f_{ctd,fl} = f_{ctm} \times (1.6 - h/1000)/\gamma_m$$

M_{cr}	=	11864 Nmm/m'
		11.86 kNm/m'

$$M_{un} = f_{ctd,fl}\,(h^2/6)$$

Negative (hogging) bending moment

a	0.73 -	$a = \pi/4\lambda$
b	3.65 -	$b = 5a$
$B\lambda a$	0.32 -	$B\lambda_x = e^{-\lambda x}.\sin\lambda\,x$
$B\lambda b$	-0.01 -	
$M_{n,max}$	-10.90 kNm	$M = [-q/2\lambda^2].(B\lambda_a - B\lambda_b)$
	-11.15 kNm	$M_{n,max} = M/(1-v^2)$

Situation b:

Unity checks

Situation a		
UC	0.90	$UC = M_{p,max}/M_{cr}$
Situation b		
UC	0.94	$UC = |M_{n,max}/M_{cr}|$

Appendix B. CRACK-WIDTH CALCULATION APPROACH

This appendix provides further elaboration on the crack-width calculations that have been done for the design approach. The jointless concrete floors are said to only crack when the bending cracking moment M_{crack} is reached. The minimum thicknesses of the concrete ground floors are set to ensure that the floors only crack in pure bending, as the minimum thickness ensures that the drying shrinkage won't develop uniform tension components that could form cracks.

Through horizontal forces equilibrium and bending moments equilibrium the system of two equations, based on Fig. B-1, can be solved. The unknowns height of the concrete compressive zone h_x and the strain in the outer fibre of steel fibre reinforced concrete tension zone $\varepsilon_{ft,max}$ will be solved. The bending cracking moment M_{crack} is calculated with the flexural tensile strength $f_{ctm,fl}$:

$$M_{crack} = \frac{1}{6} \cdot b \cdot h^2 \cdot f_{ctm,fl} \tag{B.1}$$

with

$$f_{ctm,fl} = \left(1.6 - \frac{h}{1000}\right) \cdot f_{ctm} \tag{B.2}$$
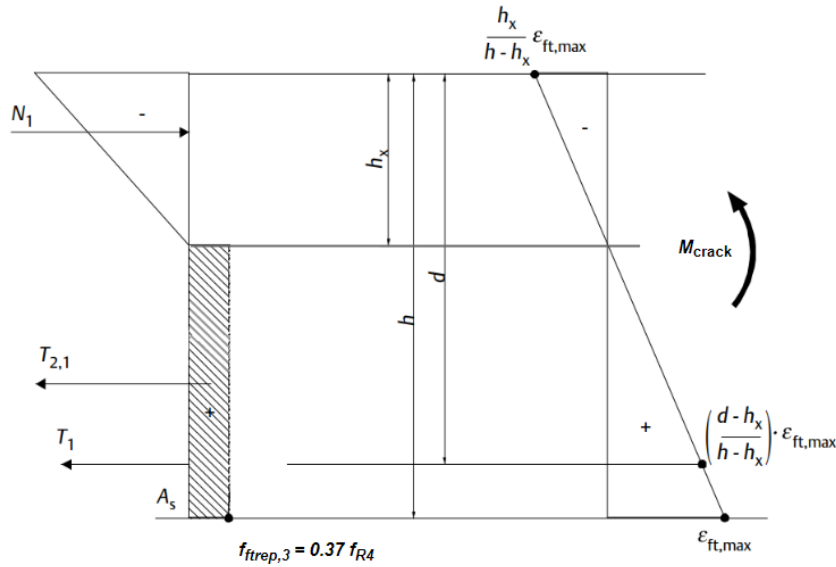
Fig. B-1 Stress and strain diagram for steel fibre reinforced concrete cross-section loaded in bending in serviceability limit state, figure adapted from (CURNET, 2007).

As the bending moment is set to be the cracking moment, bending moment equilibrium follows as:

$$M_{crack} = \frac{2}{3} h_x N_1 + \frac{1}{2} \left(h - h_x \right) T_{2.1} + (d - h_x) T_1 \tag{B.3}$$

Horizontal forces equilibrium must also be satisfied:

$$\Sigma H = 0 \rightarrow N_1 = T_1 + T_{2.1} \tag{B.4}$$

Where:

$$N_1 = 0.5 \, h_x b \, E_{cm} \varepsilon_{ft,max} \left(\frac{h}{h - h_x}\right) \tag{B.5}$$

$$T_1 = A_s \sigma_s = A_s E_s \varepsilon_s = A_s E_s \left(\frac{d - h_x}{h - h_x} \right) \varepsilon_{ft,max} \qquad (B.6)$$

$$T_{2.1} = b \ h - h_x \ (0.37 f_{R4}) \qquad (B.7)$$

For this system of equations to be solved the values have to be specified. It is not possible to solve this system and rewrite the equations where the height of the compression zone h_x is written in the remaining terms. The height of the concrete compressive zone must be found through an iterative approach.

To automate the process and be able to write an Excel sheet that is able to compute many calculations in quick succession the following steps have been made.

By putting Eq. (B.1) and (B.5) to (B.7) into Eq. (B.3) it can be solved where the unknown term $\varepsilon_{ft,max}$ is written in terms of h_x and the other non-specified parameters yet. For this the program Maple 2017 has been used of which the worksheet and the output that has been added into Excel is shown in Appendix C.

At first some assumptions have been made. The centre to centre distance for the top reinforcement mesh is fixed to 100 mm. Considering the control of cracking a lower c.t.c. distance is preferable, but as the practical minimum c.t.c. distance for the reinforcement mesh is 100 mm, this distance of 100 mm is considered to be the minimum and best required distance and therefore fixed. The reinforcement area A_s per meter width becomes:

$$A_s = \frac{1}{4} \pi \phi^2 \left(\frac{1000}{ctc} \right) = \frac{1}{4} \pi \phi^2 \left(\frac{1000}{100} \right) \qquad (B.8)$$

Where ϕ is the diameter of the reinforcement bars in mm. The steel reinforcement bars have a modulus of elasticity of $E_s = 200$ GPa.

As a jointless floor has large bays in both horizontal directions, when for example a floor area of 100 x 100 m is considered, cracks will arise at the top surface in both directions. Crack-widths will be larger when the floor cross-section cracks due to bending in the direction where the lower reinforcement bars of the mesh have to carry the tensile forces. For this case the effective height of the concrete cross-section d will be lower and calculated with:

$$d = h - c - 1.5 \ \phi \qquad (B.9)$$

The thickness h is the height of the concrete floor cross-section, the concrete cover is denoted as c and the reinforcement bar diameter with ϕ.

Solving and rewriting Eq. (B.3) a term for $\varepsilon_{ft,max}$ is found, line (7) in Appendix C, written in the remaining unspecified parameters. Only when specifying the remaining concrete floor parameters the horizontal forces equilibrium can be solved. Where the remaining parameters are (the notation in brackets is the notation used in the Maple worksheet):

- Compressive strength f_{cm} (fcm)
- Tensile strength f_{ctm} (fctm)
- Concrete modulus of elasticity E_{cm} (Ecm)
- Thickness h (h)
- Concrete cover c (cc)
- Reinforcement bar diameter ϕ (dd)
- Residual flexural strength f_{R4} (sr)

Once the above parameters are specified the horizontal force equilibrium can be solved where the remaining unknown the height of the concrete compressive zone h_x will be found through an iterative manner.

Once solved the steel tensile force T_1 is known, through which the needed steel stress σ_s in the cracked cross-section can be found:

$$\sigma_s = T_1/A_s \tag{B.10}$$

With the height of the concrete compressive zone known the effective tension area of the concrete $A_{c,ef}$ can be computed for which its effective height is the lesser of:

$$h_{c,ef} = 2.5 \left(c - \frac{\phi}{2} \right)$$

$$h_{c,ef} = \frac{h - h_x}{3}$$

$$h_{c,ef} = \frac{h}{2}$$

Multiplying the minimum value found with the width b the effective tension area of the concrete is found. Now the effective reinforcement ratio for the member can be found:

$$\rho_{s,eff} = \frac{A_s}{A_{c,ef}} \tag{B.11}$$

The effective reinforcement ratio $\rho_{s,eff}$ is needed in the crack-width expression and to find the maximum steel stress in a crack in the crack formation stage σ_{sr}. The latter is for hybrid reinforced concrete:

$$\sigma_{sr} = (f_{ctm} - f_{Ftsm}) \cdot (1 + \alpha_e \rho_s)/\rho_{s,eff} \tag{B.12}$$

Where the residual tensile strength from to the steel fibres interaction is $f_{Ftsm} = f_{ftrep,3}$.

The expression to calculate the crack-width at the location at the reinforcement bar is:

$$w_d = \frac{1}{2} \frac{\phi_s}{\rho_{s,eff}} \frac{(f_{ctm} - f_{Ftsm})}{\tau_{bm}} \frac{1}{E_s} (\sigma_s - \beta \sigma_{sr} + \eta_r \varepsilon_{sh} E_s) \tag{B.13}$$

The values for the terms β, η_r and τ_{bm} are listed in Table. B-1. These values are the recalibrated values as applied in the Eurocode. In this thesis the jointless floor is considered to remain in the crack formation stage where shrinkage is the imposed (long term) load.

Table. B-1 Values for β, η_r and τ_{bm} from Eq. (B.13) for various conditions.

	Crack formation stage	Stabilized cracking stage
Short term loading	$\beta = 0.6$ $\eta_r = 0$ $\tau_{bm} = 2.0\, f_{ctm}$	$\beta = 0.6$ $\eta_r = 0$ $\tau_{bm} = 2.0\, f_{ctm}$
Long term or dynamic loading	$\beta = 0.6$ $\eta_r = 0$ $\tau_{bm} = 1.6\, f_{ctm}$	$\beta = 0.4$ $\eta_r = 1$ $\tau_{bm} = 2.0\, f_{ctm}$

In bending the crack-width at the outer tensile fibre is larger than the crack-width at the location of the steel. The latter is the one calculated in Eq. (B.13) and to find the crack-width at the top surface of the jointless concrete ground floor the following expression is used:

$$w_{opp} = w_d \ (\frac{h - h_x}{d - h_x})$$

(B.14)

In the combined spreadsheet that has been run for the optimisation of the jointless concrete floor this value is used as its output.

Appendix C. MAPLE OUTPUT

This appendix shows the Maple output used to set up the Excel scheme that was able to calculate a multiple of variants within seconds. Line (15) and (16) show the steel stress and compressive strength in the outer fibre, these are example values that have been used to validate the Excel scheme.

> restart;
> hoh := 100;

$A[s] := 0.25 \cdot 3.141592654 \cdot dd^2 \cdot \left(\dfrac{1000}{hoh} \right); E[s] := 200000; d := h - cc - dd - 0.5 \cdot dd; b := 1000; fctmfl := \left(1.6 - \dfrac{h}{1000} \right) \cdot fctm;$

$$hoh := 100$$

$$A_s := 7.853981635 \, dd^2$$

$$E_s := 200000$$

$$d := h - cc - 1.5 \, dd$$

$$b := 1000$$

$$fctmfl := \left(1.6 - \dfrac{h}{1000} \right) fctm \tag{1}$$

> $M[crack] := \dfrac{1}{6} \cdot b \cdot h^2 \cdot fctmfl;$

$$M_{crack} := \dfrac{500 \, h^2 \left(1.6 - \dfrac{h}{1000} \right) fctm}{3} \tag{2}$$

> $N1 := 0.5 \cdot b \cdot xu \cdot Ecm \cdot epsilon[ft, max] \cdot \left(\dfrac{xu}{(h - xu)} \right);$

$$N1 := \dfrac{500.0 \, xu^2 \, Ecm \, \epsilon_{ft, \, max}}{h - xu} \tag{3}$$

> $T1 := A[s] \cdot E[s] \cdot \left(\dfrac{(d - xu)}{(h - xu)} \right) \cdot epsilon[ft, max];$

$$T1 := \dfrac{1.570796327 \, 10^6 \, dd^2 \, (h - cc - 1.5 \, dd - xu) \, \epsilon_{ft, \, max}}{h - xu} \tag{4}$$

> $T2 := b \cdot (h - xu) \cdot (0.37 \cdot sr);$

$$T2 := 370.00 \, (h - xu) \, sr \tag{5}$$

> $Eq(1) := M[crack] = \dfrac{2}{3} \cdot xu \cdot N1 + \dfrac{1}{2} \cdot (h - xu) \cdot T2 + (d - xu) \cdot T1;$

$$Eq(1) := \dfrac{500 \, h^2 \left(1.6 - \dfrac{h}{1000} \right) fctm}{3} = \dfrac{333.3333333 \, xu^3 \, Ecm \, \epsilon_{ft, \, max}}{h - xu} + 370.00 \left(\dfrac{h}{2} \right. \tag{6}$$

$$\left. - \dfrac{xu}{2} \right) (h - xu) \, sr + \dfrac{1.570796327 \, 10^6 \, (h - cc - 1.5 \, dd - xu)^2 \, dd^2 \, \epsilon_{ft, \, max}}{h - xu}$$

> $fx1 := solve(Eq(1), epsilon[ft, max]);$

$$fx1 := -\left(1.666666667 \, 10^6 \, (h^3 \, fctm - 1600. \, h^2 \, fctm + 1110. \, sr \, h^2 - 2220. \, sr \, h \, xu \right. \tag{7}$$

$$+ 1110. \, sr \, xu^2) \, (h - 1. \, xu) \big) / \big(3.333333333 \, 10^9 \, xu^3 \, Ecm + 1.570796327 \, 10^{13} \, cc^2 \, dd^2$$

$$+ 4.712388981 \, 10^{13} \, cc \, dd^3 - 3.141592654 \, 10^{13} \, cc \, dd^2 \, h + 3.141592654 \, 10^{13} \, cc \, dd^2 \, xu$$

$$+ 3.534291736 \, 10^{13} \, dd^4 - 4.712388981 \, 10^{13} \, dd^3 \, h + 4.712388981 \, 10^{13} \, dd^3 \, xu$$

$$+ 1.570796327 \, 10^{13} \, dd^2 \, h^2 - 3.141592654 \, 10^{13} \, dd^2 \, h \, xu + 1.570796327 \, 10^{13} \, dd^2 \, xu^2 \big)$$
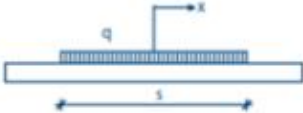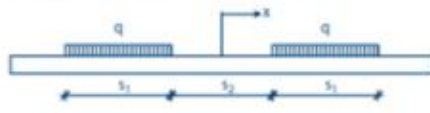
> $fcm := 38; dd := 6; hoh := 100; cc := 30; sr := 4; fctm := 5; Ecm := 35000; h := 90; E[s] := 200000;$

$$fcm := 38$$
$$dd := 6$$
$$hoh := 100$$
$$cc := 30$$
$$sr := 4$$
$$fctm := 5$$
$$Ecm := 35000$$
$$h := 90$$
$$E_s := 200000 \tag{8}$$

> $epsilon[ft, max] := fx1$

$$\epsilon_{ft,\,max} := \tag{9}$$
$$-\left(1.666666667\ 10^6\left(-2.5191000\ 10^7 - 799200.\,xu + 4440.\,xu^2\right)(90 - 1.\,xu)\right)\Big/$$
$$\left(1.166666667\ 10^{14}\,xu^3 + 1.470830849\ 10^{18} - 5.767964114\ 10^{16}\,xu\right.$$
$$\left.+\ 5.654866777\ 10^{14}\,xu^2\right)$$

> $Eq(2) := N1 = T1 + T2;$

$$Eq(2) := -\left(2.916666667\ 10^{13}\,xu^2\left(-2.5191000\ 10^7 - 799200.\,xu + 4440.\,xu^2\right)(90 \tag{10}$$
$$-\ 1.\,xu)\right)\Big/\left(\left(1.166666667\ 10^{14}\,xu^3 + 1.470830849\ 10^{18} - 5.767964114\ 10^{16}\,xu\right.\right.$$
$$\left.+\ 5.654866777\ 10^{14}\,xu^2\right)(90 - xu)\right) = -\left(9.424777964\ 10^{13}\,(51.0 - xu)\,\right($$
$$-2.5191000\ 10^7 - 799200.\,xu + 4440.\,xu^2\right)(90 - 1.\,xu)\right)\Big/\left(\,(90\right.$$
$$-\ xu)\,\left(1.166666667\ 10^{14}\,xu^3 + 1.470830849\ 10^{18} - 5.767964114\ 10^{16}\,xu\right.$$
$$\left.\left.+\ 5.654866777\ 10^{14}\,xu^2\right)\right) + 133200.00 - 1480.00\,xu$$

> **use** $RealDomain$ **in** $fx2 := solve(Eq(2), xu)$ **end use;**

$$fx2 := 15.29697530,\ -39.59408219 \tag{11}$$

> $xu := fx2[1];$

$$xu := 15.29697530 \tag{12}$$

> $epsilon[ft, max];$

$$0.003978426847 \tag{13}$$

> $N1; T1; T2$

$$218083.2797$$
$$107522.8032$$
$$110560.4766 \tag{14}$$

> $sigma[s] := \dfrac{T1}{A[s]};$

$$\sigma_s := 380.2841249 \tag{15}$$

> $f[c] := Ecm \cdot epsilon[ft, max] \cdot \left(\dfrac{xu}{(h - xu)}\right);$

$$f_c := 28.51325513 \tag{16}$$

>

159

Appendix D. CALCULATION OF M_{REP} AND $M_{W,MAX}$

The calculation of M_{rep} for a uniformly distributed load q = 75 kN/m². The maximum negative (hogging) bending moment $M_{n,max} = M_{rep} = 5.92$ kNm. The calculation of the maximum bending moment $M_{w,max} = 17.35$ kNm is done in accordance with the CUR-111 and calculated with Maple, the output is shown on the next page.

Theory of Hetényi

λ	0.00148 1/mm	$\lambda = [k/(4EI)]^{0.25} = [3k/(Eh^3)]^{0.25}$
λ	1.48 1/m'	
Characterisic length		
1/λ	677 mm	

Maximum bending moments due to UDL

Positive (sagging) bending moment

a	0.53 -	$a = \pi /4\lambda$
Bλa	0.32 -	$B\lambda_x = e^{-\lambda x}.\sin\lambda \, x$
$M_{p,max}$	5.55 kNm	$M = [q /2\lambda^2].B\lambda_a$
	5.67 kNm	$M_{p,max} = M/(1-v^2)$

Situation a:

Negative (hogging) bending moment

a	0.53 -	$a = \pi /4\lambda$
b	2.66 -	$b = 5a$
Bλa	0.32 -	$B\lambda_x = e^{-\lambda x}.\sin\lambda \, x$
Bλb	-0.01 -	
$M_{n,max}$	-5.78 kNm	$M = [-q /2\lambda^2].(B\lambda_a - B\lambda_b)$
	-5.92 kNm	$M_{n,max} = M/(1-v^2)$

Situation b:

Floor

E-modulus $E_{c,eff}$ =		17235 MPa
	E_{cm} =	1.7E+07 kN/m²
Thickness	h =	130 mm
	h =	0.13 m
Subgrade	k =	0.06 N/mm³
	k =	60000 kN/m³

Uniformly distributed load

q =	75 kN/m²

Cracking moment

f_{ctm}	=	4.00 MPa
$f_{ctd,fl}$	=	5.88 MPa

$$f_{ctd,fl} = f_{ctm} \times (1.6 - h/1000)/\gamma_m$$

M_{cr}	=	16562 Nmm/m'
		16.56 kNm/m'

$$M_{un} = f_{ctd,fl} \, (h^2 / 6)$$

Unity checks

Situation a

UC	0.34	$UC = M_{p,max}/M_{cr}$

Situation b

UC	0.36	$UC = |M_{n,max}/M_{cr}|$

> *restart*;

> $\text{epsilon}[ft, \max] := \dfrac{w[\max]}{2 \cdot (h - xu)}$; $N1 := 0.5 \cdot b \cdot xu \cdot E[c, eff] \cdot \text{epsilon}[ft, \max] \cdot \left(\dfrac{xu}{(h - xu)} \right)$;

$T1 := A[s] \cdot E[s] \cdot \left(\dfrac{(d - xu)}{(h - xu)} \right) \cdot \text{epsilon}[ft, \max]$; $T2 := b \cdot (h - xu) \cdot (0.45 \cdot fR1)$;

$$\epsilon_{ft, \max} := \frac{w_{\max}}{2h - 2xu}$$

$$N1 := \frac{0.5\, b\, xu^2\, E_{c, eff}\, w_{\max}}{(2h - 2xu)\,(h - xu)}$$

$$T1 := \frac{A_s\, E_s\, (d - xu)\, w_{\max}}{(h - xu)\,(2h - 2xu)}$$

$$T2 := 0.45\, b\, (h - xu)\, fR1 \tag{1}$$

> $E[c, eff] := 17235$; $E[s] := 200000$; $b := 1000$; $h := 130$; $hoh := 100$; $cc := 20$; $dd := 6$;

$A[s] := 0.25 \cdot 3.141592654 \cdot dd^2 \cdot \left(\dfrac{1000}{hoh} \right)$; $d := h - cc - 1.5 \cdot dd$; $b := 1000$; $w[\max] :=$

0.3; $fR1 := 4$;

$$E_{c, eff} := 17235$$
$$E_s := 200000$$
$$b := 1000$$
$$h := 130$$
$$hoh := 100$$
$$cc := 20$$
$$dd := 6$$
$$A_s := 282.7433389$$
$$d := 101.0$$
$$b := 1000$$
$$w_{\max} := 0.3$$
$$fR1 := 4 \tag{2}$$

> $eq(1) := N1 = T1 + T2$;

$$eq(1) := \frac{2.58525000\ 10^6\, xu^2}{(260 - 2xu)\,(130 - xu)} = \frac{1.696460033\ 10^7\,(101.0 - xu)}{(130 - xu)\,(260 - 2xu)} + 234000.00 \tag{3}$$

$- 1800.00\, xu$

> $fx := solve(eq(1), xu)$;

$$fx := 38.45469585,\ -183.2898479 + 189.5097130\, I,\ -183.2898479 - 189.5097130\, I \tag{4}$$

> $xu := fx[1]$;

$$xu := 38.45469585 \tag{5}$$

> $M[w, \max] := \dfrac{2}{3} \cdot xu \cdot N1 + \dfrac{1}{2} \cdot (h - xu) \cdot T2 + (d - xu) \cdot T1$;

$$M_{w, \max} := 1.734922819\ 10^7 \tag{6}$$